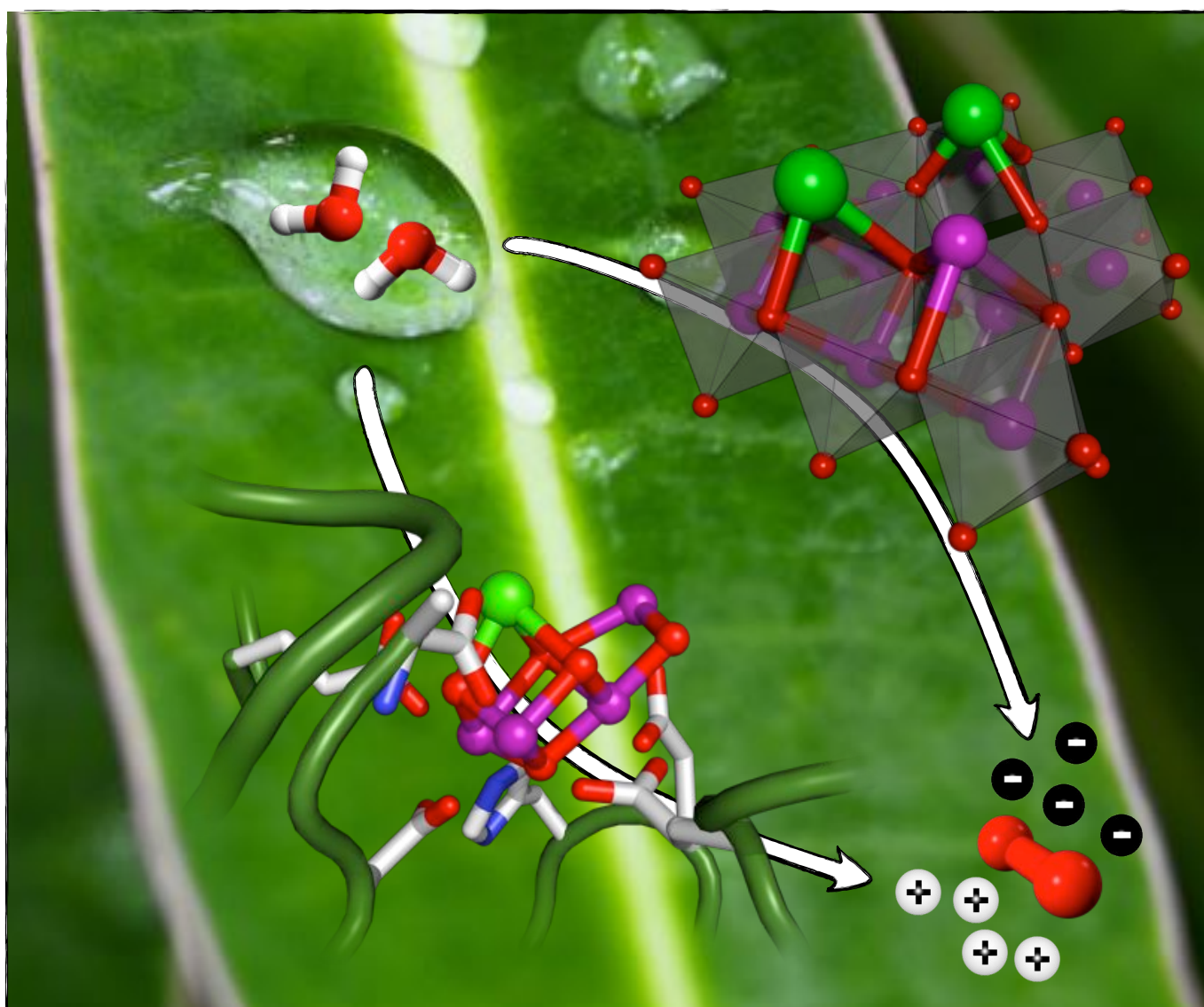


# Mixed Manganese Oxides as Biomimetic Water-Oxidation Catalysts

Promising Materials for the Production of Solar Fuels by Artificial Photosynthesis





# Mixed Manganese Oxides as Biomimetic Water-Oxidation Catalysts

Promising Materials for the Production of  
Solar Fuels by Artificial Photosynthesis

Dissertation zur Erlangung des Doktorgrades der  
Mathematisch-Naturwissenschaftlichen Fakultät der  
Christian-Albrechts-Universität zu Kiel

vorgelegt von

Mathias Wiechen

Kiel, 2013



Erster Gutachter: Prof. Dr. Felix Tuczek  
Zweiter Gutachter: Prof. Dr. Wolfgang Bensch  
Tag der mündlichen Prüfung: 17. Mai 2013  
Zum Druck genehmigt: 17. Mai 2013  
gez. Prof. Dr. Wolfgang J. Duschl, Dekan



# Abstract

To take full advantage of the enormous potential of the sun as sustainable energy source, solutions to the capture of solar energy and its conversion into readily utilizable and storable forms are urgently required. Against this background, light-driven water-splitting is an intensely discussed approach for the generation of a so called solar fuel. In reaction sequences for the production of such solar fuels, the catalysis of the water-oxidation half-reaction represents one of the major challenges.

In nature, solar energy is captured and converted during photosynthesis. In this fundamental biological process  $\text{CO}_2$ ,  $\text{H}_2\text{O}$  and light energy are used to form biomass and  $\text{O}_2$ . The water-oxidation reaction is catalyzed within the enzyme photosystem II (PSII) by a  $\mu$ -oxido bridged  $\text{CaMn}_4$  cluster, the oxygen-evolving-complex (OEC).

Inspired by the composition of the OEC, layered calcium manganese oxides of the birnessite family have been prepared prior to this work and showed promising activities in water-oxidation catalysis by far exceeding the activity of pure manganese oxides. These results raised questions concerning the role of  $\text{Ca}^{2+}$  ions in these catalytic reactions by synthetic Ca-birnessites. In case of PSII, the enzyme is known to be virtually inactive if  $\text{Ca}^{2+}$  is removed from the OEC. But the catalytic activity can be restored not only by the addition of  $\text{Ca}^{2+}$  but also  $\text{Sr}^{2+}$  ions, albeit at a reduced rate.

In the research project presented in this thesis, various layered manganese oxides were synthesized containing intercalated  $\text{Ca}^{2+}$  ions in different concentrations or  $\text{K}^+$ ,  $\text{Sr}^{2+}$ ,  $\text{Mg}^{2+}$ ,  $\text{Cd}^{2+}$ ,  $\text{Al}^{3+}$ ,  $\text{Zn}^{2+}$ ,  $\text{Pb}^{2+}$  and  $\text{Fe}^{3+}$ , respectively. A detailed analysis by EDX, AAS, thermogravimetry, SEM,  $\text{N}_2$  adsorption/desorption isotherms, IR spectroscopy and XRD revealed insights into properties of the prepared materials. A relatively high amount of water and hydroxide molecules is placed in between layers build up from edge-sharing  $\text{MnO}_6$  octahedra. The morphology of the oxide materials is influenced by their compositions, as higher amounts of additional cations incorporated in the structures are resulting in the formation of smaller, less ordered particles, exhibiting a larger specific surface area. X-ray absorption spectroscopy (XAS) carried out at the Mn K-edge of Ca-, Sr- and Mg-birnessites showed that these materials have similar atomic structures despite differences in their compositions and morphologies. Furthermore, the oxides contain structural units, resembling the  $\mu$ -oxido  $\text{CaMn}_4$  core of the OEC.

In water-oxidation experiments carried out using the prepared M-birnessites as catalysts and  $\text{Ce}^{\text{IV}}$  as well as photochemically generated  $[\text{Ru}(\text{bpy})_3]^{3+}$  as oxidants, all probed materials showed catalytic activity. However, reactivity correlated with the type of the intercalated cation and can best be formulated as  $\text{Ca}^{2+} > \text{Sr}^{2+} > \text{Mg}^{2+} / \text{Cd}^{2+} / \text{Al}^{3+} / \text{Zn}^{2+} / \text{Pb}^{2+} / \text{Fe}^{3+}$ . Also less pronounced dependencies of the reactivity on the concentration of the additional cations and the ripening periods used during the oxide syntheses could be observed. Interestingly, the relative reactivities of Ca-, Sr- and Mg-birnessites are similar to the activities in water-oxidation reported for the  $\text{Ca}^{2+}$ ,  $\text{Sr}^{2+}$  and  $\text{Mg}^{2+}$  reactivated OEC. Based on these findings, mechanistic scenarios proposed for the O–O bond formation catalyzed by the OEC were adopted to M-birnessites. In these mechanistic scenarios,  $\text{Ca}^{2+}$  (or  $\text{Sr}^{2+}$ ) ions may act as binding and activation site for substrate

water molecules. Overall, the results presented in this thesis are demonstrating that M-birnessites are promising candidates to be utilized as water-oxidation catalysts in artificial photosynthesis for sustainable energy production. Furthermore, Ca-birnessites in particular are outstanding OEC model compounds, as they mimic both structure and function of the biological paragon.

# Kurzzusammenfassung

Die Sonne bietet ein schier unbegrenztes Potential, um als saubere und nachhaltige Energiequelle zu dienen. Um dieses Potential jedoch uneingeschränkt nutzen zu können, ist es nötig, Wege zu finden, um Sonnenenergie zu absorbieren und in speicherbare, leicht zugängliche Formen zu überführen. In diesem Zusammenhang ist die lichtgetriebene Spaltung von Wasser zur Herstellung eines sogenannten solaren Brennstoffs ein vielfach diskutierter Ansatz. In solch einem Szenario stellt die katalytische Wasseroxidation einen der zentralen und besonders herausfordernden Reaktionsschritte dar.

Die Natur bedient sich hierfür der Photosynthese, während der Lichtenergie aufgenommen und zur Umwandlung von  $\text{CO}_2$  und  $\text{H}_2\text{O}$  in Biomasse und  $\text{O}_2$  eingesetzt wird. Die Wasseroxidation findet dabei im Enzym Photosystem II (PSII), genauer in dessen aktiven Zentrum, einem  $\mu$ -oxido verbrückten  $\text{CaMn}_4$ -Komplex statt. Dieser Komplex wird als OEC (von *oxygen-evolving-complex*) bezeichnet.

Der Zusammensetzung des OEC folgend wurden bereits geschichtete Calcium-Manganoxide synthetisiert, die dem natürlich vorkommenden Mineral Birnessit ähneln. Hinsichtlich der Wasseroxidation zeigten diese Materialien eine vielversprechende katalytische Aktivität, die bei weitem die von reinen Manganoxiden überstieg. Daher stellte sich die Frage, welche Rolle die  $\text{Ca}^{2+}$  Ionen bei dieser Reaktion spielen. Über den OEC ist bekannt, dass die Aktivität praktisch verloren geht, wenn  $\text{Ca}^{2+}$  aus dem Enzym entfernt wird. Jedoch kann die katalytische Aktivität wieder hergestellt werden, indem  $\text{Ca}^{2+}$  oder auch  $\text{Sr}^{2+}$  Ionen hinzugegeben werden. Allerdings erfolgt die Reaktivierung des Enzyms im Falle des  $\text{Sr}^{2+}$  nur in deutlich geringerem Umfang.

Im Rahmen der hier präsentierten Forschungsarbeit wurden verschiedene geschichtete Manganoxide synthetisiert, die  $\text{Ca}^{2+}$  Ionen in unterschiedlichen Konzentrationen, oder auch  $\text{K}^+$ ,  $\text{Sr}^{2+}$ ,  $\text{Mg}^{2+}$ ,  $\text{Cd}^{2+}$ ,  $\text{Al}^{3+}$ ,  $\text{Zn}^{2+}$ ,  $\text{Pb}^{2+}$  und  $\text{Fe}^{3+}$  enthielten. Die ausführliche Analyse der Materialien mittels EDX, AAS, Thermogravimetrie, SEM,  $\text{N}_2$  sorptions Isothermen, IR Spektroskopie und XRD ergab, dass eine relativ große Anzahl an Wasser- und Hydroxidmolekülen zwischen den Oxidschichten gebunden ist. Die Schichten selbst werden aus kantenverknüpften  $\text{MnO}_6$  Oktaedern gebildet. Es konnte gezeigt werden, dass der Einbau von größeren Mengen an zweiwertigen Kationen zur Ausbildung von Schichten führt, die eine höhere Anzahl an Fehlstellen aufweisen. Zusätzlich nimmt die Größe der Partikel ab und deren spezifische Oberfläche zu. Röntgenabsorptionsspektroskopische Messungen, die an der Mn K-Kante an Ca-, Sr- und Mg-Birnessiten durchgeführt wurden, zeigten, dass sich die Strukturen dieser Materialien auf der atomaren Ebene praktisch nicht unterscheiden. Des Weiteren konnten anhand dieser Messungen Strukturmodelle identifiziert werden, die dem  $\mu$ -oxido  $\text{CaMn}_4$  Zentrum des OEC stark ähneln.

In Experimenten zur katalytischen Wasseroxidation, in denen  $\text{Ce}^{\text{IV}}$  beziehungsweise photochemisch generiertes  $[\text{Ru}(\text{bpy})_3]^{3+}$  als Oxidationsmittel und die Birnessite als Katalysatoren verwendet wurden, zeigten alle Oxide Aktivität. Beim Vergleich der Katalyseraten konnten dann aber verschiedene Tendenzen ausgemacht werden. Am deutlichsten erschien hierbei ein Trend in Abhängigkeit der Art des interkalierten Kations, der wie folgt formuliert werden kann:  $\text{Ca}^{2+} > \text{Sr}^{2+} > \text{Mg}^{2+} / \text{Cd}^{2+} / \text{Al}^{3+} / \text{Zn}^{2+} / \text{Pb}^{2+} / \text{Fe}^{3+}$ .

Auch weniger deutliche Tendenzen wurden beobachtet, die in Zusammenhang mit der Konzentration der interkalierten Kationen oder der Dauer des Reifeprozesses der Materialien während der Synthese stehen. Besonders interessant ist an dieser Stelle, dass die relativen Katalyseraten, die für die Ca-, Sr- und Mg-Birnessite bestimmt wurden, gut mit denen übereinstimmen, die in der Literatur für den  $\text{Ca}^{2+}$ -,  $\text{Sr}^{2+}$ - und  $\text{Mg}^{2+}$ -reaktivierten OEC zu finden sind. Bestärkt durch diese Ergebnisse wurden mechanistische Modelle, die für die O–O Bindungsbildung während der Wasseroxidation am OEC vorgeschlagen worden sind, auf M-Birnessite übertragen. In diesen Szenarien spielen  $\text{Ca}^{2+}$  (oder  $\text{Sr}^{2+}$ ) Ionen möglicherweise eine entscheidende Rolle als Aktivierungs- und Bindungsstelle für Substrat-Wasser Moleküle.

Alles in allem zeigen die vorgestellten Ergebnisse, dass M-Birnessite vielversprechende Wasseroxidationskatalysatoren sind, die in künstlichen Photosyntheseprozessen ihre Anwendung finden könnten. Des weiteren sind vor allem Ca-Birnessite besonders interessante Modellverbindungen für den OEC, da sie dieses Vorbild sowohl strukturell, als auch funktionell nachahmen.

# Contents

<b>I</b>	<b>Introduction</b>	<b>1</b>
<b>1</b>	<b>The current energy situation: drawbacks and opportunities</b>	<b>3</b>
<b>2</b>	<b>Nature's process for solar energy conversion and storage: photosynthesis</b>	<b>9</b>
2.1	The photosynthetic process . . . . .	9
2.1.1	Organization of the photosynthetic process . . . . .	10
2.1.2	Light harvesting and energy transfer . . . . .	12
2.1.3	Charge separation and electron transfer . . . . .	14
2.2	The photosynthetic machinery for water-oxidation: PS II . . . . .	16
2.2.1	PSII's active site for water-oxidation: the OEC . . . . .	18
2.2.2	The OEC's reaction cycle of water-oxidation . . . . .	20
<b>3</b>	<b>A concept for alternative energy production: artificial photosynthesis</b>	<b>23</b>
3.1	The idea of artificial photosynthesis . . . . .	23
3.2	Requirements for catalysts for efficient water-splitting . . . . .	24
3.2.1	The overpotential of catalytic water-splitting . . . . .	24
3.3	Concepts for light-driven water-splitting catalysis . . . . .	25
3.3.1	Molecular and supramolecular concepts for water-splitting . . . . .	26
3.3.2	Photocatalytic semiconductor particles for water-splitting . . . . .	28
3.3.3	Electrocatalytic water-splitting . . . . .	29
3.3.4	Photo-electrochemical cells for water-splitting . . . . .	31
<b>4</b>	<b>From metal complexes to metal oxides: compounds for water-splitting</b>	<b>37</b>
4.1	Metal complexes and polyoxometallates . . . . .	37
4.2	Transition metal oxides as water-oxidation catalysts . . . . .	40
4.2.1	Cobalt and nickel oxides . . . . .	41
4.2.2	Manganese oxides . . . . .	42
<b>II</b>	<b>The research project – results and discussion</b>	<b>49</b>
<b>5</b>	<b>Motivation</b>	<b>51</b>
<b>6</b>	<b>Synthesis and general characterization of various M-birnessites</b>	<b>53</b>
6.1	M-birnessites prepared by direct synthesis . . . . .	54
6.2	M-birnessites prepared by ion exchange . . . . .	64
6.3	K/Ca-birnessites of increasing Ca <sup>2+</sup> concentration . . . . .	68
6.4	Ca-birnessites with increasing ripening time . . . . .	75

<b>7</b>	<b>Elucidation of structural details</b>	<b>81</b>
7.1	X-ray powder diffraction . . . . .	81
7.2	X-ray absorption spectroscopy . . . . .	90
7.3	Birnessites vs. the OEC, a structural comparison . . . . .	97
<b>8</b>	<b>Phylломanganates as water-oxidation catalysts</b>	<b>99</b>
8.1	Water-oxidation catalysis using Ce <sup>IV</sup> as oxidant . . . . .	100
8.2	Water-oxidation catalysis using [Ru <sup>III</sup> (bpy) <sub>3</sub> ] <sup>3+</sup> as oxidant . . . . .	115
8.3	Birnessites vs. the OEC, a comparison of the catalytic activity . . . . .	118
8.4	Possible mechanisms for the O–O bond formation . . . . .	120
<b>9</b>	<b>Experimental</b>	<b>123</b>
9.1	Synthesis of M-Birnessites . . . . .	123
9.1.1	Synthesis of M-birnessites 1-13 . . . . .	123
9.1.2	Synthesis of oxides 14-18 . . . . .	125
9.1.3	Synthesis of K/Ca-birnessites 19-29 . . . . .	126
9.1.4	Synthesis of Ca-birnessites 30-40 . . . . .	127
9.2	Water-oxidation catalysis . . . . .	128
9.2.1	Water-oxidation catalysis using Ce <sup>IV</sup> as oxidant . . . . .	128
9.2.2	Water-oxidation catalysis using [Ru <sup>III</sup> (bpy) <sub>3</sub> ] <sup>3+</sup> as oxidant . . . . .	131
9.3	Physical Measurements . . . . .	133
<b>10</b>	<b>Conclusion</b>	<b>135</b>
	<b>References</b>	<b>139</b>
	<b>Appendix</b>	<b>157</b>
A.1	Overview of the prepared samples . . . . .	157
A.2	Atomic absorption spectroscopy data . . . . .	159
A.3	Headspace gas chromatography data . . . . .	161
A.4	Oxygen-evolution traces detected in water-oxidation experiments using [Ru <sup>III</sup> (bpy) <sub>3</sub> ] <sup>3+</sup> as oxidant . . . . .	201
	<b>Acknowledgements</b>	<b>205</b>
	<b>Curriculum vitae</b>	<b>207</b>

# Abbreviations

AAS	atomic absorption spectroscopy
Ac	acetyl
ADP	adenosine diphosphate
ATP	adenosine triphosphate
ATPase	ATP synthase
ATR	attenuated total reflectance
bbcc	2,6-bis(2-benzoimidazole-4-carboxylate)- <i>p</i> -cresol
bdc	2,2'-bipyridine-6,6'-dicarboxylate
BET	Brunauer-Emmet-Teller
bpy	2,2'-bipyridine
Car	$\beta$ -carotene
Cat <sub>ox</sub>	catalyst for water-oxidation
Cat <sub>red</sub>	catalyst for (proton-)reduction
CB	conduction band of a semiconductor
Chl	chlorophyll
Cyt <i>b</i> <sub>6</sub> <i>f</i>	cytochrome <i>b</i> <sub>6</sub> <i>f</i> complex
D-P-A	donor-photosensitizer-acceptor triad
DFT	density functional theory
DME	dimethyl ether
DSA	dimensionally stable anode
DSC	dye-sensitized solar cell
EDX	energy-dispersive X-ray spectroscopy
ENDOR	electron nuclear double resonance
Et	ethyl
EPR	electron paramagnetic resonance spectroscopy
EXAFS	extended X-ray absorption fine structure
Fd	ferredoxin
FNR	ferredoxin-NADP reductase
FRET	fluorescence resonance energy transfer

FT	Fourier transformation
FTO	fluorine doped tin oxide
GC	gas-phase chromatograph
GW	gigawatt, $10^9$ W
HOMO	highest occupied molecular orbital
IR	infrared
IUPAC	International Union of Pure and Applied Chemistry
isoq	isoquinoline
ITO	indium doped tin oxide
kDa	kilo dalton
LUMO	lowest unoccupied molecular orbital
Me	methyl
MIMS	membrane-inlet mass spectrometry
MIT	Massachusetts Institute of Technology
MW	megawatt, $10^6$ W
NADP <sup>+</sup>	nicotinamide adenine dinucleotide phosphate
NADPH	reduced form of NADP <sup>+</sup>
NHE	normal hydrogen electrode
OEC	oxygen-evolving-complex, also WOC: water-oxidising-complex
P	photosensitizer
P*	photosensitizer in its excited state
P <sub>i</sub>	inorganic phosphate
pic	4-picoline
P680	reaction center of PSII
P700	reaction center of PSI
PC	plastocyanin
PCET	proton coupled electron transfer
PEC	photo electrochemical cell
PEM	polymer electrolyte membrane
PGA	3-phosphoglycerate
Ph	phenyl
Pheo	pheophytin
POM	polyoxometallate
PQ	plastoquinone

---

PQ <sub>A</sub>	firmly bound plastoquinone in PSII's electron transfer chain
PQ <sub>B</sub>	mobile plastoquinone in PSII's electron transfer chain
PQH <sub>2</sub>	plastohydroquinone (plastoquinol)
PSI	photosystem I
PSII	photosystem II
PV	photovoltaic cell
R/R <sup>-</sup>	redox relay
rpm	revolutions per minute
RuBP	ribulose 1,5 biphosphate
SEM	scanning electron microscope
t <sub>1/2</sub>	half-life
TCD	thermal conductivity detector
TEM	transmission electron microscopy
tpy	2,2':6',2''-terpyridine
tpdm	tris(2-pyridyl)methane
TW	terawatt, 10 <sup>12</sup> W
UNFCCC	United Nations Framework Convention on Climate Change
UV	ultraviolet
WOC	water-oxidizing-complex, also OEC: oxygen-evolving-complex
XANES	X-ray absorption near edge structure
XAS	X-ray absorption spectroscopy
XRD	X-ray diffraction
Y <sub>D</sub>	tyrosine D, redox active tyrosine in D2 subunit of PSII
Y <sub>Z</sub>	tyrosine Z, redox active tyrosine in D1 subunit of PSII
Y <sub>Z</sub> <sup>•</sup>	tyrosine Z radical, Y <sub>Z</sub> in its oxidized form



**Part I**

**Introduction**



# 1 The current energy situation: drawbacks and opportunities

Since the beginning of the industrial revolution in the 18<sup>th</sup> and 19<sup>th</sup> century, our society has experienced a continuous change. Beginning with innovations like the steam engine and weaving machines, continuous mechanization replaced manual human work by machines. The first innovations were followed by mass production and an expanded access to electricity. Closely related to these developments, social life and cultural environment changed drastically up to the present day. The agricultural society changed to an industrialized society, factories were build, workers migrated into cities. After the beginnings standards of living increased. Inventions like railways and automobiles for instance contributed to a higher level of personal mobility. And as a rising number of trained employees were needed, knowledge became accessible to more and more people.

Today's lifestyle is strongly reliant on mobility and technology. In developed countries, we are used to a high standard of comfort including global transportation and communication networks, ample food supply, air conditioning, refrigeration, television, electric cookers and lighting, etc. as part of our daily routines. But the sustained technological advances of our anthroposphere are coupled to a substantial growth in energy consumption. In addition, the growing global population (by now beyond 7 billion people) is accelerating energy consumption as well as the rapid development taking place in many emerging or developing economies, such as China and India.<sup>[1-5]</sup>

Up to the beginning of the 20<sup>th</sup> century, human energy demand was mainly covered by the combustion of coal that was easy and cheap to mine.<sup>[5,6]</sup> Later, oil became one of the major energy carriers.<sup>[5]</sup> In 1965, the global energy demand of about 5 terawatt (TW) was provided mainly by oil and coal, small fractions were met by natural gas and hydroelectricity.<sup>[7,8]</sup> In the following decades, nuclear energy and renewable energy sources, mainly hydroelectricity, made a growing contribution in addition to fossil fuels (Figure 1.1). In 2010, the energy demand of about 16 TW<sup>[7,8]</sup> was covered by fossil fuels, nuclear energy, hydroelectric power and also by other renewable sources.<sup>[9,10]</sup> Nevertheless, fossil fuels are still the dominating energy source, as the fossil share in final energy<sup>[11]</sup> consumption in 2010 was about 81 %.<sup>[9,10]</sup> This extensive combustion of fossil fuels is leading to a reduction of our traditional energy resources. Environmental pollution on a large scale and the emission of huge amounts of greenhouse gases like CO<sub>2</sub> are inevitable consequences. As a result, the atmospheric CO<sub>2</sub> concentration is significantly increasing<sup>[12-14]</sup> linked to the globally growing energy combustion (Figure 1.2). Although the consequences for the Earth's fragile ecosystem are hard to predict, the impacts on the global climate and our environment are already being felt. And also accidents during the processing or transport of fossil fuels have resulted in pollution on a large scale.

Nuclear energy is highly controversial. Its share in final energy consumption in 2010 was around 3 %<sup>[9,10]</sup>, producing about 250 000 t of high-level waste every year.<sup>[5]</sup> <sup>235</sup>U

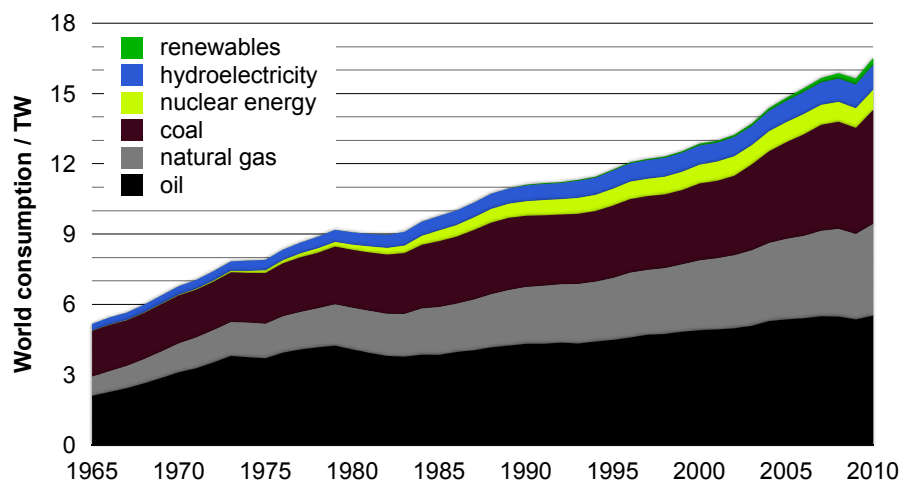


**Figure 1.1.** World primary energy<sup>[16]</sup> consumption from 1965 to 2010. In 1965, global energy demand was mainly covered by oil and coal. In 2010, oil and coal are still the major energy carriers. But renewable energy sources are becoming more and more important. Nuclear energy's share is also growing. The figure is adapted from<sup>[7]</sup>, original units were converted into TW.<sup>[8]</sup>

( $t_{1/2} = 10^{8.8} \text{ a}$ )<sup>[15]</sup> is used as a fuel in all commercial nuclear plants, generating  $^{239}\text{Pu}$  ( $t_{1/2} = 10^{4.4} \text{ a}$ )<sup>[15]</sup> by the reaction of  $^{235}\text{U}$  with neutrons.<sup>[5]</sup> After an operation period of two to three years the fuel rods are replaced, still containing unburned U and Pu and other radioactive isotopes as decay products.<sup>[5]</sup> Even if reprocessing of nuclear waste is reducing its mass, radioactivity per mass unit is increased.<sup>[5]</sup> The handling of this high-level long-lived nuclear waste is especially complicated as the radioactive decay of various elements takes hundreds to hundreds of thousands of years.<sup>[5,15]</sup> Although scenarios for disposal of nuclear waste have been planned, the enormous time periods in which the waste has to be stored is causing great security challenges.

It is absolutely crucial to identify alternatives in energy production to meet the human demand in a sustainable and environmentally friendly way. Hence, sustainable energy sources are gaining more and more attention worldwide. To restrict the impact of anthropogenic greenhouse gases on the climate system, treaties like the United Nations Framework Convention on Climate Change (UNFCCC) have been passed.<sup>[17]</sup> A growing number of countries are enacting policy targets to decrease  $\text{CO}_2$  emission and to support future energy supply by renewable energy sources.<sup>[9]</sup> For instance, the EU member states have defined the target to reduce  $\text{CO}_2$  emission by 20 % and to meet a renewable share in final energy consumption of 20 % by 2020.<sup>[18]</sup> Global new investments in renewable energies increased from 39 billion US \$ in 2004 to 257 billion US \$ in 2011 and existing renewable power generating capacity exceeded 1360 gigawatt (GW).<sup>[9]</sup> The worldwide share of renewables in final energy consumption grew to 16.7 %.<sup>[9]</sup> These 16.7 % of today's renewable final energy share are composed of biomass, hydroelectricity, ocean energy, geothermal power, wind power and solar energy (Figure 1.3).<sup>[9]</sup>

Biomass feedstocks are today's fourth largest energy source following oil, coal and natural gas, contributing about 10 % of the global primary energy<sup>[16]</sup> supply.<sup>[9]</sup> Biomass feedstocks are including products of agriculture, forestry and also by- and waste products of industries and municipalities. These energy carriers are converted to provide

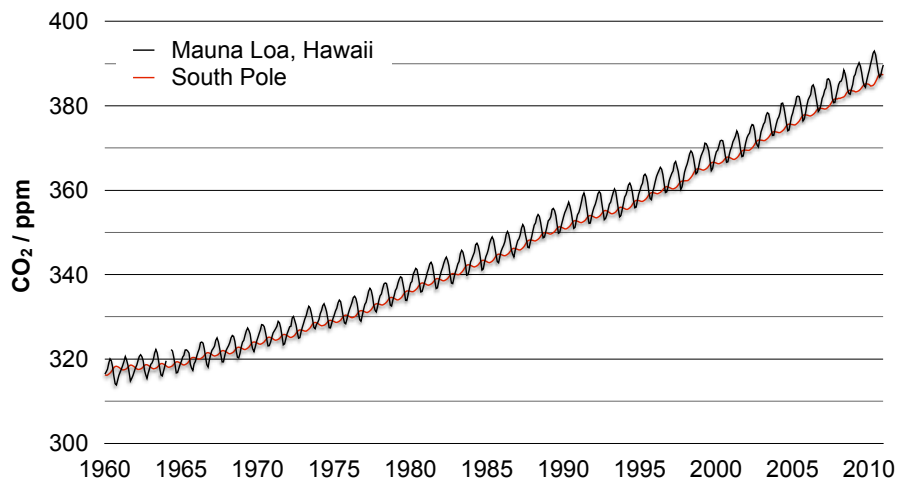


**Figure 1.2.** Atmospheric CO<sub>2</sub> concentration as recorded in Mauna Loa, Hawaii<sup>(12,13)</sup> and the south pole.<sup>(13,14)</sup> The strong growth in atmospheric CO<sub>2</sub> concentration is associated with the extensive combustion of fossil fuels (Figure 1.1). The impact on our environment is hard to predict. The jagged course of the graphs is caused by CO<sub>2</sub> consumption by photosynthesis which is mainly active in spring and summer.

energy in form of electricity, heat or transport fuels in gaseous, liquid or solid form.<sup>[9]</sup> While recycling of biomass waste seems a reasonable approach, planting of crops only for energy production is competing with food (also animal feeds) and other bio-materials production.<sup>[9]</sup>

Hydroelectricity's global total capacity was estimated as 970 GW in 2011, with a share in final energy consumption of 3.3 % in 2010.<sup>[9]</sup> Hydroelectricity is generated using turbines that are driven by falling water in reservoir or run-of-river power plants.<sup>[5,9]</sup> A major disadvantage of hydro power is its areal demand, by far higher than the demand of wind or geothermal power.<sup>[5]</sup> The area occupied by artificial water-reservoirs is about half the size of Italy.<sup>[5]</sup> And even if dams that have been constructed can be used to control water levels and thereby avoid disastrous floods<sup>[5]</sup>, the environment is permanently affected in these regions.

Also ocean energy is providing a growing part in energy production, converting mechanical energy of tides, currents and waves.<sup>[5,9]</sup> In 2011, new capacities of 254 megawatt (MW) were added, leading to a global total capacity of 527 MW.<sup>[9]</sup> The global power of tides is estimated to about 3 TW of which 0.8 TW might be accessible without stronger impact on the cycles of the biosphere.<sup>[5]</sup> 1-10 TW of the wave's energy of total 90-100 TW are thought to be exploitable. Also ocean thermal energy conversion is under discussion with a theoretical capacity of 5 TW.<sup>[5]</sup>

Geothermal energy is provided in the form of heat that can either be used directly, or converted into electricity.<sup>[5,9]</sup> The global total power capacity (around one third of total geothermal capacity) was estimated to be about 11 GW in 2011.<sup>[9]</sup> Geothermal technology is relatively simple and does not require large areas of land. But, a major drawback of geothermal energy usage is the release of pollutants like CO<sub>2</sub>, H<sub>2</sub>S and CH<sub>4</sub> into the environment.<sup>[5]</sup> And also the inhomogeneous global distribution of geothermal energy may be a limiting factor outside of regions with high geothermal activity.

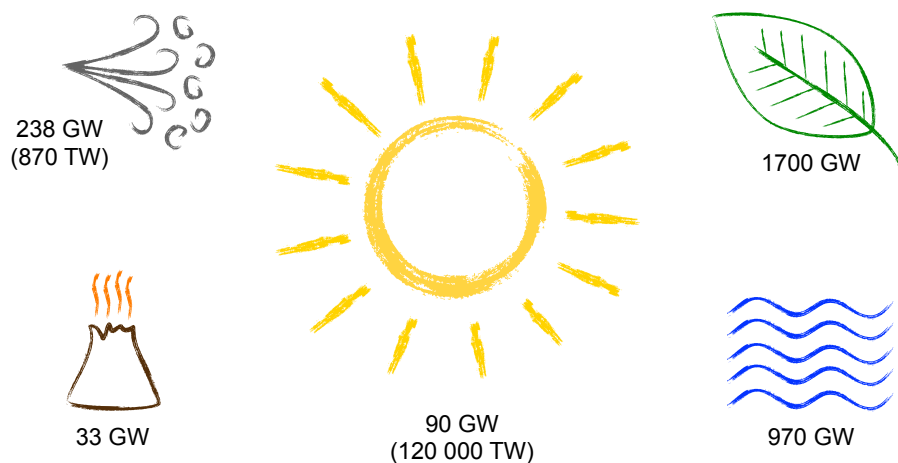


**Figure 1.3.** Overview of alternative energy resources and their capacities used today. The exploitation of geothermal energy (*lower left*) is limited to regions with high geothermal activity. Biomass (*upper right*) and hydroelectricity (*lower right*) are widely-used and are contributing a significant portion to global energy production. Solar energy (*center*) and wind energy (*upper left*) are enjoying increasing attention. If only a few percent of the theoretical potential of wind or solar energy (given in parentheses) could be converted into storable and readily utilizable forms, this would be a giant step towards the production of sustainable and clean energy, by far exceeding our needs.

The capture of kinetic wind energy using turbines had an estimated total installed power capacity of 238 GW in 2011.<sup>[9]</sup> In the year 2011, wind power was the fastest growing renewable energy source as 40 GW of new capacity were installed.<sup>[9]</sup> Approximately 870 TW of solar radiation absorbed by the Earth is converted into wind energy, which can be converted into mechanical energy with a theoretically maximum efficiency of 60%.<sup>[5]</sup> Under optimal conditions, modern wind turbines are reaching efficiencies of about 40%, showing the enormous potential of wind energy.<sup>[5]</sup> But, the wind is not blowing continuously all over the year. So wind power has to be coupled to other forms of energy production or technologies for efficient energy storage, which still have to be developed.

Solar energy is used either to generate electricity via photovoltaic cells (PVs) as well as concentrated solar thermal power plants, or in form of solar thermal heating and cooling.<sup>[9]</sup> Electricity production by PVs reached a total global capacity of almost 70 GW in 2011.<sup>[9]</sup> Concentrated solar thermal power is today mainly converted in parabolic trough power plants, the total installed capacity reached 1760 MW in 2012.<sup>[9]</sup> More than 200 million households worldwide are using hot water supplied by solar thermal heating and the capacity of solar hot water collectors was approximately 150 TWh (~ 17 GW) in 2010.<sup>[9]</sup> Altogether, the installed solar energy capacity in use today is around 90 GW. A major drawback of solar energy, similar to wind energy, is its availability. To meet energy demand when the sun is not shining, other energy sources or technologies for efficient energy storage have to be coupled to solar energy usage. Nevertheless, solar energy has by far the largest potential. On average 120 000 TW of electromagnetic radiation from the sun reaches the Earth, far in excess of our current demand of 16 TW.<sup>[2]</sup>

---

The future global energy demand has been estimated to be 30-40 TW in 2050.<sup>[1]</sup> Renewable energy sources do have a promising potential to meet this demand in a sustainable way. However, challenges have to be overcome to achieve this aim. On the one hand, existing technologies have to be optimized in order to achieve higher efficiencies and to avoid major drawbacks. New materials have to be developed to replace those in use which are costly to produce. This approach is not limited to technologies for energy production. Also, energy consuming technologies have to be optimized to decrease energy demand where possible. For instance, waste heat should be exploited efficiently.

Additionally, technologies for energy conversion and storage have to be developed. This is for example crucial to meet the energy demand of the transportation sector. Hydroelectricity, ocean energy, geothermal power, wind power and solar energy are promising energy sources for electricity and heat production, respectively. But, to provide energy accessible for transportation, the energy has to be stored either in batteries or converted into a fuel. Today, neither energy storage in batteries, nor sustainable fuel production is efficient enough to be used on a large scale.<sup>[5]</sup> Thus, research activities in these fields have to be intensified to develop methods and materials to provide tomorrow's global energy demand in a sustainable way.

Especially solar energy has a tremendous potential as a clean energy source. But only a small fraction is currently used in photovoltaics and solar thermal heating, or in the broader sense to grow biomass for energy production. To take full advantage of the enormous potential of the sun, solutions to the capture of solar energy and its conversion into readily utilizable and storable forms are urgently required. One approach to achieve the production of such a *solar fuel*, as it is called, is to take biological processes as an inspiration. In photosynthesis, solar energy is captured and stored in form of biomass (chapter 2). The ability to imitate this paragon in a simplified artificial process (chapter 3) would be a major breakthrough in sustainable energy production.

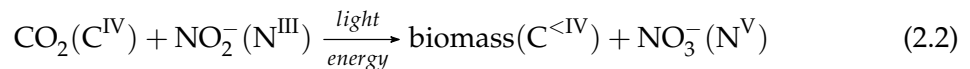
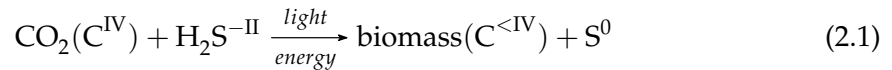


## 2 Nature's process for solar energy conversion and storage: photosynthesis

### 2.1 The photosynthetic process

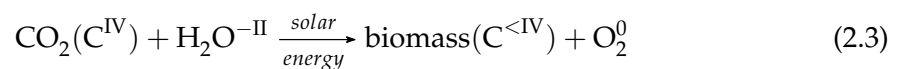
The term photosynthesis describes a biological process powering plants, algae and distinct bacteria. In this process, light energy is captured and converted into chemical energy that can be stored and re-released on demand. Photochemistry for light-harvesting and charge separation is coupled to a sequence of redox reactions to convert photons into electrons that are required for the production of the organism's energy carrier out of abundant low-energy precursors. In general, CO<sub>2</sub> is reduced and biomass in the form of carbohydrates is formed, which later can be exploited by the organisms.<sup>[19–21]</sup> Due to the diverse conditions of the different environments of photosynthetic organisms, different reaction pathways have evolved using different electron sources to provide the necessary reduction equivalents. In this connection photosynthesis is classified as anoxygenic and oxygenic photosynthesis.<sup>[19]</sup>

Anoxygenic photosynthesis is taking place in purple bacteria, green sulfur bacteria, green nonsulfur bacteria and heliobacteria.<sup>[19]</sup> The reaction sequences are denoted as anoxygenic as no molecular oxygen is produced as a by-product of the photosynthetic process. H<sub>2</sub>S<sup>[19]</sup> and also NO<sub>2</sub><sup>−[22]</sup> are for instance known electron sources to provide the reduction equivalents required for CO<sub>2</sub> conversion. A simplified and stoichiometrically non-correct equation for the oxidation of H<sub>2</sub>S and NO<sub>2</sub><sup>−</sup>, respectively, can be formulated as:



In some cases, evolution has created organisms capable to perform anoxygenic photosynthesis even under exotic conditions. To give an example, green sulfur bacteria have been discovered living in the deep sea around hydrothermal vents. These bacteria are using H<sub>2</sub>S as electron source and, as no sunlight is reaching this depth, the geothermal infrared irradiation of the hydrothermal vents is used as light source for photosynthesis.<sup>[23]</sup>

Oxygenic, or oxygen-evolving photosynthesis takes place in plants, algae and cyanobacteria.<sup>[19]</sup> Here, H<sub>2</sub>O is used as electron source for the reductive conversion of CO<sub>2</sub> into biomass. In the water-oxidation reaction of this type of photosynthetic processes a by-product essential for our lives is formed, O<sub>2</sub>.<sup>[19,20]</sup> A simplified, stoichiometrically non-correct equation for this process can be formulated as:



So oxygenic photosynthesis is evolutions process for the conversion and storage of solar energy based on abundant and non-toxic elements. And, as it is assumed that photo-

synthesis is converting solar into chemical energy at a rate of about 120 TW per year<sup>[24]</sup>, it is an outstanding paragon for sustainable energy production. But to realize a technical process for energy production inspired by photosynthesis (*artificial photosynthesis*, cf. chapter 3), it is crucial to understand the fundamental reactions of the biological paragon. Hence, a brief overview on the reaction pathways of photosynthesis taking place in plants and water-oxidation catalysis in particular (cf. section 2.2) will be given. Also, the term photosynthesis will be used synonymous with oxygenic photosynthesis in the following.

### 2.1.1 Organization of the photosynthetic process

Photosynthesis in higher plants is taking place in chloroplasts, subcellular organelles of the mesophyll cells.<sup>[20]</sup> Chloroplasts are containing an extensive system of membrane compartments, the thylakoids (Figure 2.1).<sup>[19-21]</sup> Most of the thylakoids are organized in stacks, the so called grana thylakoid membranes. The single granum stacks are interconnected by stroma thylakoid membranes, also called stroma lamellae, which are not stacked. The thylakoid membranes are containing integral membrane protein complexes including the reaction centers, the antenna pigment-protein complexes and electron carrier proteins.<sup>[19-21]</sup> Proteins also crucial for photosynthesis are located in the chloroplast's stroma which is surrounding the membrane system of thylakoids.<sup>[19,20]</sup>

The occurring chemical reactions can be grouped into light and dark reactions. The light reactions, taking place in the thylakoid membrane, are started by the absorption of sunlight by the antenna pigment-protein complexes (cf. section 2.1.2).<sup>[19-21]</sup> The excited pigments are transferring their energy to the reaction centers of the integral membrane protein complexes photosystem II (PSII) and photosystem I (PSI), where a chain of electron transfer steps is initiated (cf. section 2.1.3).<sup>[19-21]</sup> In the first photochemical event electrons are removed from the reaction center of PSII (P680).<sup>[19,20]</sup> Four oxidation equivalents (electron holes) are accumulated, before two molecules of H<sub>2</sub>O are oxidized

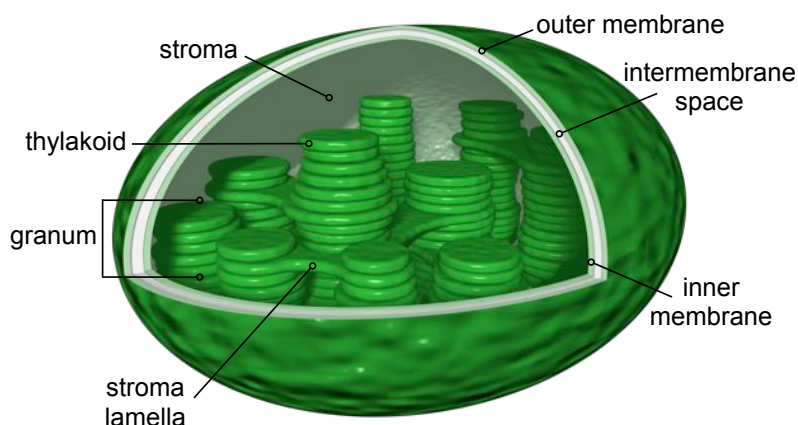


**Figure 2.1.** Schematic representation of a chloroplast.<sup>(19-21)</sup> Chloroplasts are subcellular organelles in which the processes of photosynthesis are taking place. These organelles are containing an extensive membrane system, the thylakoids, containing pigments and protein complexes.<sup>(19-21)</sup> The thylakoids are organized in stacks, the so called grana and are surrounded by the stroma. Single granum stacks are interconnected by stroma thylakoid membranes, the stroma lamellae. The light reactions of photosynthesis occur in the thylakoid membrane system.<sup>(19-21)</sup> The dark reactions occur in the stroma.<sup>(19,20)</sup>

and PSII's reaction center is re-reduced (see section 2.2 for more details).<sup>[25–29]</sup> Four electrons, four protons and one molecule of  $O_2$  are released. The protons are diffusing to the chloroplast's stroma for ATP formation by ATP synthase (ATPase). The electrons are transferred to PSI's reaction center (P700), onwards to ferredoxin (Fd) and finally to ferredoxin-NADP reductase (FNR).<sup>[19–21]</sup> FNR catalyzes the reduction of  $NADP^+$  to NADPH.<sup>[19–21]</sup>

However, PSII and PSI are not coupled directly, but rather they are spatially separated. PSII is primarily located in the stacked areas of the thylakoid membrane system, in the grana. In contrast, PSI is placed in the stroma lamellae membranes.<sup>[19–21]</sup> Thus, cofactors are involved in electron transport between PSII and PSI. The cytochrome  $b_6f$  complex (Cyt  $b_6f$ ), an integral membrane protein complex evenly distributed in grana and stroma lamellae, is involved in the transfer of electrons between PSII and PSI via plastoquinone (PQ) and the copper protein plastocyanin (PC), which acts as mobile electron shuttle in the lumen (Figure 2.2, see section 2.1.3 for more details).<sup>[19–21]</sup>

The dark reactions, also termed carbon reactions, are taking place in the stroma of the chloroplasts. In this part of the photosynthetic reaction sequence, NADPH and ATP as products of the light reactions are used for the reduction of  $CO_2$  to carbohydrates.<sup>[19,20]</sup> NADPH is providing the required reduction equivalents, originating from water-oxidation at the beginning of the reaction pathway. The process is driven by en-

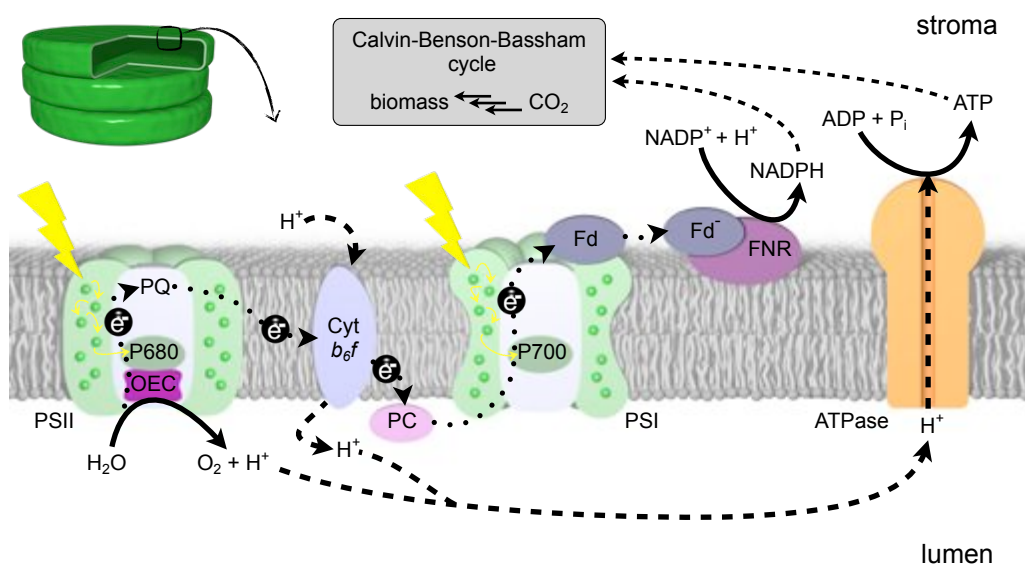


**Figure 2.2.** Schematic representation of the reaction sequence of photosynthesis.<sup>(19–21)</sup> The integral membrane proteins of the light reactions are placed in the thylakoid membrane (gray double layer, a thylakoid cross-section is shown in the upper left corner). The pigment antenna complexes of the photosystems are excited by sunlight (pigments are indicated as green dots) and transfer energy to the reaction centers of photosystem II (PSII), P680 and photosystem I (PSI), P700.<sup>(19–21)</sup> In PSII,  $H_2O$  is oxidized, protons, electrons and  $O_2$  are released. The electrons are transferred to PSI via the chain plastoquinone (PQ) – cytochrome  $b_6f$  complex (Cyt  $b_6f$ ) – plastocyanin (PC).<sup>(19–21)</sup> After light excitation, PSI is able to reduce ferredoxin (Fd) which is transferring the electrons to ferredoxin-NADP reductase (FNR). FNR reduces  $NADP^+$  to NADPH.<sup>(19–21)</sup> In addition to electron transfer, a proton gradient is build up which is used for the formation of ATP by ATP synthase (ATPase). NADPH and ATP are then utilized in the Calvin-Benson-Bassham cycle taking place in the stroma, where  $CO_2$  is converted into biomass.<sup>(19–21)</sup>

ergy released by the cleavage of ATP into ADP and  $P_i$ .<sup>[19,20]</sup> Melvin Calvin and coworkers figured out that the reductive  $CO_2$  conversion is a cyclic reaction embedding three phases, carboxylation, reduction and regeneration.<sup>[19,20,30]</sup> In the carboxylation step,  $CO_2$  is bound by carboxylation of the C5-precursor ribulose 1,5 bisphosphate (RuBP) and two equivalents of the C3-molecule 3-phosphoglycerate (PGA) are formed. In the reduction phase of the cycle, NADPH and some of the ATP is consumed, PGA is reduced to triose phosphate. In the last phase of the cycle a major part of the triose phosphate and ATP is used to regenerate RuBP. In 1961 Melvin Calvin received the Noble Prize in chemistry for his research on this reaction cycle.<sup>[30,31]</sup> The reaction sequence is also named Calvin-cycle. His colleagues Andrew Benson and James Bassham have as well been acknowledged for their contribution as the reaction sequence is also known as the Calvin-Benson-Bassham cycle.<sup>[19]</sup>

### 2.1.2 Light harvesting and energy transfer

The process of photosynthesis is starting with harvesting of light energy by the antenna pigment-protein complexes.<sup>[19-21]</sup> Pigment molecules are absorbing photons and are thus transferred into their excited state. The collected energy is then funneled to the reaction centers of PSII and PSI where charge separation is taking place (*cf.* section 2.1.3).<sup>[19-21]</sup>

Depending on the photosynthetic organism, various pigments can be found. Different types of carotenoids are present in all of these organisms.<sup>[19,20]</sup> The inner antenna complexes of PSII for example are containing  $\beta$ -carotene (Figure 2.3, *top*) and chlorophyll *a*.<sup>[32-36]</sup> Carotenoids are linear molecules featuring a delocalized  $\pi$  electron system. In oxygenic photosynthetic organisms, the carotenoids usually have ring structures at both ends of the linear part of the molecule.<sup>[19,20]</sup>

Chlorophylls are another class of pigments found in all photosynthetic organisms. In higher plants, green algae and cyanobacteria, chlorophyll *a* and *b* (Figure 2.3, *bottom*) are present.<sup>[19,20]</sup> In anoxygenic photosynthetic bacteria, several bacteriochlorophylls are found.<sup>[19,20]</sup> Chlorophylls are chelate complexes,  $Mg^{2+}$  is bound as central atom. The macrocyclic ligand is structurally related to porphyrins and chlorins which both are heterocyclic macrocycles composed of four pyrrole or three pyrrole and one pyrroline subunits respectively.<sup>[19,20]</sup> Chlorophylls do show an additional five-membered ring attached to the macrocycle (ring E in Figure 2.3). The cyclic subunits A to D are derived from pyrrole, while ring D is in a reduced state. The chlorophyll macrocycle exhibits an extensive delocalized  $\pi$  electron system extended over the heterocyclic subunits except of ring D.<sup>[19]</sup>

Bilins are a further category of pigments which are present in several photosynthetic organisms.<sup>[19,20]</sup> These pigments are tetrapyrroles, but in contrast to chlorophylls, they are linear open-chain molecules. Here, bilins are mentioned for sake of completeness, but they will not be discussed in the following.

Carotenoids and chlorophylls are absorbing different wavelength of the spectrum of light.<sup>[19,20]</sup> Carotenoids exhibit absorption bands in the region of 400 to 500 nm.<sup>[19,20]</sup> Here, transitions from the ground state ( $S_0$ ) to the second excited singlet state ( $S_2$ ) occur.<sup>[19]</sup> The lifetime of the  $S_2$  state is on the subpicosecond time scale, so its nonradiative decay to the first excited singlet state ( $S_1$ ) is very fast. The direct excitation from  $S_0$  to the  $S_1$  state is excluded by transition rules because of the symmetry of the carotenoid molecules.<sup>[19]</sup> The also nonradiative relaxation of the  $S_1$  to the  $S_0$  state is very fast and

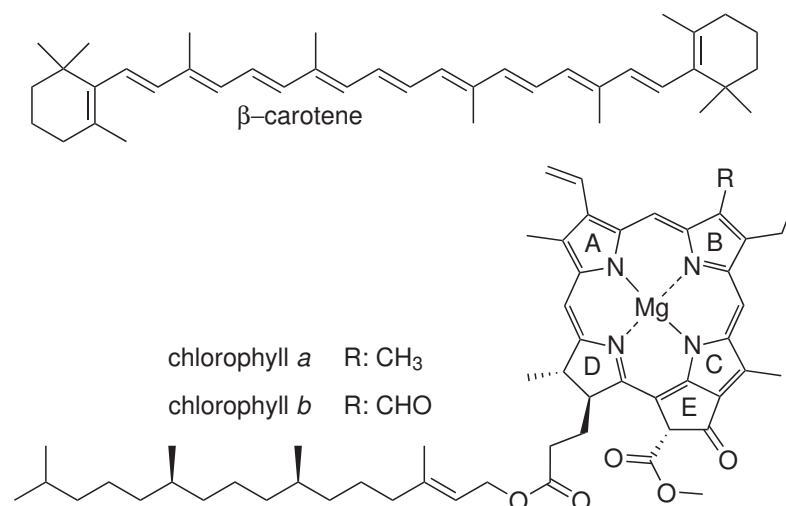


**Figure 2.3.** Molecular structures of  $\beta$ -carotene (*top*) and chlorophyll *a* and *b* (*bottom*).<sup>[19,20]</sup> These molecules are the pigments of the antenna pigment-protein complexes of PSII and PSI in higher plants, green algae and cyanobacteria.<sup>[19,20]</sup> Carotenoids show a linear structure. Chlorophylls are macrocycles build up from heterocyclic subunits derived from pyrrole. These subunits are labeled A to D. Ring E is additionally attached to the macrocycle.<sup>[19,20]</sup>

takes place on the picoseconds time scale.<sup>[19]</sup> But, despite the fast decay of the excited- to the ground state, energy transfer from excited carotenoids to chlorophylls is feasible as it is even faster.

Chlorophylls exhibit two extensive absorption bands, in the blue range and in far red range of the light spectrum. The absorption band in the blue range is termed B or also Soret band, named after the swiss scientist Jacques-Louis Soret who first detected this band.<sup>[37]</sup> The absorption bands in the red range are denoted as Q bands, further divided into  $Q_x$  and  $Q_y$ , whereat the subscribed characters are indicating polarized transitions along the molecular axes *x* and *y*. The  $Q_x$  band is much weaker than the strong  $Q_y$  band, and in chlorophyll *a*, for example, not well resolved.<sup>[19]</sup> Anyway, in a simplified view, B and Q bands of the chlorophyll pigments are due to  $\pi \rightarrow \pi^*$  transitions from the two highest occupied molecular orbitals (HOMOs) to the two lowest unoccupied molecular orbitals (LUMOs).<sup>[19]</sup>

To use the absorbed light energy to drive the further reaction steps of photosynthesis, energy has to be trapped. The energy is funneled by the pigments of the antenna-complexes, to the reaction centers P680 and P700 via fluorescence resonance energy transfer (FRET) and Dexter energy transfer.<sup>[19,20,38,39]</sup>

The fluorescence resonance energy transfer, or Förster resonance energy transfer describes the energy transition from an excited pigment (donor) to a second molecule (acceptor).<sup>[19,40,41]</sup> The process was first described in 1948 by the physical chemist Theodor Förster.<sup>[42]</sup> In this mechanism, energy transfer to the acceptor is taking place through nonradiative dipole-dipole coupling.<sup>[19,40,41]</sup> The efficiency ( $E_T$ ) of the process is firstly dependent on the donor-acceptor distance ( $R$ ):<sup>[41]</sup>

$$E_T = \frac{R_0^6}{R_0^6 + R^6} \quad (2.4)$$

Eq. 2.4 clearly shows that the FRET effect is strongly decreasing by an increasing donor-acceptor distance  $R$ . In general FRET occurs at distances lower than 80 Å.<sup>[41]</sup> But  $E_T$  also depends on the Förster distance ( $R_0$ ).  $R_0$  is defined as the donor-acceptor distance at which the energy transition has an efficiency of 50 %.<sup>[19,40,41]</sup> The Förster distance on the other hand is dependent on the orientation of the transition dipole moments ( $\kappa^2$ ), the integral of overlapping of the donor emission- and acceptor absorption spectrum ( $J$ ), the quantum yield of the donor ( $\phi_D$ ) and the refractive index of the surrounding medium:<sup>[41]</sup>

$$R_0 = 8.79 \cdot 10^{-5} \cdot (J \cdot \kappa^2 \cdot n^{-4} \cdot \phi_D)^{1/6} \text{Å} \quad (2.5)$$

The Dexter transfer denotes the energy transition via an electron exchange mechanism<sup>[38,43]</sup>, named after David L. Dexter who described the process in 1953.<sup>[44]</sup> The exchange interaction requires an overlap of the wavefunctions of donor and acceptor and is thus only taking place over short distances.<sup>[38,43]</sup> It can be illustrated as simultaneous exchange of two electrons between the energy donor and the acceptor, obeying spin conservation in the reaction pair. Not only spin-allowed, but also spin-forbidden excited states are involved<sup>[38]</sup>, making this the dominant mechanism in triplet-triplet energy transfer.<sup>[38,43]</sup> The transfer rate constant ( $k_{ET}$ ) given in eq. 2.6 is dependent on the distance between the donor and the acceptor ( $r$ ), the integral of the spectral overlap ( $J$ ) and the Planck constant ( $h$ ).  $L$  and  $P$  are constants in a complex relation to experimentally determinable quantities.<sup>[43]</sup>

$$k_{ET} \propto \frac{h}{2\pi} \cdot P^2 \cdot J \cdot e^{-2r/L} \quad (2.6)$$

Summarized, in these two energy transfer mechanisms the distance, the relative orientation, the spectral overlap and the overlap of the wavefunctions, respectively, are crucial for an efficient transition of the absorbed light energy. The quantum efficiency of the light-harvesting process in photosynthesis is considerably above 90 %.<sup>[19,20,27]</sup> But the outstanding quantum yield is due to a less advantageous energy efficiency.<sup>[27]</sup> The direction of the energy transfer process is determined by the energy of the pigments. As the light energy is funneled from higher energy pigments (carotenoids) to lower energy pigments (chlorophylls) of the antenna complexes. In the final step of the funneling cascade the energy is transferred to the reaction centers P680 and P700, which are pigments of the lowest energy.<sup>[19,20]</sup>

### 2.1.3 Charge separation and electron transfer

P680 is the photochemical reaction center of PSII.<sup>[19–21,27]</sup> The name stands for pigment 680, where the number is indicating its absorption maximum at a wavelength of 680 nm. P680 is formed by two chlorophyll dimers.<sup>[19–21,27,45]</sup> These dimers are also termed special pairs. In analogy to PSII, the reaction center chlorophylls of PSI, P700, are named after their absorption maximum at 700 nm.<sup>[19–21]</sup> Excited by the energy funneled through the antenna pigments to the reaction centers, P680 and P700 are transferred into their excited states P680\* and P700\*, respectively.<sup>[19,20]</sup>

After the reaction centers of PSII and PSI have been excited by light absorption and energy transfer from the pigment antenna-protein complexes, a multi step electron transfer chain is started (Figure 2.4).<sup>[19,20,27,45]</sup> In this chain, P680\* and P700\* are acting as electron donors, releasing an electron by oxidative quenching of each of the excited states.<sup>[19–21]</sup> The reaction centers are connected by several cofactors resulting in directed electron

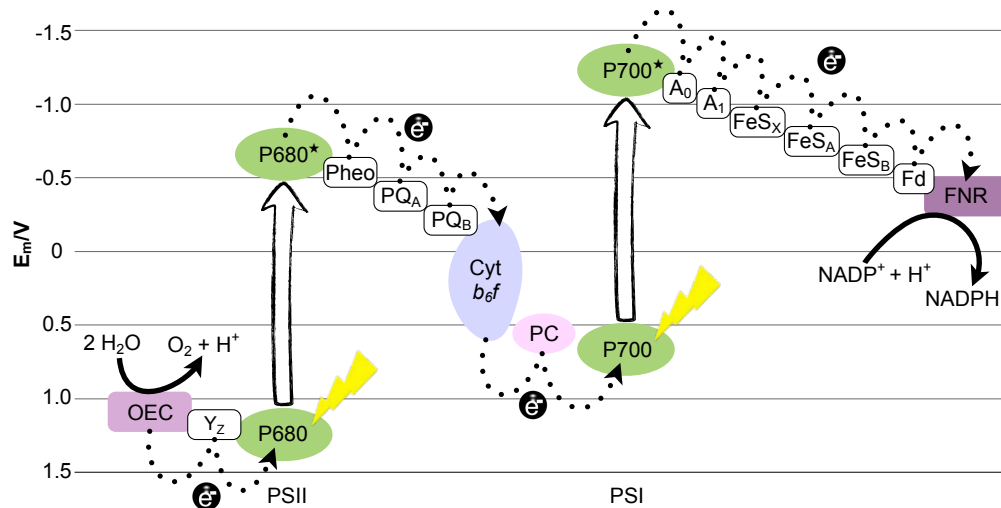


**Figure 2.4.** The redox potentials of the electron transfer chain of the photosynthetic light reactions illustrated in the Z scheme.<sup>(19,20,46)</sup> The reaction centers in their excited states, P680\* and P700\*, are acting as electron donors, starting the electron transfer process.<sup>(19–21)</sup> From P680, electrons are passed to P700 via Pheo, PQs, the integral membrane protein complex Cyt *b<sub>6</sub>f*, and the small and mobile protein PC.<sup>(19–21)</sup> Electron holes are transported to the CaMn<sub>4</sub>O<sub>5</sub> cluster of the OEC where they are accumulated and refilled by water-oxidation.<sup>(25–29)</sup> P700 transfers the electron via a chlorophyll A<sub>0</sub>, plastoquinone A<sub>1</sub> and the iron-sulfur protein triad Fe<sub>x</sub>-Fe<sub>A</sub>-Fe<sub>B</sub> to Fd. Fd is transporting the electron to FNR, the protein that reduces NADP<sup>+</sup> to NADPH. The cyclic electron transport<sup>(19–21)</sup> is not shown in the scheme.

transport, charge separation and build-up of the required redox potentials for H<sub>2</sub>O oxidation and NADP<sup>+</sup> reduction.<sup>[19–21]</sup>

P680\* is acting as initial electron donor, starting the electron transfer chain. By transmitting an electron to a Pheo in direct vicinity, the radical pair P680<sup>+</sup> Pheo<sup>-</sup> is formed.<sup>[26–29,45]</sup> P680<sup>+</sup> is the strongest biological oxidant known, providing an oxidizing potential of  $\sim +1.3$  V.<sup>[47,48]</sup> Thus, on the donor side, a tyrosine residue next to P680, the tyrosine Z (Y<sub>Z</sub>), is oxidized by P680<sup>+</sup> forming the Y<sub>Z</sub> radical.<sup>[26–29,45]</sup> P680<sup>+</sup> is re-reduced to P680. Y<sub>Z</sub> again is a strong oxidant showing a potential of  $\sim +1.2$  V<sup>[27,47,48]</sup> and is able to oxidize PSII's catalyst for water-oxidation in single-electron redox steps.<sup>[25–29]</sup> This catalyst is a CaMn<sub>4</sub>O<sub>5</sub> cluster which forms the OEC (*cf.* section 2.2.1).<sup>[36]</sup> In this cluster, four oxidation equivalents (electron holes) are accumulated before two molecules of H<sub>2</sub>O are oxidized and one dioxygen molecule, four protons and four electrons are released.<sup>[25–29]</sup> The four accumulated electron holes in the CaMn<sub>4</sub>O<sub>5</sub> cluster are refilled by the four released electrons and the cluster is re-reduced. So, the absorption of four photons by PSII is necessary for the formation of one O<sub>2</sub> molecule from 2 H<sub>2</sub>O (*cf.* section 2.2.2).<sup>[25–29]</sup>

On the acceptor side, the Pheo<sup>-</sup> radical is passing its electron to PQ<sub>A</sub> and further to PQ<sub>B</sub>.<sup>[26–29,45]</sup> PQ<sub>A</sub> is a firmly bound plastoquinone which is, under normal conditions, only reduced to the semiquinone level.<sup>[19,20,27,45]</sup> In contrast, PQ<sub>B</sub> is a mobile plastoquinone that is reduced and protonated to plastohydroquinone (PQH<sub>2</sub>) in two steps.<sup>[19,20,26–29,33,45]</sup> PQH<sub>2</sub> is then migrating out of PSII, diffusing through the lipid matrix of the thylakoid membrane to the quinone pool. A PQH<sub>2</sub> molecule from the quinone pool is then migrating along to the integral membrane protein complex

Cyt  $b_6f$ .<sup>[19-21,26,27]</sup> By this stepwise electron transfer, released electrons and electron holes are spatially separated, avoiding charge recombination. A detailed illustration of PSII's electron transfer chain is given in section 2.2, Figure 2.6.

Cyt  $b_6f$  accepts the two electrons from PQH<sub>2</sub>, which is re-oxidized to PQ.<sup>[19-21,26,27]</sup> One of these electrons is used in a cyclic electron transfer process for proton transport through the thylakoid membrane.<sup>[19-21]</sup> The other electron is donated to an iron-sulfur cluster of the so called Rieske protein subunit as part of a linear transportation pathway to PSI.<sup>[19-21]</sup> In the next step of this linear pathway, the electron is passed to the cytochrome  $f$  subdomain. Cytochrome  $f$  then reduces plastocyanin (PC).<sup>[19-21]</sup> PC is a small, water-soluble copper protein which is mobile in the thylakoid's lumen. Hence, electron transport to PSI's site in the stroma lamellae membranes is achieved.<sup>[19-21]</sup>

The electron donated by PC is accepted by P700<sup>+</sup>, which is formed by oxidative quenching of P700\*.<sup>[19-21]</sup> The electron released by P700\* is thought to be accepted by a chlorophyll, termed as A<sub>0</sub>.<sup>[19-21]</sup> A<sub>0</sub> is reducing a quinone (A<sub>1</sub>), which is passing the electron to a triad of membrane associated iron-sulfur proteins, FeS<sub>X</sub>, FeS<sub>A</sub> and FeS<sub>B</sub>.<sup>[19-21]</sup> Along the transfer chain, the electron is then donated to ferredoxin (Fd). Fd is a small water-soluble iron-sulfur protein, transporting the reduction equivalent to the membrane bound protein ferredoxin-NADP reductase (FNR).<sup>[19-21]</sup> In the final step of this electron transportation cascade FNR is reducing NADP<sup>+</sup> to NADPH, the reduction equivalent for CO<sub>2</sub> conversion in the Calvin-Benson-Bassham cycle.<sup>[19-21]</sup>

## 2.2 The photosynthetic machinery for water-oxidation: PS II

Photosystem II (PSII) is the enzyme where sunlight-driven water-oxidation occurs as partial reaction of photosynthesis.<sup>[19-21,25-29,49-51]</sup> As described above, from this reaction the reduction equivalents are derived to convert CO<sub>2</sub> to biomass as energy storage (*cf.* section 2.1).<sup>[19-21]</sup> Thus, in PSII the reaction sequence of biological solar energy conversion and storage starts. But the functions of PSII are not only interesting as a part of photosynthesis, but also as a paragon for water-oxidation catalysis as partial reaction of sustainable energy production<sup>[26-29]</sup>, the topic of this thesis (see part II).

To drive the biological water-oxidation, light has to be harvested, the collected energy has to be converted. Oxidation equivalents showing a suitable potential have to be build-up. Water molecules have to be channeled to their corresponding active site, products have to be transported out of the protein complex. Channeling processes as well as single reaction steps have to be regulated, side reactions should be avoided. Also protection and repair mechanisms are crucial.<sup>[19-21,25-29]</sup> To achieve all these functions, PSII is a multi domain integral membrane protein complex located in the thylakoid membrane, mainly in grana stacks (*cf.* section 2.1.1).<sup>[19-21,25-29,32-36]</sup> The protein complex is a homodimer (Figure 2.5).<sup>[32-36]</sup> Each monomer consists of about 20 subunits, containing a multitude of cofactors and has a mass of about 350 kDa.<sup>[32-36]</sup>

In addition to the protein chains, in crystal structures of PSII of the cyanobacteria *Thermosynechococcus elongatus*<sup>[32-34]</sup> and *Thermosynechococcus vulcanus*<sup>[35,36]</sup>, 35 (or 36<sup>[32,35]</sup>) chlorophyll  $a$  and 11  $\beta$ -carotene molecules have been identified. Thirteen of these chlorophyll and three of the carotene pigments are found in subunit CP43. Sixteen chlorophylls and four carotenes are found in CP47.<sup>[33,36]</sup> Subunits CP43 and CP47 are forming PSII's core antenna complexes, absorbing light energy and transferring it to the reaction center (*cf.* section 2.1.2).<sup>[27,32-34,36,45]</sup> Under high light conditions, chlorophyll  $a$  triplet states can be populated.<sup>[19,27,32,33,45]</sup> Singlet oxygen then can be formed by

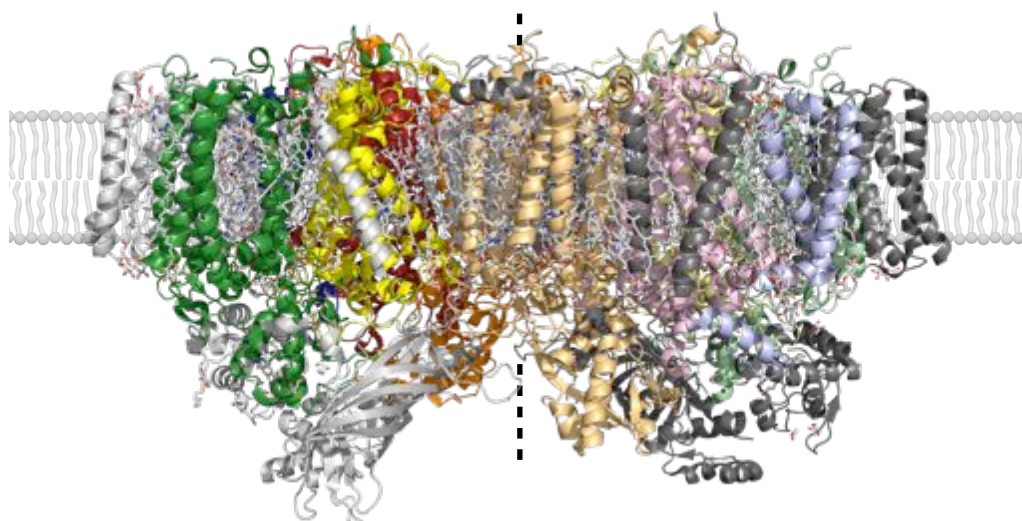


**Figure 2.5.** Crystal structure of PSII of *Thermosynechococcus vulcanus* at a resolution of 1.9 Å.<sup>[36]</sup> The integral membrane protein complex is a heterodimer placed in the thylakoid membrane (indicated in the background). The monomers (*left*, light gray and saturated colors; *right*, dark gray and pale colors) are located around a  $C_2$ -axis (dashed line). Each monomer has a mass of 350 kDa and consists of 20 subunits (of which PsbY was not found in this structure).<sup>[36]</sup> The main subunits are D1 (yellow), D2 (red), CP43 (green), CP47 (orange) and Cyt *b559* (blue). Additionally, several cofactors and detergents are present (shown as stick models). The figure is drawn using the coordinates from the structural analysis presented in<sup>[36]</sup>.

the reaction of molecular oxygen with the chlorophyll's triplet state, inducing oxidative damage of the enzyme. To protect PSII against this over excitation and the oxidative damage, certain  $\beta$ -carotenes are most likely quenching chlorophyll *a* triplet- and oxygen singlet states.<sup>[19,27,32,33,45]</sup>

D1 and D2 are the reaction center subunits. The chlorophylls of the reaction center (P680) as well as the cofactors of the electron transfer chain, pheophytin (Pheo) and the plastoquinones (PQs) are bound to these two domains.<sup>[27,32–36,45]</sup> The binding site of the mobile plastoquinone, PQ<sub>B</sub> is part of D1.<sup>[33,45]</sup> In contrast, the firmly bound plastoquinone is part of D2.<sup>[33]</sup> Electron transfer from PQ<sub>A</sub> to PQ<sub>B</sub> is mediated by a nonheme Fe coordinated by histidine side chains of D1 and D2 and a bicarbonate.<sup>[32,35]</sup> Two tyrosines are part of the amino acid sequences of D1 and D2, one placed in each subunit (Figure 2.6). The tyrosine in D1 is termed Y<sub>Z</sub> and, as mentioned above (*cf.* section 2.1.3), in its oxidized form as neutral Y<sub>Z</sub><sup>•</sup> radical, it oxidizes the CaMn<sub>4</sub>O<sub>5</sub> cluster of the OEC (*cf.* section 2.2.1), which is also a part of D1.<sup>[25–29,32–36]</sup> Tyrosin D (Y<sub>D</sub>) as a part of the sequence of D2 is not directly involved in electron transfer but is supposed to bias the transfer processes and is most likely playing a key role in relaxation of the OEC in the dark (*cf.* section 2.2.2).<sup>[32,33,45]</sup> A histidine is placed in direct vicinity of Y<sub>Z</sub> and Y<sub>D</sub> (H<sub>D1</sub> and H<sub>D2</sub> in Figure 2.6). These histidines are supposed to build hydrogen bonds to Y<sub>Z</sub> and Y<sub>D</sub> (indicated as dashed lines in Figure 2.6), likely playing a key role in stabilizing the formed tyrosine radicals.<sup>[32,45,52,53]</sup>

The heme containing subdomain cytochrome *b559* is, together with a chlorophyll *a* and  $\beta$ -carotene attached to D2 (*rightmost* in Figure 2.6), forming a secondary electron pathway.<sup>[32,33,45]</sup> If the lifetime of P680<sup>+</sup> is increased by an interruption of the electron feed from water-oxidation, it can be reduced by the secondary transfer route.<sup>[32,33,45]</sup> In

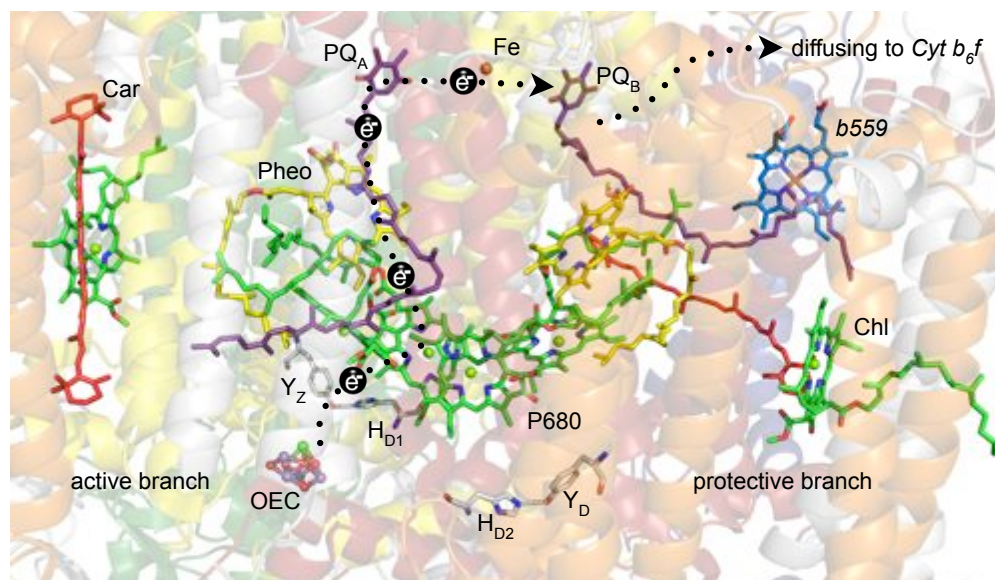


**Figure 2.6.** Reaction center and electron transfer chain of PSII. <sup>(27,32,33,45)</sup> Electrons originating in H<sub>2</sub>O oxidation are transferred from the OEC via Y<sub>Z</sub>, P680, Pheo and P<sub>QA</sub> to P<sub>QB</sub>. P<sub>QB</sub> is then reduced to PQH<sub>2</sub> and diffusing out of PSII. <sup>(32,33,45)</sup> A secondary electron transfer chain is formed by a Chl and Car bound to D2 (right) and cytochrome *b559* (*b559* heme is shown in blue, upper right). <sup>(32,33,45)</sup> The secondary transfer chain has a protective function, transporting electrons to Y<sub>D</sub>. Histidines H<sub>D1</sub> and H<sub>D2</sub> are building hydrogen bonds to Y<sub>Z</sub> and Y<sub>D</sub>, respectively. <sup>(32,45,52,53)</sup> Protein subunits are indicated in the background (color code as in Figure 2.5). The figure is drawn using the coordinates from the structural analysis presented in <sup>(36)</sup>.

addition, Loll *et al.* suggested regulation of PQ diffusion by cytochrome *b559*.<sup>[33]</sup>

Several lipids have been found in the crystal structures.<sup>[32–34,36]</sup> It has been proposed that these lipids are important mediators for the dimerization process of PSII as lipids are located at the monomer-monomer interface.<sup>[34]</sup> Further lipids are surrounding the reaction center and are also discussed to facilitate the exchange of damaged subunits.<sup>[33,34]</sup>

## 2.2.1 PSII's active site for water-oxidation: the OEC

The oxygen-evolving-complex (OEC), also termed as water-oxidizing-complex (WOC) is PSII's active site for water-oxidation. It consists of a  $\mu$ -oxido ( $\mu$ -O<sup>2-</sup>) bridged CaMn<sub>4</sub> cluster, coordinated by oxidation stable carboxylate and nitrogen moieties of the surrounding amino acids.<sup>[25–29,32,33,36,49–51]</sup> A detailed structural analysis of the OEC by X-ray diffraction was challenging due to radiation damage<sup>[29,54]</sup> and poor resolutions. However, several models were proposed based on joint methods of X-ray crystallography, X-ray absorption spectroscopy (XAS), electron paramagnetic resonance spectroscopy (EPR) and computational methods.<sup>[25–29,32,33,50,51,55]</sup>

In 2011, Umena *et al.* published a crystal structure of PSII isolated from the cyanobacterium *Thermosynechococcus vulcanus* at a resolution of 1.9 Å.<sup>[36]</sup> The orientation of the subunits is well corresponding to previously published structures. New informations on the composition as well as on the arrangement of the atoms of the OEC could be obtained. It has been shown that three Mn and the Ca of the CaMn<sub>4</sub> cluster are interconnected by four  $\mu_3$ -O-ligands, forming a distorted cubane like motif. The fourth Mn and a fifth O is attached to one edge of this cube, also by  $\mu$ -O-bridging, forming a unit

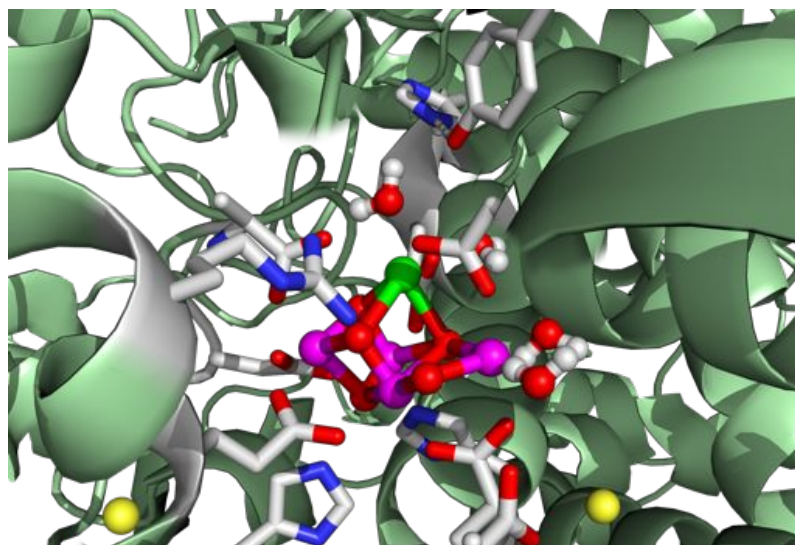


**Figure 2.7.** The oxygen-evolving-complex (OEC) of *Thermosynechococcus vulcanus*.<sup>[36]</sup> A  $\text{CaMn}_4\text{O}_5$  cluster (center) is biology's water-oxidation catalyst.<sup>[25–29,36,49–51]</sup> The cluster is coordinated by Arg, Asp, Glu and His side chains as well as an Ala C-terminus as ligands.<sup>[36]</sup> Also, four  $\text{H}_2\text{O}$  molecules bound to the cluster could be located, most likely including substrate water. Biology's oxidant  $\text{Y}_Z$  (as well as its neighbour  $\text{H}_{\text{D}1}$ , connected by a hydrogen bond, top) is also a part of the OEC. In direct vicinity, two chlorides have been identified (bottom, left and right). Color code: Ca in green, Mn in purple, O in red, N in blue, C in light gray, H in white, Cl in yellow. The figure is drawn using the coordinates from the structural analysis presented in<sup>[36]</sup>.

which is referred to as a distorted chair form (Figure 2.7).<sup>[36]</sup> Thus, the center of the OEC can be specified as a  $\text{CaMn}_4\text{O}_5$  cluster. But it is important to note that Mn-Mn distances are elongated in comparison to related structural models proposed previously.<sup>[32,55,56]</sup> This may best be explained by photoreduction of the  $\text{CaMn}_4\text{O}_5$  cluster by exposure of PSII to high X-ray radiation intensities during crystallography.<sup>[29,54]</sup>

Furthermore, it has been shown that the  $\text{CaMn}_4\text{O}_5$  cluster is coordinated by amino acid residues of subunits D1 and CP43. Namely, these ligands are: three aspartates, two glutamates, two histidines and one carboxylate of alanine of D1 and a glutamate as well as an arginine of CP43 (also shown in Figure 2.7).<sup>[36]</sup> Four molecules of  $\text{H}_2\text{O}$  as additional ligands of the  $\text{CaMn}_4\text{O}_5$  cluster have been found. This environment is resulting in a sixfold coordination of each Mn and a sevenfold coordination of Ca.<sup>[36]</sup> Two of the water molecules are bound to Ca, connecting the cluster with  $\text{Y}_Z$  via a network of hydrogen bonds. This network of hydrogen bonds also includes the other water molecules bound to the OEC and is building a channel to the lumen.<sup>[36]</sup> Thus, this channel is proposed to act as an exit pathway for protons released in a proton coupled electron transfer (PCET).<sup>[36]</sup> It also has been suggested by Umena *et al.*, that one of the bound water molecules could act as substrate for the oxygen evolution reaction (*cf.* section 2.2.2).<sup>[36]</sup>

Two chlorides have been found in vicinity of the  $\text{CaMn}_4\text{O}_5$  cluster.<sup>[36,57,58]</sup> These chlorides are positioned at the entrance of channels proposed as proton exit to the luminal bulk phase, or substrate water inlet channels.<sup>[34,36,45,57–60]</sup> Also channels for  $\text{O}_2$  removal have been postulated, reaching from the OEC to the lumen.<sup>[45,59–61]</sup>

## 2.2.2 The OEC's reaction cycle of water-oxidation

In the late sixties, Joliot *et al.* described a polarographic method which allowed the investigation of  $O_2$  production by excitation of suspensions of algae or chloroplasts by single saturating flashes.<sup>[62]</sup> Using this method, Kok and coworkers observed a correlation between the number of oscillating flashes and oxygen production, as they found maxima of  $O_2$  formation at flashes number three, seven and eleven. They postulated a four step mechanism, where a reaction- or trapping center accumulates four oxidizing equivalents as positive charges. The states of this trapping center were denoted as  $S_0^-$ ,  $S^+$ ,  $S^{2+}$ ,  $S^{3+}$  and  $S^{4+}$ -state, the charges are indicating the stored oxidizing equivalents.<sup>[63]</sup>

Today, Kok's S-state cycle is still considered, but a more detailed picture of the water-oxidation reaction has been developed.<sup>[25–29]</sup> The accumulation of oxidizing equivalents is achieved by stepwise single electron oxidation of the OEC which is thus cycling through the S-states (termed as  $S_0$  to  $S_4$ , indices are giving the stored oxidizing equivalents).<sup>[25–29]</sup> As described above,  $Y_Z$  is acting as oxidant. To facilitate the four-fold oxidation of the OEC by  $Y_Z$ , charge compensation for redox potential leveling is crucial.<sup>[26–29]</sup> For this  $\mu$ -OH bridges, as well as terminal hydroxido groups and bound water molecules have been proposed to be involved in proton coupled electron transfer (PCET) and possibly also in the O–O bond formation step.<sup>[28,29,64–66]</sup> The amino acid environment is involved in proton abstraction and transfer in water-oxidation catalyzed by PSII.<sup>[28,29,36,45,60,61]</sup> The electrons are mainly removed from the Mn centers of the  $CaMn_4$  complex. It is mostly assumed that each S-state transition up to  $S_3$  is implying an oxidation of  $Mn^{III}$  to  $Mn^{IV}$ .<sup>[25–29]</sup>

The  $S_1$ -state is the (longterm) dark stable state. The oxidation states of the Mn centers in  $S_1$  are broadly accepted to be  $Mn_2^{III}Mn_2^{IV}$ .<sup>[25–29]</sup> After absorption of a photon

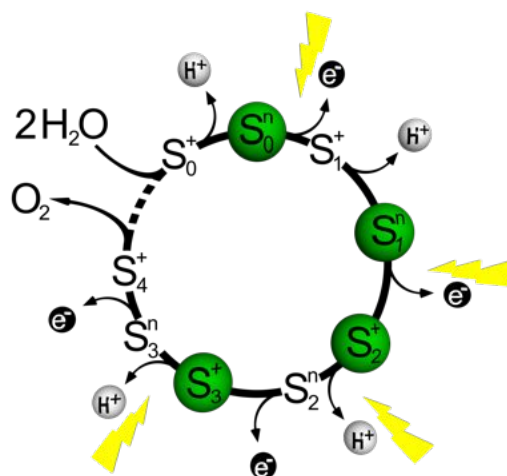


**Figure 2.8.** Schematic representation of the water-oxidation reaction cycle, including PCET for redox potential leveling.  $S_1^n$ ,  $S_2^n$ ,  $S_3^n$  and  $S_0^n$  (green spheres) are stable intermediates and correspond to  $S_1$ ,  $S_2$ ,  $S_3$  and  $S_0$  respectively.  $S_1^n$  is the dark stable state. After absorption of a photon (indicated as yellow flash), alternating electron and proton removal steps are induced.<sup>(67–70)</sup> In the  $S_3^n \rightarrow S_0^n$  transition, the O–O bond is formed,  $O_2$  is released and one or two molecules of water are rebound to the OEC.<sup>(25,27–29)</sup> After the absorption of four photons, the OEC is again in its dark stable state ( $S_1^n$ ). The index gives the accumulated oxidizing equivalents, while + (positive) or n (neutral) are indicating the charge relative to the dark stable  $S_1$  state. The figure is redrawn from<sup>(69)</sup> and<sup>(70)</sup>.

(first flash), one  $\text{Mn}^{\text{III}}$  ion of the  $\text{CaMn}_4\text{O}_5$  cluster is oxidized by  $Y_Z$  leading to oxidation states of  $\text{Mn}_1^{\text{III}}\text{Mn}_3^{\text{IV}}$  in  $S_2$ .<sup>[25-29]</sup> For the  $S_2 \rightarrow S_3$  transition (absorption of a second photon) either a Mn centered<sup>[64,71-73]</sup> oxidation to  $\text{Mn}_4^{\text{IV}}$ , or a ligand centered oxidation<sup>[25,74-76]</sup> has been proposed.  $S_4$  is postulated as transient state that rapidly decays to  $S_0$  ( $\text{Mn}_3^{\text{III}}\text{Mn}_1^{\text{IV}}$ ).<sup>[25,27-29]</sup> In the  $S_3 \rightarrow S_0$  transition, no Mn centered oxidation occurs. More likely an oxygen centered oxidation takes place, forming an oxyl radical ( $\text{O}^-$ ) that is then involved in O–O bond formation.<sup>[25-29]</sup> So, after the absorption of a third photon (third flash),  $\text{O}_2$  is released and one or two water molecules are rebound to the  $\text{CaMn}_4\text{O}_5$  cluster. By the absorption of a fourth photon, the cluster is oxidized to the  $S_1$  state and a full reaction cycle has been accomplished. Additional intermediates have been described in respect of alternating electron and proton removal steps.<sup>[67-70]</sup> A water-oxidation cycle including these intermediates is shown in Figure 2.8.

It also has been shown that the structure of the  $\text{CaMn}_4\text{O}_5$  complex is changing by the S-state transitions of the water-oxidation reaction cycle (Figure 2.9).<sup>[26,64,77]</sup> This is not only reflecting the structural flexibility of this cluster, but has also consequences for water-oxidation mechanisms. For instance, it has been concluded that deprotonation of a  $\mu\text{-OH}$  bridge occurs during the  $S_0 \rightarrow S_1$  transition.<sup>[26,64,77]</sup> The deprotonation of such a  $\mu\text{-OH}$  is resulting in a slightly shorter Mn–Mn distance. The formation of additional  $\mu_3\text{-oxido}$  bridges in the  $S_2 \rightarrow S_3$  transition has been observed associated with Mn oxidation.<sup>[26,64,77]</sup> These results are indicating the involvement of  $\mu\text{-O}$  and  $\mu\text{-OH}$  bridges in proton management and are very likely showing possible routes for substrate water binding and deprotonation.

Several scenarios for the O–O bond formation in water-oxidation catalyzed by the OEC have been proposed.<sup>[26,29]</sup> It is mostly assumed that a peroxide intermediate is formed in the  $S_3 \rightarrow S_0$  transition as the rate-limiting step, whereat bridging  $\mu\text{-O}^{2-}$  or oxyl groups ( $\text{O}^-$ ), as well as hydroxide or water molecules are playing a key role (Figure

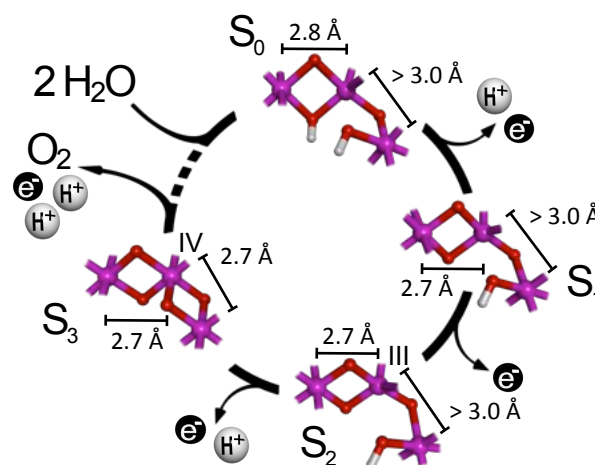


**Figure 2.9.** Electronic changes of the OEC during S-state transitions are accompanied by structural changes.<sup>(64)</sup> For the  $S_0 \rightarrow S_1$  transition, the deprotonation of a  $\mu\text{-OH}$  ligand has been detected. During the  $S_2 \rightarrow S_3$  transition, additional  $\mu\text{-O}$  bridges are very likely formed. For simplification only three of the four Mn ions of the  $\text{CaMn}_4$  complex are shown. Color code: Mn in purple, O in red. The figure is redrawn from<sup>(64)</sup>.

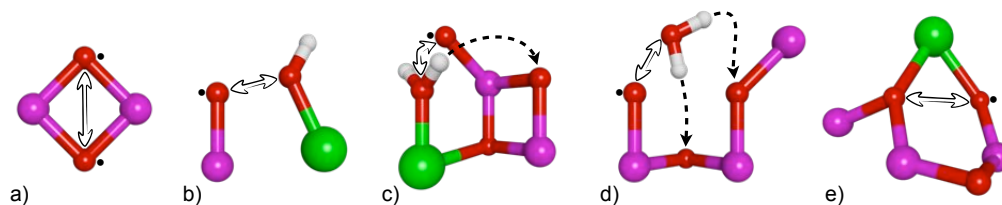


**Figure 2.10.** Proposed mechanisms for O–O bond formation in water-oxidation catalyzed by the OEC. During the  $S_3 \rightarrow S_0$  transition, a peroxide intermediate could be formed by coupling of two  $\mu$ -O ligands, participation of  $\mu$ -O $^{\cdot-}$  radicals has been suggested (a, e).<sup>[49,55,78]</sup> A nucleophilic attack of the substrate in form of hydroxide-<sup>[79]</sup> (b) or water molecules<sup>[26,29,32,80,81]</sup>, activated by  $Ca^{2+}$  (b,c), as well as a direct attack of an outer sphere water<sup>[77,82,83]</sup> (d) is under discussion. In c) and d) proton abstraction mechanisms involving neighboring  $\mu$ -O ligands are also indicated. Color code: Ca in green, Mn in purple, O in red, H in light gray. The figure is redrawn from<sup>[29]</sup>.

2.10).<sup>[26,29]</sup> Bridging oxyl- or oxido ligands could be activated to form a peroxide intermediate either from two bridging  $\mu$ -O $^{2-/-}$  ligands<sup>[49,78]</sup> (Figure 2.10, a), or a  $\mu_2$ - and a  $\mu_3$ -O $^{2-/-}$ , both coordinated to Mn on the one side and to Ca at the other<sup>[55]</sup> (Figure 2.10, e). As shown in Figure 2.10, b) and c), the nucleophilic attack of a hydroxide<sup>[79]</sup> or of a water molecule<sup>[26,29,32,80,81]</sup> bound and activated by Ca (or also Mn), to a terminal oxygen (Mn<sup>V</sup>=O or Mn<sup>IV</sup>–O $^{\cdot}$ ) has been proposed. A direct attack of an outer sphere H<sub>2</sub>O on a terminal oxido ligand bound to Mn is also conceivable (Figure 2.10, d).<sup>[77,82,83]</sup> The possible involvement of  $\mu$ -O ligands in the essential proton management process is indicated in route c) and d) in Figure 2.10.

The role of  $Ca^{2+}$  in water oxidation-catalysis is not known in detail yet. It has been shown by several research teams that it is strongly influencing the catalytic activity of the OEC, as water-oxidation is inhibited if calcium is removed from the protein.<sup>[84–89]</sup> The catalytic activity of the OEC can be reactivated by addition of  $Ca^{2+}$  to the  $Ca^{2+}$ -depleted enzyme. The activity can also be restored by the addition of  $Sr^{2+}$  ions, though the observed reactivity is lower.<sup>[84–86,90]</sup> On the contrary, the addition of  $Mg^{2+}$  ions does not result in the reactivation of the OEC.<sup>[84,86]</sup>

Lately Cox *et al.* demonstrated by a combined EPR/<sup>55</sup>Mn-ENDOR/DFT analysis that the electronic structure of the OEC is not changed significantly by  $Ca^{2+} \rightarrow Sr^{2+}$  replacement.<sup>[91]</sup> In a comparison of <sup>55</sup>Mn-ENDOR data of *Thermosynechococcus elongatus* and previously published data of spinach<sup>[92–94]</sup>, the observed changes by  $Ca^{2+} \rightarrow Sr^{2+}$  exchange were in fact less than the differences between the two species.<sup>[91]</sup> But as  $Sr^{2+}$ -substituted PSII shows a reduced activity anyway, Cox *et al.* inferred that  $Ca^{2+}$  is actively involved in the biological catalytic process.

It has been assumed that the  $Ca^{2+}$  ion is either acting as activation (Figure 2.10, e), or as activation and binding site (Figure 2.10, b and c) for the substrate in form of water or hydroxide molecules.<sup>[36,79,80,95–97]</sup> It also could play a key role as a factor supporting S-state advancement.<sup>[96,97]</sup> Nevertheless, many mechanistic details of water-oxidation catalyzed by the OEC remain to be elucidated.

# 3 A concept for alternative energy production: artificial photosynthesis

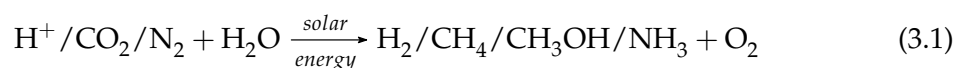
## 3.1 The idea of artificial photosynthesis

The identification of alternatives in energy production is absolutely crucial to meet human energy demand in a sustainable way (*cf.* chapter 1). As the amount of solar energy hitting the Earth is absolutely tremendous and by far exceeding our needs, solar energy is enjoying increasing attention. However, presently only a very small fraction is used by photovoltaics, solar heating or in the broader sense to grow biomass for energy production. One of the great challenges to take full advantage of the enormous potential of the sun as sustainable energy source is to capture solar energy and convert it into useful and storable forms.

Already in 1912, the Italian scientist Giacomo Ciamician was thinking about solutions for this challenge. Estimating the amount of solar energy stored by plants, he proposed it should be possible to use stored solar energy in the form of fast growing plants to meet the energy demand of his days.<sup>[6]</sup> But he was also going one step further. Instead of growing plants, Ciamician suggested, it should be possible to find artificial photochemical reactions to capture solar energy hitting the Earth. And by the use of capable catalysts, it should be possible to mimic the light-driven conversion of CO<sub>2</sub> into biomass taking place in plants during photosynthesis (*cf.* chapter 2). By developing this approach, Ciamician stated, it should be feasible to form CH<sub>4</sub> as a fuel by a sunlight-driven transformation of CO<sub>2</sub> and H<sub>2</sub>O.<sup>[6]</sup>

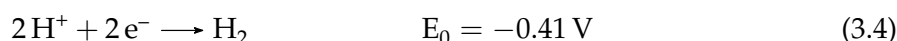
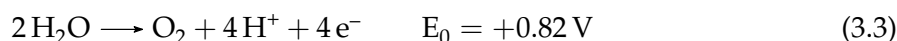
Today, Ciamician's image of mimicking the chemistry of photosynthesis has gained the attention of researchers around the world, as the generation of so called *solar fuels* by *artificial photosynthesis* is of great interest. But it also is clear that the complex reaction sequences of photosynthesis (*cf.* chapter 2) can not be easily duplicated by a technical process. Rather it is necessary to simplify the natural paragon and cut it down to fundamental processes that can then be transferred into concepts for artificial photosynthesis.

To meet the enormous human energy demand in a sustainable way, abundant and non-toxic starting materials are required. H<sup>+</sup>, CO<sub>2</sub> and N<sub>2</sub> are possible abundant reactants to be reduced to fuels like H<sub>2</sub>, CH<sub>4</sub>, MeOH, EtOH, DME or NH<sub>3</sub>, which are currently all under discussion as promising candidates (eq. 3.1).<sup>[5,98]</sup>



In all of these scenarios, the reduction equivalents needed to generate the solar fuel are derived from H<sub>2</sub>O, as it seems to be the only suitable electron source available on the required scale. Furthermore, hydrogen evolved from H<sub>2</sub>O has a promising potential to be used as clean, carbon free energy carrier whose consumption would only produce H<sub>2</sub>O as a waste product. Thus, water splitting for H<sub>2</sub> production (eq. 3.2) is currently the most intensely discussed and investigated approach.<sup>[1-5,27,29,99-103]</sup> This reaction is generally separated into oxidation and reduction half-reactions. In water-oxidation (eq.

3.3), two H<sub>2</sub>O molecules are converted into O<sub>2</sub>, four protons and four electrons (reduction equivalents) in a process resembling the overall reaction of PSII. In the reduction half-reaction, the released protons are reduced to H<sub>2</sub> (eq. 3.4) by the electrons generated in the water-oxidation half-reaction. The redox potentials for eqs. 3.3 and 3.4 are given for pH=7 *vs.* NHE.<sup>[15]</sup> In addition to being directly usable for energy production in fuel cells, hydrogen can also be used in further reaction steps to produce fuels like CH<sub>4</sub>, CH<sub>3</sub>OH or NH<sub>3</sub> (see above).<sup>[5,98]</sup>



## 3.2 Requirements for catalysts for efficient water-splitting

As simple as water-splitting seems to be taking eq. 3.2 into account, it is extremely challenging to develop systems that drive this reaction using sunlight. Suitable redox potentials have to be provided by light-harvesting molecular dyes or solid state absorbers, which should ideally capture a large portion of the solar spectrum and convert photons into high-energy electrons and holes. The single-electron photochemistry of the dyes has to be coupled to the much slower multi-electron redox chemistry of water-oxidation and proton-reduction catalysts. Suitable materials have to be found in order to accumulate oxidation equivalents (electron holes) to facilitate water-oxidation on the one hand and to accumulate reduction equivalents (electrons) for the reductive generation of a solar fuel on the other hand. To prevent recombination by back-reactions, efficient, long-lasting charge separation is crucial. Finally, all components have to be coupled to achieve the water-splitting reaction in an artificial photosynthetic system (*cf.* section 3.3).

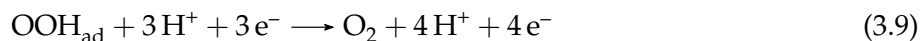
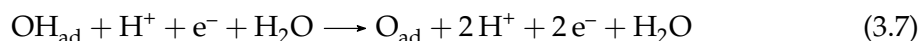
### 3.2.1 The overpotential of catalytic water-splitting

In general, the term *overpotential* describes a kinetic phenomenon in electrochemistry.<sup>[29]</sup> It is determined by processes taking place at the electrode-electrolyte junction. For instance, limitations of the electron transfer at low currents, of the diffusion of reactants and products or of the reaction rates, which might be unable to keep pace with electron transfer are contributing to the phenomenon.<sup>[29,104]</sup> The overpotential ( $\eta$ ) is defined as the deviation of an observed electrode potential ( $E$ ) from the theoretical ( $E_r$ ).<sup>[104]</sup>

$$\eta = E - E_r \quad (3.5)$$

In electrocatalysis, the overpotential describes a kinetic hinderance of elementary reaction steps.<sup>[29]</sup> It is described as a function of the current for the reaction step with the highest kinetic activation barrier, which is the rate limiting step.<sup>[29]</sup>

The elementary reaction steps of the electrocatalytic water-splitting mechanism are not known in detail today and will most likely also vary with the used electrocatalyst. Nevertheless, mechanistic schemes have been proposed based on investigations and theoretical computational studies.<sup>[29]</sup> For instance, Rossmeisl *et al.* performed DFT calculations to analyze the electrochemical water-splitting process catalyzed by metal- and metal-oxide electrodes.<sup>[105,106]</sup> In an acidic environment they assumed the following reaction steps to take place during oxygen evolution at the anode:



For the generation of hydrogen at the cathode, they considered the following elementary steps:



In this proposed mechanistic scheme,  $\text{OH}_{\text{ad}}$ ,  $\text{O}_{\text{ad}}$  and  $\text{OOH}_{\text{ad}}$  as well as  $\text{H}_{\text{ad}}$  are adsorbed intermediates at active sites on the surface of the electrodes.<sup>[105,106]</sup> Most of the processes contributing to the overall overpotential for water-splitting are related to the water-oxidation reactions (eqs. 3.6 to 3.9).<sup>[105,107]</sup> The formation of the peroxide intermediate (eq. 3.8) is the most unfavorable reaction step, which occurs only at high potentials.<sup>[29,105,106]</sup>

Rossmeisl and coworkers further found a linear scaling relation between the adsorption energy of the intermediates. Based on this linear binding energy relation, the catalytic activity in oxygen evolution can be described as a function of the binding energy of oxygen to the surface.<sup>[105]</sup> In this case, the oxygen binding energy is directly related to the overpotential. Too weak but also too strong binding are both lowering the catalytic rate, so that an optimization of the binding energy is a key step towards the rational design of more efficient catalysts to be used in artificial photosynthetic systems.<sup>[29,106]</sup>

However, the four single-electron steps of this mechanistic model eqs. 3.6 to 3.9 for electrocatalytic water-oxidation at metal or metal-oxide surfaces are all oxygen centered. It is important to note that the most steps of the four step single-electron mechanism (eq. 3.3) suggested for water-oxidation catalyzed by the OEC are manganese centered, while oxygen centered oxidation is discussed to take place only in one step (*cf.* section 2.2.2).<sup>[25-29,64]</sup> The formation of unfavorable intermediates like OOH eq. 3.8 can thereby be avoided. Mechanistic models proposing metal centered single-electron steps, but also two- or three-electron steps are potential routes for water-oxidation as well, depending on the respective catalyst and the applied oxidizing potential.

### 3.3 Concepts for light-driven water-splitting catalysis

Even though Ciamician's idea of the reductive formation of a solar fuel using electrons obtained from catalytic water-oxidation is about a hundred years old<sup>[6]</sup>, the quest for capable photo- and redox-catalysts is still at its beginning. Nevertheless, in the last decades research on the water-oxidation process of biological photosynthesis was intensified to broaden the understanding of water-oxidation catalysis (*cf.* section 2.2.2). Promising research progress was achieved as first synthetic redox-catalysts were found. The best water-oxidation catalysts known today belong to the compound classes of transition-metals, their -oxido complexes, -polyoxometallates (POMs) or -oxides, respectively (*cf.* chapter 4). Additionally semiconductor photocatalysts are under investigation.

Interdisciplinary research projects on water-splitting catalysis were followed by different research communities. Heterogeneous electro catalysis at electrode surfaces or

by oxidic bulk materials deposited on electrodes, heterogeneous catalysis by suspended particles, homogeneous catalysis by POMs and metal complexes as well as biocatalytic water-splitting are of interest.<sup>[29]</sup> For the combination of photo- and redox-catalysis to reach the allover light-driven water-splitting reaction, molecular- (section 3.3.1), semiconductor based- (section 3.3.2) and electrocatalytic concepts (section 3.3.3) as well as designs for photo electrochemical cells (PECs) for solar fuels production (section 3.3.4) are under investigation.

### 3.3.1 Molecular and supramolecular concepts for water-splitting

In 1979 Kirch *et al.* presented a concept for water-splitting under the irradiation of sunlight. In this proposed system, water-oxidation and -reduction half-reactions are separated into subsystems divided by a membrane. Each of the subunits contains a suitable dye (photosensitizer) for light-harvesting and a catalyst for water-oxidation and proton-reduction, respectively. Both subsystems are coupled by a redox relay (R/R<sup>-</sup>), which is able to transfer electrons across the membrane (Figure 3.1, *top*).<sup>[98]</sup>

Similar to photosynthesis, the reaction sequence is supposed to start with the absorption of light by the photosensitizers P, which thereby reach their excited states (P<sup>\*</sup>). P<sup>\*</sup> then can either be quenched by releasing an electron (oxidative quenching, eq. 3.12), or by capturing an electron (reductive quenching, eq. 3.13).<sup>[98]</sup> Electrons or electron holes are generated that can then be transferred to the catalyst for water-oxidation (Cat<sub>ox</sub>) and the catalyst for (proton-)reduction (Cat<sub>red</sub>), respectively.



If oxidative quenching occurs, the reaction sequence is starting with an electron release by P<sup>\*</sup> to obtain P<sup>+</sup>. In the water-oxidation subsystem, the released electron is donated to R/R<sup>-</sup>. P<sup>+</sup> is then capturing a single electron from Cat<sub>ox</sub> and is thereby re-reduced back to P. In the proton-reduction subsystem, the electron released by P<sup>\*</sup> is directly transferred to Cat<sub>red</sub>. P<sup>+</sup> is then re-reduced by capturing an electron provided by the oxidation half-reaction transferred via R/R<sup>-</sup>.

If reductive quenching occurs, the reaction sequence is starting with the uptake of an electron by P<sup>\*</sup> to yield P<sup>-</sup>. In the oxidative subunit, P<sup>\*</sup> is oxidizing Cat<sub>ox</sub> directly, forming P<sup>-</sup> which is re-oxidized by R. In the reductive subunit, P<sup>\*</sup> is abstracting an electron from R<sup>-</sup>, forming P<sup>-</sup> which is then reducing Cat<sub>red</sub>. P<sup>-</sup> is thereby re-oxidized to P.

Cat<sub>ox</sub> and Cat<sub>red</sub> are redox catalysts for accumulating oxidation- and reduction equivalents, respectively, to couple the single-electron steps of photochemistry with the multi-electron redox reactions of water-oxidation and proton-reduction. After the fourfold electron abstraction of P<sup>+</sup> and P<sup>\*</sup>, respectively, four oxidizing equivalents are accumulated in Cat<sub>ox</sub> and water-oxidation occurs. One molecule of O<sub>2</sub>, four protons and four electrons are released, re-reducing Cat<sub>ox</sub>. For proton-reduction, two reduction equivalents (electrons) have to be accumulated in Cat<sub>red</sub> before the reduction of two protons to one molecule of H<sub>2</sub> can take place.<sup>[98]</sup>

Kirch *et al.* proposed their system based on their investigations of the light-driven proton-reduction half-reaction using [Ru(bpy)<sub>3</sub>]<sup>2+</sup> as P, [Rh(bpy)<sub>3</sub>]<sup>3+</sup> as a relay and colloidal platinum as Cat<sub>red</sub>.<sup>[98]</sup>

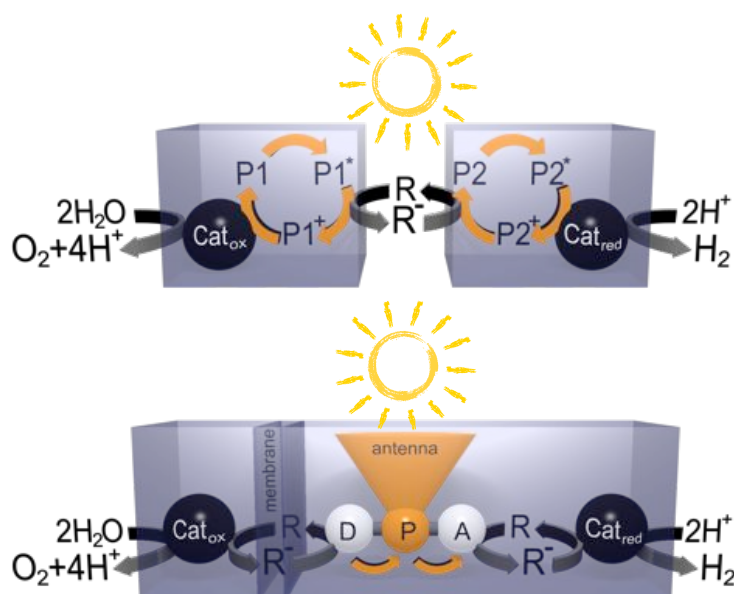


**Figure 3.1.** Designs for artificial photosynthetic systems. Excited by sunlight, photosensitizers P1 and P2 (*top*)<sup>(27,98)</sup> or an antenna complex coupled to a donor-photosensitizer-acceptor triad (D-P-A) (*bottom*)<sup>(5,108)</sup> are excited by sunlight. Driven by this energy, electrons provided by the water-oxidation half-reaction catalyzed by  $\text{Cat}_{\text{ox}}$  (*left*) are transferred by  $\text{R}/\text{R}^-$  to  $\text{Cat}_{\text{red}}$  (*right*) where the reductive formation of the solar fuel takes place. The crucial charge separation is achieved by using spatially separated photosensitizers (*top*) or the D-P-A triad (*bottom*). The figure is redrawn from refs.<sup>(27,98)</sup> (*top*) and refs.<sup>(5,108)</sup> (*bottom*).

In 2008, Balzani *et al.* introduced an alternative design for a light-driven water-splitting device (Figure 3.1, *bottom*).<sup>[108]</sup> Similar to the proposed system of Kirch *et al.*, the water-splitting half-reactions taking place at  $\text{Cat}_{\text{ox}}$  and  $\text{Cat}_{\text{red}}$  are separated by a membrane.

But instead of using molecular dyes as photosensitizers, Balzani *et al.* proposed to attach a supramolecular antenna complex for light-harvesting directly to a donor-photosensitizer-acceptor triad (D-P-A) for charge separation.<sup>[5,108]</sup> The antenna complex is thereby acting like the antenna pigment-protein complexes of PSII and PSI (*cf.* section 2.1.2). Photons of light are absorbed and the collected energy is funneled to an artificial reaction center (D-P-A). The reaction center is then acting as initial electron donor, starting the electron transfer chain. In this chain, electrons released by water-oxidation at  $\text{Cat}_{\text{ox}}$  are transferred to the D-P-A triad via  $\text{R}/\text{R}^-$ . D is re-reducing the reaction center P, which has previously donated an electron to A.  $\text{Cat}_{\text{red}}$  is then accumulating the reduction equivalents transferred via  $\text{R}/\text{R}^-$  to facilitate the formation of  $\text{H}_2$  as a solar fuel. As antenna complexes, dendrimers based on  $\text{Ru}^{2+}$  and  $\text{Os}^{2+}$  complexes or on zinc porphyrins and also organic dendrimers are under discussion. The antenna complexes are proposed to be attached to metal complexes as artificial reaction centers.<sup>[108]</sup>

### 3.3.2 Photocatalytic semiconductor particles for water-splitting

On absorption of light of sufficient energy, semiconductors are able to excite electrons into higher energy levels and thereby overcome the band gap of the semiconductor. When electrons are excited from the valence band to the conduction band of the semiconductor, electron-hole pairs are generated which can be utilized for water-splitting. The energy of the absorbed light as well as the energy of the excited electrons is depending on the band gap of the semiconductor. The efficiency of light-harvesting can be affected by tuning the band gap of certain semiconductors e. g. by different doping.

Taking into account the standard potential of the water-splitting reaction of 1.23 V (eq. 3.2), semiconductors with a band gap of  $\geq 1.23$  eV, corresponding to photons of wavelengths of about 1000 nm or shorter, theoretically have the potential to be used for water-splitting. However, to drive water-splitting effectively, the required energy has been reported as 1.6 to 2.4 eV per generated electron-hole pair (*cf.* section 3.3.4).<sup>[109]</sup> This amount of energy corresponds to light with wavelengths between 780 to 500 nm. The higher energy requirement arises because of energy losses attributable to recombination of generated electron-hole pairs and kinetic overpotentials at the semiconductor-liquid junction (*cf.* section 3.2.1).<sup>[109]</sup> Following this consideration, concepts based on photocatalytic semiconductor particles as catalysts for light-driven water-splitting have been proposed. In two distinct designs, overall light-driven water-splitting should either be achieved by a single semiconductor catalyst<sup>[110]</sup> (Figure 3.2), or by two different types of semiconductors separating water-oxidation and -reduction in a Z scheme like fashion.<sup>[110-112]</sup>

In systems using one photocatalytic semiconductor simultaneously as  $\text{Cat}_{\text{ox}}$  and  $\text{Cat}_{\text{red}}$ , no electron transfer between the catalyst particles is necessary. However, the redox potential provided by the generated electron-hole pairs of one particle has to be sufficient to drive both half-reaction, water-oxidation and -reduction. On the contrary, if two photocatalytic semiconductors are used, one as  $\text{Cat}_{\text{ox}}$  and one as  $\text{Cat}_{\text{red}}$ , redox potentials can be tuned either for water-oxidation, or for proton-reduction. Also a broader range of the light spectrum is available.<sup>[110]</sup> Electron transfer between  $\text{Cat}_{\text{ox}}$  and  $\text{Cat}_{\text{red}}$  can then

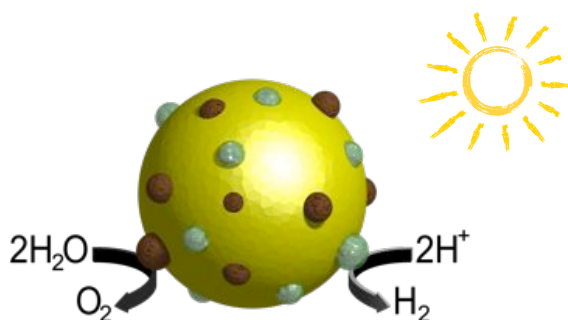


**Figure 3.2.** Concept for light-driven water-splitting using a photocatalytic semiconductor particle as light absorbing entity (yellow sphere). When the semiconductor is absorbing sunlight, an electron-hole pair is generated which can be utilized for water-splitting. By decorating the photocatalyst with co-catalysts for water-oxidation (brown) and -reduction (green), higher efficiencies can be achieved. For example, water-splitting was observed using GaN/ZnO particles, decorated with  $\text{Mn}_3\text{O}_4$  for  $\text{O}_2$  evolution and Rh/ $\text{Cr}_2\text{O}_3$  core/shell nano particles for  $\text{H}_2$  formation.<sup>[113]</sup> In another scheme for light-driven water-splitting two photocatalysts are used, one for the oxidative, one for the reductive half-reaction.

occur directly, or facilitated through mediators (R/R').<sup>[110–112]</sup>

Albeit even higher requirements have to be met when a single photocatalytic semiconductor is used, general conditions are quite similar for both concepts. As described above, the band gap of the respective catalyst has to be suitable for the absorption of visible light (i. e. sunlight) and the accessible redox potentials have to be suitable to the water-splitting reaction (eq. 3.2) or its half-reactions (eqs. 3.3 and 3.4). In both arrangements, the semiconductor particles have to be stable against corrosion under the harsh reaction conditions of high oxidation potentials in the presence of O<sub>2</sub>.

Nevertheless, systems following both approaches have already been prepared. By decorating the semiconductor surface with co-catalysts, the water-splitting efficiency could be increased. For example, Kazuhiko Maeda, Kazunari Domen *et al.* developed a two-step system using WO<sub>3</sub> for the oxidative and ZrO<sub>2</sub>/TaON for the reductive half-reaction, both modified with Pt as co-catalyst, attaining an efficiency of 6.3 %. As mediator to facilitate electron transfer, IO<sub>3</sub><sup>-</sup>/I<sup>-</sup> was used.<sup>[110,114]</sup> Kudo *et al.* successfully prepared a BiVO<sub>4</sub> (Cat<sub>ox</sub>) - SrTiO<sub>3</sub>/Rh (Cat<sub>red</sub>) system, modifying SrTiO<sub>3</sub>/Rh with Pt and Ru, respectively, as co-catalyst for H<sub>2</sub> evolution. Here Fe<sup>2+</sup>/Fe<sup>3+</sup> was used as redox relay, but a direct inter-particle electron transfer has also been reported.<sup>[111]</sup> Water-splitting systems using one type of semiconductors have been realized by modifying GaN/ZnO with Mn<sub>3</sub>O<sub>4</sub> for O<sub>2</sub>- and Rh/Cr<sub>2</sub>O<sub>3</sub> core/shell nano particles for H<sub>2</sub> evolution as well as NaTaO<sub>3</sub> modified with NiO for H<sub>2</sub> generation.<sup>[113]</sup>

### 3.3.3 Electrocatalytic water-splitting

Electrocatalytic water-splitting, also termed as water electrolysis, is the splitting of water into O<sub>2</sub> and H<sub>2</sub> (eq. 3.2) driven by energy supplied by electricity. Its long history began in 1789 when Troostwijk and Deiman were the first who published experiments on water electrolysis.<sup>[115,116]</sup> In these experiments, gold wires were used as electrodes connected to an electrostatic generator based on friction. Placed next to each other in a glass tube filled with water, gas evolution was observed at the gold electrodes caused by the electric discharges of the generator. The gas evolved in their experiments was collected and then explosively converted by an electric spark.<sup>[115,116]</sup> Referring to Cavendish who previously had demonstrated that water is formed when a 2:1 mixture of H<sub>2</sub> and O<sub>2</sub> is exposed to such an electric spark<sup>[116,117]</sup>, they concluded they had produced and recombined H<sub>2</sub> and O<sub>2</sub>.<sup>[115,116]</sup> In the years to follow, Pearson and also Nicholson and Carlisle as well observed water electrolysis.<sup>[116,118,119]</sup> Allesandro Volta's reproducible source of constant voltage, his *electric pile* published in 1800, was a major leap for electrochemistry and also for electrocatalytic water-splitting.<sup>[116,118,119]</sup> Volta probably also applied his pile to water electrolysis at this time.<sup>[119]</sup>

About 70 years later, in 1866, August Wilhelm von Hofmann described an apparatus for electrolyzing water and also for the quantification of the evolved gases, O<sub>2</sub> and H<sub>2</sub> (Figure 3.3).<sup>[120]</sup> In his assembly, Hofmann used a three-branched glass tube filled with aqueous diluted acid (usually H<sub>2</sub>SO<sub>4</sub>), whereat the acid is added as electrolyte.<sup>[15]</sup> One branch is open at the upper end and is used as a reservoir for the aqueous solution. The other two branches are of equal size and are closed at the upper end by a stop-cock. Platinum electrodes are placed at the bottom of these tubes. All three branches are connected to each other, assuring a free exchange of the solution in the whole system. Connected to a current source, gas evolution can be observed at the electrodes. Today it is known that catalysis on platinum is taking place under the initial formation of Pt-oxido motifs on the electrode surface.<sup>[121]</sup> At the anode, water is oxidized to O<sub>2</sub> (eq. 3.3),

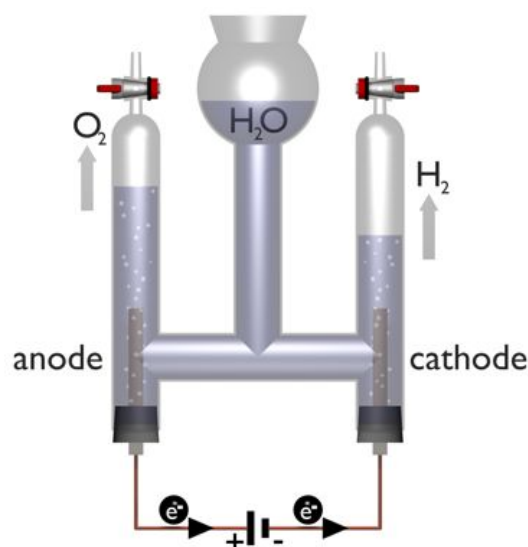


**Figure 3.3.** The Hofmann voltameter, an apparatus for water electrolysis described in 1866.<sup>[120]</sup> The three branched glass vessel is filled with an aqueous diluted acid (usual  $\text{H}_2\text{SO}_4$ ) acting as the electrolyte.<sup>[15]</sup> The central branch is open and used as a reservoir. Platinum electrodes are placed at the bottom of the outer branches. Connected to a battery or an other current source, gas evolution can be observed at the electrodes as water-splitting occurs. At the anode (*left*) water is oxidized to  $\text{O}_2$  (eq. 3.3). At the cathode (*right*) water is reduced to  $\text{H}_2$  (eq. 3.4).

at the cathode protons are reduced to  $\text{H}_2$  (eq. 3.4).<sup>[15,120]</sup>

In modern electrolyzers the electrocatalytic water-splitting is not directly carried out at the surface of solid electrodes like the platinum sheet of the Hofmann voltameter. Instead, the catalysts are deposited on electrode surfaces. In alkaline water electrolyzers, so called dimensionally stable anodes (DSA) are used, thin films of ruthenium- or iridium oxide directly supported on metallic titanium.<sup>[122–124]</sup> In polymer electrolyte membrane (PEM) electrolyzers, porous carbon electrodes coated with platinum as a cathode and with noble metal oxides like iridium or ruthenium as anodes are the currently most widely used set-ups.<sup>[124–126]</sup> Not only the electrode materials, but also the construction of these electrolyzer cells are different. In alkaline electrolyzers, gastight membranes, so called diaphragms, are separating the anode and cathode compartments. Charge transfer through the diaphragm is permitted by  $\text{OH}^-$  ion exchange but gas exchange between the anodic- and cathodic region is prohibited. In PEM electrolyzers, the polymer membrane is acting as electrolyte and is also separating anode and cathode. Protons are able to permeate through the polymer membrane from the anodic to the cathodic region while gas exchange is inhibited.<sup>[29]</sup>

Today, commercially available electrolyzers typically have efficiencies of up to 80%.<sup>[5]</sup> However, major drawbacks of current electrocatalytic water-splitting devices are the expensive precious metals used in the distinct electrolyzers as well as to their complex constructions. In consequence, hydrogen production by water electrolysis is quite expensive today and only used to generate hydrogen of especially high purity.<sup>[5,29]</sup> To make water electrolysis, or electrocatalytic water-splitting, more attractive for alternative energy production, more cost-effective approaches have to be found.

A promising step towards sustainable water electrolysis is the exchange of expen-

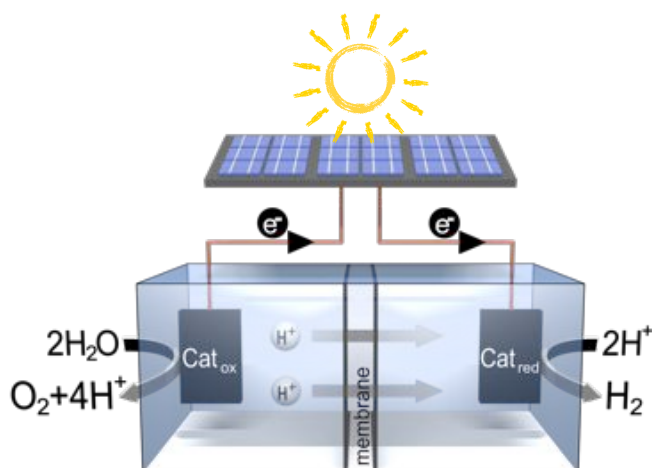


**Figure 3.4.** Design for an electrolysis cell for light-driven water-splitting. In this scheme, catalysts for water-oxidation ( $\text{Cat}_{\text{ox}}$ ) and proton-reduction ( $\text{Cat}_{\text{red}}$ ) are used as electrodes separated by a proton or hydroxide permeable membrane. Sunlight is converted into electric energy by a photovoltaic cell, coupled to the electrodes to apply the required redox potentials for water-oxidation (*left*) to provide reduction equivalents for proton reduction (*right*) to generate  $\text{H}_2$  as a solar fuel.

sive precious metals by electrocatalysts based on cheap and abundant transition metals, deposited on electrode surfaces. In this context the preparation of catalytic electrodes for water-splitting based on  $\text{Co}$ <sup>[127–130]</sup>,  $\text{Mn}$ <sup>[131–133]</sup>,  $\text{Ni}$ <sup>[134,135]</sup>, or  $\text{NiMoZn}$ <sup>[136,137]</sup> respectively, as well as  $\text{Cu}$ <sup>[138]</sup> has been published. In addition, the electrolyzer construction also has to be simplified to reduce costs.

In order to achieve sustainable, light-driven water-splitting, an optimized electrolyzer could be coupled to photovoltaic cells (PVs). In such a scenario, solar energy is captured by the PV and converted into electrical energy to provide the required potentials for water-oxidation and proton-reduction (Figure 3.4). Alternatively, other renewable power sources like hydroelectricity, geothermal power or wind power may be coupled to electrolyzers as well to convert electricity into a fuel in a sustainable way. The promising potential of such an approach has already been demonstrated, as a commercial power plant in East Germany combining wind power and  $\text{H}_2$  production from water-splitting was connected to the electric network in 2011.<sup>[139]</sup>

### 3.3.4 Photo-electrochemical cells for water-splitting

When electrocatalysts are directly coupled to photochemical semiconductors, integrated devices for light-driven water splitting can be constructed. This approach combines the promising potential of semiconductors for light-harvesting (section 3.3.2) and electrochemical water-splitting (section 3.3.3). Similar to PVs, the semiconductors are used to generate a photocurrent from the absorption of sunlight. In photo electrochemical cells (PECs) for light-driven water-splitting, the photocurrent is then directly applied to the electrocatalysts at which water-oxidation and proton-reduction occurs.

The requirements for the photocatalytic semiconductors are similar to those in water-splitting systems based on suspended semiconductor particles (*cf.* section 3.3.2). A band gap of  $\geq 1.23$  eV is necessary to facilitate water-splitting, corresponding to the absorption of light with a wavelength of  $\leq 1000$  nm. Ideally, the full solar spectrum should be

captured to convert a maximum number of photons into reduction equivalents.

The efficiency of light-harvesting can not only be enhanced by tuning the band gap of certain semiconductors by doping with different materials. Also the use of a combination of components has been reported. When p- and n-doped semiconductors are stacked, a p-n-junction is resulting at the semiconductors' interface (Figure 3.5, *left*).<sup>[109,140]</sup> At this p-n-junction, recombination of electrons from the n-doped side and electron-holes from the p-doped side occurs. Thereby, the number of mobile charges directly around the junction is reduced, the so called *depletion region* is build.<sup>[140]</sup> In this depletion region, a negative charge is induced in the p-doped semiconductor, while the n-doped is positively charged. This is resulting in an electric field and a build-in potential.<sup>[140]</sup> When photons of sufficient light energy are exciting electrons, an electron flow to the positive side of the field is started. If the sides of the cell on the opposite of the junction are connected, an electric current from the n- to the p-side is generated.<sup>[5]</sup> A build-up of the potential provided by the cell and also a rapid directed charge transfer is then achieved by combining materials with p-n-junctions in multi-junction configurations. Additionally, the efficient harvesting of a broader range of wavelengths of light can be achieved by multi-junction semiconductors.

Another option to increase the efficiency of light-harvesting is to immobilize suitable molecular dyes at a semiconductor's surface (Figure 3.5, *right*). When the dye is absorbing light, it is transferred into its excited state. From the excited state, the dye is transmitting, or injecting, an electron into the conduction band (CB) of the semiconductor, thus generating a charge at the semiconductor-dye interface (*cf.* oxidative quenching, section 3.3.1).<sup>[141–145]</sup> In dye-sensitized solar cells (DSCs), dye-sensitized semiconductor

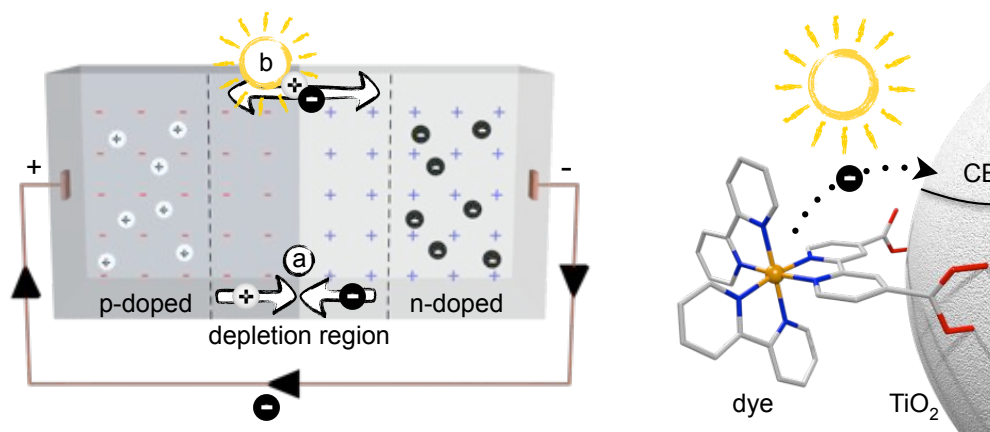


**Figure 3.5.** Schemes for the conversion of photons into electrons. *Left:* Schematic representation of a p-n-junction. By recombination of electrons and electron-holes in the vicinity of the junction (a), the depletion region is formed and an electric field is generated leading to the build-in potential.<sup>[140]</sup> When electrons are mobilized by absorption of light, an electron flow to the positive side of the field is started (b), inducing a photocurrent that can for example be applied to electrocatalysts.<sup>[5]</sup> *Right:*  $[\text{Ru}(\text{bpy})_2(\text{bpy}(\text{COO})_2)]^{2+/3+}$  sensitized  $\text{TiO}_2$  (color code: Ru in orange, C in gray, N in blue, O in red) as an example for dye sensitized semiconductors. As the dyes exhibit an absorption maximum in the visible range, which is different from the absorption maximum of the semiconductors, a larger portion of the incident light can be harvested. In its excited state, the dye is injecting an electron into the conduction band (CB) of the semiconductor, increasing light-harvesting efficiency. Deposited on indium (ITO) or fluorine (FTO) doped tin-oxides, such assemblies are suitable light-harvesting components to be used in PECs for light-driven water-splitting.

particles are immobilized at a conducting surface like indium doped tin oxide (ITO) or fluorine doped tin oxide (FTO) as anodes. Since the first breakthrough achieved by Grätzel and O'Reagan in 1991<sup>[141]</sup>, research in DSCs is experiencing increasing attention.<sup>[142–145]</sup>

The first water-splitting PEC was introduced in 1972 by Fujishima and Honda.<sup>[146]</sup> They connected  $\text{TiO}_2$  as photocatalytic anode for UV light-harvesting and water-oxidation to a platinum cathode for  $\text{H}^+$  reduction. Yoneyama *et al.* expanded this approach by combining two photocatalytic electrodes,  $\text{TiO}_2$  as photoanode and p-GaP as a photocathode.<sup>[147]</sup> In addition to further studies of the  $\text{TiO}_2$ /p-GaP system, Nozik reported the construction of a n-GaP/p-GaP PEC.<sup>[148]</sup> In these approaches, corrosion of the GaP semiconductors was limiting the stability of the PECs. To avoid the corrosion of the semiconductors, Kainthla *et al.* constructed a PEC using a Pt coated p-InP/Zn photocathode as  $\text{Cat}_{\text{red}}$  and a Mn-oxide coated n-GaAs photoanode as  $\text{Cat}_{\text{ox}}$ . The Pt and Mn-oxide coatings are acting as protective layers. They achieved an increased stability of the cell and a solar to hydrogen conversion efficiency of 8.2 %.<sup>[149]</sup>

More complex approaches for PECs based on multi-junction semiconductors were followed, often using precious metals as redox catalysts. Lin *et al.* constructed a wireless PEC (Figure 3.6) based on an amorphous silicon solar cell in a triple n-i-p (n-doped-intrinsic-p-doped Si) stack configuration on Ti support.  $\text{RuO}_2$  coated on the Ti support was used as  $\text{Cat}_{\text{ox}}$ , Pt as  $\text{Cat}_{\text{red}}$ .<sup>[150]</sup> In this device they were able to increase the steady-state solar to chemical conversion efficiency to 5 %, in comparison to maximum efficiencies of around 3 % of previously published n-i-p Si based PECs.<sup>[151–153]</sup> Rocheleau *et al.* also presented a wireless PEC based on amorphous silicon, coated with CoMo alloy as a catalyst for  $\text{H}_2$  evolution, and  $\text{NiFe}_2\text{O}_x$  as a catalyst for water-oxidation.<sup>[154]</sup> This PEC was showing promising long-term stability and a solar to hydrogen conversion efficiency of 7.5 %. Licht *et al.* presented a wireless PEC with a conversion efficiency of 18.5 %. This high efficiency was achieved by decorating a multi-junction AlGaAs/Si semiconductor configuration with  $\text{Pt}_{\text{black}}$  as  $\text{Cat}_{\text{red}}$  and  $\text{RuO}_2$  as  $\text{Cat}_{\text{ox}}$ .<sup>[155]</sup>

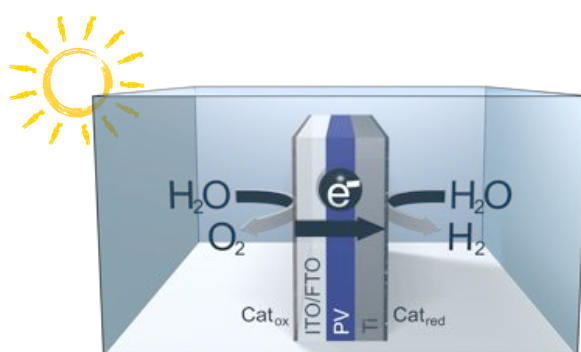


**Figure 3.6.** Wireless PEC design for light-driven water-splitting. In this design, photocatalytic semiconductors in multi-junction configurations (PV) are directly coupled to electrocatalysts for water-oxidation ( $\text{Cat}_{\text{ox}}$ ) and proton-reduction ( $\text{Cat}_{\text{red}}$ ). In order to prevent corrosion of the semiconductors, conducting supports like titanium foil (Ti), indium doped tin oxide (ITO) or fluorine doped tin oxide (FTO) can be used as protective layers and interfaces to the electrocatalysts.

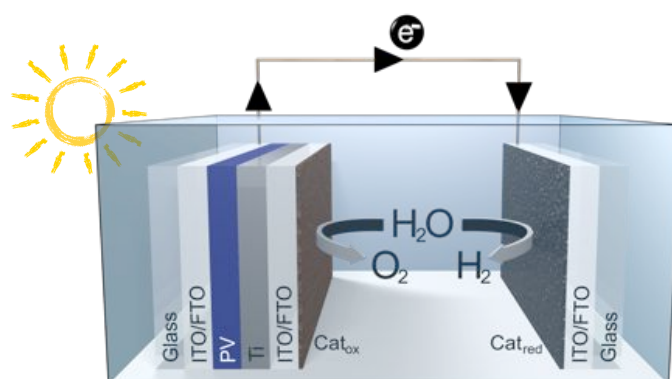


**Figure 3.7.** Wired PEC design for light-driven water-splitting. In this design, either the electrocatalyst for water-oxidation ( $\text{Cat}_{\text{ox}}$ ) or for proton-reduction ( $\text{Cat}_{\text{red}}$ ) is directly coupled to a photocatalytic semiconductor in multi-junction configuration (PV). The other catalyst is then connected by an ohmic contact. In order to prevent the corrosion of the semiconductors, conducting supports like Ti, ITO or FTO can be used as protective layers and interfaces to the electrocatalysts.

Khaselev and Turner prepared PECs following a wired cell design. In such an approach, either  $\text{Cat}_{\text{ox}}$  or  $\text{Cat}_{\text{red}}$  is directly deposited onto a multi-junction semiconductor and the other catalyst is connected to the opposite side of the PV by an ohmic contact (Figure 3.7). They used GaAs/GaInP and also Ge doped triple-junction amorphous Si semiconductor configurations.<sup>[156,157]</sup> As anode, Pt was coated onto the PV, as cathode, Pt was connected via an ohmic contact. In case of the GaAs/GaInP PEC, an efficiency of over 16 % could be achieved while the efficiency of the Si based PEC was about 7.8 %.<sup>[157]</sup>

Recently, a remarkable breakthrough was achieved by the Nocera group at MIT. They succeeded in the construction of PECs virtually completely based on abundant materials. They decorated a Ge doped amorphous Si triple-junction PV with a Co catalyst as  $\text{Cat}_{\text{ox}}$  and used a NiMoZn catalyst as  $\text{Cat}_{\text{red}}$ . In a wired configuration they achieved an efficiency of 4.7 % and 2.5 % in wireless configuration.<sup>[136,137]</sup>

As mentioned above, the light-harvesting efficiency can also be increased by immobilizing molecular dyes at the semiconductor's surface to prepare DSCs. Also these DSCs have been used to construct PECs for light-driven water-splitting. Here  $\text{TiO}_2$ <sup>[158–160]</sup>, NiO<sup>[161]</sup>, Nb- and W-oxides<sup>[162]</sup> as well as graphene carbon nitride<sup>[163]</sup> have been used as semiconductors modified with organic molecules<sup>[161,162]</sup>, Mg-phthalocyanine<sup>[163]</sup> or Ru-complexes<sup>[158–160]</sup> as dyes. For water-oxidation or reduction, respectively, the use of catalysts based on Mn<sup>[158,159]</sup>, Co<sup>[161]</sup>, Ir<sup>[160,162]</sup> and Pt<sup>[162,163]</sup> has been reported.

A possible design of a PEC for light-driven water-splitting based on DSCs is shown in Figure 3.8. In this design,  $\text{Cat}_{\text{ox}}$  is attached to the semiconductors of the DSC. When electrons are injected from the dye to the CB of the semiconductor, electron holes are accumulated in  $\text{Cat}_{\text{ox}}$ , an electron flow is started. Via an ohmic contact, the electrons are then transferred from the conducting support of the DSC (for example ITO or FTO) to  $\text{Cat}_{\text{red}}$ .  $\text{Cat}_{\text{red}}$  may be a solid electrode or an electrocatalyst deposited onto a conductive support.

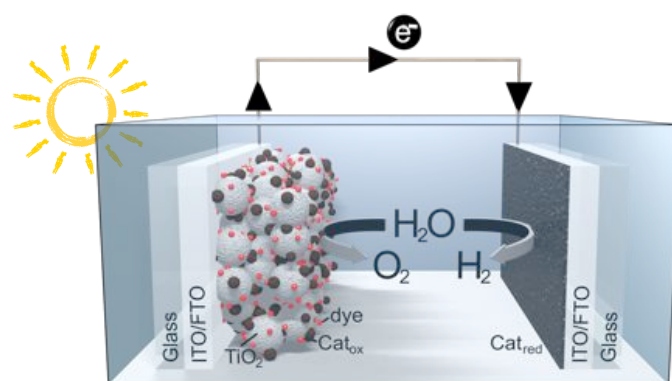


**Figure 3.8.** Scheme for a PEC based on a DSC-like design. When dye molecules are injecting electrons to the semiconductor, an electron flow is started to the conducting support of the DSC (ITO/FTO). The electrons are transmitted to  $\text{Cat}_{\text{red}}$  connected to the support of the DSC by an ohmic contact, in order to provide reduction equivalents for  $\text{H}_2$  formation. Electron holes for water-oxidation are accumulated in  $\text{Cat}_{\text{ox}}$ , which is attached to the semiconductor particles of the DSC.

The different research projects in homogeneous as well as heterogeneous water-splitting catalysis have demonstrated a huge potential for an application in sustainable energy production. Furthermore, the investigation of light-driven water-splitting has contributed to a better understanding on how to couple light-harvesting and water-splitting catalysis.

However, the identification of efficient materials based on abundant elements to act as  $\text{Cat}_{\text{ox}}$  and  $\text{Cat}_{\text{red}}$  remains to be a major challenge. For the most part, expensive and rare materials have been used, the overall solar to hydrogen conversion efficiency is poor and/or the final systems were not stable for sufficiently long periods. These facts are limiting the potential for an application in sustainable energy production. Thus, methods and materials have to be developed to replace the currently used components by affordable, stable and efficient materials.



## 4 From metal complexes to metal oxides: compounds for water-splitting

The investigation of compounds for water-splitting is motivated by two challenges. Model compounds of the active site of metalloenzymes are fundamental tools in bioinorganic chemistry. Structural and/or functional mimics of biology's catalyst for water-oxidation, the OEC of PSII, are important to elucidate details of the photosynthetic water-oxidation reaction mechanism (*cf.* chapter 2). In addition, compounds showing catalytic activity in water-oxidation or proton-reduction are needed to achieve overall water-splitting for H<sub>2</sub> production as carrier for renewable energy (*cf.* chapter 3).

Over the last decades, a multitude of transition metal complexes as well as their polyoxometallates and oxides has been studied extensively in this context. As the number of such compounds is very large, only a small number of selected examples will be described below to illustrate the different concepts.

### 4.1 Metal complexes and polyoxometallates

Transition metal complexes are common model compounds in bioinorganic chemistry to mimic the active site of metalloenzymes. Often such model compounds are more accessible than their biological paragons. Also, the possibilities for a detailed experimental analysis of their properties are much larger. In case of the OEC's CaMn<sub>4</sub>O<sub>5</sub> cluster together with its amino acid environment, it is difficult to develop systems mimicking this unit due to its complex arrangement. A common strategy has thus been to develop simplified structural models. In this regard, a large variety of multinuclear manganese complexes has been prepared as OEC mimics, often containing [Mn<sub>2</sub>(μ-O)] or [Mn<sub>2</sub>(μ-O)<sub>2</sub>] cores, comprising combinations of Mn<sup>II</sup>, Mn<sup>III</sup> and Mn<sup>IV</sup> bound by various chelating ligands.<sup>[101,103,164–167]</sup>

As an example from from the Kurz group, Berends *et al.* recently reported the synthesis as well as the spectroscopic and electrochemical characterization of the mono μ-oxido bridged dinuclear Mn<sup>III</sup> complex [Mn<sub>2</sub><sup>III,III</sup>(tpdm)<sub>2</sub>(μ-O)(μ-OAc)<sub>2</sub>]<sup>2+</sup> (Figure 4.1, a).<sup>[168,169]</sup> In electrochemical experiments, they were able to show that the complex can be oxidized in single-electron steps, forming Mn<sub>2</sub><sup>III,IV</sup> and Mn<sub>2</sub><sup>IV,IV</sup> species, respectively. Furthermore, the authors carried out O<sub>2</sub> evolution experiments in aqueous solutions of H<sub>2</sub>O<sub>2</sub>, HSO<sub>5</sub><sup>-</sup> and the single-electron oxidant Ce<sup>IV</sup>. In the case of H<sub>2</sub>O<sub>2</sub> and HSO<sub>5</sub><sup>-</sup>, O<sub>2</sub> evolution could be observed. In the experiments using Ce<sup>IV</sup> as oxidant, no O<sub>2</sub> evolution could be observed. In contrast to H<sub>2</sub>O<sub>2</sub>, HSO<sub>5</sub><sup>-</sup>, Ce<sup>IV</sup> is a single electron oxidant which is not oxygen transferring. It has been reported that oxygen evolved from reactions using H<sub>2</sub>O<sub>2</sub> and HSO<sub>5</sub><sup>-</sup> is not, or not entirely originating from bulk H<sub>2</sub>O. If Ce<sup>IV</sup> is used as oxidant instead and oxygen evolution is taking place, both atoms of the O<sub>2</sub> molecule are originating from bulk H<sub>2</sub>O (*cf.* section 8.1).<sup>[170,171]</sup> Thus, the authors concluded that this complex is not capable of catalyzing the water-oxidation reaction.

However, in another study, Berends and coworkers followed a strategy introduced by Kaneko *et al.*<sup>[172]</sup> and adsorbed their  $\text{Mn}_2^{\text{III,III}}$  complex,  $[\text{Mn}_2^{\text{III,IV}}(\mu\text{-O})_2(\text{tpy})_2(\text{H}_2\text{O})_2]^{3+}$ ,  $\text{Mn}^{\text{III}}(\text{OAc})_3$  and  $\text{Mn}^{\text{II}}\text{SO}_4$  on clay.<sup>[168,173,174]</sup> Again,  $\text{O}_2$  evolution experiments were carried out using  $\text{Ce}^{\text{IV}}$  as oxidant. With the exception of the adsorbed  $\text{Mn}^{\text{II}}\text{SO}_4$ , all manganese-clay hybrids showed catalytic activity in water-oxidation. Based on this catalytic study and EPR spectroscopy, the formation of multi nuclear Mn-aggregates on the clay's surface as active water-oxidation catalyst has been concluded (Figure 4.1, b).<sup>[103,168,173]</sup>

Another recent example for a dinuclear manganese complex inspired by the OEC has been published by Karlsson *et al.*<sup>[175]</sup> They prepared a chelating ligand containing imidazole and carboxylate groups coordinating two Mn centers. The authors reported their compound as the first known manganese complex capable to perform as water-oxidation catalyst in homogeneous solution using the single-electron oxidant  $[\text{Ru}(\text{bpy})_3]^{3+}$ . Furthermore, Karlsson *et al.* presented a crystal structure, showing a dimerization of their complex in the solid state yielding  $[\text{Mn}_2(\text{bbcc})(\mu\text{-OMe})(\text{OMe})_2]_2$  (Figure 4.1, c).<sup>[175]</sup> The formation of this dimer may indicate that the catalytically active species is not the dinuclear, but rather a tetranuclear complex which also may form in solution.

In 1997, the Dismukes group introduced the complex  $[\text{Mn}_4\text{O}_4(\text{O}_2\text{P}(\text{Ph})_2)_6]$ , showing a cubane-like motif formed by four  $\mu$ -oxido bridged Mn centers (Figure 4.1, d).<sup>[176]</sup> Later,  $\text{O}_2$  evolution under illumination of this complex was demonstrated, originating in the ejection of a phosphinate ligand under the formation of the cationic species of the complex.<sup>[78,177]</sup> About a decade after its introduction, the  $[\text{Mn}_4\text{O}_4(\text{O}_2\text{P}(\text{Ph})_2)_6]$  compound was exchanged into a Nafion polymer matrix deposited on a conducting surface. The electrode prepared in this way showed promising activity in electrocatalytic water-oxidation.<sup>[178]</sup> Recently, Hocking *et al.* reported that  $[\text{Mn}_4\text{O}_4(\text{O}_2\text{P}(\text{Ph})_2)_6]$  within the Nafion layer is acting as a precursor, forming nanoparticles of a birnessite like layered Mn-oxide as catalytically active species (*cf.* section 4.2.2).<sup>[131]</sup>

Not only manganese complexes are of interest in water-oxidation catalysis, or more general, in water-splitting. In this respect, complexes based on transition metals like Ru, Ir, Co or Ni have also been extensively studied.<sup>[99,179–183]</sup>

In the early 1980s, Meyer and coworkers introduced the mono  $\mu$ -oxido-bridged dinuclear ruthenium complex  $[(\text{bpy})_2(\text{H}_2\text{O})\text{Ru}^{\text{III}}\text{ORu}^{\text{III}}(\text{H}_2\text{O})(\text{bpy})_2]^{4+}$ , also known as the *blue dimer* (Figure 4.1, e). It was the first homogeneous catalyst capable to perform water-oxidation by the use of the single-electron oxidant  $\text{Ce}^{\text{IV}}$ .<sup>[184,185]</sup> Electrochemical investigations demonstrated that the  $\text{Ru}_2^{\text{III,III}}$  species can be sequentially oxidized to a  $\text{Ru}_2^{\text{V,V}}$  state. The fourfold oxidation of the blue dimer is coupled to the release of four protons, the complex  $[(\text{bpy})_2(\text{O})\text{Ru}^{\text{V}}\text{ORu}^{\text{V}}(\text{O})(\text{bpy})_2]^{4+}$  is formed.<sup>[185,186]</sup> A mechanism for water-oxidation has been proposed in which a peroxide intermediate is build under the attack of water on one of the  $\text{Ru}^{\text{V}}=\text{O}$  sites.<sup>[186]</sup> This  $[(\text{bpy})_2(\text{HOO})\text{Ru}^{\text{IV}}\text{ORu}^{\text{IV}}(\text{OH})(\text{bpy})_2]^{4+}$  intermediate then reacts further to release  $\text{O}_2$  and the  $\text{Ru}_2^{\text{III,III}}$  starting compound is formed again.<sup>[186]</sup>

A variety of mono- and polynuclear ruthenium complexes comprising a  $\text{Ru}=\text{O}$  group are known today in which ruthenium can reach oxidation states as high as  $\text{Ru}^{\text{V}}$  and  $\text{Ru}^{\text{VI}}$ .<sup>[181]</sup> The attack of a solvent water molecule on this highly electrophilic  $\text{Ru}^{\text{V/VI}}=\text{O}$  group is an often suggested mechanism for O–O bond formation during water-oxidation catalysis.<sup>[29,181,182]</sup> But also the interaction of two  $\text{Ru}=\text{O}$  species has been reported.<sup>[181,182]</sup> For instance, Duan *et al.* carried out water-oxidation experiments using  $\text{Ce}^{\text{IV}}$  as oxidant and the mononuclear ruthenium complex  $[\text{Ru}^{\text{II}}(\text{bdc})(\text{pic})_2]$  as a catalyst.<sup>[187]</sup> They were

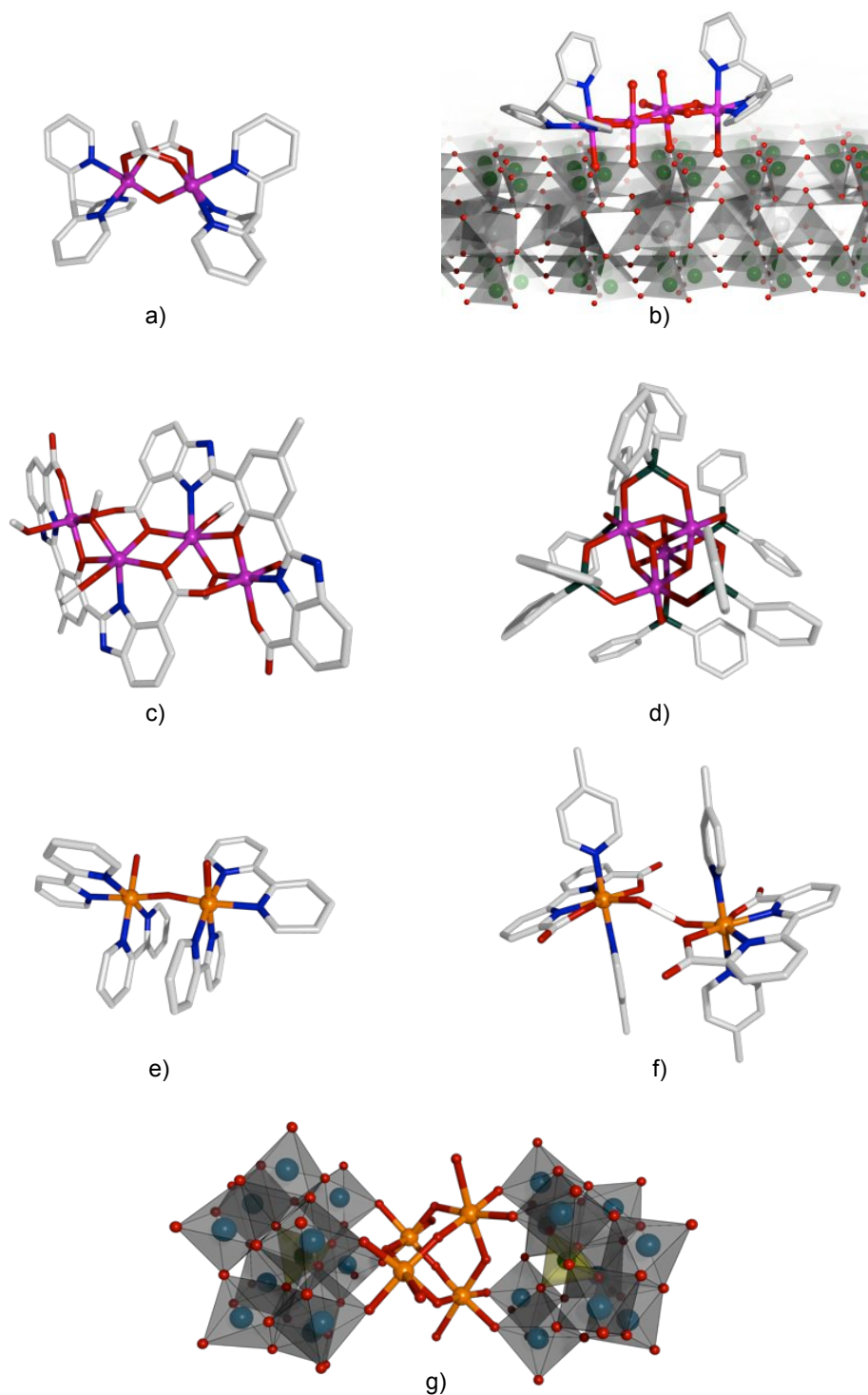


**Figure 4.1.** Structural (a, c, d) and functional (b, e-g) model compounds for water-oxidation. a)  $(\text{Mn}_2(\text{tpdm})_2(\mu\text{-O})(\mu\text{-OAc})_2)^{2+}$  (169), b) proposed cluster formed by immobilization of a) on a clay surface (168,173), c)  $(\text{Mn}_2(\text{bbcc})(\mu\text{-OMe})(\text{OMe})_2)_2$  (175), d)  $(\text{Mn}_4\text{O}_4(\text{O}_2\text{P}(\text{Ph})_2)_6)$  (176), e)  $((\text{bpy})_2(\text{H}_2\text{O})\text{RuORu}(\text{H}_2\text{O})(\text{bpy})_2)^{4+}$  (184), f)  $(\mu\text{-}(\text{HOHOH})\text{-}(\text{Ru}(\text{bdc})(\text{pic})_2)_2)^{3+}$  (187), g)  $(\text{Ru}_4(\mu\text{-O})_4(\mu\text{-OH})_2(\text{H}_2\text{O})_4(\gamma\text{-SiW}_{10}\text{O}_{36})_2)^{10-}$  (188). Counter ions and protons (except of bridging H (white) in f) are omitted for clarity. Color code: Mn in purple, Ru in orange, C in gray, O in red, N in blue, P in dark green; in b and g: Si in green, polyhedra in gray (b) or yellow (g), W in steel blue, Al in light gray, polyhedra of both in gray.

able to isolate and characterize the dimer  $[\mu\text{-(HOHOH)-(Ru}^{\text{IV}}\text{(bdc)(pic)}_2)_2]^{3+}$  which is formed as an intermediate during the water-oxidation reaction. In this dimer, the seven-coordinated ruthenium centers are bridged by a hydrogen bond formed between water ligands (Figure 4.1, f).<sup>[187]</sup> By exchanging the 4-picoline (pic) ligand by isoquinoline (isoq), they obtained the mononuclear complex  $[\text{Ru}^{\text{II}}\text{(bdc)(isoq)}_2]$  showing a much improved water-oxidation rate in experiments using  $\text{Ce}^{\text{IV}}$ .<sup>[189]</sup> On the basis of DFT calculations, they demonstrated that  $[\text{Ru}^{\text{II}}\text{(bdc)(isoq)}_2]$  most likely forms a  $\text{Ru}^{\text{IV}}\text{-O-O-Ru}^{\text{IV}}$  intermediate during the water-oxidation cycle, stabilized by stacking interactions of isoq ligands arranged in parallel.<sup>[189]</sup> These results are supporting the proposed mechanism of dimerization of two  $\text{Ru}=\text{O}$  species for O–O bond formation.

Co based catalysts are also gaining interest to facilitate the water-oxidation reaction.<sup>[183]</sup> For instance, a polyoxometallate (POM) comprising a  $\text{Co}_4\text{O}_4$  core as catalytically active unit has been presented by the Hill group. In this POM, the core is stabilized by oxidation resistant polytungstate ligands, forming  $[\text{Co}_4(\text{H}_2\text{O})_2(\alpha\text{-PW}_9\text{O}_{34})_2]^{10-}$ .<sup>[190]</sup> In experiments on water-oxidation using  $[\text{Ru}(\text{bpy})_3]^{3+}$  as single electron oxidant,  $\text{O}_2$  evolution was demonstrated. Furthermore, the authors were able to show that the catalytic activity is not the result of the decomposition of the POM or of the formation of a cobalt oxide.<sup>[190]</sup> Thus, this  $\text{Co}_4$ -POM is a promising example of homogeneous water-oxidation catalysis based on abundant metals.

In addition, the groups of Hill and Bonchio presented a  $\text{Ru}_4$ -POM as water-oxidation catalyst.<sup>[191,192]</sup> In this POM, the ruthenium core is stabilized by two  $[\gamma\text{-SiW}_{10}\text{O}_{36}]^{8-}$  ligands, forming  $[\text{Ru}_4^{\text{IV}}(\mu\text{-O})_4(\mu\text{-OH})_2(\text{H}_2\text{O})_4(\gamma\text{-SiW}_{10}\text{O}_{36})_2]^{10-}$  (Figure 4.1, g).<sup>[188,191-194]</sup> It has been shown that this POM is able to catalyze water-oxidation using the single electron oxidants  $\text{Ce}^{\text{IV}}$  and  $[\text{Ru}(\text{bpy})_2]^{3+}$ .<sup>[188,191-194]</sup> Furthermore, a reaction cycle with single-electron oxidation steps of the  $\text{Ru}_4^{\text{IV}}$  core up to  $\text{Ru}_4^{\text{V}}$  has been proposed.<sup>[188,193]</sup>

Summarized, several approaches using coordination compounds are resulting in the formation of active water-oxidation catalysts. While the metal centers of ruthenium complexes are able to cycle at least between three oxidation states ( $\text{Ru}^{\text{III}}$ ,  $\text{Ru}^{\text{IV}}$  and  $\text{Ru}^{\text{V}}$ ), the centers of the manganese complexes are only cycling between  $\text{Mn}^{\text{III}}$  and  $\text{Mn}^{\text{IV}}$  during the observed redox processes. This difference in the redox properties is indicating why even mononuclear Ru complexes ( $\text{Ru}^{\text{II}}\text{-Ru}^{\text{VI}}$ ) are able to catalyze the water-oxidation reaction and why multi nuclear species ( $\geq \text{Mn}_4$ ) are required for Mn catalyzed water-oxidation. As mentioned above, the synthesis of clay hybrids as well as POMs are promising approaches to stabilize  $\mu\text{-O}$  bridged, multi-nuclear Mn or Co arrangements, respectively, to obtain active water-oxidation catalysts. Another approach to build multi-core,  $\mu\text{-O}$  bridged systems based on abundant elements will be discussed below, the preparation of first row transition metal oxides.

## 4.2 Transition metal oxides as water-oxidation catalysts

In the late 1980s, Harriman *et al.* screened various transition metal oxides for their ability to catalyze water-oxidation under photochemical conditions.<sup>[195]</sup> In their test system, they used the single-electron oxidant  $[\text{Ru}(\text{bpy})_3]^{3+}$ , generated by irradiation ( $\lambda > 350 \text{ nm}$ ) of  $[\text{Ru}(\text{bpy})_3]^{2+}$  in the presence of  $\text{S}_2\text{O}_8^{2-}$  as electron acceptor and the respective oxide as heterogeneous catalysts in the form of particles suspended in aqueous solution.<sup>[195]</sup>

In the Harriman study,  $\text{IrO}_2$ ,  $\text{Co}_3\text{O}_4$ ,  $\text{RuO}_2$ ,  $\text{Rh}_2\text{O}_3$ ,  $\text{Mn}_2\text{O}_3$  and  $\text{NiCo}_2\text{O}_4$  were showing promising activity. As described previously, iridium, rhodium and ruthenium based water-oxidation catalysts already have been used in electrolyzers and PECs, either elemental or in form of their oxides (*cf.* chapter 3). But as these elements are rare and thus quite expensive, Co-, Ni- and Mn-oxides are enjoying increasing attention as potential water-oxidation catalysts for alternative energy production.

### 4.2.1 Cobalt and nickel oxides

About twenty years after the screening of Harriman *et al.*, Matthew Kanan and Daniel Nocera reported the preparation of a Co-oxide catalyst film, showing promising activity in electrocatalytic water-oxidation.<sup>[127]</sup> In their experiments, the Co-oxide film was electrodeposited in situ from a potassium phosphate buffered aqueous solution of  $\text{Co}^{2+}$  onto an ITO electrode, a Pt mesh was used as counter electrode. Subsequently to the catalyst's deposition, water electrolysis was carried out under ambient conditions.<sup>[127]</sup>

These first experiments were followed by a more detailed analysis of the Co-oxide catalyst film. It has been shown that the electrodeposition of the catalyst is not limited to the phosphate buffer, but the presence of proton acceptors is required.<sup>[196–199]</sup> When proton accepting electrolytes (like borate or phosphate buffers) are used, catalytic water-oxidation is possible even in salt water containing high concentrations of NaCl.<sup>[197]</sup> The deposition on alternative substrates like glassy carbon, FTO or nickel metal as well as on photoanodes has also been discussed and investigated.<sup>[3,200–204]</sup>

A detailed structural analysis of the Co-oxide film has been carried out by XAS, deriving a picture of structural motifs present in the catalyst.<sup>[29,128,129,199,205]</sup> In this analysis  $\text{CoO}_6$  octahedra were identified as central subunits of the oxide structure.<sup>[29,128,129,199,205]</sup> Edge sharing  $\text{CoO}_6$  octahedra are forming single layers comprising an extensive network of  $\mu$ -oxido bridged  $\text{Co}^{\text{III}}$  ions (Figure 4.2).<sup>[29,128,129,199,205]</sup> Additionally, cubane like  $\text{Co}_4(\mu\text{-O})_4$  motifs are present as a part of the  $\mu$ -oxido network of the oxide layer and most likely also connected (corner sharing) to other cubane motifs (Figure 4.2, *left and center*).<sup>[29,128,129,199,205]</sup> The phosphate molecules of the electrolyte are not involved in the bridging pattern, but may occupy terminal positions to complete peripheral Co-octahedra.<sup>[128,129,199]</sup>

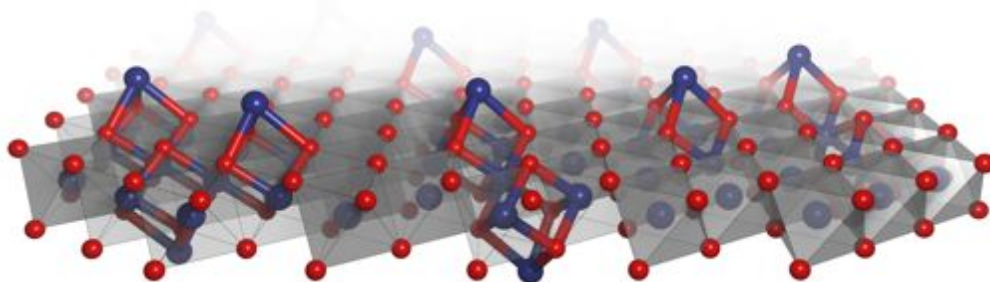


**Figure 4.2.** Schematic representation of a sheet of catalytically active Co-oxide films. Edge sharing  $\text{Co}^{\text{III}}\text{O}_6$  octahedra (gray) are forming layers, which are stacked above each other resulting in the Co-oxide structure. As a second structural motif,  $\text{Co}_4(\mu\text{-O})_4$  cubanes (ball and stick models, Co in dark blue, O in red) have been identified as part of the extensive network of  $\mu$ -oxido bridged  $\text{Co}^{\text{III}}$  ions. Additional cations and water molecules are placed in the interlayer space.

Risch *et al.* investigated the influence of anions and redox-inert cations of the buffer system on the formation and function of the Co-oxide films. They exchanged the potassium phosphate electrolyte of the initial study<sup>[127]</sup> by KOAc, LiOAc, KCl and CaCl<sub>2</sub> and addressed the effect on the atomic structure of the deposited Co-oxide catalyst as XAS was performed at the Co, K, and Ca K-edges.<sup>[199]</sup> The comparison of experimental and calculated EXAFS spectra of the K-Co-catalyst showed that only about 10 % of the K<sup>+</sup> ions are bound to the layers, forming KCo<sub>3</sub>(μ-O)<sub>4</sub> cubanes, while most of the K<sup>+</sup> ions are distributed statistically in the Co-oxide's interlayer space as discussed in previous studies.<sup>[29,129,198]</sup> In case of the Ca-Co-oxide deposits, Risch and coworkers concluded the participation of about 40 % of the Ca<sup>2+</sup> ions in the formation of CaCo<sub>3</sub>(μ-O)<sub>4</sub> motifs. However, no major difference has been observed in catalytic activity of the Co-oxide films in dependence of the present cation.<sup>[199]</sup>

As described in section 3.3.4, the Nocera group recently demonstrated the potential of the Co-oxide catalyst for large scale application, as they prepared a PEC based on abundant materials using the Co-film as water-oxidation catalyst directly coupled to a PV based on amorphous silicon, achieving light-driven water-splitting.<sup>[136,137]</sup>

Recently, also the preparation of nickel based films as active water-oxidation catalysts has been demonstrated. In analogy to the Co-oxide catalyst described above<sup>[127]</sup>, Dinçä *et al.* reported the electrodeposition of a catalytically active Ni-oxide film from an aqueous borate electrolyte containing Ni<sup>2+</sup>.<sup>[134]</sup> As substrate, ITO and FTO electrodes were used. Based on electrochemical characterizations of the Ni-oxide anode, the authors suggested the requirement of buffering electrolytes for catalysis as discussed for the Co-oxide film.<sup>[134,196-199]</sup>

In order to determine the oxidation state of Ni and to define structural details of the amorphous Ni-oxide film, XAS experiments were carried out again by the Dau group. In this study, Risch *et al.* identified edge-sharing NiO<sub>6</sub> octahedra forming layers of μ-oxido bridged Ni-centers, similar to the structure of the Co-oxide catalyst shown in Figure 4.2. On basis of the EXAFS data, the presence of Ni<sub>4</sub>(μ-O)<sub>4</sub> cubane like motifs could neither be evidenced nor excluded. XANES data were corresponding to a mean Ni oxidation state between +III and +IV, but closer to +IV.<sup>[135]</sup>

Using a sol-gel process, Sun and coworkers were able to prepare a Ni-oxide coated Si photoelectrode for light-driven water-oxidation.<sup>[206]</sup> They suggested that the Ni-oxide coating in this device has three functions. First, the oxide film serves as protection layer to prevent corrosion of the Si photoelectrode. Second, the Ni-oxide film is acting as promising water-oxidation catalyst. And third, the overpotential of the oxygen evolution half-reaction is further increased by the potential of the NiO<sub>x</sub>/n-Si junction.<sup>[206]</sup> However, the successful coating of a photoanode with a Ni-oxide as water-oxidation catalyst is showing the promising potential of such materials in addition to Co-oxide to be used in an approach for solar water-splitting for alternative energy production.

## 4.2.2 Manganese oxides

In the late 1970s, Morita *et al.* successfully prepared Mn-oxide electrodes as anodes for electrocatalytic water-splitting.<sup>[207,208]</sup> In the following years Trasatti as well as Matsumoto *et al.* investigated transition metal oxides as anode materials for water electrolysis. In addition to the candidates pictured above they found Mn-oxides to be catalytically active, well corresponding to the screening of Harriman *et al.*<sup>[195,209,210]</sup>

Comparing these heterogeneous water-oxidation catalysts to the molecular Mn-complexes<sup>[169,175,176]</sup> and their clay adsorbates<sup>[168,172-174]</sup> (see section 4.1), it seems to be a reasonable approach to extend the dinuclear  $\mu$ -oxido bridged complex to a multi nuclear  $\mu$ -oxido bridged Mn network found in oxides to achieve catalytic activity.<sup>[103]</sup> Further, the Mn oxidation state is supposed to play a key role. The Pourbaix diagram for manganese given in Figure 4.3 is showing that  $\text{Mn}^{\text{IV}}$ -oxides are thermodynamically able to oxidize water over a broad pH-range.<sup>[211,212]</sup> During water-oxidation catalysis, Mn-centers of such an oxide may cycle through the oxidation states  $\text{Mn}^{\text{III}}$  and  $\text{Mn}^{\text{IV}}$ .

From this perspective a very interesting question arises when the  $\mu$ -oxido bridged centers of Mn-oxides are compared to biology's water-oxidation catalyst (*cf.* section 2.2.1): are Mn-oxides structural *and* functional model compounds of the  $\text{CaMn}_4\text{O}_5$  cluster of the oxygen-evolving-complex? Looking again at the  $\mu$ -oxido bridged  $\text{CaMn}_4$  core of the OEC (section 2.2.1, Figure 2.7), this cluster could be considered as Mn-oxide particle embedded in the protein matrix of PSII.<sup>[103]</sup> Indeed, Shafirovich *et al.* introduced  $\text{MnO}_2$  as inorganic model of the OEC already in 1981.<sup>[213]</sup> The authors also successfully demonstrated the ability of their model compound to catalyze the water-oxidation reaction using the single-electron oxidant  $[\text{Ru}(\text{bpy})_3]^{3+}$ . Further, Shafirovich *et al.* discussed their results in relation to the reaction cycle of the OEC suggested by Kok *et al.*<sup>[63]</sup> and proposed  $\text{MnO}_2$  as a functional PSII model.<sup>[213]</sup>

Based on these findings and considerations, requirements can be derived as a starting point for the rational design of Mn-oxides as active water-oxidation catalysts as well as structural and functional OEC model compounds. These requirements are a Mn oxidation state between  $\text{Mn}^{3+}$  and  $\text{Mn}^{4+}$ , a high Mn-nuclearity and a flexible  $\mu$ -oxido linkage between the Mn-centers.<sup>[103]</sup>

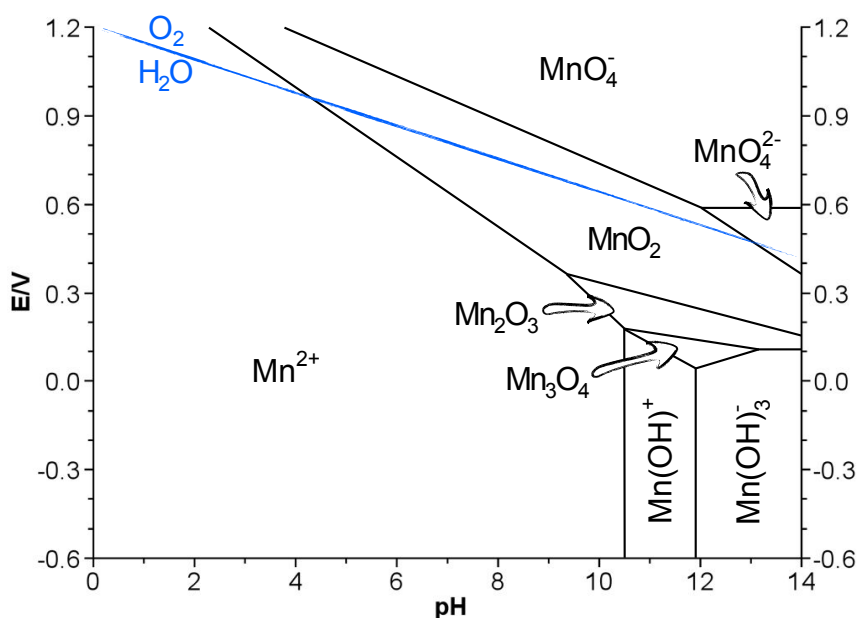


**Figure 4.3.** Simplified Pourbaix diagram for manganese illustrating the stability of Mn species as a function of pH and  $E$ . The thermodynamic potential of  $\text{Mn}^{\text{IV}}$ -oxides ( $\text{MnO}_2$ ) is suitable to the potential required for water-oxidation (blue line) over a broad pH-range. Modified from<sup>[211,212]</sup>.

$\alpha$ -Mn<sub>2</sub>O<sub>3</sub>,  $\beta$ -MnO<sub>2</sub> and CaMn<sub>2</sub>O<sub>4</sub>

Inspired by the previous work on Mn-oxides as catalysts in photochemical<sup>[195,213]</sup> as well as electrochemical<sup>[207–210]</sup> water-oxidation and by the composition of the OEC, the Kurz group started in 2009 to synthesize various Mn-oxides and to probe their ability to act as water-oxidation catalysts.

Mohammad Mahdi Najafpour prepared  $\alpha$ -Mn<sub>2</sub>O<sub>3</sub> as well as CaMn-oxides, representing the OEC's composition and Mn oxidation state.<sup>[214,215]</sup> He compared their catalytic activity to commercial  $\beta$ -MnO<sub>2</sub> and  $\alpha$ -Mn<sub>2</sub>O<sub>3</sub>. In this study,  $\beta$ -MnO<sub>2</sub> showed no activity while the commercial as well as the synthesized  $\alpha$ -Mn<sub>2</sub>O<sub>3</sub> and the prepared CaMn-oxide showed oxygen-evolution in experiments using the single-electron oxidants Ce<sup>IV</sup> and photochemically generated [Ru(bpy)<sub>3</sub>]<sup>3+</sup>. The activity of some of the CaMn-oxides by far exceeded the activity of the  $\alpha$ -Mn<sub>2</sub>O<sub>3</sub> samples. Furthermore, the prepared CaMn-oxide was heated to different temperatures, resulting in a variation of the catalytic activity. While the activity in water-oxidation was increased by heating the sample to 400°C instead of 60°C, the activity was virtually lost after heating to 1000°C.<sup>[214]</sup>

The samples heated to 60°C and 400°C were amorphous powders. By heating the oxide up to 1000°C, a crystalline phase was formed which was identified as marokite (CaMn<sup>III</sup><sub>2</sub>O<sub>4</sub>). Like  $\alpha$ -Mn<sub>2</sub>O<sub>3</sub> (Figure 4.4, *left*), marokite is showing a coordinatively saturated three dimensional  $\mu$ -oxido bridged network of metal centers (Figure 4.4, *right*). In collaboration with the Dau group, the amorphous, catalytically active powders were identified as layered Mn-oxides by XAS. Instead of an ordered three dimensional network, these materials exhibited a disordered structure with a high number of layer defects and a Mn oxidation state between +III and +IV (for details see section 7.2).<sup>[215]</sup> These disordered layered Mn-oxide structures seem to be in a better agreement with the requirements of a flexible  $\mu$ -oxido linkage defined above than the structures of the inactive  $\beta$ -MnO<sub>2</sub>, or the slightly active  $\alpha$ -Mn<sub>2</sub>O<sub>3</sub> and marokite. Thus, the structures of naturally occurring Mn-oxide minerals with layered and tunneled structures will be discussed below.

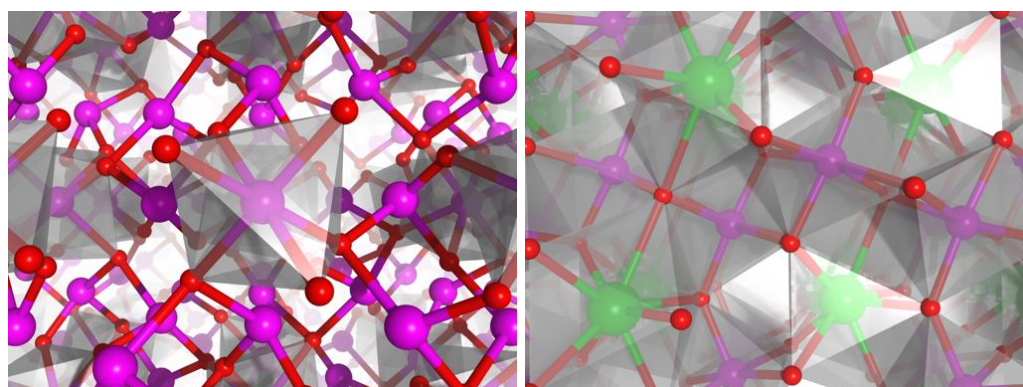


**Figure 4.4.** Sections of the structures of  $\alpha$ -Mn<sub>2</sub>O<sub>3</sub> (*left*) and the CaMn<sub>2</sub>O<sub>4</sub> oxide marokite (*right*). Both oxides exhibit a three dimensional  $\mu$ -oxido bridged network of Mn or Ca and Mn ions, respectively. Only a poor activity in water-oxidation catalysis was observed for both materials.<sup>(214)</sup>

### Manganese oxides with tunneled structures

Tunneled and also layered manganese oxides do share a common structural motif, the  $\text{MnO}_6$  octahedron. In tunneled Mn-oxides, edge-sharing octahedra are forming chains or sheets of different sizes that are sharing corners with neighboring chains or sheets to build the complex structure. The distinct Mn-oxides are classified by the size of the tunnels, i. e. the number of octahedra which are building the edges of cross sections of the tunnels.<sup>[216]</sup>

The most stable and abundant tunneled Mn-oxide structure is pyrolusite ( $\beta\text{-MnO}_2$ ). In this structure, edge-sharing  $\text{MnO}_6$  octahedra are building chains with the width of a single octahedron. These chains are sharing corners with neighboring octahedra to form a tunneled but saturated one octahedron by one octahedron (1X1) structure (Figure 4.5, a). Because of the small size of the formed tunnels, no other chemical species are accommodated.<sup>[216]</sup> The coordinatively saturated linkage between the octahedra is limiting the flexibility of the  $\mu$ -oxido network as well as the number of open coordination sites for water binding and activation. Thus, the saturated nature of the  $\beta\text{-MnO}_2$  structure has been suggested to inhibit water-oxidation catalysis.<sup>[103,215]</sup>

In ramsdellite ( $\text{MnO}_2$ ), sheets are formed by two rows of edge-sharing  $\text{MnO}_6$  octahedra. In the corner sharing pattern, these sheets are interconnected to build one by two (1X2) tunnels (Figure 4.5, b). The 1X2 tunnels are quite small, but minor fractions of  $\text{H}_2\text{O}$ ,  $\text{Na}^+$  and  $\text{Ca}^{2+}$  are supposed to be located in these channels.<sup>[216]</sup>

Hollandite ( $\text{Na/K/Ba/Pb}_{0.8-1.5}\text{Mn}_8^{\text{III,IV}}\text{O}_{16}$ ) is also build up from double chains of edge-sharing octahedra. But the corner sharing sheets are connected differently, building two by two (2X2) tunnels (not shown). Mono- or divalent cations as well as  $\text{H}_2\text{O}$  molecules are placed inside of the channels showing a wide range of compositions.<sup>[216]</sup>

Romanechite ( $\text{Ba}_{0.66}\text{Mn}_5^{\text{III,IV}}\text{O}_{10} \cdot 1.34\text{H}_2\text{O}$ ) is based on double and triple chains which are forming two by three (2X3) channels (Figure 4.5, c). In naturally occurring romanechites,  $\text{Na}^+$ ,  $\text{K}^+$ ,  $\text{Ca}^{2+}$  and  $\text{Sr}^{2+}$  are present in the tunnels in addition to  $\text{Ba}^{2+}$  and  $\text{H}_2\text{O}$ .<sup>[216]</sup>

In todorokite ( $\text{Na/K/Ca}_{0.3-0.5}\text{Mn}_6^{\text{III,IV}}\text{O}_{12} \cdot 3.5-4.5\text{H}_2\text{O}$ ), sheets of three rows of edge-sharing  $\text{MnO}_6$  octahedra are interconnected in a corner sharing pattern resulting in the formation of square tunnels (Figure 4.5, d), measuring three octahedra by a side (3X3). In the tunnels,  $\text{H}_2\text{O}$  molecules and  $\text{Ba}^{2+}$  ions are present in a 2:1 ratio, but also metal ions like  $\text{Ni}^{2+}$  and  $\text{Co}^{2+}$  can be found.<sup>[216]</sup>

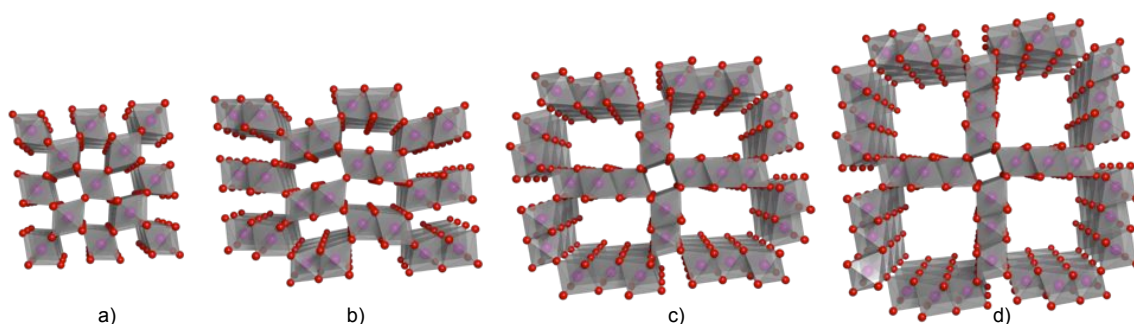


**Figure 4.5.** Schematic representation of the structures of the tunneled manganese oxides a) pyrolusite (1X1), b) ramsdellite (1X2), c) romanechite (2X3) and d) todorokite (3X3). In these tunneled oxides, edge-sharing  $\text{MnO}_6$  octahedra (octahedra in gray, Mn in purple, O in red) are forming chains (a) or sheets (b-d). These chains and sheets are sharing corners of the octahedra to form tunnels of different size.<sup>[216]</sup>

In addition to these well defined structures, mixtures and intergrown species are known. Nsutite ( $\gamma$ - $\text{MnO}_2$ ) for example is an intergrowth of pyrolusite (1X1) and ramsdellite (1X2) but showing also larger tunnels, defects and grain boundaries with minor amounts of several cations like  $\text{Na}^+$ ,  $\text{Ca}^{2+}$  or  $\text{Al}^{3+}$  present in the structure.<sup>[216]</sup> Intergrowths of todorokites (3X3) have been identified revealing tunnels measuring 3X4 up to 3X9 octahedra in the cross section.<sup>[216]</sup>

A common feature of all of these tunneled Mn-oxides is the presence of Mn in the oxidation state +IV and, in structures showing larger tunnels, also in the oxidation state +III.<sup>[216]</sup> The mixed valent character may contribute to a higher flexibility of the  $\mu$ -oxido linkage between the Mn centers. Unsaturated  $\mu_2$ -O(H) bridges present in these structures are likely necessary to catalyze the water-oxidation reaction and incomplete octahedra may act as coordination site for substrate water.<sup>[103,215]</sup>

### Manganese oxides with layered structures: phylломanganates

In layered manganese oxides, edge-sharing  $\text{MnO}_6$  octahedra are forming two-dimensional sheets. In contrary to tunneled oxides, these sheets are not interconnected in three dimensional patterns but they are stacked above each other to form a superior layered structure. In the interlayer space water molecules, additional cations and even layers with other compositions can be found.<sup>[216]</sup>

For instance, in lithiophorite ( $\text{LiAl}_2[\text{Mn}_2^{\text{IV}}\text{Mn}^{\text{III}}]\text{O}_6(\text{OH})_6$ ), sheets of edge-sharing  $\text{MnO}_6$  octahedra are stacked alternating with sheets of edge-sharing  $\text{Al}(\text{OH})_6$  octahedra. The respective sheets are interconnected by H-bonds that are formed between  $\mu$ -OH bridges of the Al/Li layers and  $\mu$ -O bridges of the Mn layers. In the Al-layers, every third octahedral site is occupied by Li. For charge balance, every third  $\text{Mn}^{\text{III}}$  center is exchanged by  $\text{Mn}^{\text{IV}}$ . The analysis of lithiophorite minerals has shown that Ni, Cu and Co are substituting into the structure. Ni and Cu ions are mainly found to be placed in the Al/Li layers while Co ions are placed in the Mn layers.<sup>[216]</sup>

In chalcophanite ( $\text{ZnMn}_3^{\text{IV}}\text{O}_7 \cdot 3\text{H}_2\text{O}$ ) every seventh octahedral site of the  $\text{MnO}_6$  sheets is vacant.  $\text{Zn}^{2+}$  ions coordinated by water molecules are placed above and below the vacancies. Structures in which the position of  $\text{Zn}^{2+}$  is occupied by  $\text{Ni}^{2+}$  or  $\text{Mg}^{2+}$  also have been found.<sup>[216]</sup>

The structure of the mineral group of birnessites ( $\text{Na/Ca/Mn}^{\text{II}}\text{Mn}_7^{\text{IV}}\text{O}_{14} \cdot 2.8\text{H}_2\text{O}$ ) is quite similar to chalcophanite. Edge sharing  $\text{MnO}_6$  octahedra are forming layers, water molecules and additional cations are placed in the interlayer space (Figure 4.6, left). The known birnessite minerals are poorly crystalline, complicating a detailed analysis of the structures. However, Na-, K- and Mg birnessite phases were investigated using transmission electron microscopy (TEM) and powder X-ray diffraction (XRD). The analysis has shown the layers of  $\text{MnO}_6$  octahedra and that water molecules and the additional cations are occupying different positions in the interlayer space. The layers spacing has been determined to be about 7 Å.<sup>[216]</sup>

Birnessites can be easily prepared via comproportionation reactions of  $\text{Mn}^{2+}$  and  $\text{MnO}_4^-$  in alkaline solution containing additional mono- or divalent cations (see chapter 6 for more details). A broad variety of compositions can be synthesized by ion-exchange.<sup>[217,218]</sup> The precipitate initially formed under these conditions is structurally similar to birnessites but shows an interlayer spacing of 10 Å. These birnessite like structures are named buserite.<sup>[216]</sup> The larger interlayer distance of these buserites is caused by an additional layer of water molecules (Figure 4.6, right). Upon drying, the structure collapses to the birnessite structure with an interlayer distance of 7 Å, the additional

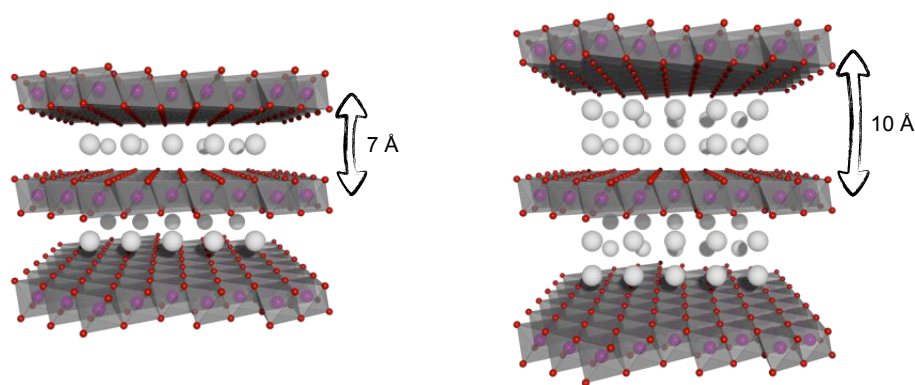


**Figure 4.6.** Schematic representation of the structures of the layered Mn-oxide minerals birnessite (*left*) and buserite (*right*). Edge sharing MnO<sub>6</sub> octahedra (Mn in purple, O in red, octahedra in gray) are forming layers that are stacked above each other. Water molecules (indicated as white spheres) and additional cations (not shown) are placed in between the layers. Both structures are quite similar but are differing in the interlayer spacing (7 Å in birnessites, 10 Å in buserites) caused by different amounts of intercalated water molecules as indicated by the white spheres. Upon drying of a buserite, a layer of water is removed from the structure and a birnessite is formed.

layer of water molecules is removed.<sup>[216,217]</sup>

Vernadite is another variety of birnessite, also showing poor crystallinity. Based on powder XRD patterns, it has been suggested that the structure is disordered in the layer-stacking direction. Analysis of the composition of vernadites showed the presence of K, Mg, Ca, Ba, and Fe as well as 15 to 25 weight-percent water as part of the oxide structure.<sup>[216]</sup>

Similar to the tunneled Mn-oxides, those with a layered structure are also comprising an extended  $\mu$ -oxido linkage between the Mn centers. Vacancies may contribute to a high flexibility of this connection pattern. Also unsaturated  $\mu_2$ -O(H) bridges and uncompleted octahedra may be present.

However, in lithiophorite, potential coordination sites may not be accessible due to the network of hydrogen-bonds between the Al/Li- and the Mn layers. But in chalcophanite and birnessite like oxides, vacancies and open unsaturated coordination sites are accessible, perhaps. Especially the possibility to vary the composition of synthetic birnessites quite easily is making this class of oxides interesting candidates for a possible application in water-oxidation catalysis. To the best of my knowledge, no study has been reported yet, investigating systematically the activity of various tunneled and layered Mn-oxides in water-oxidation catalysis.



## **Part II**

# **The research project – results and discussion**



## 5 Motivation

Against a background of rising energy costs as well as a rising public awareness of the consequences of the extensive combustion of fossil fuels, sustainable energy sources are becoming more and more important (*cf.* chapter 1). Solar energy has a tremendous potential as clean and abundant energy source as about 120 000 TW<sup>[2]</sup> of electromagnetic radiation from the sun constantly reaches the Earth, far in excess of our current usage of 16 TW.<sup>[7]</sup> To take full advantage of the enormous potential of the sun, methods for the capture of solar energy and its conversion into readily utilizable and storable forms are urgently required.

In nature, solar energy is captured and converted by the highly complex process of photosynthesis. Reduction equivalents provided by the oxidation of water are utilized to convert CO<sub>2</sub> into biomass (*cf.* chapter 2).<sup>[19,20]</sup> Light-driven water-oxidation is carried out by photosystem II (PSII), a transmembrane cofactor-protein complex embedded in the thylakoid membranes of plants and cyanobacteria.<sup>[19,20]</sup> PSII's active site for water-oxidation is the oxygen-evolving-complex (OEC), a  $\mu$ -oxido bridged CaMn<sub>4</sub> cluster, which is coordinated to oxidation stable amino acid residues of the protein environment.<sup>[26,29,36]</sup>

Following the reaction sequence of photosynthesis, approaches for sunlight-driven water-splitting are under investigation to meet the global energy demand in a sustainable way (artificial photosynthesis, *cf.* chapter 3). In schemes for artificial photosynthesis, catalysis of the water-oxidation half-reaction represents one of the major challenges.<sup>[1,3-5,27,29,100,103]</sup> As the OEC is built up from abundant elements, it is an interesting blueprint for the development of affordable synthetic materials to act as water-oxidation catalysts. In addition, a detailed analysis of compounds mimicking the OEC in structure and/or function is important to contribute to a better understanding of the biological water-oxidation reaction. In this connection, transition metal complexes, but also transition metal oxides are of interest and have been studied extensively (*cf.* chapter 4).<sup>[99,101,103,127,165,180,183,213]</sup>

Inspired by the composition of the OEC, in 2009 Najafpour synthesized and characterized manganese oxides as water-oxidation catalysts during his research project in the Kurz group at Christian-Albrechts-Universität Kiel. Najafpour demonstrated that catalytically highly active water-oxidation catalysts can be obtained, when Ca<sup>2+</sup> ions are incorporated into the oxides' structure.<sup>[214]</sup> The catalytic activity of these CaMn oxides by far exceeded the activity of  $\alpha$ -Mn<sub>2</sub>O<sub>3</sub>, a material that has been identified as active water-oxidation catalyst already in the 1980s.<sup>[195]</sup> In collaboration with the Dau group of Freie Universität Berlin, the active CaMn oxide catalysts could be identified as layered manganese oxides of the birnessite family. Such oxides contain structural features resembling the OEC's CaMn<sub>4</sub> core.<sup>[215]</sup> The findings of the detailed analysis of Najafpour's highly active Ca-birnessites raised two fundamental questions:<sup>[214,215]</sup>

- what is the role of the Ca<sup>2+</sup> ions in water-oxidation catalysis?
- is it possible to adopt mechanistic scenarios postulated for water-oxidation catalyzed by the OEC to Ca-birnessites?

Furthermore, requirements were suggested which have to be met by Mn based compounds to show activity in water-oxidation catalysis as well as to function as OEC model systems:<sup>[103,215]</sup>

- a multinuclear ( $\geq \text{Mn}_4(\mu\text{-O}/\text{OH})_x$ ) bridged manganese core is necessary for the accumulation of four oxidizing equivalents by the abstraction of four electrons at potentials  $> +1$  V in one electron oxidation steps,
- redox potential leveling is crucial, thus charge compensation has to be realized by proton coupled electron transfer or ligand exchange,
- the  $\mu\text{-O}(\text{H})$  core has to be stabilized by a flexible ligand framework in order to facilitate the necessary changes in geometry related to changes of the oxidation state,
- open coordination sites are necessary to bind and activate substrate  $\text{H}_2\text{O}$  molecules.

Following these considerations and Najafpour's promising results in water-oxidation catalysis, I started a detailed investigation of mixed layered manganese oxides as water-oxidation catalysts. A study of the literature on birnessite-like oxides revealed that these materials are easy to prepare in a wide range of compositions. Thus I decided to synthesize and characterize various birnessites and to investigate their ability to act as water-oxidation catalysts. By a comparison of the properties of these materials and their oxygen evolution rates, we hoped to broaden the understanding of water-oxidation catalyzed by Mn based materials, especially birnessite-like oxides. In these studies, the role of  $\text{Ca}^{2+}$  ions in water-oxidation catalysis was of particular interest.

## 6 Synthesis and general characterization of various M-birnessites

Within the scope of the research project discussed in this thesis, various M-birnessites (M represents additional cations present in the structure) were synthesized following a route established by Luo *et al.*<sup>[217]</sup> The authors reported the preparation of Na-buserites (*cf.* section 4.2.2) by comproportionation reactions of  $\text{Mn}^{2+}$  and  $\text{MnO}_4^-$  in aqueous alkaline solution, also containing  $\text{Na}^+$  and  $\text{Mg}^{2+}$  ions. The comproportionation reactions were resulting in the formation of dark brown suspensions, which were subsequently aged at 40 °C for a period of one to four days. It was shown that the crude products obtained in this way belong to the buserite family of layered manganese oxides (*cf.* section 4.2.2). After the ripening process, Luo and coworkers filtered off the obtained precipitates, resuspended them in  $\text{H}_2\text{O}$  and carried out a second aging step to stabilize the buserite phase.<sup>[217]</sup> They also demonstrated that birnessites (*cf.* section 4.2.2) can be prepared following the comproportionation route and dry the obtained precipitate instead of stabilizing the buserite structure.<sup>[217,218]</sup>

In the studies presented herein, two different strategies for the preparation of various M-birnessites as potential water-oxidation catalysts were derived from this route. In a first approach, the  $\text{Mg}^{2+}$  ions present in Luo's first reaction step were substituted by several metal ions in different concentrations in order to prepare M-birnessites of varying compositions (section 6.1). In a second approach, a Ca-buserite was synthesized as a precursor, which was subsequently used in ion exchange experiments to obtain various M-birnessites (section 6.2). Inspired by the composition of the OEC (a  $\text{CaMn}_4\text{O}_5$  cluster), the investigations focused especially on Ca-birnessites. Therefore, materials with varying concentrations of  $\text{Ca}^{2+}$  ions present in the synthesis (section 6.3) as well as CaMn oxides with stepwise increased ripening periods of up to ten days (section 6.4) were prepared.

A detailed analysis of the synthesized M-birnessites is crucial in order to identify factors influencing the activity of these materials in water-oxidation catalysis. The composition of the various M-birnessites was thus studied by energy-dispersive X-ray spectroscopy (EDX), atomic absorption spectroscopy (AAS) and thermogravimetry. The specific surface areas of the oxide materials as well as the porosity of their particles were investigated by the measurement of nitrogen adsorption/desorption isotherms. The specific surface areas of the materials can be derived from the isotherms according to the Brunauer-Emmet-Teller (BET) theory.<sup>[219]</sup> Informations on the porosity of the materials can be obtained from the shape of the plot. In the IUPAC classification, six types of isotherms are distinguished, which are characteristic for adsorption at microporous (type I), nonporous or macroporous (type II, III) and mesoporous (type IV, V) adsorbents, or for a stepwise type of adsorption (type VI).<sup>[220-222]</sup> To gain insights into the effect of the modified synthesis parameters on the morphology of the oxides particles, scanning electron microscope (SEM) images were taken. Furthermore, infrared (IR) spectra of the solids were recorded.

## 6.1 M-birnessites prepared by direct synthesis

In previous work by the Kurz group, Najafpour demonstrated in his study that birnessite like manganese oxides containing  $\text{Ca}^{2+}$  ions are promising water-oxidation catalysts.<sup>[214]</sup> In comparison to “Mn only” oxides, the catalytic activity of these materials is much higher.<sup>[195,213,214]</sup> A detailed analysis of these materials revealed that the Ca-birnessite materials are mimicking biology’s paragon, the OEC, not only in its function, but also in its composition and in distinct structural features.<sup>[215]</sup> Based on the similarities of the synthetic oxide catalysts and the OEC, we proposed that  $\text{Ca}^{2+}$ , as inPSII (cf. section 2.2.2), also plays a key role in bioinspired water-oxidation catalyzed by synthetic manganese oxide catalysts.<sup>[103,214,215,223]</sup>

In order to investigate the influence of  $\text{Ca}^{2+}$  and other cations on water-oxidation catalyzed by layered manganese oxides in more detail, I followed ion exchange experiments carried out for the OEC. I prepared M-birnessites containing virtually no divalent cations (1) or different amounts of  $\text{Ca}^{2+}$  (2, 3),  $\text{Sr}^{2+}$  (4, 5) and  $\text{Mg}^{2+}$  (6, 7), respectively.<sup>[223]</sup> In addition to this set of birnessites containing alkaline earth cations, the synthesis was carried out in the presence of  $\text{Cd}^{2+}$  (8, 9),  $\text{Al}^{3+}$  (10, 11),  $\text{Zn}^{2+}$  (12) and  $\text{Pb}^{2+}$  (13). 12 and 13 were synthesized and characterized by Michael Poschmann in his BSc thesis.<sup>[224]</sup> Following the synthetic route described by Luo *et al.*<sup>[217]</sup>, aqueous solutions of  $\text{Mn}^{\text{II}}(\text{AcO})_2$  and the respective additional cation were added dropwise to aqueous solutions of KOH or NaOH resulting in the precipitation of  $\text{Mn}(\text{OH})_2$ .<sup>[217]</sup> To this suspension, a solution of  $\text{KMnO}_4$  was added, resulting in the oxidation of  $\text{Mn}(\text{OH})_2$  in the presence of the additional cations and the formation of suspensions containing manganese oxides most likely in the form of buserites. The obtained oxides were then aged and subsequently dried (1-7) or dried directly (8-13, for details of the syntheses see section 9.1.1).

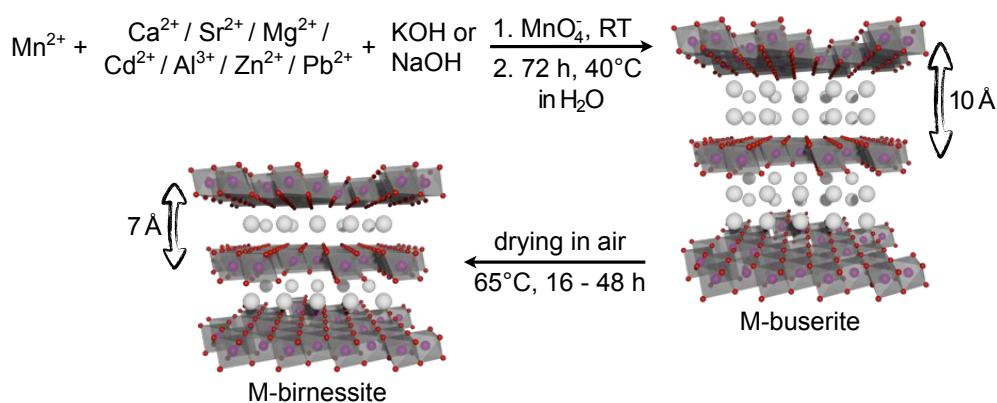


**Figure 6.1.** Scheme for the synthesis of M-birnessites 1-13. Following the route described by Luo *et al.* aqueous solutions containing  $\text{Mn}^{2+}$  ions as well as additional cations were added to aqueous alkaline solutions, resulting in the formation of a slurry of  $\text{Mn}(\text{OH})_2$ . By the addition of  $\text{MnO}_4^-$ ,  $\text{Mn}(\text{OH})_2$  was oxidized in the presence of the additional cations, resulting in the formation of a M-buserite phase. After a ripening period of 72 h, the M-buserite precipitates were dried to yield M-birnessites. In case of the synthesis of the M-birnessites 8-13, the ripening step was omitted.

### Analysis of the oxide compositions

The composition of the oxide materials was investigated by AAS and EDX in order to determine the manganese content (Table A.5) and the molar metal ion ratios, respectively (Table 6.1). Based on the results, the oxides can be best formulated as  $K_{0.31}$ - (1),  $Ca_{0.14}$ - (2),  $Ca_{0.27}$ - (3),  $Sr_{0.18}$ - (4),  $Sr_{0.27}$ - (5),  $Mg_{0.13}$ - (6),  $Mg_{0.28}$ - (7),  $Cd_{0.16}$ - (8),  $Cd_{0.29}$ - (9),  $Al_{0.02}$ - (10),  $Al_{0.03}$ - (11),  $Zn_{0.20}$ - (12) and  $Pb_{0.30}$ -birnessite (13), where the indices represent the M:Mn molar ratio for the cations of interest.

The oxides 1, 2 and 3 were prepared out of solutions containing  $K^+$ ,  $Ca^{2+}$  and  $Mn^{II/VII}$  ions, with Ca:Mn ratios of 0.01 (1), 0.15 (2) and 0.29 (3), respectively. This Ca:Mn ratio is well reflected by the composition of the oxides, showing molar ratios of 0.02 (1), 0.14 (2) and 0.27 (3). As a consequence of the low  $Ca^{2+}$  concentration used in the synthesis of 1,  $K^+$  is the dominant cation intercalated in between the layers of the  $K_{0.31}$ -birnessite.

A similar trend can be observed in case of the M-birnessites prepared in the presence of  $Sr^{2+}$ ,  $Mg^{2+}$  and  $Cd^{2+}$ . In the syntheses of these oxides,  $M^{2+}$ :Mn ratios of 0.15 (4, 6, 8) and 0.29 (5, 7, 9), respectively, were present in solution of the synthetic mixtures. Except for Sr-birnessite 4 in which the Sr:Mn ratio is slightly more deviating from the metal ion

**Table 6.1. Molar ratios (per Mn) and water content (in weight %) of 1-13 as determined by EDX and thermogravimetry.**

Compound <sup>a</sup>		$Na^+/K^+$ <sup>b</sup>	$M^{2+/3+}$	Mn	$M_{total}/Mn$	$H_2O^c$
$K_{0.31}$ -birnessite	(1)	0.31	0.02 ( $Ca^{2+}$ )	1	0.33	10
$Ca_{0.14}$ -birnessite	(2)	0.05*	0.14 ( $Ca^{2+}$ )	1	0.19	15
$Ca_{0.27}$ -birnessite	(3)	0.03	0.27 ( $Ca^{2+}$ )	1	0.30	18
$Sr_{0.18}$ -birnessite	(4)	0.08	0.18 ( $Sr^{2+}$ )	1	0.26	12
$Sr_{0.27}$ -birnessite	(5)	0.01	0.27 ( $Sr^{2+}$ )	1	0.28	11
$Mg_{0.13}$ -birnessite	(6)	0.19*	0.13 ( $Mg^{2+}$ )	1	0.32	13
$Mg_{0.28}$ -birnessite	(7)	0.17	0.28 ( $Mg^{2+}$ )	1	0.45	14
$Cd_{0.16}$ -birnessite	(8)	0.15	0.16 ( $Cd^{2+}$ )	1	0.31	
$Cd_{0.29}$ -birnessite	(9)	0.15	0.29 ( $Cd^{2+}$ )	1	0.44	
$Al_{0.02}$ -birnessite	(10)	0.24	0.02 ( $Al^{3+}$ )	1	0.26	
$Al_{0.03}$ -birnessite	(11)	0.26	0.03 ( $Al^{3+}$ )	1	0.29	
$Zn_{0.20}$ -birnessite <sup>[224]</sup>	(12)	0.22	0.20 ( $Zn^{2+}$ )	1	0.42	
$Pb_{0.30}$ -birnessite <sup>[224]</sup>	(13)	0.38	0.30 ( $Pb^{2+}$ )	1	0.68	

<sup>a</sup> The synthesized M-birnessites are labelled according to the additional  $M^{2+/3+}$  cation ( $M^+$  for 1) intercalated in between the manganese oxide layers. Indices describe the respective M:Mn molar ratio. <sup>b</sup>  $Na^+(*)$  or  $K^+$  ions are originating from the hydroxide bases used for the syntheses. <sup>c</sup> Weight losses observed in thermogravimetric analyses of 1-7 up to 400 °C were assumed to originate entirely from the elimination of water molecules from the oxide materials. For the other oxides, no thermogravimetric analysis was carried out.

ratio of the solution, the content of  $M^{2+}$  ions is in a good agreement with the expected composition. Furthermore, it is notable that the Mg- (6, 7) as well as the Cd-birnessites (8, 9) are containing higher amounts of  $K^+$  or  $Na^+$  ions in comparison to the Ca- (2, 3) and Sr-birnessites (4, 5).

In the syntheses of oxides **10** and **11**, solutions containing  $Mn^{2+}$  and  $Al^{3+}$  (Al:Mn ratios of 0.15 and 0.29) were added to KOH, resulting in the formation of a much more viscous slurry, most likely consisting of suspended particles of a mixed  $Mn^{II}/Al^{III}$  hydroxide. After the addition of  $KMnO_4$ , a brown slurry was obtained similar to the syntheses of the other M-birnessites. The analysis of the composition of the products showed that only 0.02 (**10**) or 0.03 (**11**)  $Al^{3+}$  ions per Mn were present in the precipitate.  $K^+$  is the dominating additional cation accommodated in the structures.

Observations during the syntheses as well as the found composition of the prepared oxides are indicating that the  $Mn^{II}/Al^{III}$  hydroxide phase likely formed in the first reaction step has been resolved when  $KMnO_4$  was added. This could probably be explained by the oxidation of  $Mn^{2+}$  ions of the mixed hydroxide resulting in precipitation of a birnessite like manganese oxide. Due to the high pH of the reaction mixture, the  $Al^{3+}$  ions previously bound in the mixed hydroxide may then be present in solution in form of  $[Al(OH)_4]^-$  anions.

However, these results are demonstrating that Al-birnessites cannot be prepared following the synthetic route described by Luo *et al.* In order to obtain Al-birnessites, a variation of the reaction conditions, especially of the pH, is necessary. In this context it is important to note that the form in which  $Al^{3+}$  ions are present in aqueous solution are strongly dependent on the pH. In addition to  $Al(OH)_3$  and  $[Al(OH)_4]^-$  which are present at higher pH values, clusters like  $[Al_{13}O_4(OH)_{24}(H_2O)_{12}]^{7+}$  are known to form at a pH range of about 4-8.<sup>[15]</sup> Such clusters have also been identified in so called pillared clays. In these clay materials, the  $[Al_{13}O_4(OH)_{24}(H_2O)_{12}]^{7+}$  ions are placed as a kind of spacer (or pillar) of 0.98 nm · 1.09 nm · 0.97 nm in size<sup>[225]</sup> in between the clay's layers, resulting in an interlayer distance of around 20 Å.<sup>[225-230]</sup>

On the other hand, it has been reported that lithiophorite (a Mn/Al oxide with alternating sheets of edge-sharing  $MnO_6$  and  $Al(OH)_6$  octahedra, *cf.* section 4.2.2) can be synthesized from birnessites under reflux in the presence of  $Al^{3+}$  at pH values of 5 to 9.<sup>[231]</sup> This route might be a starting point for the development of strategies for the synthesis of Al-birnessites via ion exchange.

Michael Poschmann prepared M-birnessites containing  $Zn^{2+}$  (**12**) and  $Pb^{2+}$  (**13**) for his BSc thesis.<sup>[224]</sup> In his syntheses he employed  $M^{2+}$ :Mn ratios of about 0.22. The analysis of the composition of these oxides showed that it is possible to accommodate these ions in the layered manganese oxide structure, as  $Zn^{2+}$  and  $Pb^{2+}$  ions were found in  $M^{2+}$ :Mn ratios of 0.20 and 0.30, respectively. The higher amount of intercalated  $Pb^{2+}$  ions is indicating a higher affinity of the birnessite layers to bind  $Pb^{2+}$ , well corresponding to the literature.<sup>[216,232,233]</sup> In both oxides also high amounts of  $K^+$  were found, as the  $K^+$ :Mn ratio in the  $Zn_{0.20}$ -birnessite was 0.22 and 0.38 in the  $Pb_{0.30}$ -birnessite.

Overall, these results are showing that  $M^{2+}$ -birnessites containing the respective metal ions in different concentrations can be prepared by simple comproportionation reactions. Even if an excess of monovalent cations is present, the composition of the oxides can be mainly controlled by the  $M^{2+}$ :Mn ratio employed in the synthesis, well corresponding to low binding affinities reported for monovalent metal ions.<sup>[216,233,234]</sup>  $M^{3+}$ -birnessites containing significant amounts of  $Al^{3+}$  can not be prepared following this route. In contrast,  $Pb^{2+}$  ions are bound in higher concentrations.

1-13 are showing different affinities to bind  $K^+$  and  $Na^+$ , respectively. While Ca- (2, 3) and Sr-birnessites (4, 5) are only binding small amounts of monovalent metal ions, the amount is significantly higher in the Mg- (6, 7), Cd- (8, 9), Zn- (12) and Pb-birnessites (13). Interestingly, this trend seems to be more dependent on the type of the accommodated  $M^{2+}$  ion, than on its concentration. This may indicate that the type of the additional metal ions is strongly influencing the structure of the birnessites, as a higher amount of positive charges may be necessary for the compensation of negatively charged layers in case of oxides 6-13, probably caused by manganese vacancies.

Thermogravimetric analyses were carried out for oxides 1-7 in the temperature range from 25 °C to 1000 °C in air (for details see section 9.3). The analyses show weight losses of about 10-20 % in the temperature range from 25 °C to 400 °C (Figure 6.2).  $K_{0.31}$ -birnessite (1) shows the least,  $Ca_{0.27}$  (3) the highest reduction of its mass (Table 6.1). These losses can most likely be assigned to the removal of weakly bound water molecules placed in the interlayer space of the oxides .

A further weight reduction of about 15-30 % was observed in the temperature range from 400 °C up to 1000 °C. For such high temperatures, it is known that binary manganese oxides like  $MnO_2$  undergo phase transitions coupled to oxygen release. The manganese centers are thereby stepwise reduced from  $Mn^{4+}$  via  $Mn^{3+}$  to  $Mn^{2+}$ .<sup>[15]</sup> As the oxidation state of the synthetic birnessites 1-7 was determined to be close to +IV<sup>[223]</sup> (cf. section 7.2) and considering also Najafpour's results<sup>[214]</sup>, it is proposed that similar phase transitions including oxygen release as well as the reduction of manganese centers also occur here.

The recorded thermogravimetric data are supporting the identification of the prepared materials as water-containing  $Mn^{3+/4+}$  oxides. The slight deviation of the course of the plots in Figure 6.2 is likely the result of minor differences in the composition, i. e. the water content, the type and the concentration of additional metal cations intercalated

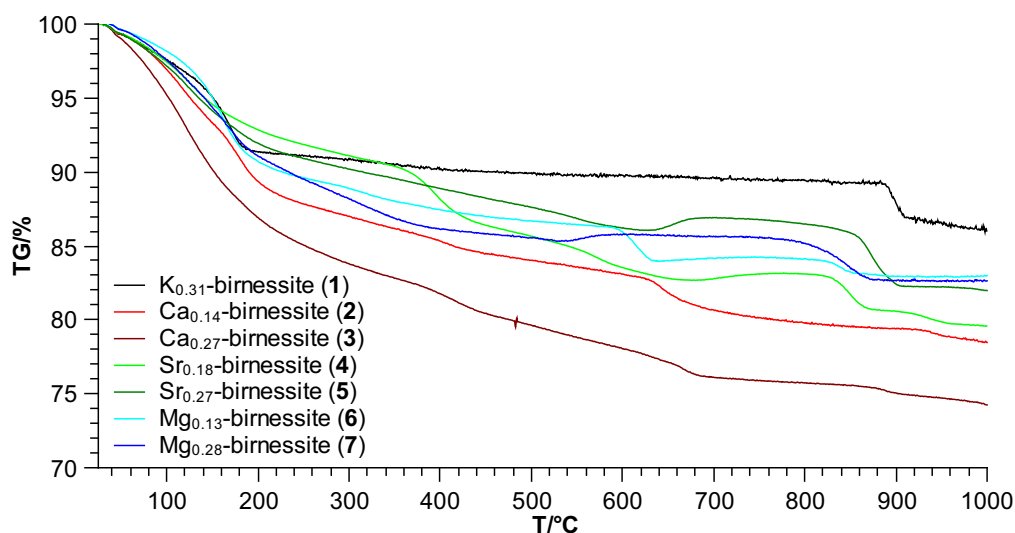


**Figure 6.2.** Thermogravimetric analyses of M-birnessites 1-7. The oxide samples were heated to 1000 °C at a rate of  $4\text{ °C} \cdot \text{min}^{-1}$  in airflow. The observed weight loss of about 10-20 % in the temperature range from 25 °C up to about 400 °C is most likely caused by the elimination of water molecules weakly bound to the birnessite layers. At higher temperatures, the weight loss is best explained by phase transitions coupled to oxygen release.

in between the birnessite layers. However, the elemental analysis of **1-13** as well as the thermogravimetric results of **1-7** are showing striking similarities of the composition of these oxide materials.

### Particle shape, specific surface area and IR spectroscopy

In order to investigate the influence of the different cations on the morphology of the prepared M-birnessites, SEM images of the oxide particles of **2-7**, **12** and **13** were taken (Figure 6.3). These images are clearly illustrating that the incorporation of various metal ions in different concentrations has an effect on the particle shape and on their diameter. The observed particle size is on the micrometer scale, but the size distribution is inhomogeneous in all cases. Thus, the composition of the synthetic birnessites or the type and concentration of the additional cations in the synthetic mixture are strongly influencing their morphology.

A comparison of the SEM images of Ca-birnessites **2** and **3** shows that the intercalation of larger amounts of  $\text{Ca}^{2+}$  ions into the structure results in the formation of smaller particles (Figure 6.3, *a, b*). The same effect can be observed for the incorporation of two different concentrations of  $\text{Mg}^{2+}$  ions. The SEM image of  $\text{Mg}_{0.13}$ -birnessite **6** shows defined particles of an angular shape (Figure 6.3, *e*), while the particles of  $\text{Mg}_{0.28}$ -birnessite **7** are less defined and clearly smaller (Figure 6.3 *f*). On the contrary, the incorporation of higher amounts of  $\text{Sr}^{2+}$  is leading to the formation of larger particles as shown by the SEM images of  $\text{Sr}_{0.18}$ -birnessite **4** and  $\text{Sr}_{0.27}$ -birnessite **5** (Figure 6.3, *c* and *d*). The particles of  $\text{Zn}_{0.20}$ -birnessite **12** (Figure 6.3, *g*) show an angular shape of relatively large size, similar to those of  $\text{Mg}_{0.13}$ -birnessite **6**. The particles of  $\text{Pb}_{0.30}$ -birnessite **13** (Figure 6.3, *h*) have a shape comparable to that of the Ca-birnessites.

However, SEM images only probe outer surfaces and thus offer only limited information on the morphologies of the prepared particles. It is not possible to distinguish if aggregates are formed or if larger, single particles are dominating the M-birnessite's morphology. If the birnessite particles are formed of aggregates in the solid state, they may fall apart when the oxides are suspended in water. It also has to be noted that the particle size is probably affecting the potential of the oxides to act as water-oxidation catalysts. Smaller particles are showing larger surface areas compared to larger particles of the same morphology. Assuming a statistically distribution of catalytically active units on the particles surfaces, an enlargement of the surface area could lead to an improved activity in individual cases.

For further investigations of the prepared materials,  $\text{N}_2$  adsorption/desorption isotherms were recorded at  $-196\text{ }^\circ\text{C}$  (see section 9.3 for experimental details). In Figure 6.4, the plots of Ca-birnessites **2** and **3** (*left*) as well as Sr-birnessite **4** and **5** (*right*) are shown. These exemplary adsorption/desorption isotherms are indicating that the synthetic oxide materials are non- or macroporous (type II, *right*) or mesoporous as an adsorption hysteresis can be observed for **2** and **3** (type IV, *left*). Considering the layered structures assumed for the oxide materials with interlayer distances of about  $7\text{ \AA}$  (*cf.* sections 4.2.2 and 7.1), pore diameters of 2-50 nm (macropores) or even above 50 nm (mesopores) cannot arise from the birnessite structure itself. Thus, the observed adsorption hystereses are most likely indicating the presence of textural pores, meaning the formation of pores in between aggregated particles.

The specific surface areas of the oxide powders were found to vary from 30 up to  $230\text{ m}^2 \cdot \text{g}^{-1}$  (Table 6.2). For the  $\text{K}_{0.31}$ -,  $\text{Ca}_{0.14}$ - and  $\text{Ca}_{0.27}$ -birnessite, surface areas of 55

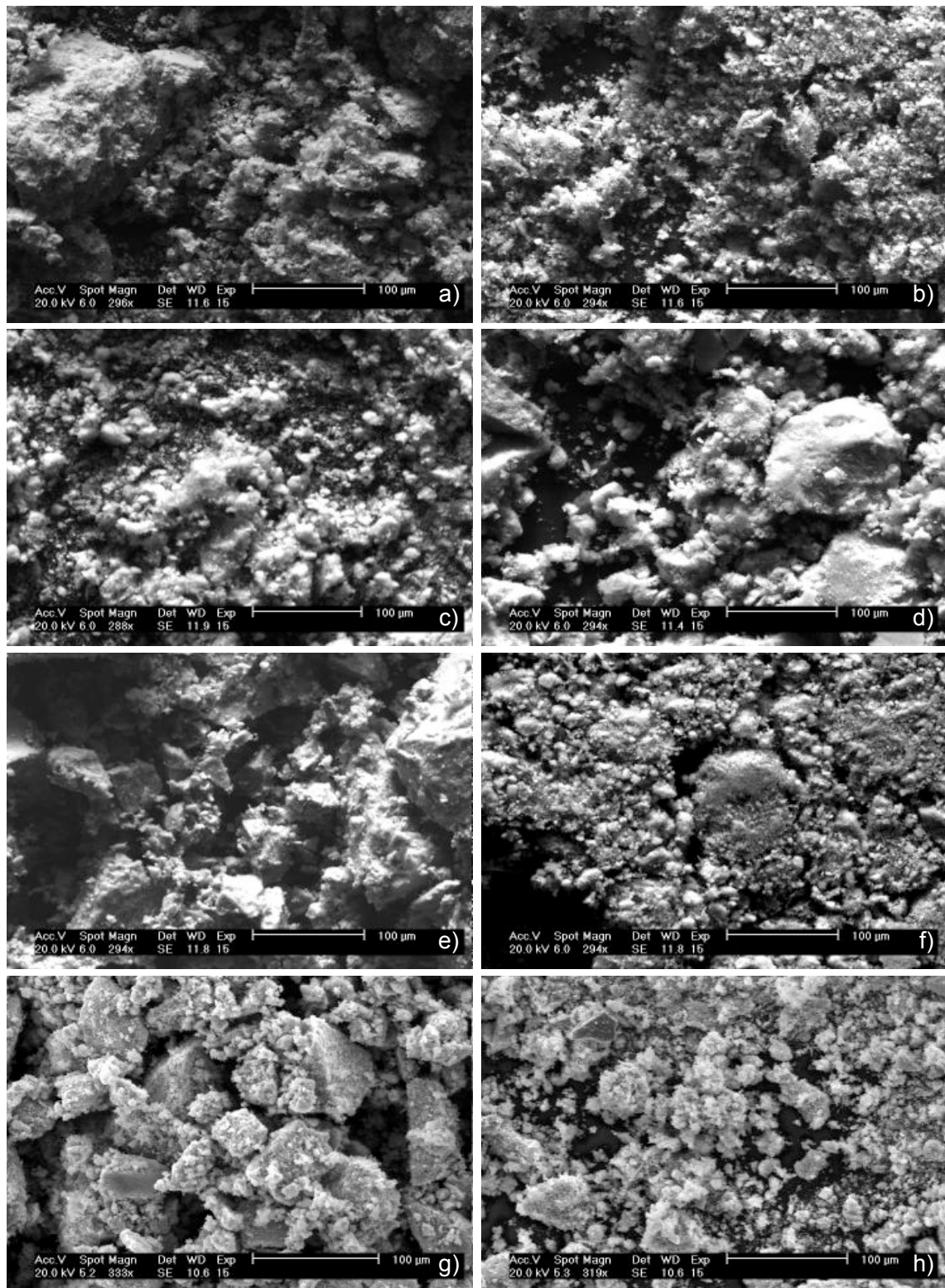


**Figure 6.3.** SEM images of  $\text{Ca}_{0.14^-}$  (2, a),  $\text{Ca}_{0.27^-}$  (3, b),  $\text{Sr}_{0.18^-}$  (4, c),  $\text{Sr}_{0.27^-}$  (5, d),  $\text{Mg}_{0.13^-}$  (6, e),  $\text{Mg}_{0.28^-}$  (7, f),  $\text{Zn}_{0.20^-}$  (12, g) and  $\text{Pb}_{0.30^-}$ -birnessite (13, h) in  $\sim 300\times$  magnification. In all cases, the particle size distribution is on the micrometer scale but inhomogeneous. When larger amounts of  $\text{Ca}^{2+}$  or  $\text{Mg}^{2+}$  cations are incorporated into the oxides, smaller particles are formed. In contrast, an increased  $\text{Sr}^{2+}$  ion concentration is leading to the formation of larger particles (d, e).

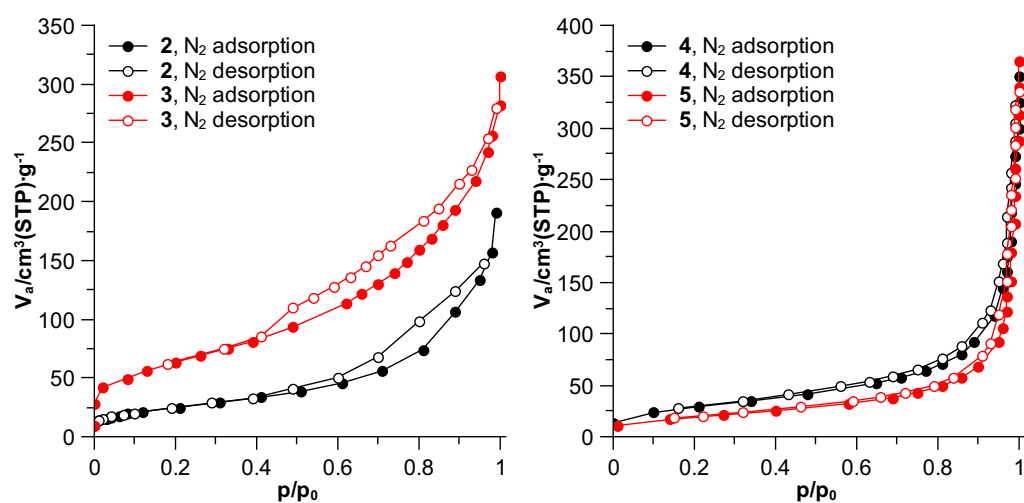


**Figure 6.4.** N<sub>2</sub> adsorption/desorption isotherms of Ca<sub>0.14</sub>- (2) and Ca<sub>0.27</sub>- (3) (left) as well as Sr<sub>0.18</sub>- (4) and Sr<sub>0.27</sub>-birnessites (5) (right), representative for 1-13. The isotherms were recorded at  $-196\text{ }^{\circ}\text{C}$  after activation of the oxide samples at  $120\text{ }^{\circ}\text{C}$  for 2 h. The adsorption hystereses of the isotherms left are indicating that mesoporous textural pores are present, while the isotherms on the right are typical for nonporous or macroporous materials.

**Table 6.2. Surface areas ( $S_{\text{BET}}$ ) of 1-13.**

Compound		Surface area/ $\text{m}^2 \cdot \text{g}^{-1}$
K <sub>0.31</sub> -birnessite	(1)	55
Ca <sub>0.14</sub> -birnessite	(2)	95
Ca <sub>0.27</sub> -birnessite	(3)	230
Sr <sub>0.18</sub> -birnessite	(4)	105
Sr <sub>0.27</sub> -birnessite	(5)	70
Mg <sub>0.13</sub> -birnessite	(6)	75
Mg <sub>0.28</sub> -birnessite	(7)	130
Cd <sub>0.16</sub> -birnessite	(8)	55
Cd <sub>0.29</sub> -birnessite	(9)	75
Al <sub>0.02</sub> -birnessite	(10)	65
Al <sub>0.03</sub> -birnessite	(11)	50
Zn <sub>0.20</sub> -birnessite <sup>[224]</sup>	(12)	30
Pb <sub>0.30</sub> -birnessite <sup>[224]</sup>	(13)	70

Numbers given in the table are rounded  $S_{\text{BET}}$  values obtained from nitrogen adsorption/desorption isotherms.

(1), 95 (2) and  $230 \text{ m}^2 \cdot \text{g}^{-1}$  (3) were found, indicating that the incorporation of higher amounts of  $\text{Ca}^{2+}$  ions is leading to a surface enlargement. This trend can also be observed for the cases of the Mg-birnessites 6 and 7 as well as the Cd-birnessites 8 and 9. Here, surface areas of  $75$  (6) and  $55 \text{ m}^2 \cdot \text{g}^{-1}$  (8) were found for the birnessites containing lower  $\text{M}^{2+}$  concentrations. The surface area of the oxides containing higher amounts of  $\text{Mg}^{2+}$  or  $\text{Cd}^{2+}$  was determined to be  $130$  (7) and  $75 \text{ m}^2 \cdot \text{g}^{-1}$  (9), respectively. In contrast, the addition of higher amounts of  $\text{Sr}^{2+}$  is leading to a decreased surface area, as shown by the area of  $105 \text{ m}^2 \cdot \text{g}^{-1}$  determined for the  $\text{Sr}_{0.18}$ -birnessite 4 and  $70 \text{ m}^2 \cdot \text{g}^{-1}$  for the  $\text{Sr}_{0.27}$ -birnessite 5. The well defined, angular  $\text{Zn}_{0.20}$ -birnessite particles are showing the lowest surface area of about  $30 \text{ m}^2 \cdot \text{g}^{-1}$ . For the  $\text{Pb}_{0.30}$ -birnessite, a value of  $70 \text{ m}^2 \cdot \text{g}^{-1}$  was determined.

The observed correlation of surface enlargement and the increased concentrations of incorporated cations found for Ca-, Mg- and Cd-birnessites is corresponding well to the correlation of the  $\text{Ca}^{2+}/\text{Mg}^{2+}/\text{Cd}^{2+}$  concentrations and the particle sizes estimated from SEM images. The surface areas determined for Sr-birnessites 4 and 5 is also well corresponding to the evaluation of the SEM images, as the formation of larger particles induced by a higher concentration of  $\text{Sr}^{2+}$  ions in the case of 5 is resulting in a smaller surface area compared to 4.

IR spectroscopy is a useful tool to characterize and distinguish different manganese oxides. With this method it is not only possible to analyze well ordered, crystalline materials, but also information on amorphous powders can be obtained. In addition to XRD techniques, IR spectroscopy has thus already been used in several studies to characterize manganese oxides with tunneled and layered structures.<sup>[234–242]</sup>

Tunneled and layered manganese oxides are showing similar structural features, as these materials are composed of corner or edge-sharing  $\text{MnO}_6$  octahedra and accommodate water molecules and additional cations within their cavities (*cf.* section 4.2.2). Thus, IR spectra of these oxides are quite similar. In the range of  $3600 \text{ cm}^{-1}$  to  $2500 \text{ cm}^{-1}$  and at around  $1500 \text{ cm}^{-1}$  wavenumbers, broad bands are observed which can be assigned to water molecules placed in the cavities or to hydroxide moieties bound to intercalated metal cations.<sup>[235–239]</sup> In the range of  $800 \text{ cm}^{-1}$  to  $200 \text{ cm}^{-1}$  wavenumbers, extensive bands characteristic for lattice Mn-O vibrations are found.<sup>[235,237–241]</sup>

In this range also fingerprint like bands appear, allowing to distinguish between individual manganese oxide structures. IR spectra of the tunneled manganese oxide todorokite, for instance, are showing characteristic bands at about  $750 \text{ cm}^{-1}$  and  $640 \text{ cm}^{-1}$ .<sup>[234,235,239,242]</sup> In spectra of ramsdellite, which is also a tunneled manganese oxide, fingerprint bands can be observed at about  $740 \text{ cm}^{-1}$  and  $690 \text{ cm}^{-1}$ .<sup>[241]</sup> In layered manganese oxides like busserites and birnessites, bands in this region are absent.<sup>[235,239]</sup> The structures of busserites and birnessites are again very similar, but in the case of busserites an additional feature in the region between  $800 \text{ cm}^{-1}$  and  $600 \text{ cm}^{-1}$  wavenumbers appears.<sup>[235]</sup>

However, due to the similarities of the structures, it is difficult to distinguish between highly disordered todorokites, busserites and birnessites as the band sharpness is related to the crystallinity of the oxide materials.<sup>[235]</sup> Furthermore, Potter and Rossman observed variations in the band position and relative intensities in the IR spectra of different birnessite samples.<sup>[235]</sup> They thus concluded that birnessites exhibit a characteristic basic structure, but differ in details.

The ATR IR spectra of M-birnessites **1-13** show broad bands in the region of  $3600\text{ cm}^{-1}$  to  $2500\text{ cm}^{-1}$  and around  $1500\text{ cm}^{-1}$  wavenumbers, as well as extensive, but poorly resolved bands below  $700\text{ cm}^{-1}$  (Figures 6.5 and 6.6). The bands can be assigned to the expected features of layered or tunneled manganese oxides: water molecules and hydroxide moieties bound in the cavities as well as Mn–O lattices. Bands characteristic for tunneled oxides are absent. Thus, the IR spectra are indicating that the prepared materials are disordered phylломanganates of the birnessite family.<sup>[234–242]</sup>

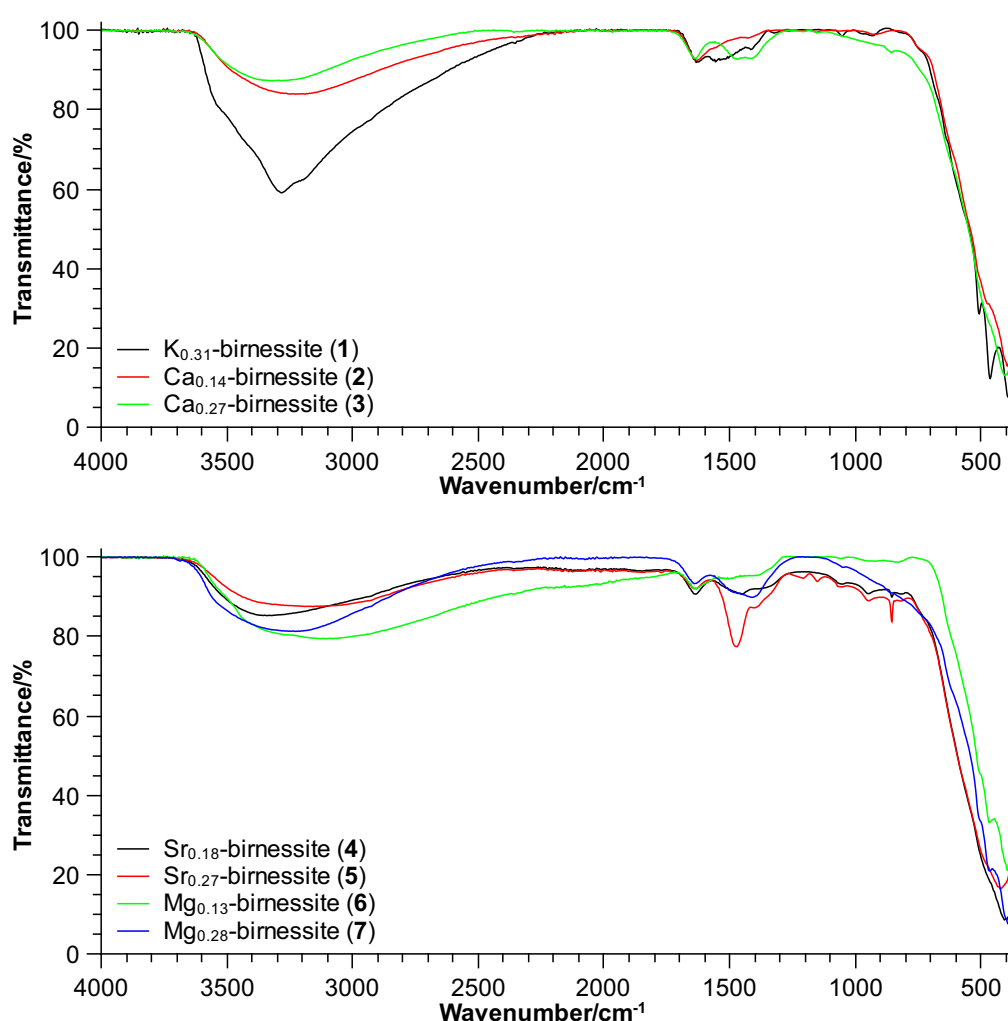


**Figure 6.5.** ATR IR spectra of **1-7** showing features typical for birnessites: bands that can be assigned to a relatively high content of bound water and hydroxide moieties bound to intercalated cations ( $3600\text{--}2500\text{ cm}^{-1}$ ,  $1800\text{--}1200\text{ cm}^{-1}$ ) as well as to Mn–O vibrations ( $< 700\text{ cm}^{-1}$ ). The broad shape of the bands is indicating that the oxides' structures are poorly ordered.

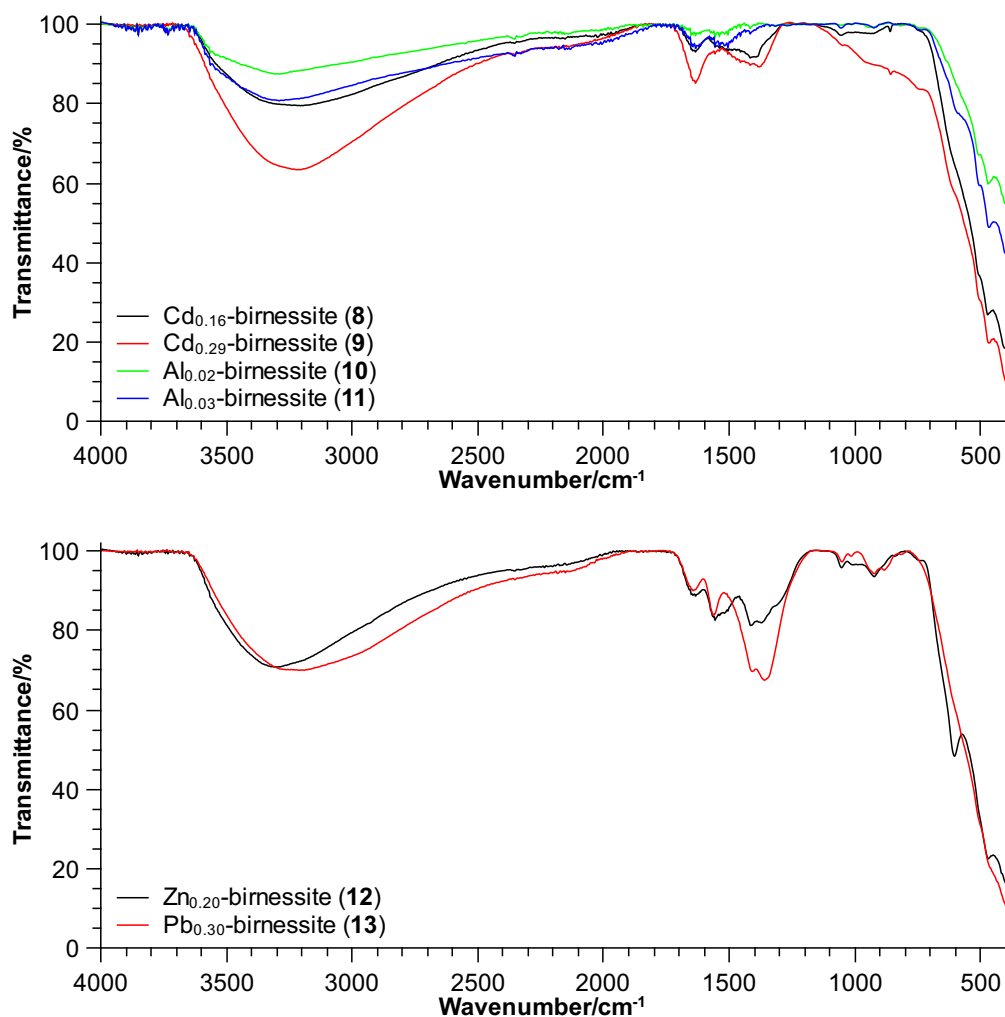


**Figure 6.6.** ATR IR spectra of **8-13** showing features typical for birnessites: bands that can be assigned to a relatively high content of bound water and hydroxide moieties bound to intercalated cations ( $3600\text{-}2500\text{ cm}^{-1}$ ,  $1800\text{-}1200\text{ cm}^{-1}$ ) as well as to Mn–O vibrations ( $< 700\text{ cm}^{-1}$ ). The broad shape of the bands is indicating that the oxides' structures are poorly ordered.

## 6.2 M-birnessites prepared by ion exchange

In an alternative approach for the synthesis of M-birnessites of different compositions, a Ca-buserite was prepared as a precursor which was subsequently used in ion exchange experiments (for details see section 9.1.2). The Ca-buserite was prepared following the route described by Luo *et al.*<sup>[217]</sup> After a washing step, portions of the Ca-buserite slurry were suspended and stirred in solutions containing  $\text{Ca}^{2+}$ ,  $\text{Mn}^{2+}$ ,  $\text{Zn}^{2+}$ ,  $\text{Fe}^{2+}$  and  $\text{Fe}^{3+}$ , respectively, in order to cause a cation exchange (Figure 6.7). This part of the project was carried out by Thorben Reinert in scope of an internship.<sup>[243]</sup>

In order to investigate if it is possible to incorporate redox active metal ions in the M-birnessite structure and to study their influence on the activity in water-oxidation catalysis, we decided to use  $\text{Mn}^{2+}$ ,  $\text{Fe}^{2+}$  and  $\text{Fe}^{3+}$  in the ion exchange step. Additionally, the redox inert cations  $\text{Ca}^{2+}$  and  $\text{Zn}^{2+}$  were used as a reference. In the following, the prepared materials are termed as  $\text{Ca}_{\text{ex}}^{2+}$ -birnessite (**14**),  $\text{Mn}_{\text{ex}}^{2+}$ -birnessite (**15**),  $\text{Zn}_{\text{ex}}^{2+}$ -birnessite (**16**),  $\text{Fe}_{\text{ex}}^{2+}$ -birnessite (**17**) and  $\text{Fe}_{\text{ex}}^{3+}$ -birnessite (**18**), the index *ex* is indicating that these oxides were prepared from ion exchange experiments.

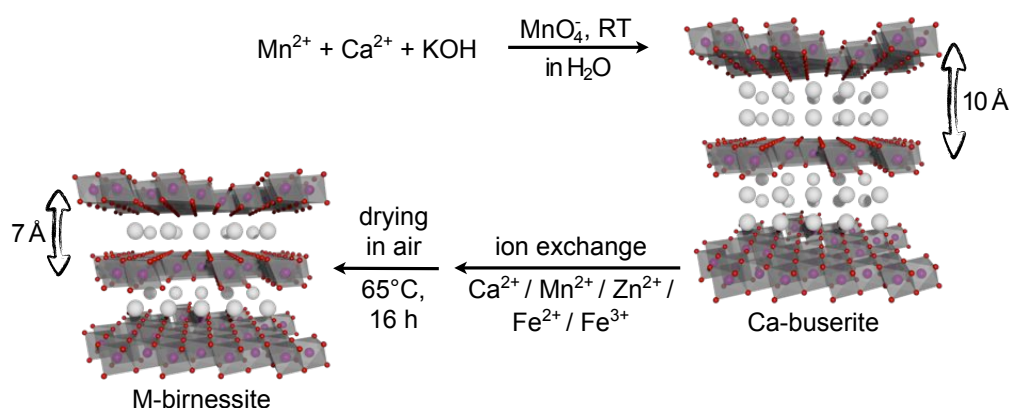


**Figure 6.7.** Scheme for the synthesis of oxides **14-18**. Following the route described by Luo *et al.*, a solution of  $\text{Mn}^{2+}$  and  $\text{Ca}^{2+}$  ions was added to aqueous KOH resulting in the formation of a suspension of  $\text{Mn}(\text{OH})_2$  in  $\text{H}_2\text{O}$ . By the addition of a  $\text{MnO}_4^-$  solution,  $\text{Mn}(\text{OH})_2$  was oxidized in the presence of  $\text{Ca}^{2+}$  to obtain the Ca-buserite precursor. After a washing step, the Ca-buserite slurry was suspended in the solution for the ion exchange step and stirred overnight. The resulting precipitates were dried to yield the respective M-birnessites.

### Analysis of the oxide compositions

The composition of the products obtained from ion exchange was analyzed by AAS and EDX in order to determine the manganese content (Table A.6) and the molar metal ion ratios (Table 6.3), respectively. The EDX analysis of the ion exchange products is showing that the ions used to substitute  $\text{Ca}^{2+}$  are present in the obtained materials. In contrast to the directly prepared M-birnessites (**1-13**), no potassium ions originating from the KOH base were remaining in the oxide structures of **14-18**. Nevertheless, ion exchange was not successful in all attempts.

In case of  $\text{Ca}_{\text{ex}}^{2+}$ -birnessite **14**, the presence of Ca as well as of Mn ions was detected in a Ca:Mn molar ratio of 0.30. Of course it can not be determined in which reaction step the  $\text{Ca}^{2+}$  ions were incorporated into the birnessite's structure. In the synthesis, a Ca:Mn ratio of 0.29 was employed. So, in the ion exchange step  $\text{Ca}^{2+}$  has probably

**Table 6.3. Metal ion ratios (per Mn) of 14-18 as determined by EDX. (243)**

Compound		K <sup>+</sup>	Ca <sup>2+</sup>	M <sub>exchanged</sub> <sup>2+/3+</sup>	Mn	M <sub>total</sub> /Mn
Ca <sub>ex</sub> -birnessite <sup>a</sup>	(14)	—	0.30	—	1	0.30
Mn <sub>ex</sub> -oxide <sup>b,c</sup>	(15)	—	4 · 10 <sup>-3</sup>	—	1	—
Zn <sub>ex</sub> -birnessite	(16)	—	0.02	0.78 (Zn <sup>2+</sup> )	1	0.80
Fe <sub>ex</sub> <sup>2+</sup> -oxide <sup>c</sup>	(17)	—	—	144.17 (Fe <sup>2+</sup> )	1	144.17
Fe <sub>ex</sub> <sup>3+</sup> -birnessite	(18)	—	0.01	0.84 (Fe <sup>3+</sup> )	1	0.85

<sup>a</sup> As the ion exchange experiments were carried out using a previously synthesized Ca-buserite, it is not possible to distinguish previously intercalated Ca<sup>2+</sup> or exchanged Ca<sup>2+</sup> ions. <sup>b</sup> It is not possible to get information on intercalated Mn ions from EDX data. Thus, the ratio of intercalated Mn ions to those of the MnO<sub>6</sub> layers can not be given here. <sup>c</sup> Further analysis of **15** and **17** showed that the Mn-oxide phase was dissolved during the ion exchange experiment and other oxide phases have been formed.

been substituted (by other Ca<sup>2+</sup> ions), but the total amount of incorporated Ca<sup>2+</sup> ions was not affected. In Zn<sub>ex</sub><sup>2+</sup>-birnessite **16**, only residues of Ca<sup>2+</sup> ions are present and a Zn:Mn molar ratio of 0.78 has been determined. The low amount of Ca<sup>2+</sup> and the high amount of Zn<sup>2+</sup> in the product indicates that ion exchange was successful. The EDX analysis of Fe<sub>ex</sub><sup>3+</sup>-birnessite **18** is showing a similar result. A low amount of Ca<sup>2+</sup> ions present in the structure and a Fe:Mn molar ratio of 0.84 is again pointing to a successful substitution of the calcium ions. The results are again in a good agreement with reported binding affinities of different cations to birnessites.<sup>[216,232-234]</sup>

In case of Mn<sub>ex</sub><sup>2+</sup>-oxide **15**, only traces of Ca<sup>2+</sup> were left. Compared to the other oxide materials, a higher Mn content was found in the AAS analysis (Table A.6). However, the substitution of Mn<sup>2+</sup> for Ca<sup>2+</sup> was not successful, as a further analysis of the resulting powders showed that in this experiment the birnessite structure is not retained, but rather transformed into other manganese oxide phases (see below and section 7.1). The same applies to Fe<sub>ex</sub><sup>2+</sup>-oxide **17**. Here, no Ca<sup>2+</sup> was found to be left in the product. Additionally, a Fe:Mn molar ratio of about 144 is clearly showing that the buserite phase has been dissolved and an iron oxide was most likely formed instead (see below and section 7.1).

### Particle shape, specific surface area and IR spectroscopy

Again, N<sub>2</sub> adsorption/desorption isotherms were recorded at -196 °C in order to determine the specific surface area of the oxide powder particles and their surface constitution (see section 9.3). The isotherms shown in Figure 6.8 are indicating that the prepared materials are also non- or macroporous (**14**, **15**, **16**, **18**, type II isotherms) and mesoporous (**17**, type IV isotherm), respectively. This is in good agreement with the results for M-birnessites **1-13** and is again pointing to the presence of textural pores.

The specific surface area of the oxides was calculated using BET theory and was found to vary between 70 m<sup>2</sup> · g<sup>-1</sup> for the Mn<sub>ex</sub><sup>2+</sup>-birnessite and 425 m<sup>2</sup> · g<sup>-1</sup> for the Fe<sub>ex</sub><sup>3+</sup>-birnessite (Table 6.4). The Ca<sub>ex</sub>- (**14**) and Zn<sub>ex</sub>-birnessite (**14**) are showing surface areas of 170 (**14**) and 115 m<sup>2</sup> · g<sup>-1</sup> (**16**). Fe<sub>ex</sub><sup>2+</sup>-oxide **17** exhibits a surface area of 265 m<sup>2</sup> · g<sup>-1</sup>.

It is not surprising that the phase transitions occurred in the ion exchange steps of **15** and **17** are resulting in a change of the specific surface area. Interestingly, also the specific surface areas determined for **14**, **16** and **18** are differing greatly, even though ion exchange was successful in these cases. These results are indicating that the ion exchange reaction is influencing the morphology of the prepared particles, even if no redox active metal cations are incorporated in the structure and no major structural changes can be observed.

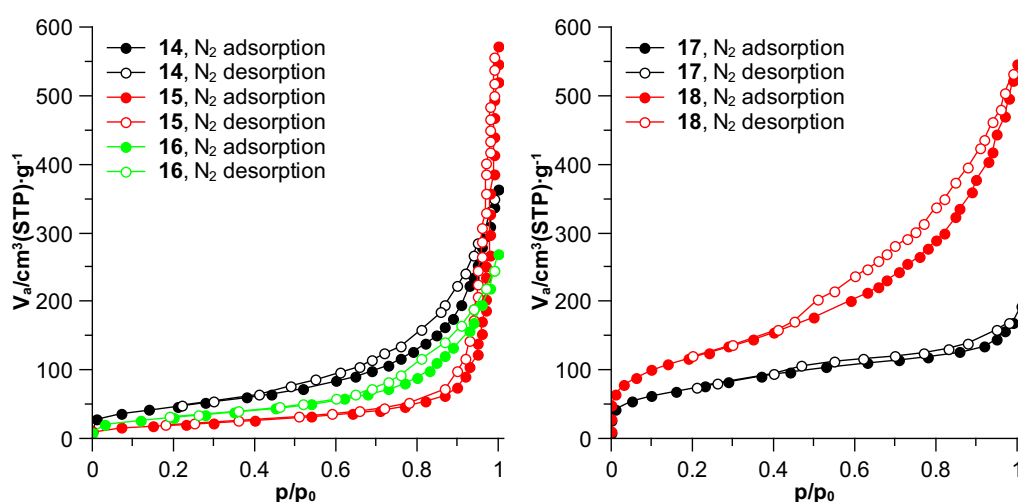


**Figure 6.8.**  $N_2$  adsorption/desorption isotherms of  $Ca_{ex}$ -birnessite (**14**),  $Mn_{ex}$ -oxide (**15**) and  $Zn_{ex}$ -birnessite (**16**) (left) as well as  $Fe_{ex}^{2+}$ -oxide (**17**) and  $Fe_{ex}^{3+}$ -birnessite (**18**) (right). The isotherms were recorded at  $-196\text{ }^\circ\text{C}$  after activation of the oxide samples at  $120\text{ }^\circ\text{C}$  for 2 h. The adsorption hysteresis of the isotherm of **18** right is indicating that mesoporous textural pores are present, while the other isotherms are typical for nonporous or macroporous materials.

**Table 6.4. Surface areas ( $S_{BET}$ ) of oxides 14-18. <sup>(243)</sup>**

Compound	Surface area/ $m^2 \cdot g^{-1}$
$Ca_{ex}$ -birnessite ( <b>14</b> )	170
$Mn_{ex}$ -oxide ( <b>15</b> )	70
$Zn_{ex}$ -birnessite ( <b>16</b> )	115
$Fe_{ex}^{2+}$ -oxide ( <b>17</b> )	265
$Fe_{ex}^{3+}$ -birnessite ( <b>18</b> )	425

Numbers given in the table are rounded  $S_{BET}$  values obtained from nitrogen adsorption/desorption isotherms.

The ATR IR spectra of the ion exchange products **14-18** are giving insights into some structural details of the materials (Figure 6.9). As described above, the composition of  $\text{Ca}_{\text{ex}}$ -birnessite **14**,  $\text{Zn}_{\text{ex}}$ -birnessite **16** and  $\text{Fe}_{\text{ex}}^{3+}$ -birnessite **18** is indicating that the ion exchange step followed by drying under mild conditions was resulting in the formation of M-birnessites. The IR spectra of **14**, **16** and **18** confirm these results, as the expected features for layered manganese oxides were detected. Broad bands in the region of  $3600\text{ cm}^{-1}$  to  $2500\text{ cm}^{-1}$  and around  $1500\text{ cm}^{-1}$  wavenumbers, assigned to  $\text{H}_2\text{O}$  molecules and OH moieties bound to interlayer cations are present. Also extensive, but poorly resolved bands below  $700\text{ cm}^{-1}$ , assigned to Mn–O lattices vibrations can be found. Bands characteristic for tunneled oxides are absent. Furthermore, the broad and poorly resolved bands are indicating a low degree of order of the oxide structures of **14**, **16**, **17** and **18**.

Interestingly, the IR spectrum of  $\text{Fe}_{\text{ex}}^{2+}$ -oxide **17**, of which the found composition is clearly showing that virtually no manganese oxide phase is present after ion exchange, is showing relatively similar bands. The presence and the shape of these bands is indicating that the structure of **17** also contains birnessite-like structural elements. Krishnamurti and Huang reported that lepidocrocite,  $\gamma\text{-FeO(OH)}$ , can be found as a precipitation product formed in the presence of birnessites out of a solution containing  $\text{Fe}^{2+}$  ions.<sup>[244]</sup> They also demonstrated that the  $\text{Mn}^{4+}$  centers of the birnessite are reduced to  $\text{Mn}^{2+}$ . Lepidocrocite is formed of layers of  $\text{Fe}^{\text{III}}\text{O}_6$  octahedra which are interconnected by a network of hydrogen bonds between hydroxide layers.<sup>[245]</sup> Indeed, the recorded IR spectrum of **17** is similar to a spectrum of lepidocrocite found on the literature.<sup>[246]</sup>

In contrast, the IR spectrum of  $\text{Mn}_{\text{ex}}$ -oxide **15** features very sharp bands, completely different from those observed for birnessites. Thus, the spectrum is clearly demonstrating that a transition to another, relatively ordered, manganese oxide phase occurred during the synthesis. A comparison with several IR spectra of various manganese oxides found in the literature resulted in the identification of the prepared material as manganite.<sup>[235]</sup> Manganite is one of the polymorphs of  $\text{MnO(OH)}$  with Mn in the oxidation state +III, showing a similar crystal structure to pyrolusite.<sup>[216,247]</sup> Consequently, the structure is built of chains of edge-sharing  $\text{MnO}_6$  octahedra which are interconnected in a corner-sharing pattern (*cf.* section 4.2.2 and Figure 4.5). In this structure, every second  $\mu\text{-O}^{2-}$  ligand is replaced by  $\mu\text{-OH}^-$ .<sup>[216]</sup>

The combined analysis by EDX and IR spectroscopy is in good agreement with results reported in the literature. Birnessites are able to act as an oxidant and if this is the case the  $\text{Mn}^{4+}$  centers of the manganese oxide layers are reduced to  $\text{Mn}^{2+}$ .<sup>[216,244,248,249]</sup> This means that Ca-buserite has most likely oxidized the  $\text{Mn}^{2+}$  and  $\text{Fe}^{2+}$  ions, respectively, during the ion exchange step of the preparation of  $\text{Mn}_{\text{ex}}$ -oxide **15** and  $\text{Fe}_{\text{ex}}^{2+}$ -oxide **17**. Thereby it can be explained how  $\text{MnO(OH)}$  and  $\text{FeO(OH)}$  phases were formed in these reactions.

These results are demonstrating that the synthesis of birnessites containing intercalated redox active metal ions of a reduced state cannot be achieved via ion exchange as redox reactions with these ions occur instead.

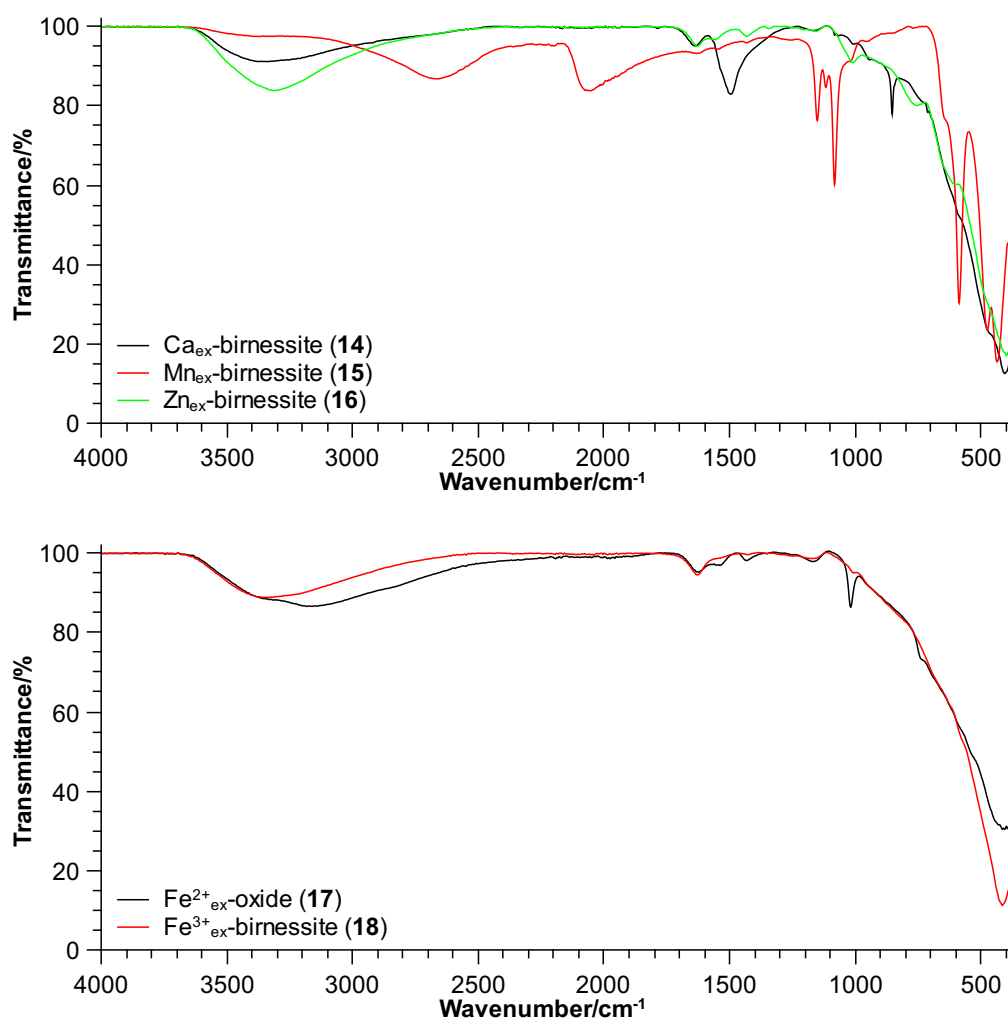


**Figure 6.9.** ATR IR spectra of birnessites **14-18**. **14**, **16** and **18** are showing bands that can be assigned to a relatively high content of bound water ( $3600\text{-}2500\text{ cm}^{-1}$ ), the presence of OH-groups ( $1800\text{-}1200\text{ cm}^{-1}$ ) and to Mn–O vibrations ( $< 700\text{ cm}^{-1}$ ). The similar bands in the IR spectrum of **17** are indicating that similar features may also be present in the formed Fe-oxide which is most likely lepidocrocite,  $\gamma\text{-FeO(OH)}$ .<sup>(246)</sup> The spectrum of **15** is clearly different, indicating that another, more ordered Mn-oxide phase has been formed under the applied reaction conditions, which is most likely manganite,  $\gamma\text{-MnO(OH)}$ .<sup>(235)</sup>

### 6.3 K/Ca-birnessites of increasing $\text{Ca}^{2+}$ concentration

In order to study the influence of the amount of  $\text{Ca}^{2+}$  ions on the birnessite particles' morphology and on the catalytic activity in water-oxidation in more detail, a set of K/Ca-birnessites was synthesized with an increasing  $\text{Ca}^{2+}$  ion concentration (Figure 6.10). To prepare this set of K/Ca-birnessites (**19-29**), the synthesis was carried out according to the route described above for the oxides **1-3** (cf. section 6.1). However, the concentration of  $\text{Ca}^{2+}$  ions employed in the first reaction step was increased in a stepwise fashion beginning with no  $\text{Ca}^{2+}$  ions up to a  $\text{Ca}^{2+}:\text{Mn}^{2+}$  molar ratio of 1 (for details see section 9.1.3).

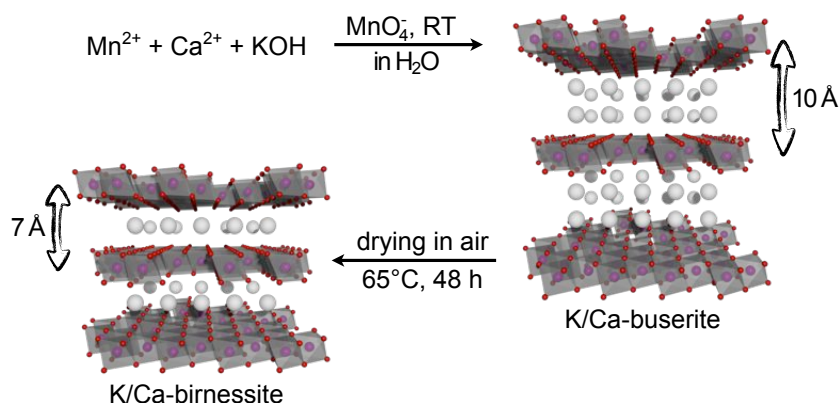


**Figure 6.10.** Scheme for the synthesis of K/Ca-birnessites **19-29**. Following the route described by Luo *et al.*, aqueous solutions containing  $\text{Mn}^{2+}$  ions as well as  $\text{Ca}^{2+}$  ions in increasing concentrations were added to aqueous  $\text{KOH}$ , resulting in the formation of a  $\text{Mn}(\text{OH})_2$  slurry. By the addition of  $\text{MnO}_4^-$ ,  $\text{Mn}(\text{OH})_2$  was oxidized in the presence of the additional cations, giving Ca-buserite precipitates. The Ca-buserite precipitates were then dried under mild conditions to yield Ca-birnessites. In these syntheses, the ripening step has been omitted.

### Analysis of the oxide compositions

Similar to the characterization of M-birnessites **1-18**, the composition of the K/Ca-birnessites **19-29** was again analyzed by AAS (Table A.7) and EDX (Table 6.5). As in section 6.1, the prepared materials are termed as K- (**19**) or Ca-birnessites (**20-29**) and the indices are giving the K/Ca:Mn molar ratio of the respective metal cation.

The synthesis carried out in the absence of  $\text{Ca}^{2+}$  ions was resulting in the formation of  $\text{K}_{0.28}$ -birnessite **19**. The addition of calcium ions in a  $\text{Ca}^{2+}:\text{Mn}_{\text{total}}$  ratio of 0.04 was leading to the incorporation of 0.04 Ca ions per Mn center of the oxide structure of **20**, thus  $\text{Ca}^{2+}$  is completely removed from the solution in this synthesis. A stepwise increase of the  $\text{Ca}^{2+}$  ion concentration in the syntheses was leading to the incorporation of an increasing amount of  $\text{Ca}^{2+}$  ions. In the syntheses of **21-25**,  $\text{Ca}^{2+}:\text{Mn}_{\text{total}}$  ratios of 0.07-0.22 were employed, increasing the  $\text{Ca}^{2+}$  amount in steps of 0.05 respective to the  $\text{Mn}^{2+}$  concentration (for details see Table 9.3). The Ca:Mn ratios found for oxides **21-25** were 0.08-0.21 and are thus corresponding well to these synthesis conditions (see Table 6.5) indicating again a near complete removal of  $\text{Ca}^{2+}$  from solution during buserite formation.

To prepare the Ca-birnessites **26-29**, the  $\text{Ca}^{2+}$  share was increased even further in steps of 0.10 (**26**, **27**) and 0.25 (**28**, **29**), respectively, giving molar  $\text{Ca}^{2+}:\text{Mn}_{\text{total}}$  ratios of 0.29-0.73. Even at these higher concentrations, the incorporated amount of calcium ions is well corresponding to the metal ion ratios employed in the syntheses, yielding  $\text{Ca}_{0.28}$ - (**26**),  $\text{Ca}_{0.36}$ - (**27**),  $\text{Ca}_{0.54}$ - (**28**) and  $\text{Ca}_{0.67}$ -birnessite (**29**).

On the contrary to the composition of the M-birnessites **1-9**, no trend can be observed for the incorporation of  $\text{K}^+$  ions (*cf.* Table 6.1). Only at concentrations of  $\text{Ca}^{2+}$  ions of more than 0.28 per Mn, the amount of  $\text{K}^+$  found in the oxides **19-29** is significantly decreased. This effect may be explained by changes in the processing of the materials during the syntheses. In case of birnessites **1-7**, the precipitates were filtered off and washed, while **19-29** were centrifuged and resuspended for washing (*cf.* sections 9.1.1 and 9.1.3). Thus, the amount of monovalent metal ions, intercalated in between the

**Table 6.5. Metal ion ratios (per Mn) of 19-29 as determined by EDX.**

		K <sup>+</sup>	Ca <sup>2+</sup>	Mn	M <sub>total</sub> /Mn
K <sub>0.28</sub> -birnessite	(19)	0.28	—	1	0.28
Ca <sub>0.04</sub> -birnessite	(20)	0.33	0.04	1	0.37
Ca <sub>0.08</sub> -birnessite	(21)	0.28	0.08	1	0.36
Ca <sub>0.10</sub> -birnessite	(22)	0.46	0.10	1	0.56
Ca <sub>0.15</sub> -birnessite	(23)	0.46	0.15	1	0.61
Ca <sub>0.17</sub> -birnessite	(24)	0.40	0.17	1	0.57
Ca <sub>0.21</sub> -birnessite	(25)	0.21	0.21	1	0.41
Ca <sub>0.28</sub> -birnessite	(26)	0.22	0.28	1	0.50
Ca <sub>0.36</sub> -birnessite	(27)	0.10	0.36	1	0.46
Ca <sub>0.54</sub> -birnessite	(28)	0.03	0.54	1	0.57
Ca <sub>0.67</sub> -birnessite	(29)	0.03	0.67	1	0.70

birnessite layers may rather be influenced by the washing step during the synthesis than by other cations present in the structure.

However, the results are showing that the composition of the oxides can be regulated by the synthesis conditions, even under higher Ca<sup>2+</sup> concentrations. The Ca:Mn molar ratios found in the oxides are well corresponding to the employed synthesis conditions.

### Particle shape, specific surface area and IR spectroscopy

In order to investigate the influence of the variation in the Ca<sup>2+</sup> ion concentration on the morphology of the prepared K/Ca-birnessites **19-29**, SEM images of the oxide particles of **19**, **22**, **25** and **29** were taken at 2000x and 100 000x magnification (Figure 6.11). The SEM images at 2000x magnification are showing a trend similar to that observed for the K<sub>0.31</sub>- (**1**), Ca<sub>0.14</sub>- (**2**) and Ca<sub>0.27</sub>-birnessites (**3**) described above (*cf.* section 6.1, Figure 6.3), as the formation of smaller particles can be observed with an increasing concentration of Ca<sup>2+</sup> ions present in the oxide structures.

The largest and most defined particles can be found for K<sub>0.28</sub>-birnessite **19**, albeit with an inhomogeneous particle size distribution ranging from about 100 μm down to the nanometer scale (Figure 6.11, *a, b*). In a comparison of the SEM images, the Ca<sub>0.10</sub>-birnessite **22** particles are apparently smaller, showing a relatively homogeneous size distribution of about 1-10 μm (Figure 6.11, *c*). At a larger magnification, the particles of **22** are showing a ragged surface morphology (Figure 6.11, *d*). With a further increase of the Ca<sup>2+</sup> ion concentration, even smaller particles with a homogeneous size distribution are formed as shown by the images of Ca<sub>0.21</sub>- (**25**) and Ca<sub>0.67</sub>-birnessites (**29**) (Figure 6.11, *e, g*). At higher magnification, the ragged structuring of the particle surface can also be observed for Ca<sub>0.21</sub>-birnessite **25** (Figure 6.11, *f*). The Ca<sub>0.67</sub>-birnessite particles are not showing this ragged pattern but a texture on the nanometer scale (Figure 6.11, *h*).

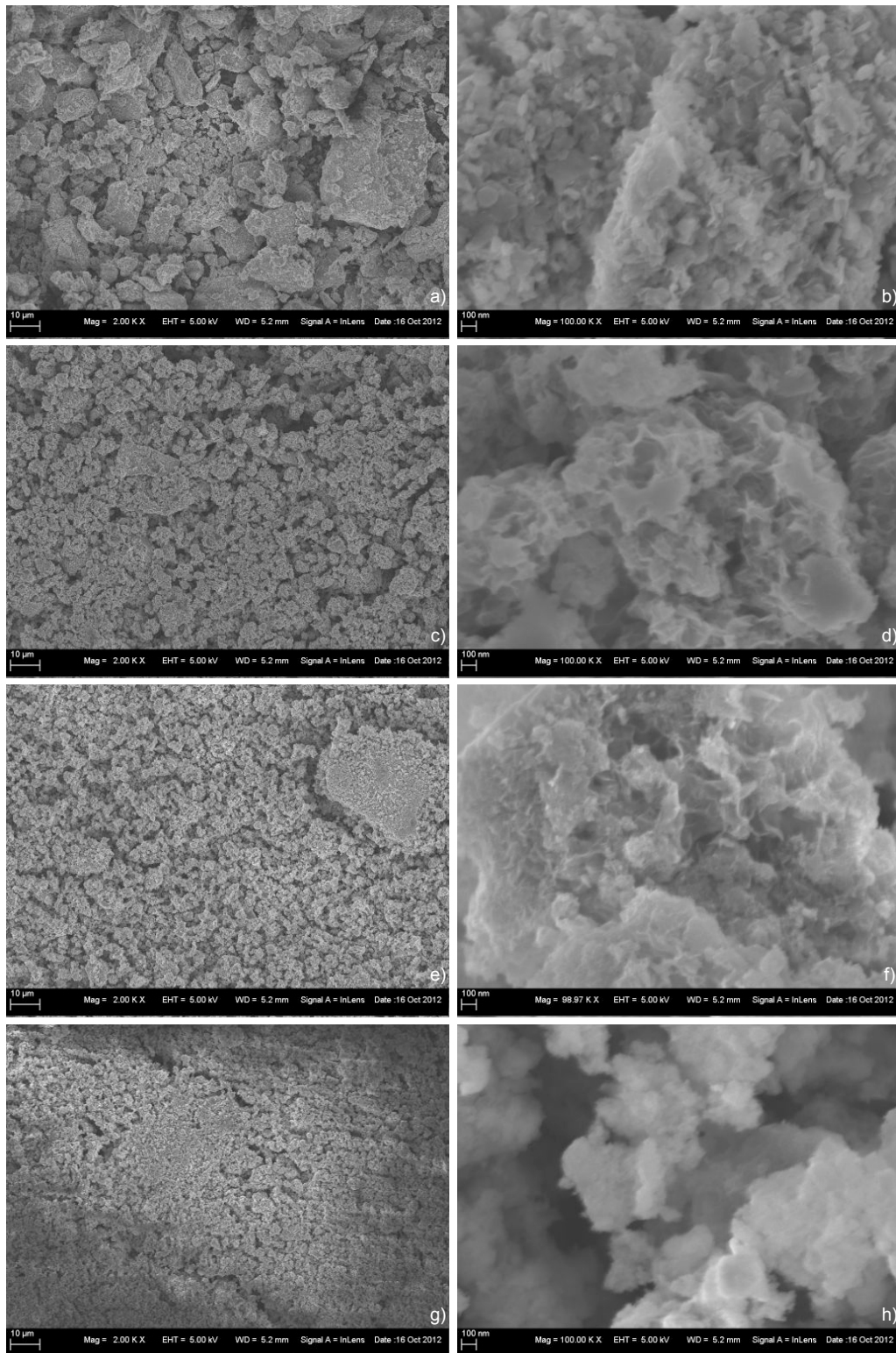


**Figure 6.11.** SEM images of  $\text{K}_{0.28}$ - (19, a, b),  $\text{Ca}_{0.10}$ - (22, c, d),  $\text{Ca}_{0.21}$ - (25, e, f) and  $\text{Ca}_{0.67}$ - birnessites (29, g, h) at 2000x (left) and 100000x magnification (right). With increasing  $\text{Ca}^{2+}$  ion concentrations intercalated in the birnessites' structure, smaller particles with a more homogeneous size distribution are formed.

In order to analyze the influence of the increasing  $\text{Ca}^{2+}$  ion concentrations of birnessites **19-29** on the specific surface and the porosity of the materials,  $\text{N}_2$  adsorption/desorption isotherms were measured at  $-196\text{ }^\circ\text{C}$  (see section 9.3).

In Figure 6.12, the isotherms of  $\text{K}_{0.28}$ -birnessite **19** and  $\text{Ca}_{0.10}$ -birnessite **22** (*left*) as well as  $\text{Ca}_{0.21}$ -birnessite **25** and  $\text{Ca}_{0.67}$ -birnessite **29** (*right*) are shown. As discussed for the other isotherms presented above, the curves are indicating that the materials are non- or macroporous (**29**, type II isotherm) or mesoporous as an adsorption hysteresis can be observed (**19**, **22**, **25**, type IV isotherm). Thus, textural pores may be present.

The specific surface areas determined according to the BET theory are well corresponding to the observations from the SEM images. With exceptions of **22**, **23** and **29**, the specific surface area of the oxides is continuously growing with increasing  $\text{Ca}^{2+}$  ion concentrations. Even the outliers are in the expected range as  $\text{Ca}_{0.10}$ - (**22**) and  $\text{Ca}_{0.15}$ -birnessites (**23**) exhibit relatively low calcium concentrations and low surface areas, while the  $\text{Ca}_{0.67}$ -birnessite (**29**) with a high calcium concentration is showing a relatively large surface area. Thus, a correlation of the surface area and the amount of  $\text{Ca}^{2+}$  ions incorporated in the oxide structures can be derived from the presented data.

Ca-birnessites **19-29** were also analyzed using IR spectroscopy. The ATR IR spectra shown in Figure 6.13 show broad bands in the region of wavenumbers of  $3600\text{ cm}^{-1}$  to  $2500\text{ cm}^{-1}$  and around  $1500\text{ cm}^{-1}$  as well as extensive, but poorly resolved bands below  $700\text{ cm}^{-1}$ . Thus, the characteristic spectral features expected for birnessites are again present: water molecules and hydroxide moieties bound in the interlayer space as well as Mn–O lattices. Bands characteristic for tunneled oxides are absent. The IR spectra are thus indicating that the prepared materials of this set are, as in the syntheses before, disordered phyllomanganates of the birnessite family.<sup>[234–242]</sup>

Furthermore, the presence of additional bands in the region of  $1200\text{ cm}^{-1}$  to  $700\text{ cm}^{-1}$  is indicating that features are present in these materials, which cannot be assigned to structural motifs of Ca-birnessites. As these bands are relatively weak and also overlap with the IR bands of the birnessite structure, a classification of the additional motifs is not feasible on the basis of these spectra. However, a possible scenario is that a significant amount of  $\text{CO}_2$  from air is dissolved in the alkaline reaction mixture during the extended synthesis time, probably resulting in the formation of small amounts of  $\text{CaCO}_3$ . Based on the recorded powder XRDs, an advanced analysis of the additional structural motifs will be given (*cf.* section 7.1).

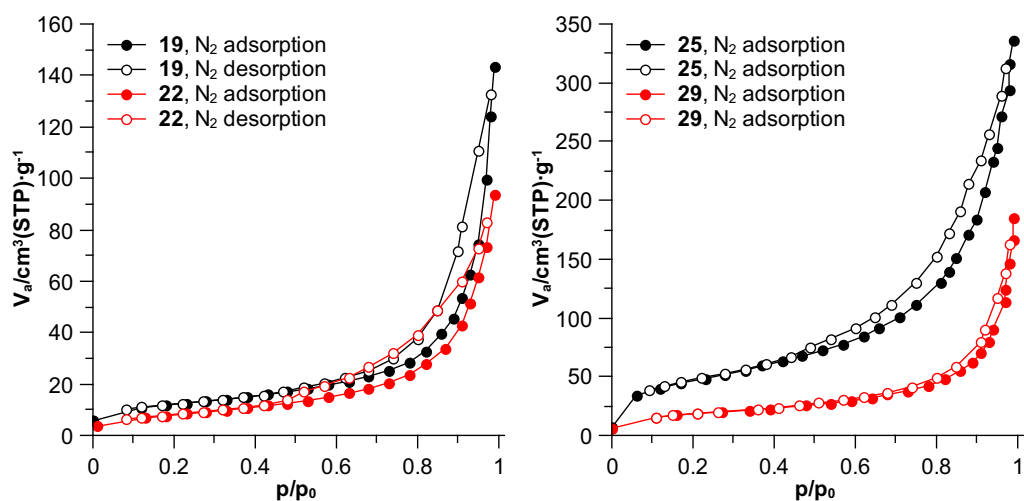


**Figure 6.12.**  $\text{N}_2$  adsorption/desorption isotherms of  $\text{K}_{0.28}$ -birnessite **19** and  $\text{Ca}_{0.10}$ -birnessite **22** (left) as well as  $\text{Ca}_{0.21}$ - (**25**) and  $\text{Ca}_{0.67}$ -birnessites (**29**) (right). The isotherms were recorded at  $-196\text{ }^\circ\text{C}$  after activation of the oxide samples at  $120\text{ }^\circ\text{C}$  for 2 h. The adsorption hystereses of the isotherms of **19**, **22** and **25** are indicating that mesoporous textural pores are present, while the isotherm of **29** is typical for a nonporous or macroporous materials.

**Table 6.6.** Surface areas of K/Ca-birnessites 19-29, determined by  $\text{N}_2$  adsorption/desorption.

Compound	Surface area/ $\text{m}^2 \cdot \text{g}^{-1}$
$\text{K}_{0.28}$ -birnessite ( <b>19</b> )	40
$\text{Ca}_{0.04}$ -birnessite ( <b>20</b> )	50
$\text{Ca}_{0.08}$ -birnessite ( <b>21</b> )	65
$\text{Ca}_{0.10}$ -birnessite ( <b>22</b> )	30
$\text{Ca}_{0.15}$ -birnessite ( <b>23</b> )	55
$\text{Ca}_{0.17}$ -birnessite ( <b>24</b> )	90
$\text{Ca}_{0.21}$ -birnessite ( <b>25</b> )	165
$\text{Ca}_{0.28}$ -birnessite ( <b>26</b> )	175
$\text{Ca}_{0.36}$ -birnessite ( <b>27</b> )	245
$\text{Ca}_{0.54}$ -birnessite ( <b>28</b> )	275
$\text{Ca}_{0.67}$ -birnessite ( <b>29</b> )	225

Numbers given in the table are rounded  $S_{\text{BET}}$  values obtained from nitrogen adsorption/desorption isothermes.

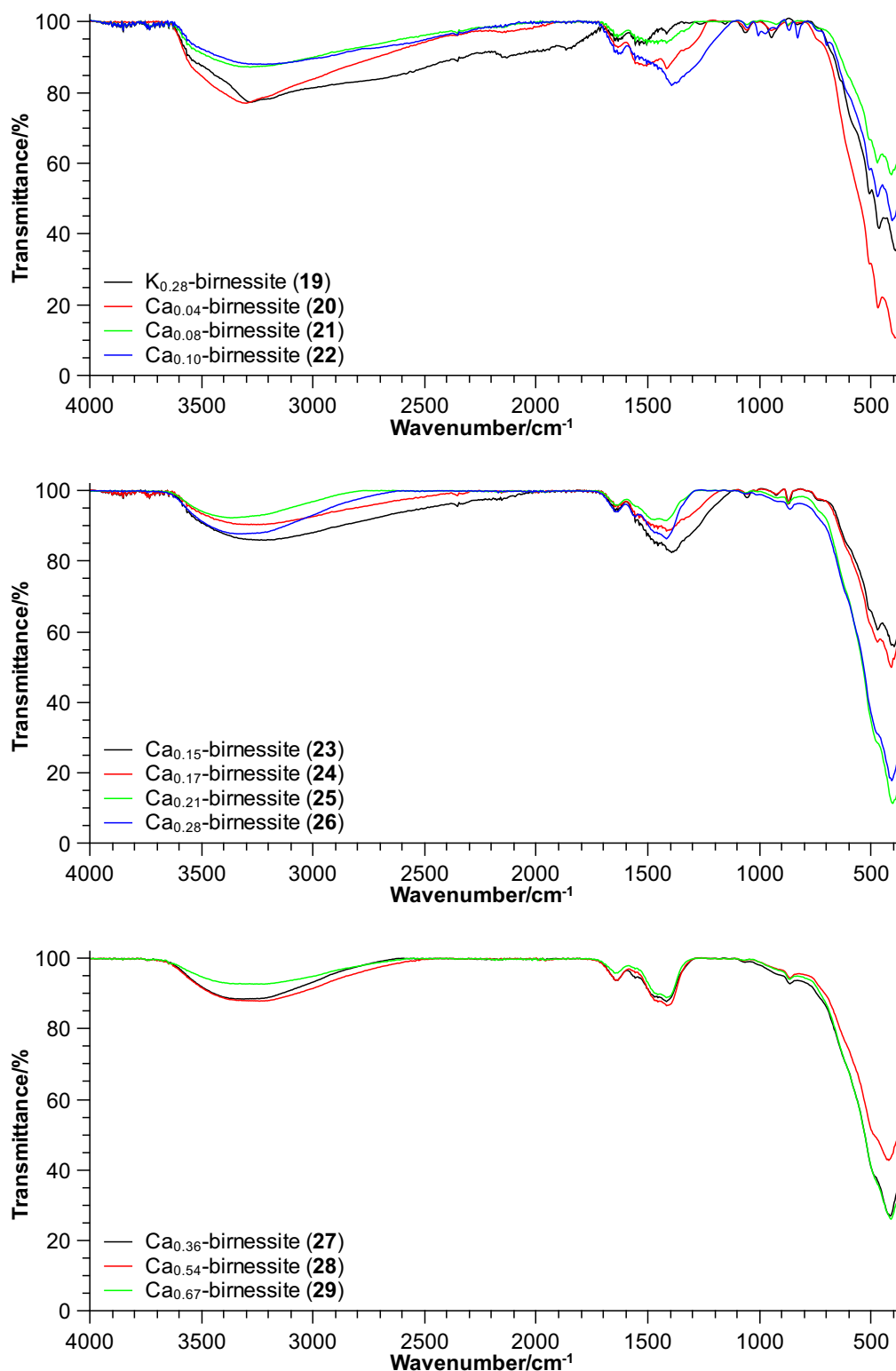


**Figure 6.13.** ATR IR spectra of **19-29** showing features typical for birnessites: bands that can be assigned to a relatively high content of bound water and hydroxide moieties bound to intercalated cations ( $3600\text{--}2500\text{ cm}^{-1}$ ,  $1800\text{--}1200\text{ cm}^{-1}$ ) as well as Mn–O vibrations ( $< 700\text{ cm}^{-1}$ ). The low sharpness of the bands is indicating that the oxides' structures are poorly ordered. Additional bands in the region of  $1200\text{ cm}^{-1}$  to  $700\text{ cm}^{-1}$  in some spectra are indicating the presence of other components.

## 6.4 Ca-birnessites with increasing ripening time

When Luo *et al.* presented their route to synthesize manganese oxides of the birnessite family, they also reported the preparation of uniform large size particles of about 10  $\mu\text{m}$  by extending the ripening time to 15 days.<sup>[217]</sup> Furthermore, they investigated the crystallization of birnessites and found a correlation between the ripening time and the crystallinity of the materials.<sup>[218]</sup>

In order to investigate the influence of the ripening time on the structure of Ca-birnessites and their ability to act as water-oxidation catalysts, a set of Ca-birnessites was prepared and ripened for periods of up to 10 days (for more details see section 9.1.4). Similar to the syntheses described above, a solution containing  $\text{Mn}^{2+}$  and  $\text{Ca}^{2+}$  was added to KOH, resulting in the precipitation of  $\text{Mn}(\text{OH})_2$ , which was subsequently oxidized using  $\text{KMnO}_4$ . The same Ca:Mn molar ratio as for the preparation of oxides **3** and **26** was used, but the ripening period was carried out from 0 to up to 240 hours (Figure 6.14). The period used to prepare the oxides **30-40** is in the following indicated as index in the notation of the respective Ca-birnessites.

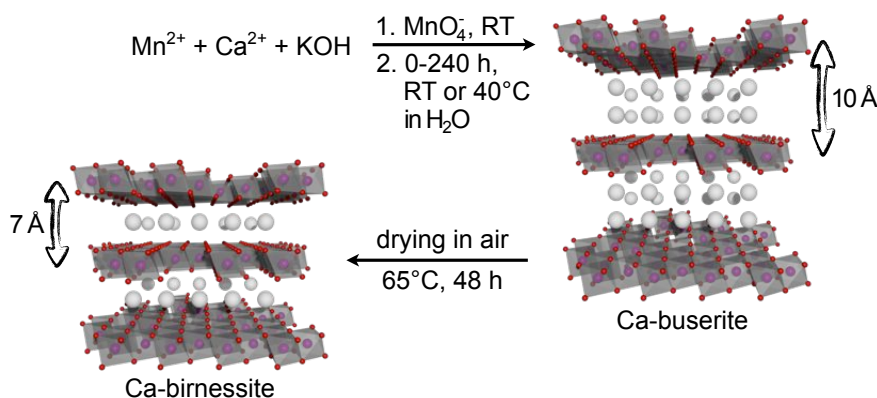


**Figure 6.14.** Scheme for the synthesis of Ca-birnessites **30-40**. Following the route described by Luo *et al.* an aqueous solution containing  $\text{Mn}^{2+}$  ions as well as  $\text{Ca}^{2+}$  ions was added to aqueous KOH, resulting in the formation of a  $\text{Mn}(\text{OH})_2$  slurry. By the addition of  $\text{KMnO}_4$ ,  $\text{Mn}(\text{OH})_2$  was oxidized, resulting in the formation of Ca-buserite precipitates. After a ripening period of 0 up to 240 h, the Ca-buserite precipitates were dried under mild conditions to yield Ca-birnessites.

### Analysis of the oxide compositions

The composition of the oxide materials **30-40** was again investigated by AAS and EDX in order to determine the manganese content (Table A.8) and the molar metal ion ratios, respectively (Table 6.7). Even though the synthesis conditions were kept constant apart from the ripening time, the composition of the prepared materials differs slightly.

For the synthesis of Ca-birnessites **30-40**, a Ca:Mn molar ratio of 0.29 was used. In the oxides, ratios of 0.19-0.28 were found. The K:Mn ratio also differs, showing values of 0.02 up to 0.30. As no trend can be derived from the presented data, the changes in ripening time are most likely not the reason for the variations of the composition of the prepared oxides. The variation of the K:Mn ratio in the oxides may be explained by the washing step, which is hard to carry out in an identical manner for each batch. But as the Ca:Mn ratio found in the other Ca-birnessites was well corresponding to the

**Table 6.7. Metal ion ratios (per Mn) of 30-40 as determined by EDX.**

Compound		K <sup>+</sup>	Ca <sup>2+</sup>	Mn	M <sub>total</sub> /Mn
Ca <sub>0h</sub> -birnessite	(30)	0.02	0.27	1	0.29
Ca <sub>1h</sub> -birnessite	(31)	0.04	0.24	1	0.28
Ca <sub>2h</sub> -birnessite	(32)	0.10	0.25	1	0.35
Ca <sub>4h</sub> -birnessite	(33)	0.03	0.26	1	0.29
Ca <sub>8h</sub> -birnessite	(34)	0.12	0.22	1	0.34
Ca <sub>12h</sub> -birnessite	(35)	0.30	0.24	1	0.54
Ca <sub>24h</sub> -birnessite	(36)	0.19	0.22	1	0.41
Ca <sub>48h</sub> -birnessite	(37)	0.11	0.21	1	0.32
Ca <sub>120h</sub> -birnessite	(38)	0.06	0.28	1	0.34
Ca <sub>168h</sub> -birnessite	(39)	0.12	0.19	1	0.31
Ca <sub>240h</sub> -birnessite	(40)	0.03	0.26	1	0.29

employed synthesis conditions, the relatively large deviation here can not be explained by different conditions of the washing step. Weighing errors in addition to errors of the determination of the metal ion ration can rather explain these variations. However, compared to the Ca-birnessites of which the preparation has been described above (2, 3, 14, 20-29), the oxides 30-40 all exhibit a medium amount of incorporated Ca<sup>2+</sup> ions.

### Particle shape, specific surface area and IR spectroscopy

For a further analysis of the prepared powders of the Ca-birnessites 30-40, SEM images and N<sub>2</sub> adsorption/desorption isotherms were recorded. The SEM images, taken at magnifications of 20 000x, are showing no significant difference between the particles of the distinct oxides (Figure 6.16). The shapes of the particles as well as their size distribution is inhomogeneous but relatively similar. The expected formation of more crystalline Ca-birnessites could not be observed from the SEM images.

It has to be noted that Luo *et al.* investigated buserites and birnessites with different additional ion types and concentrations, respectively, in comparison to those prepared here.<sup>[217,218]</sup> As parameters like particle size and particle size distribution are dependent on the birnessites' composition, the crystallinity of the particles may be affected as well by the composition and could thus explain why the elongated ripening period in this study was not leading to the formation of particles with a visibly changed shape or a more homogeneous size distribution.

The porosity and the specific surface areas of Ca-birnessites 30-40 were determined by N<sub>2</sub> adsorption/desorption isotherms, recorded at -196 °C (see section 9.3). In the isotherms (Figure 6.15), the appearance of a small hysteresis is again indicating the presence of textural pores, formed in between of aggregating particles. The specific surface areas were derived from the isotherms according to the BET theory.

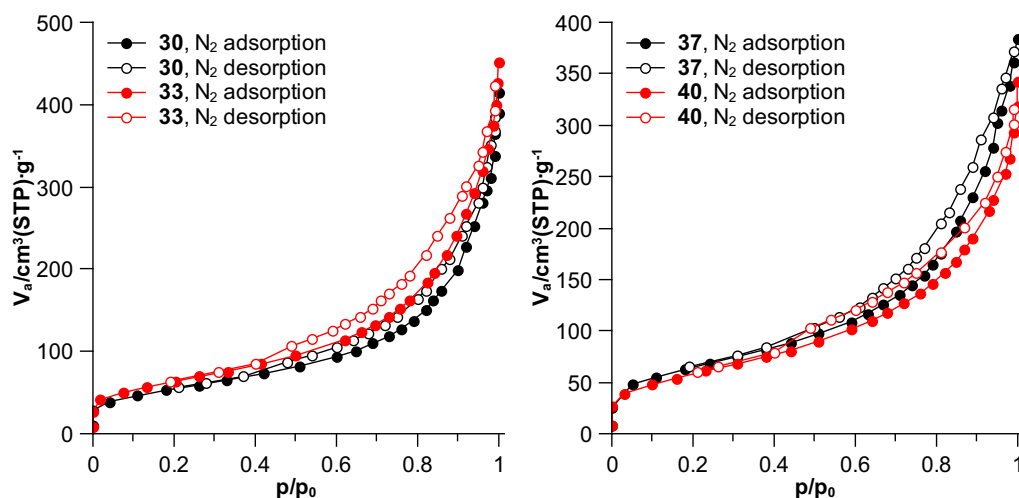


**Figure 6.15.** N<sub>2</sub> adsorption/desorption isotherms of Ca<sub>0h</sub>-birnessite **30** and Ca<sub>4h</sub>-birnessite **33** (*left*) as well as Ca<sub>48h</sub>-birnessite **37** and Ca<sub>240h</sub>-birnessite **40** (*right*). The isotherms were recorded at  $-196\text{ }^{\circ}\text{C}$  after activation of the oxide samples at  $120\text{ }^{\circ}\text{C}$  for 2 h. The adsorption hystereses of the isotherms are indicating that mesoporous textural pores are present.

**Table 6.8.** Surface areas ( $S_{\text{BET}}$ ) of M-birnessite, determined by N<sub>2</sub> adsorption/desorption.

Compound		Surface area/ $\text{m}^2 \cdot \text{g}^{-1}$
Ca <sub>0h</sub> -birnessite	(30)	200
Ca <sub>1h</sub> -birnessite	(31)	270
Ca <sub>2h</sub> -birnessite	(32)	220
Ca <sub>4h</sub> -birnessite	(33)	230
Ca <sub>8h</sub> -birnessite	(34)	180
Ca <sub>12h</sub> -birnessite	(35)	110
Ca <sub>24h</sub> -birnessite	(36)	175
Ca <sub>48h</sub> -birnessite	(37)	235
Ca <sub>120h</sub> -birnessite	(38)	265
Ca <sub>168h</sub> -birnessite	(39)	155
Ca <sub>240h</sub> -birnessite	(40)	215

Numbers given in the table are rounded  $S_{\text{BET}}$  values obtained from nitrogen adsorption/desorption isotherms.

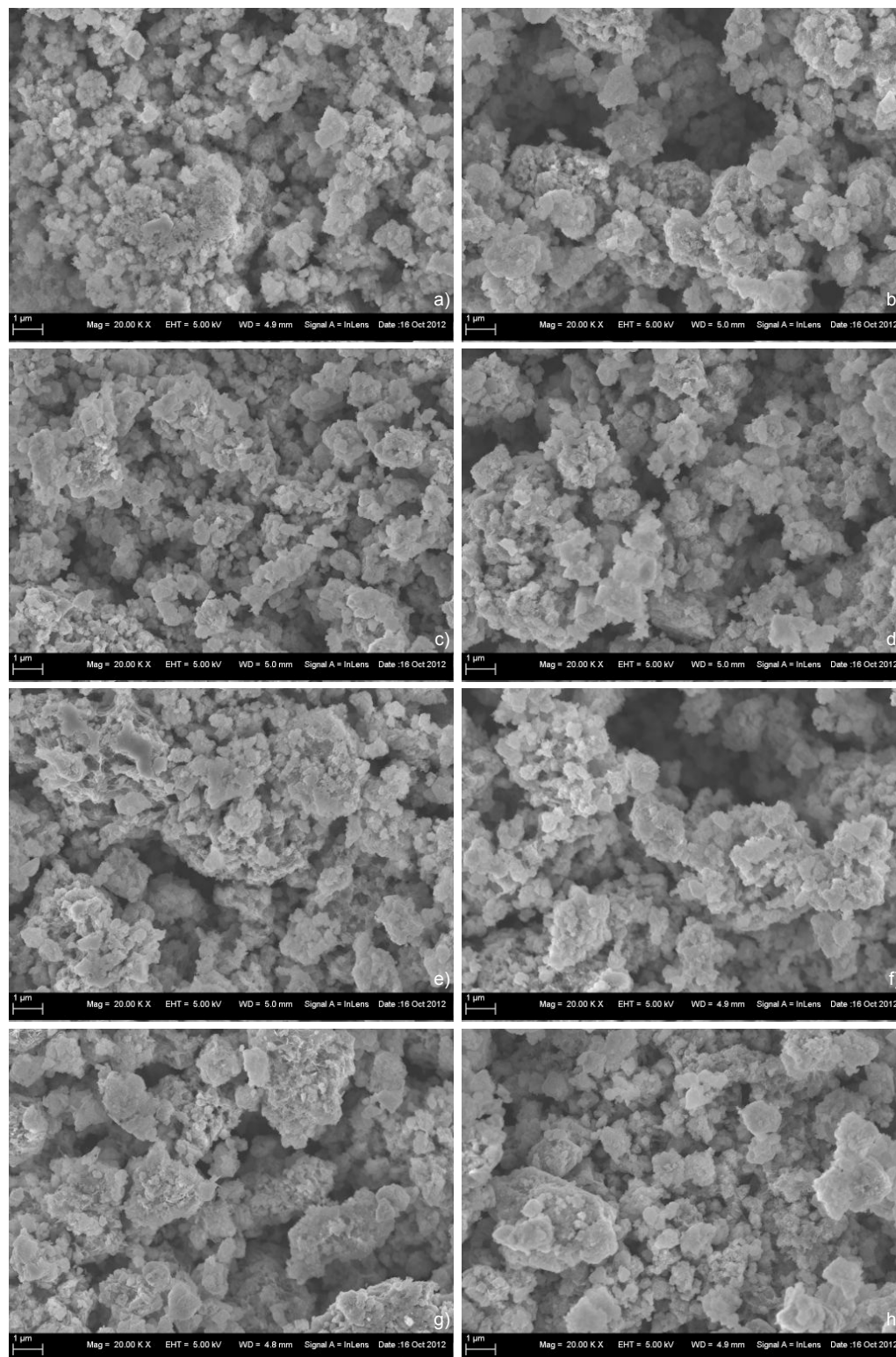
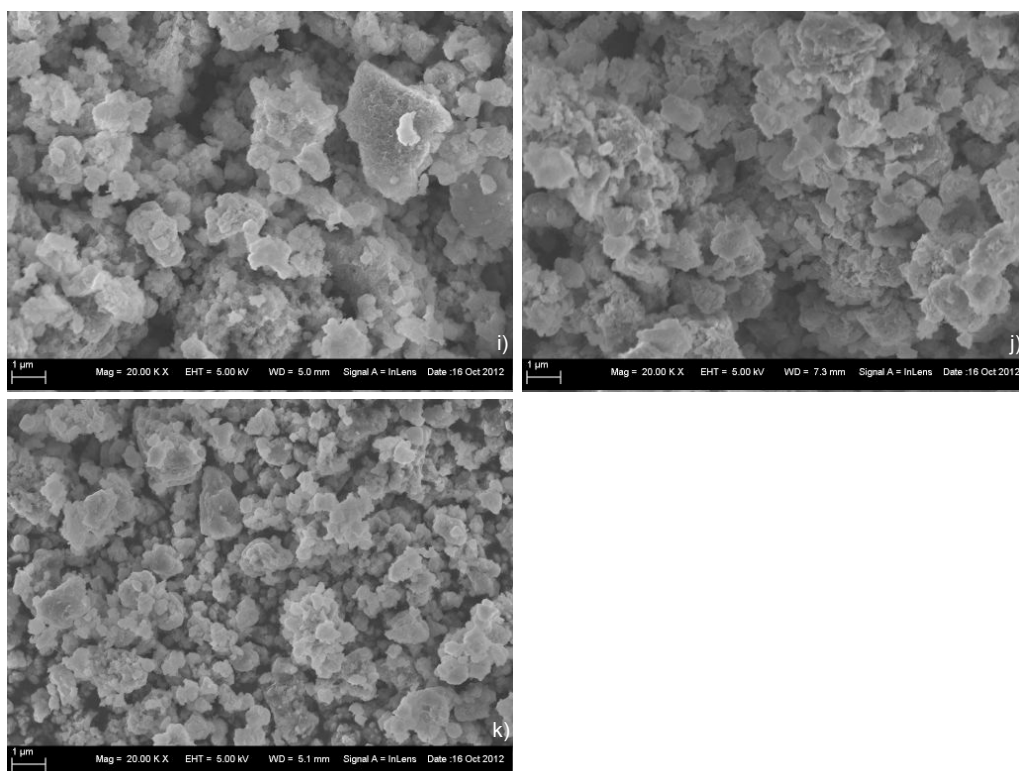


**Figure 6.16.** SEM images of  $\text{Ca}_{0\text{h}}^-$  (**30**, a),  $\text{Ca}_{1\text{h}}^-$  (**31**, b),  $\text{Ca}_{2\text{h}}^-$  (**32**, c),  $\text{Ca}_{4\text{h}}^-$  (**33**, d),  $\text{Ca}_{8\text{h}}^-$  (**34**, e),  $\text{Ca}_{12\text{h}}^-$  (**35**, f),  $\text{Ca}_{24\text{h}}^-$  (**36**, g),  $\text{Ca}_{48\text{h}}^-$ -birnessite (**37**, h),  $\text{Ca}_{120\text{h}}^-$  (**38**, i),  $\text{Ca}_{168\text{h}}^-$  (**39**, j) and  $\text{Ca}_{240\text{h}}^-$ -birnessite (**40**, k). No correlation between different ripening periods and particle shapes can be observed.



Continuation of Figure 6.16.

The values vary between  $110$  and  $270 \text{ m}^2 \cdot \text{g}^{-1}$  (Table 6.8). But also here, no trend correlated to the ripening time could be observed.  $\text{Ca}_{1\text{h}}$ -birnessite **31** exhibits the largest surface area of about  $270 \text{ m}^2 \cdot \text{g}^{-1}$ . As it was expected that more crystalline phases are formed with an increasing ripening time the surface areas of the following oxides should decrease. This can be observed when looking at the surface area of  $\text{Ca}_{2\text{h}}$ -birnessite **32** of  $220 \text{ m}^2 \cdot \text{g}^{-1}$ , but this tendency does not continue. With a surface area of about  $265 \text{ m}^2 \cdot \text{g}^{-1}$ , the  $\text{Ca}_{120\text{h}}$ -birnessite **38** shows the second largest value. On the contrary,  $\text{Ca}_{12\text{h}}$ -birnessite **35** exhibits the smallest surface area observed in this set of  $110 \text{ m}^2 \cdot \text{g}^{-1}$ .

Comparing the specific surface area of the Ca-birnessites **30-40** to their  $\text{Ca}^{2+}$  content, also no correlation is evident.  $\text{Ca}_{1\text{h}}$ -birnessite **31**, the oxide with the largest surface area and  $\text{Ca}_{12\text{h}}$ -birnessite **35**, the one with the smallest surface area are both containing  $0.24 \text{ Ca}^{2+}$  ions per Mn.  $\text{Ca}_{48\text{h}}$ -birnessite **37** and  $\text{Ca}_{168\text{h}}$ -birnessite **39** are both containing relatively small amounts of  $\text{Ca}^{2+}$  ions and are showing surface areas of  $235$  and  $155 \text{ m}^2 \cdot \text{g}^{-1}$ , respectively. Considering also the oxide's content of  $\text{K}^+$  ions, it is conspicuous that the materials showing the largest surface areas are containing only small amounts of  $\text{K}^+$ . The  $\text{Ca}_{12\text{h}}$ -birnessite **35** showing the smallest surface area is containing the highest amount of  $\text{K}^+$  ions with a K:Mn ratio of  $0.30$ . But on the other hand,  $\text{Ca}_{48\text{h}}$ -birnessite **37** and  $\text{Ca}_{168\text{h}}$ -birnessite **39** are containing similar amounts of  $\text{K}^+$  ions with quite different surface areas of  $235$  and  $155 \text{ m}^2 \cdot \text{g}^{-1}$ , respectively.

Furthermore, ATR IR spectra were recorded of Ca-birnessites **30-40**, showing the expected bands characteristic for  $\text{H}_2\text{O}$  and  $\text{OH}^-$  moieties as well as of Mn–O lattice vibrations of birnessites. Bands in the range of  $1200 \text{ cm}^{-1}$  to  $700 \text{ cm}^{-1}$  indicating the presence of additional structures can also be observed here (*cf.* sections 6.3 and 7.1).

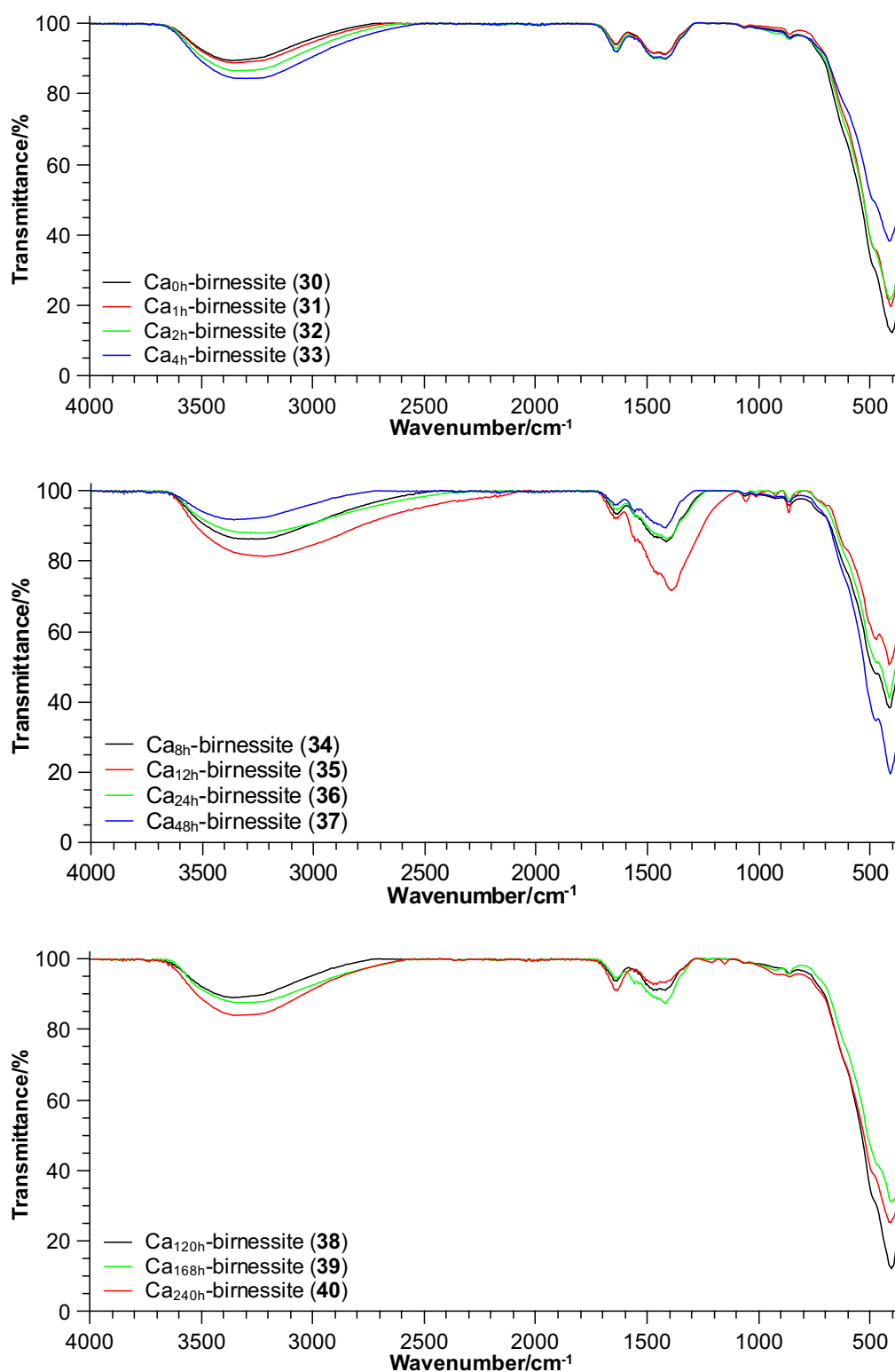


**Figure 6.17.** ATR IR spectra of **19-29** showing features typical for birnessites: bands that can be assigned to a relatively high content of bound water and hydroxide moieties bound to intercalated cations ( $3600\text{--}2500\text{ cm}^{-1}$ ,  $1800\text{--}1200\text{ cm}^{-1}$ ) as well as Mn–O vibrations ( $< 700\text{ cm}^{-1}$ ). The low sharpness of the bands is indicating that the oxides' structures are poorly ordered. Additional bands in the region of  $1200\text{ cm}^{-1}$  to  $700\text{ cm}^{-1}$  in some spectra are indicating the presence of another phase.

## 7 Elucidation of structural details

The chemical and physical analysis of the prepared materials 1-40 discussed in chapter 6 revealed a first overview of the composition of the oxide powders, of the primary structures and of the presence of additional structural motifs. However, at this point the analyses did not reveal details of the arrangement of the overall structure or of the individual motifs. So far, additional phases which were indicated in several IR spectra could not be identified, either.

To shed light on these topics, a more detailed analysis of the oxide powders was carried out by X-ray techniques. A qualitative phase analysis of oxides 1-40 was carried out via powder X-ray diffraction (XRD). Additionally, X-ray absorption spectroscopy (XAS) measurements were carried out by our collaboration partners, the group of Prof. Holger Dau from Freie Universität Berlin. XANES spectra allowed to determine the mean manganese oxidation state of selected M-birnessite samples (1-7) and the analysis of the EXAFS spectra provided information about structural details.

### 7.1 X-ray powder diffraction

In X-ray diffraction techniques, the bending of waves around small objects of the same dimension as the incident wavelength and the periodic order of atoms in a crystalline material are used to obtain informations on the structure of a sample on the atomic scale. The spectrum of X-ray radiation is comprising wavelengths comparable to atomic distances in solid state bodies. When a X-ray beam of such wavelengths is hitting a crystalline solid sample, the beam is reflected by the crystal's regular array of atoms, producing an individual diffraction pattern. The angle between the incident X-ray beam and the crystallographic planes of the sample is crucial for the occurrence of constructive and destructive interference between the waves scattered at the successive planes. Diffraction reflections with strong intensities can only be observed in case of constructive interference between the waves. The condition for this case is described in Bragg's law (eq. 7.1 and Figure 7.1).<sup>[250]</sup>

$$n\lambda = 2d \sin \theta \quad (7.1)$$

According to this equation, constructive interference occurs when the path difference ( $2d \sin \theta$ ) of the incident ray scattered at different planes is an integer of the wavelength ( $\lambda$ ,  $n$  is an integer given by the order). The path difference is defined by the distance of the scattering planes ( $d$ ) and the angle between the planes and the incident ray ( $\theta$ ).<sup>[250]</sup> Furthermore, the interference of the X-ray waves is influenced by the scattering power of individual atoms, which in first approximation is proportional to the element's electron count.<sup>[250]</sup>

So, if a crystal is irradiated with monochromatic X-ray beams, diffraction can be observed only at distinct angles given by the crystal lattice planes. By measuring angle dependent intensities of the diffracted beams in different crystal orientations, structural informations can be obtained from the diffraction data.<sup>[250]</sup> As the position and the type of the atoms in the lattice are influencing the X-ray diffraction, even two crystals with a

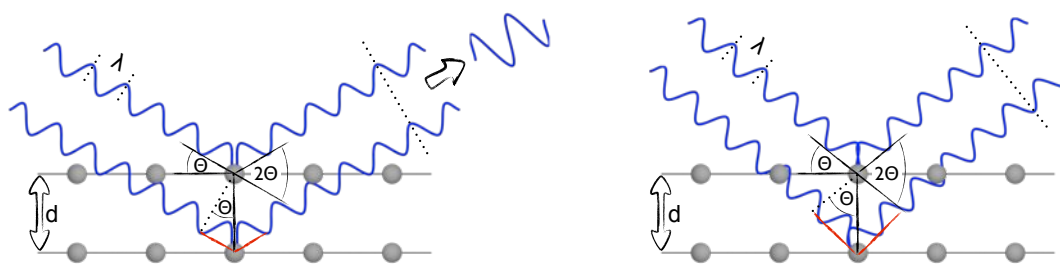


**Figure 7.1.** Schematic representation of Bragg's law. If an X-ray beam is impinging on a crystalline sample, scattering of the rays occurs at the lattice planes. In dependence of the incidence angle and the distance between the lattice planes, constructive (*left*) and destructive (*right*) interference between the scattered waves occurs. In case of constructive interference, when the path difference of the waves ( $2d \sin \theta$ , red lines) is an integer of the wavelength ( $\lambda$ ), a diffraction reflection with strong intensity can be observed. This effect is exploited in structural analyses. <sup>[250]</sup>

similar structure but different composition, or different phases of the same composition are often showing characteristically different diffraction patterns. <sup>[250]</sup>

X-ray diffraction is not limited to the analysis of single crystals, also structural details of crystalline powders can be determined. In this case, the crystallites in the powder sample are statistically oriented. Thus, an incident X-ray beam is not only scattered at a certain lattice plane, but rather at various lattice planes for which the diffraction condition given in Bragg's law is complied randomly. <sup>[250]</sup> Such a measurement is resulting in a powder XRD pattern, characteristic for the analyzed samples. A sample can thus be identified by a comparison of the position and intensity of observed reflections to databases containing a multitude of recorded powder XRD patterns. <sup>[250]</sup> Furthermore, the distance of the crystallographic planes can be calculated from the position of the obtained reflections. If the Miller indices of these planes are known, the dimension of the unit cell can be determined. <sup>[250]</sup> By the Rietveld method, crystal structure models can be refined based on powder XRD patterns. This method can also be used for the calculation of lattice parameters, crystallite size and to determine atom positions. <sup>[251,252]</sup>

Considering the amount of information that can be obtained from XRD patterns, it is no surprise that also various natural and synthetic birnessites have been analyzed extensively by powder X-ray diffraction. Using this technique, manganese oxides of the birnessite family have for instance been identified as important products of bacteriogenic oxidation of  $\text{Mn}^{2+}$  in seawater. <sup>[253–255]</sup> The formation mechanism <sup>[218,238,256]</sup> or structural details of various synthetic birnessites were investigated as well. <sup>[240,248,256–261]</sup>

The various birnessites prepared for the presented research project were also analyzed by powder X-ray diffraction in order to elucidate more details of the structures that have formed under the applied reaction conditions. In Figure 7.2, a theoretical powder XRD pattern derived from unit cell parameters of a crystalline Mg-birnessite <sup>[248]</sup> and patterns measured for M-birnessites 1-13 are shown. The theoretical pattern is showing an intense reflection of the 001 lattice plane at  $12.6^\circ 2\theta$ , corresponding to the typical distance between the  $\text{MnO}_6$  layers in birnessites of about 7 Å. Accordingly, the reflection of the 002 plane can be found at  $25.2^\circ 2\theta$ . Beginning at about  $35^\circ 2\theta$ , several less pronounced reflections of other lattice planes are present. These reflections give information about layer symmetry and can thus be employed to identify birnessite polytypes. <sup>[270]</sup>

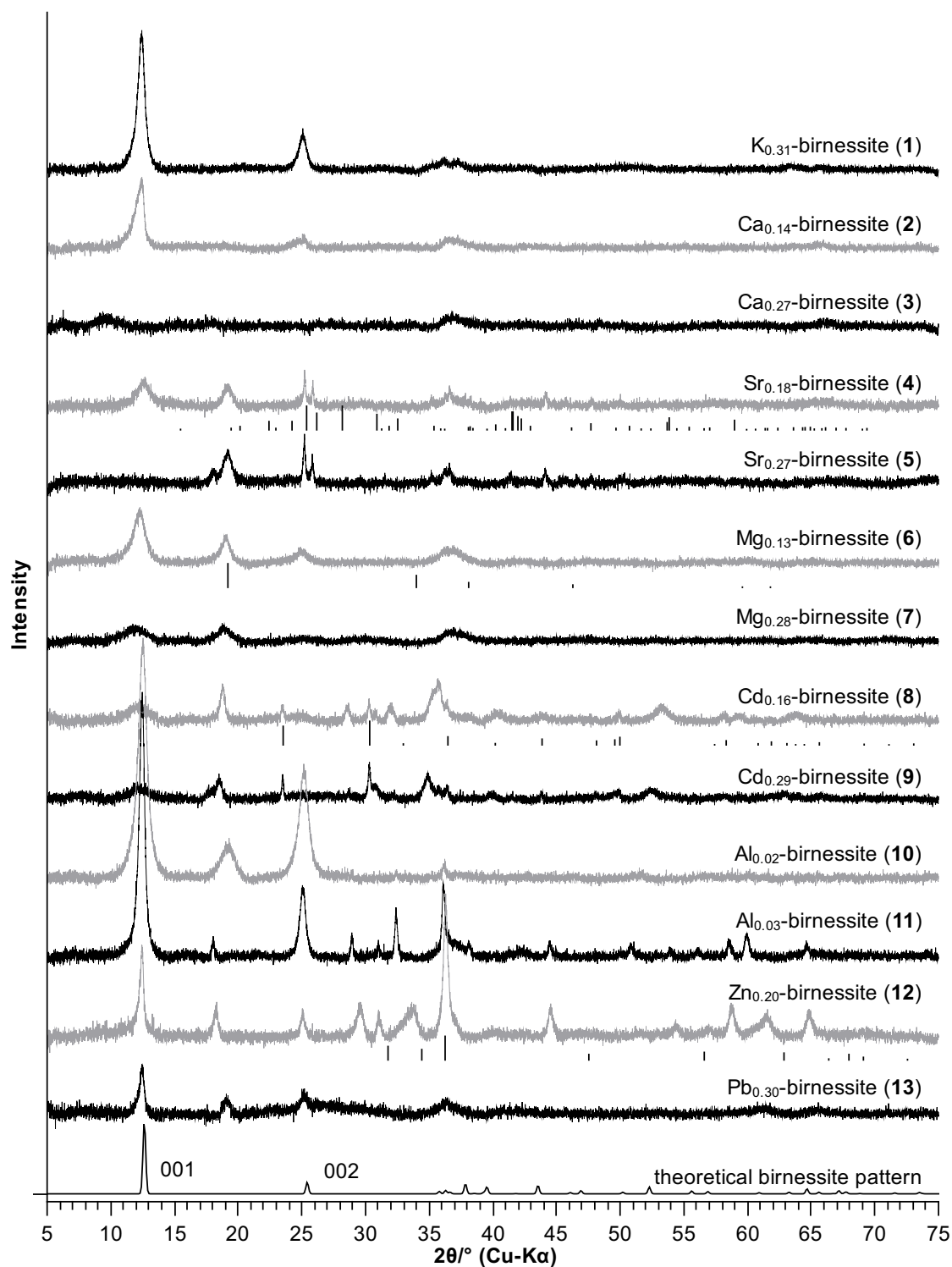


**Figure 7.2.** Powder XRD patterns of M-birnessites **1-13** as well as calculated Bragg reflections for a perfectly ordered Mg-birnessite structure.<sup>(248)</sup> In addition to the birnessite's 001 and 002 reflections present in the patterns (except of **3, 5**), various other reflections could be observed. The additional reflections are indicating the formation of other phases and can most likely be assigned to feitknechtite<sup>(262)</sup> (indicated below **6**),  $\text{Cd}(\text{CO}_3)_3$ <sup>(263)</sup> (indicated below **8**) and zinc oxide<sup>(264)</sup> or hydroxide<sup>(265,266)</sup> (indicated below **12**), respectively. The pair of reflections in the patterns of **4** and **5** have previously been observed for a barium manganese oxide<sup>(267,268)</sup>, prepared from the reaction of  $\text{Ba}(\text{OH})_2$  with  $\text{KMnO}_4$ .<sup>(268,269)</sup>

Comparing the recorded XRD patterns of the prepared oxides **1-13** with the theoretical one, it can be seen that the birnessite's 001 and 002 reflections are the strongest observable signals in most patterns, giving interlayer distances of about 7.0-7.4 Å (Table 7.1). For oxides **3** and **5**, the birnessite's 001 reflection is absent and a layer distance could thus not be determined. In the patterns of **4** and **7-9**, the characteristic 001 and 002 reflections are very weak. Together with the poor signal to noise ratio that can be generally observed in these patterns, this is indicating a high grade of disorder of the oxide structures. A further analysis of the layer symmetry is thus not feasible. However, in combination with the determined composition, the recorded IR spectra (*cf.* section 6.1) and the XAS analysis (*cf.* section 7.2), oxides **1-13** can be classified as amorphous layered manganese oxides of the birnessite family.

The appearance of additional reflections in the XRD patterns of **4-13** is indicating the presence of additional phases. Due to the low signal to noise ratio, these other phases can not be surely identified. Nevertheless, suggestions based on a database comparison are given below. The expected Bragg reflections of the suggested phases are indicated in Figure 7.2 as vertical lines below the measured XRD patterns of the respective M-birnessites. In several of the presented XRD patterns (**6-13**), a reflection appears in the region of 17-19° 2 $\theta$ . This reflection can most likely be assigned to feitknechtite ( $\beta$ -Mn<sup>III</sup>O(OH)), indicated below **6**), or probably to pyrochroite (Mn<sup>II</sup>(OH)<sub>2</sub>).<sup>[248,262]</sup> These two layered manganese oxide phases have been reported to form as intermediates in the synthesis of M-birnessites.<sup>[218,248]</sup> In the XRD patterns of Sr-birnessites **4** and **5**, two rel-

**Table 7.1. Interlayer distances of 1-13 determined by XRD.**

Compound		Interlayer distance / Å
K <sub>0.31</sub> -birnessite	(1)	7.1
Ca <sub>0.14</sub> -birnessite	(2)	7.1
Ca <sub>0.27</sub> -birnessite	(3)	—
Sr <sub>0.18</sub> -birnessite	(4)	7.0
Sr <sub>0.27</sub> -birnessite	(5)	—
Mg <sub>0.13</sub> -birnessite	(6)	7.2
Mg <sub>0.28</sub> -birnessite	(7)	7.4
Cd <sub>0.16</sub> -birnessite	(8)	7.2
Cd <sub>0.29</sub> -birnessite	(9)	7.3
Al <sub>0.02</sub> -birnessite	(10)	7.1
Al <sub>0.03</sub> -birnessite	(11)	7.1
Zn <sub>0.20</sub> -birnessite <sup>[224]</sup>	(12)	7.1
Pb <sub>0.30</sub> -birnessite <sup>[224]</sup>	(13)	7.1

Interlayer distances were derived from powder XRD patterns from the characteristic 001 reflection in the range of 12-13° 2 $\theta$  (Figure 7.2). In case of M-birnessites **3** and **5** this characteristic reflection is absent.

atively sharp reflections appear in the region of  $\sim 25^\circ 2\theta$ . A similar pair of signals has previously been observed for a barium manganese oxide<sup>[267,268]</sup> (indicated below **4**), prepared from reactions of hot barium hydroxide with potassium permanganate.<sup>[268,269]</sup> The presence of these similar reflections may indicate the formation of a structurally related phase of a strontium manganese oxide. The powder XRD patterns of the Cd-birnessites **8** and **9** are containing several additional reflections. These signals are well corresponding to expected reflections of  $\text{CdCO}_3$  (indicated below **8**).<sup>[263]</sup> Considering the strong alkaline pH of the reaction medium, it seems reasonable that a relatively high amount of  $\text{CO}_2$  from the air is dissolved in the aqueous base, resulting in the precipitation of cadmium carbonate. The sharpest additional reflection in the pattern of  $\text{Zn}_{0.20}$ -birnessite **12** at about  $36^\circ 2\theta$  can tentatively be assigned to a ZnO phase<sup>[264]</sup> (indicated below **12**), but also  $\text{Zn}(\text{OH})_2$  phases exhibit a sharp reflection at this position<sup>[265,266]</sup> (indicated below **16**, Figure 7.3). However, as only a single corresponding reflection is existing, the assignment of a particular phase is highly speculative. For further reflections, like those found in the pattern of  $\text{Al}_{0.03}$ -birnessite **11**, no phases were found matching XRD patterns on the database *and* the found composition of the respective oxides.

The composition and the IR spectra of the ion exchange products **14-18** showed that ion exchange was not successful in all cases. In Figure 7.3, powder XRD patterns of these compounds are compared to the theoretically expected birnessite reflections. None of the patterns of **14-18** is showing these expected reflections. Instead, only signals are present which are indicating other phases. In the powder pattern of  $\text{Ca}_{\text{ex}}$ -birnessite **14**

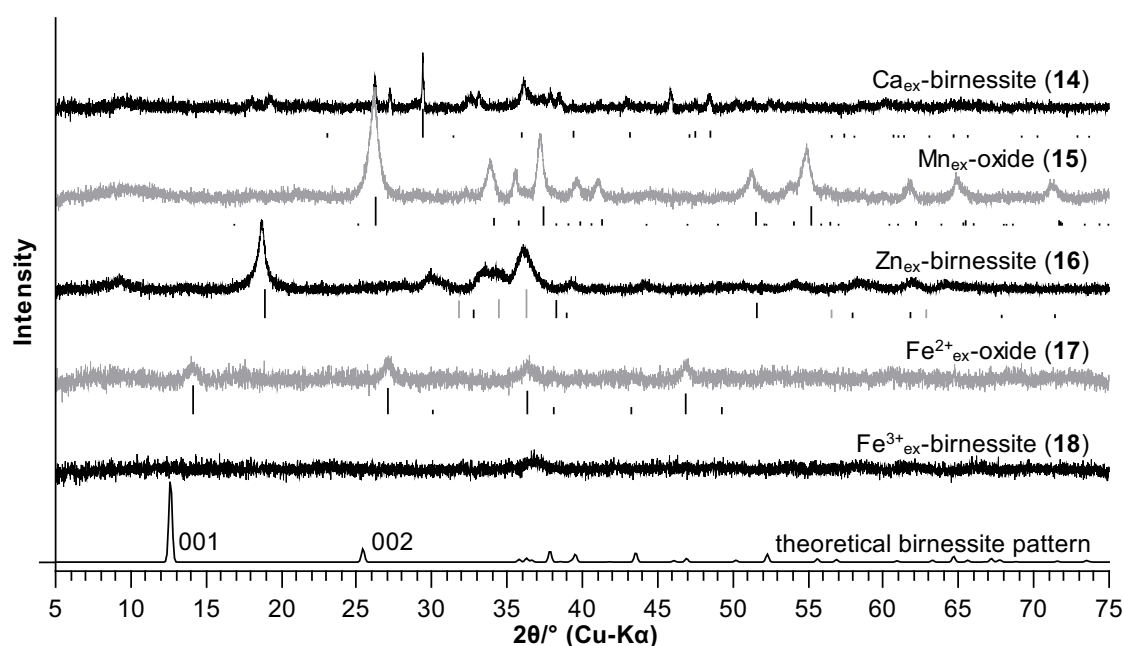


**Figure 7.3.** Powder XRD patterns of M-birnessites **14-18** as well as calculated Bragg reflections for a perfectly ordered Mg-birnessite structure.<sup>(248)</sup> The 001 and 002 reflections expected for birnessites are absent, but other reflections could be observed. For **14**, a  $\text{CaCO}_3$  phase was found.<sup>(271)</sup> **15** could be identified as manganite.<sup>(247)</sup> In **16**, zinc oxide<sup>(264)</sup> (not indicated) or hydroxide phases<sup>(265,266)</sup> (black and gray lines) are most likely present. **17** could be identified as the iron oxide hydroxide lepidochrochite.<sup>(272)</sup> Expected reflections for these phases are indicated below the respective XRD patterns.

a remarkably sharp reflection can be observed at a  $2\theta$  angle of  $29.4^\circ$ . This reflection is well corresponding to a signal expected for calcite ( $\text{CaCO}_3$ ).<sup>[271]</sup> Other, less pronounced reflections are also well corresponding to the expected diffraction pattern of calcite (indicated below **14**). Referring to the determined composition and also to the recorded IR spectra of **14**, it is most likely that the calcite particles are present in addition to an X-ray amorphous layered manganese oxide phase.

In case of  $\text{Mn}_{\text{ex}}$ -oxide **15**, it is to be assumed that another manganese oxide phase was formed exclusively during the ion exchange step. Signals which could be assigned to a birnessite-like structure are neither present in the IR spectrum, nor in the powder XRD pattern. In contrast, the XRD pattern of **15** shows several reflections which are characteristic for manganite ( $\gamma\text{-Mn}^{\text{III}}\text{O}(\text{OH})$ ), indicated below **15**.<sup>[247]</sup> The powder pattern is thus well corresponding to the IR spectrum. Consequently, a comproportionation reaction between  $\text{Mn}^{2+}$  and the  $\text{Mn}^{4+}$  centers of the birnessite's  $\text{MnO}_6$  layers most likely occurred during the ion exchange step, resulting in the formation of the found  $\gamma\text{-MnO}(\text{OH})$  phase (*cf.* section 6.2).

The diffraction pattern of  $\text{Zn}_{\text{ex}}$ -birnessite **16** is showing reflections that can probably be assigned to  $\text{ZnO}$ <sup>[264]</sup> or  $\text{Zn}(\text{OH})_2$  phases<sup>[265,266]</sup> (indicated below **16**). Similar to  $\text{Zn}_{0.20}$ -birnessite **12**, only one of several expected reflections of  $\text{ZnO}$  or  $\text{Zn}(\text{OH})_2$  is matching the recorded powder diffraction pattern. A classification of the additional phase is thus not possible. Considering also the recorded IR spectrum as well as the composition of **16**, a considerably fraction of this oxide powder is supposed to show an amorphous birnessite-like structure.

In the case of the  $\text{Fe}_{\text{ex}}^{2+}$ -oxide **17**, the previously described characterization showed that no significant amount of manganese is present in the structure. In analogy to **15** it has thus already been suggested (*cf.* section 6.2), that  $\text{Fe}^{2+}$  ions were oxidized by the  $\text{Mn}^{4+}$  centers of the Ca-buserite precursor, resulting in the formation of an iron oxide phase of a layered (and thus birnessite-like) structure. Unfortunately, sharp reflections are absent in the XRD pattern of **17**. But the weak signals which are present are well corresponding with reflections expected for the layered iron oxide hydroxide lepidocrocite ( $\gamma\text{-Fe}^{\text{III}}\text{O}(\text{OH})$ ), indicated below **17**.<sup>[272]</sup> In combination with the IR spectrum of **17**, the phase formed during the redox reaction in between the manganese oxide precursor and  $\text{Fe}^{2+}$  ions in solution can be identified as lepidocrocite.

Based on the powder XRD pattern of  $\text{Fe}_{\text{ex}}^{3+}$ -birnessite **18**, no further analysis is possible as no reflections can be observed. Considering again the composition and the IR spectrum of **18**, it can nonetheless be concluded that a X-ray amorphous manganese oxide phase most likely of the birnessite family has been formed, similar to **14** and **16**.

As mentioned above, K/Ca-birnessites **19-29** were prepared in order to study the influence of the concentration of exogenous  $\text{Ca}^{2+}$  ions on the oxides' structure and their catalytic activity. The SEM images showed a relation between the  $\text{Ca}^{2+}$  ion concentration and the particle size. In all of the IR spectra of these oxide materials, the expected features for birnessite-like structures were present (*cf.* section 6.3). In order to get a more detailed insight into the formed structures, powder XRD patterns were also measured for this set of synthetic manganese oxides (Figure 7.4). The pattern of  $\text{K}_{0.28}$ -birnessite **19** is clearly showing the expected 001 and 002 reflections of the birnessite structure. Additional signals can most likely be assigned to a feitknechtite phase (indicated below **19**).<sup>[262]</sup> In the powder XRD patterns of Ca-birnessites **20-22**, the same reflections can be observed, but the intensities are decreasing with an increasing  $\text{Ca}^{2+}$  ion concentration.

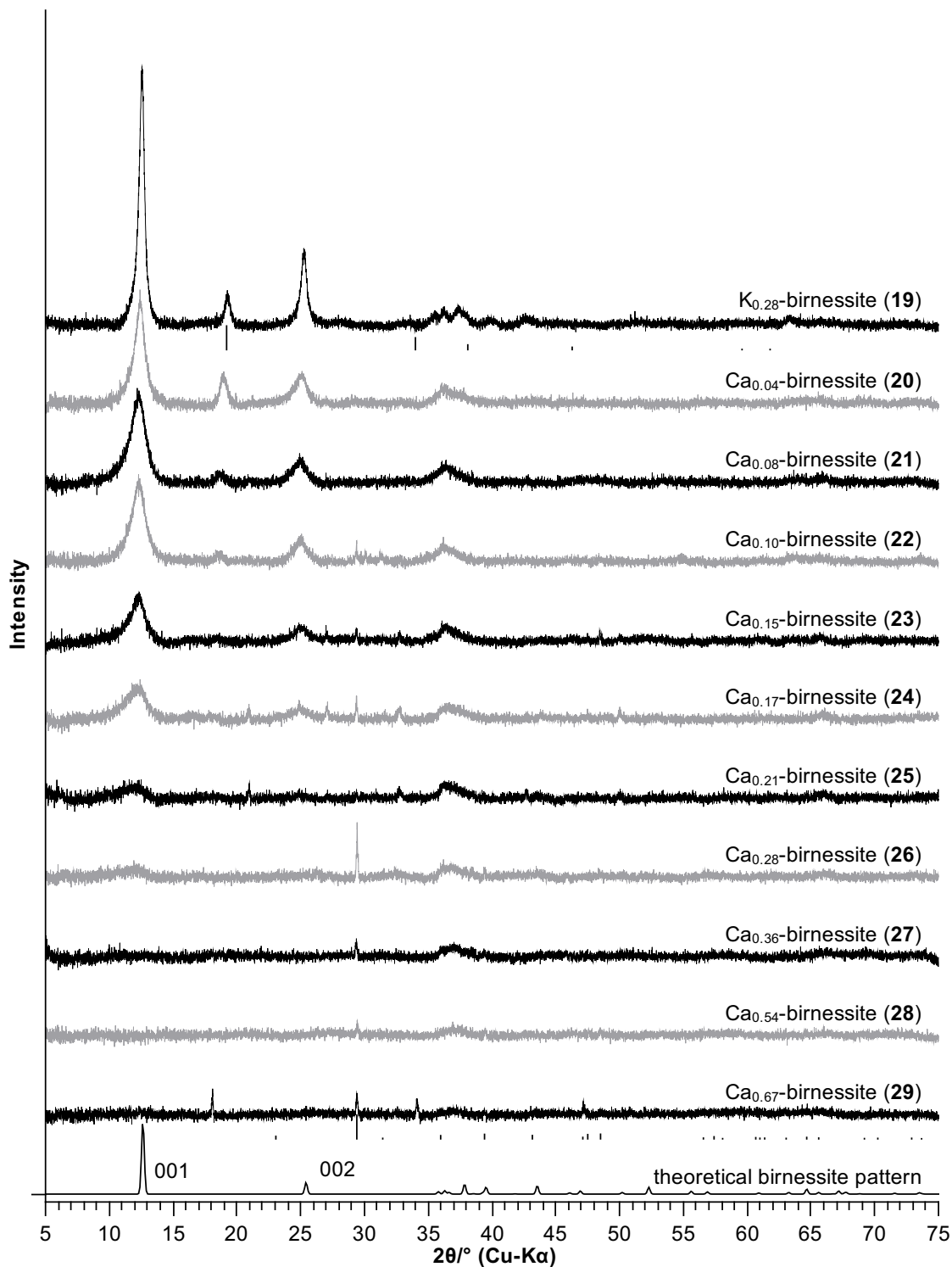


**Figure 7.4.** Powder XRD patterns of M-birnessites **19-29** as well as calculated Bragg reflections for a perfectly ordered Mg-birnessite structure.<sup>(248)</sup> The expected 001 and 002 reflections of birnessites are well pronounced for K/Ca-birnessites with lower  $\text{Ca}^{2+}$  ion concentrations. With increasing  $\text{Ca}^{2+}$  ion concentration, the intensity of these reflections is decreasing until these are completely absent. Additional reflections present in several XRD patterns can most likely be assigned to feichtnechtite<sup>(262)</sup> (indicated below **19**) or  $\text{CaCO}_3$ <sup>(271)</sup> (indicated below **29**).

**Table 7.2. Interlayer distances of 19-29 determined by XRD.**

Compound		Interlayer distance/Å
K <sub>0.28</sub> -birnessite	(19)	7.0
Ca <sub>0.04</sub> -birnessite	(20)	7.1
Ca <sub>0.08</sub> -birnessite	(21)	7.1
Ca <sub>0.10</sub> -birnessite	(22)	7.2
Ca <sub>0.15</sub> -birnessite	(23)	7.2
Ca <sub>0.17</sub> -birnessite	(24)	7.2
Ca <sub>0.21</sub> -birnessite	(25)	7.3
Ca <sub>0.28</sub> -birnessite	(26)	—
Ca <sub>0.36</sub> -birnessite	(27)	—
Ca <sub>0.54</sub> -birnessite	(28)	—
Ca <sub>0.67</sub> -birnessite	(29)	—

Interlayer distances were derived from powder XRD patterns from the characteristic 001 reflection in the range of 12-13° 2θ (Figure 7.2). In the cases of the Ca-birnessites **26-29**, this characteristic reflection is absent.

This trend continues with a further increase of the amount of Ca<sup>2+</sup>. For Ca<sub>0.21</sub>-birnessite **25**, the 001 signal is relatively broad and poorly pronounced, the 002 reflection is not visible any more. On the basis of the 001 reflection in the 2θ region of 12-13°, interlayer distances between 7.0 and 7.3 Å could be determined for oxides **19-25** (Table 7.2). As this reflection is absent in the patterns of **26-29**, the interlayer distance could not be determined in these cases.

In addition to diffraction patterns assigned to birnessite or feitknechtite phases, further reflections are present in the powder patterns of **22-24** and **26-29**. These additional reflections can again most likely be assigned to a CaCO<sub>3</sub> phase formed from dissolved CO<sub>2</sub> (indicated below **29**).<sup>[271]</sup> Considering here also the determined composition and the recorded IR spectra of **19-29**, the formation of birnessite-like structures can be concluded even for these samples, for which an identification was not feasible from the XRD patterns. Furthermore, a trend for the influence of the exogenous ion concentration is clearly visible. The decreasing intensities of the characteristic birnessite reflections and their absence, respectively, is demonstrating that an increase of the Ca<sup>2+</sup> concentration is resulting in the formation of less ordered structures.

For the preparation of Ca-birnessites **30-40**, ion concentrations similar to those used in the synthesis of the amorphous Ca-birnessites **3** and **26** were applied, but the ripening period was varied from 0-240 h. If the relation between aging and crystallinity reported by Luo *et al.*<sup>[218]</sup> can be transferred to the prepared Ca-birnessites, an increase of the degree of order of the materials should be observed with increasing ripening time. In Figure 7.5, the measured powder XRD patterns of Ca-birnessites **30-40** are compared to the theoretical birnessite pattern.<sup>[248]</sup> None of the experimental patterns is showing the

characteristic birnessite 001 and 002 reflections. Signals expected for feitknechtite and pyrochroite, the potential intermediates in the birnessite crystallisation mechanism<sup>[218]</sup>, are absent as well. The only phase that can be identified in these XRD patterns is  $\text{CaCO}_3$  (indicated below 40).<sup>[271]</sup> Together with the recorded IR spectra, it can be concluded that amorphous Ca-birnessites have most likely formed also in this case. But the XRD patterns are clearly showing that elongated ripening periods are not resulting in the formation of crystalline birnessites here. The composition of these synthetic oxide materials seems to have a greater influence on the order of the resulting phase.

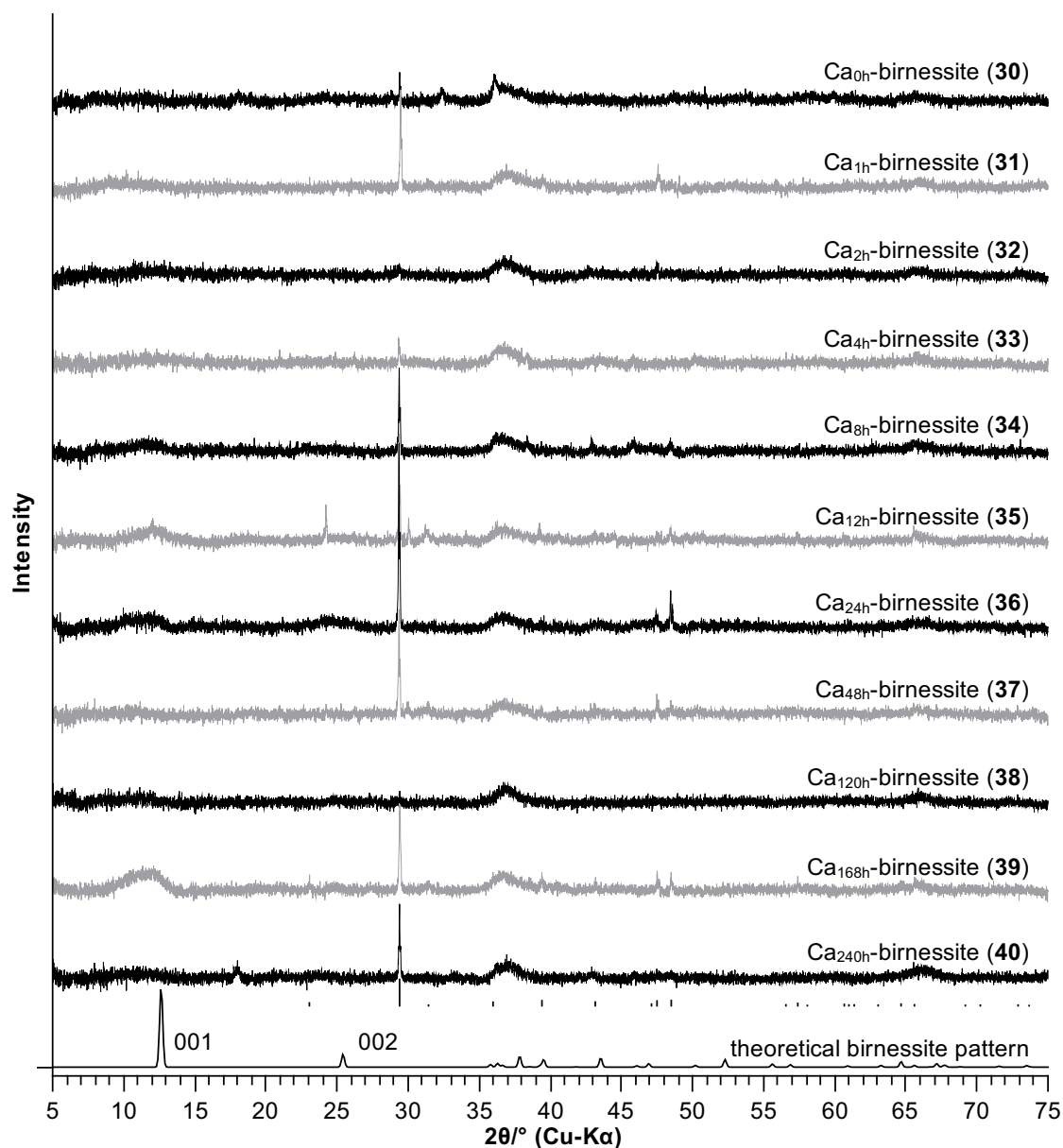


**Figure 7.5.** Powder XRD patterns of Ca-birnessites **30-40** as well as calculated Bragg reflections for a perfectly ordered Mg-birnessite structure.<sup>[248]</sup> Reflections expected for birnessites are completely absent. Only reflections characteristic for  $\text{CaCO}_3$  can be observed (indicated below **40**).<sup>[271]</sup>

## 7.2 X-ray absorption spectroscopy

When a X-ray beam of sufficient energy is hitting an atom, a photon of the beam is absorbed whereby a core electron is promoted out of its shell. In X-ray absorption spectroscopy (XAS), this interaction of X-rays at energies near the core-level binding energy of the absorbing electron and above is studied in detail. XAS is thereby providing information on the oxidation state of the studied atomic species and on its local atomic environment without the requirement of crystallinity.<sup>[273,274]</sup>

X-ray absorption spectra can roughly be divided into two domains: X-ray absorption near edge structure (XANES) and extended X-ray absorption fine structure (EXAFS). XANES is addressing X-ray energies near the binding energy of the core level electrons of the analyzed atomic species. When a sample is irradiated with X-rays of increasing energy, there is a sharp rise in absorption at energies equal to the binding energy of the core electrons. This absorption edge is corresponding to the creation of a photoelectron (Figure 7.6, left). As each element has its individual core level binding energy, the position of the absorption edge is dependent on the atom type which is analyzed. Furthermore, the electronic states which are available for the generation of photoelectrons are crucial and strongly influence the shape of the XANES spectra. The available electronic states are determined by the atomic species as well as the bonding conditions. Additionally, the XANES regime is sensitive to multiple backscattering of the photoelectron by surrounding atoms. Thus, XANES spectra are providing information on the mean oxidation state and the coordination geometry of an examined element.<sup>[273–275]</sup>

The EXAFS regime of a spectrum is addressing the absorption of X-rays of higher energies, well above the threshold energy level. Again, the states available for the photoelectron are playing a key role. But this regime is dominated by backscattering of the

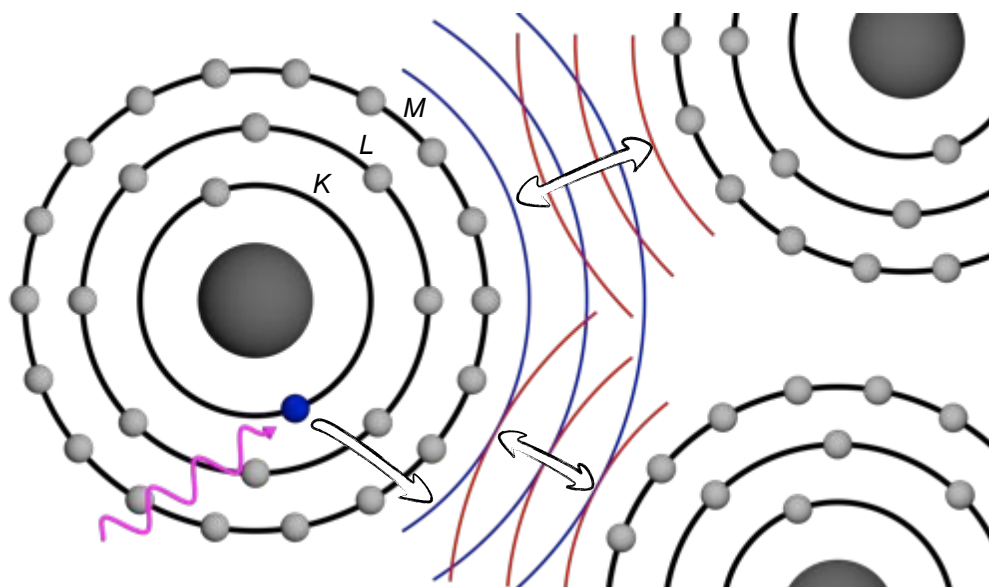


**Figure 7.6.** Schematic representation of X-ray absorption and the resulting emission of a photoelectron (blue sphere and lines). The XANES regime of a spectrum is specific for each element and its environment and provides information on the oxidation state and coordination geometry. The EXAFS regime of a spectrum is dominated by constructive and destructive interferences with the photoelectron backscattered (red lines) at neighboring atoms and thus provides information on the local atomic environment.

created photoelectron. When a core level electron is absorbing a X-ray photon and is thereby promoted to the continuum, the created photoelectron can be scattered from a surrounding atom, back to the absorbing atom (Figure 7.6, right). The backscattering effect is strongly influenced by the type and the distance of the surrounding atoms. The backscattered photoelectron is then modulating the wave function of the photoelectron at the absorbing atom. As a result, an oscillation can be observed which is affected by constructive and destructive interferences. The EXAFS regime is thus providing information on the distance and the type of neighboring atoms, whereby structural moieties can be identified.<sup>[273,274]</sup>

Fortunately we had the opportunity to collaborate with the group of Prof. Holger Dau from Freie Universität Berlin in order to carry out XAS experiments. In this collaboration, XANES and EXAFS spectra of M-birnessites 1-7 were recorded at the Mn K-edge in order to determine the mean Mn oxidation states and the manganese binding motifs for these synthetic oxides.<sup>[223]</sup> Previously, XAS has already been successfully used to characterize the structures of Najafpour's calcium manganese oxide catalysts, where spectra were recorded at the Mn and Ca K-edge.<sup>[215]</sup> The experiments as well as the evaluation of these studies were carried out by the Dau group, mainly by Dr. Ivelina Zaharieva. Thus, only an overview will be given below. For a more detailed discussion of the XAS results, the interested reader is referred to <sup>[215]</sup> and <sup>[223]</sup> as well as the respective supplementary information.

XANES spectra of M-birnessites 1-7 are presented in Figure 7.7. These spectra exhibit smooth and featureless edge rises, previously assigned to layered manganese oxides.<sup>[259]</sup> Additionally, spectra of MnO, Mn<sub>2</sub>O<sub>3</sub> and  $\beta$ -MnO<sub>2</sub> as reference materials for oxides with a known Mn oxidation state are shown. As briefly discussed above, the mean oxidation state of a studied element can be estimated from the characteristic edge-position

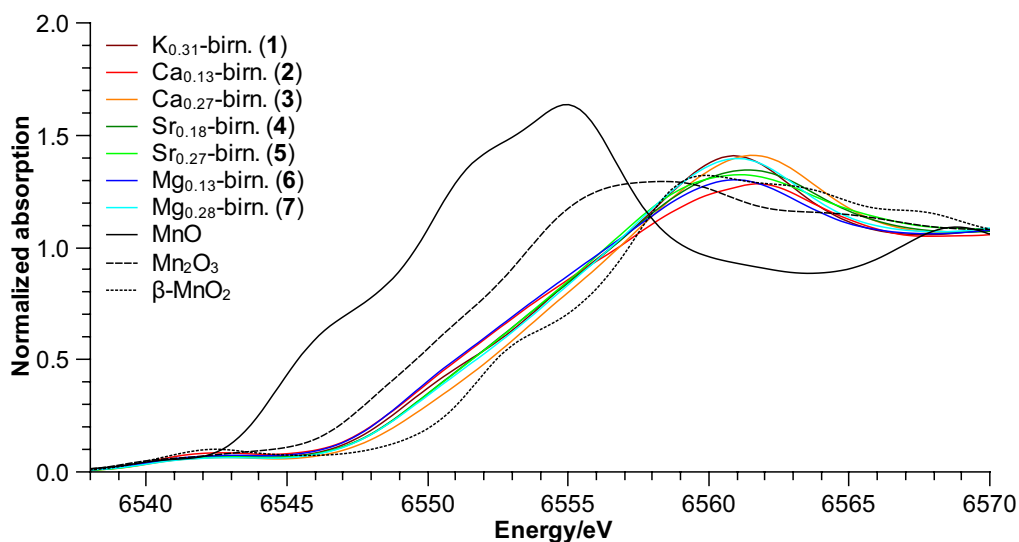


**Figure 7.7.** XANES spectra of 1-7 (colored lines) and MnO, Mn<sub>2</sub>O<sub>3</sub> and  $\beta$ -MnO<sub>2</sub> used as reference compounds (black lines). Smooth featureless edge rises and low pre-edge intensities are typical for birnessite-like manganese oxides. Average Mn oxidation states could be estimated from edge-rise energies which are indicative for values between 3.5 and 3.8.<sup>(223)</sup>

**Table 7.3. Mean Mn oxidation states of 1-7 determined by XANES.**

Compound		Mean Mn oxidation state
K <sub>0.31</sub> -birnessite	(1)	3.6
Ca <sub>0.14</sub> -birnessite	(2)	3.5
Ca <sub>0.27</sub> -birnessite	(3)	3.8
Sr <sub>0.18</sub> -birnessite	(4)	3.6
Sr <sub>0.27</sub> -birnessite	(5)	3.6
Mg <sub>0.13</sub> -birnessite	(6)	3.5
Mg <sub>0.28</sub> -birnessite	(7)	3.8

The mean Mn oxidation state of 1-7 was calculated from the edge positions in the XANES spectra after calibration with MnO, Mn<sub>2</sub>O<sub>3</sub> and  $\beta$ -MnO<sub>2</sub> as references with known oxidation state.

energy.<sup>[273,275]</sup> By a comparison of the edge-position of our samples to that of the references and a calculation of the characteristic edge-position energy<sup>[73]</sup>, we obtained values ranging from 3.5 to 3.8 for the average oxidation states of the Mn centers in oxides 1-7 (Table 7.3).<sup>[223]</sup> In the previous study, the oxidation state of Najafpour's birnessite-like active water-oxidation catalysts was also estimated to be 3.8.<sup>[215]</sup> The results of both studies are indicating that these M-birnessites contain primarily Mn<sup>4+</sup> with a small fraction of Mn<sup>3+</sup> or Mn<sup>2+</sup> ions. Based on the XANES results, the ratio between Mn<sup>3+</sup> and Mn<sup>2+</sup> ions present in these materials cannot be determined. However, the XANES data are well corresponding to the composition, the IR spectra and the XRD patterns of 1-7 discussed above (*cf.* chapter 6 and section 7.1). These results are also well corresponding to the analyses of birnessite-like manganese oxides by other researchers, who reported that Mn<sup>3+</sup> ions are placed above and below layer vacancies as well as within the layers of edge sharing MnO<sub>6</sub> octahedra.<sup>[254,258]</sup>

Characteristic atomic distances and structural moieties could be derived by the Berlin team from EXAFS results. First, the background of the post edge regime of the recorded X-ray absorption spectra was subtracted. Then, the EXAFS spectra were converted to an equidistant wavenumber axis (so called *k*-space in Å<sup>-1</sup>). In order to compensate the drop in oscillations with energy, the spectra were weighed by *k*<sup>3</sup>. The resulting plots of  $\chi(k)$  vs. *k* are shown in Figure 7.8 (*left*, gray lines), together with the Fourier transformation (FT) of the data (*right*, gray lines).<sup>[223]</sup>

The peaks in the FT of the EXAFS spectra are corresponding to neighboring atoms of oxygen, manganese or alkaline earth metal cations of the X-ray absorbing manganese centers. The distances of these backscattering atoms to the absorbing Mn ions is corresponding to the peak positions, where it has to be noted that the distances are underestimated by 0.3-0.4 Å.<sup>[73,273]</sup> Accurate interatomic vectors as well as coordination numbers can only be derived from simulations of the EXAFS data (Figure 7.8, black lines). These simulations were performed by least squares curve fitting of the *k*<sup>3</sup> weighed oscillations in the *k*-space.<sup>[223]</sup>

The first peak in the FT of the EXAFS spectra of M-birnessites 1-7 can be assigned to

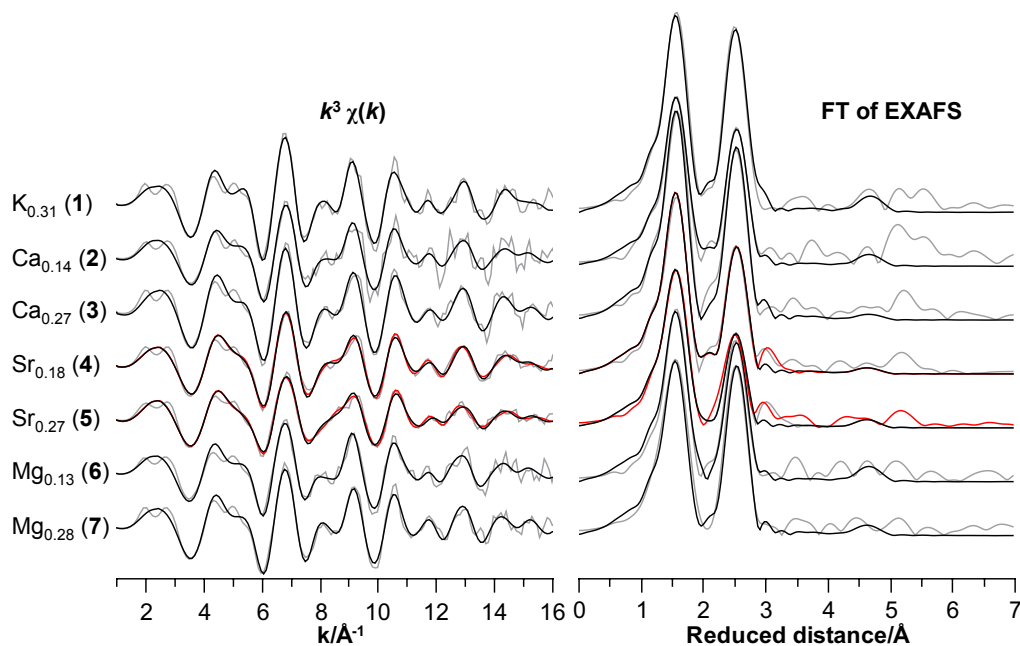


**Figure 7.8.**  $k^3$ -weighted extended range EXAFS spectra (*left*) and FT of EXAFS spectra of 1-7 (*right*). Experimental spectra are presented in gray. EXAFS simulation results for a fit with two short Mn–Mn distances (black lines) and in case of Sr-birnessites **4** and **5** also including a Mn–Sr distance of 3.3 Å (red lines) are shown. The fit parameters are given in Table 7.4.<sup>[223]</sup>

an octahedral ligand sphere of oxygen atoms coordinated to the Mn centers (Figure 7.9). Most of the Mn–O distances are showing typical values for  $\text{Mn}^{\text{IV}}\text{O}_6$  octahedra of about 1.9 Å (Table 7.4).<sup>[276]</sup> For about 20 % of the Mn–O distances, values of approximately 2.3 Å were found. These longer distances are indicating the presence of  $\text{Mn}^{\text{II}}\text{–O}$  bonds or  $\text{Mn}^{\text{III}}\text{O}_6$  octahedra showing two elongated Mn–O distances due to the typical Jahn-Teller distortion often observed for the environment of  $\text{Mn}^{\text{III}}$  ions.<sup>[277,278]</sup> M-birnessites **2**, **4**, **5** and **6**, the oxides with a lower mean Mn oxidation state, exhibit also a higher content of these longer  $\text{Mn}^{\text{II/III}}\text{–O}$  distances (*cf.* Tables 7.3 and 7.4).<sup>[223]</sup>

The second intensive peak in the FT spectra can be assigned to di- $\mu$ -oxido bridged Mn centers (Figure 7.9).<sup>[176,255,279]</sup> EXAFS simulations revealed Mn–Mn distances of about 2.9 Å for such units. These results are in a good agreement with layered manganese oxides, as di- $\mu$ -O(H) bridged Mn ions showing similar Mn–Mn distances are the dominating bridging motif in these materials.<sup>[255,279]</sup> A high heterogeneity of this shell, indicated by relatively high Debye-Waller parameters, is probably resulting from  $\text{Mn}^{3+}$  ions present in the layers of edge sharing  $\text{MnO}_6$  octahedra. As mentioned above, the presence of  $\text{Mn}^{3+}$  ions within the layer has previously been reported, namely for synthetic and bacteriogenic triclinic birnessites.<sup>[254,258]</sup> Furthermore, the intensities of this peak in the FT EXAFS spectra are well corresponding to the XANES data. A higher amount of  $\text{Mn}^{3+}$  ions present within the layers should contribute to a higher heterogeneity, which could well explain the observed decreased peak intensities for the M-birnessites with lower mean Mn oxidation states (**2**, **4**, **5** and **6**).<sup>[223]</sup>

At a reduced distance of about 3 Å, a less dominant peak can be observed (Figure 7.9), which is predicted for  $\mu$ -oxido bridged metal ions in cubane like motifs.<sup>[215,280]</sup> This peak is best resolved for the Sr-birnessites **4** and **5** (see inset in Figure 7.9). EXAFS

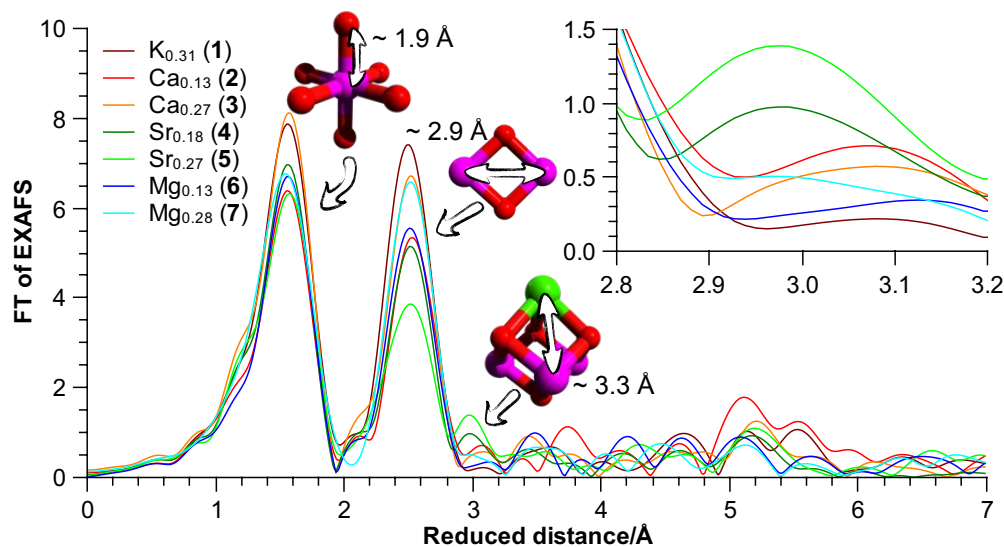


**Figure 7.9.** FT of EXAFS spectra of 1-7 together with structural motifs (O in red, Mn in purple,  $M^{2+}$  in green) assigned to each peak. The region showing a signal corresponding to a cubane like  $MMn_3(\mu-O)_4$  motif (2.8 - 3.2 Å) is presented enlarged in the inset.

simulations including a Mn–Sr shell (red lines in Figure 7.8) revealed a distance of about 3.3 Å. A coordination number of about 0.5  $Sr^{2+}$  ions per X-ray absorbing Mn ion was determined (Table 7.4). A similar  $M^{2+}Mn_3(\mu-O)_4$  cubane like unit is most likely also present in Ca-birnessites 2 and 3, but the corresponding peak cannot be resolved reliably.<sup>[223]</sup>

These results are in good agreement to the data obtained from XANES and EXAFS spectra measured at the Mn K-edge of Najafpour’s manganese oxides. In this previous study, a mean Mn oxidation state of 3.8 was determined for the two active manganese oxide catalysts. The FT of the EXAFS spectra showed similar peaks, indicating comparable atomic distances and, considering the relatively similar composition of Najafpour’s oxides to the Ca-birnessites 2 and 3 discussed here, also similar structures of the materials.<sup>[215]</sup>

In this study, EXAFS spectra were also measured at the Ca K-edge. By a comparison of the Mn K-edge and the Ca K-edge data, two Mn–Ca distances of about 3.1 Å and 3.8 Å, respectively, could be identified. The shorter one can be assigned to  $CaMn_3(\mu-O)_4$  cubanes. A comparison of the coordination numbers obtained from the Mn and Ca K-edge spectra indicated that  $Mn_4(\mu-O)_4$  moieties<sup>[280]</sup> may also be present. The longer Mn–Ca vector of about 3.8 Å identified in the spectra is indicating the presence of  $Ca^{2+}$  ions above and below Mn layer vacancies, bound to  $MnO_6$  layers in a three corner sharing  $CaO_x$  unit.<sup>[248,255,281,282]</sup> Further Ca–Ca vectors are indicating a quasi statistical distribution of  $Ca^{2+}$  ions above and below the disordered layers of edge sharing  $MnO_6$  octahedra.<sup>[215]</sup>

The low magnitude of peaks in the FT of the EXAFS spectra at longer distances indicates a low extend of long-range order in the materials of both studies.<sup>[199]</sup> However, a weak FT peak can be observed at  $\sim 5.1$  Å, which can be assigned to a Mn–Mn distance of about 5.8 Å. This longer Mn–Mn distance is equal to two Mn–Mn distances of about 2.9 Å and corresponds to a pattern of three Mn ions linearly arranged in a di- $\mu$ -O(H)

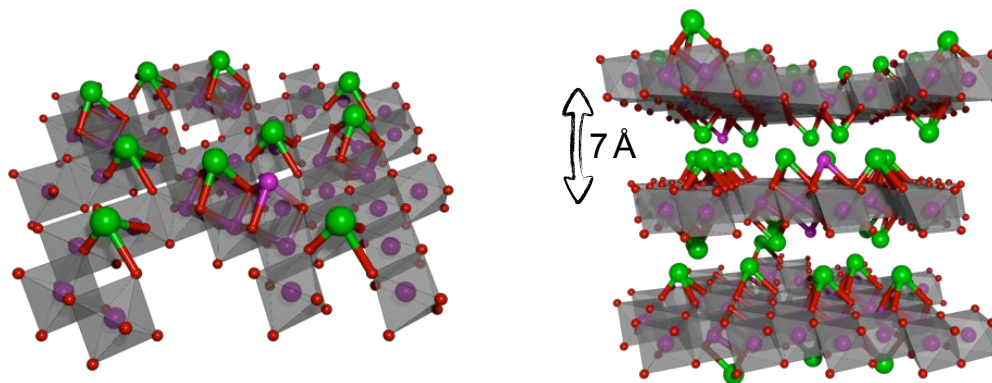


**Figure 7.10.** Structural model for a section of a M-birnessite layer (*left*) and the layer stacking pattern (*right*). The layer is built from edge sharing  $\text{MnO}_6$  octahedra with a high number of vacancies (octahedra in grey, Mn in purple,  $\text{M}^{2+}$  in green, O in red). The  $\text{M}^{2+}$  ions are placed above/below of Mn vacancies in three corner sharing  $\text{MO}_x$  units, or form corners of  $\text{M}_3\text{Mn}_3(\mu\text{-O})_4$  cubanes.  $\text{Mn}^{2+}$  or  $\text{Mn}^{3+}$  ions in the interlayer space could form the corners of  $\text{Mn}_4(\mu\text{-O})_4$  cubes. The graphic is based on an idealized layer of  $\text{MnO}_6$  octahedra.<sup>[223]</sup>

bridged pattern.<sup>[215,223]</sup> As this peak is even smaller in the spectra of the oxides with higher  $\text{M}^{2+}$  concentrations, we conclude as before that a more extensive disorder of the oxides is resulting from higher concentrations of secondary ions. This is also in a good agreement with the absence of the 001 reflection in the XRD patterns of M-birnessites **3** and **5** and the decreasing intensity of this reflection in respect to the increased  $\text{Ca}^{2+}$  ion concentration observed for K/Ca-birnessites **19-29** (*cf.* section 7.1).<sup>[223]</sup>

Overall, the XANES and the EXAFS data are in good agreement and both indicate the presence of layered manganese oxide structures for oxides **1-7**, typical for the birnessite family. Distances for mono- $\mu$ -oxido bridged Mn centers found in tunneled manganese oxides were not found.<sup>[259]</sup> A model of a birnessite structure is presented in Figure 7.10, drawn from the information provided by powder X-ray diffraction and X-ray absorption spectroscopy. Edge sharing  $\text{MnO}_6$  octahedra are forming disordered layers showing a high number of vacancies.  $\text{M}^{2+}$  ions are placed above and below these vacancies in a three corner sharing motif.<sup>[255,281,282]</sup>  $\text{Ca}^{2+}$ ,  $\text{Sr}^{2+}$  and  $\text{Mg}^{2+}$  ions placed above  $\text{MnO}_6$  octahedra are involved in the formation of  $\text{M}^{2+}\text{Mn}_3(\mu\text{-O})_4$  cubes. Manganese ions intercalated in between the layers may also be present, forming probably  $\text{Mn}_4(\mu\text{-O})_4$  motifs. Similar structures are most likely also formed in the cases of Ca-birnessites **14**, **20-40** and M-birnessites **8**, **9**, **12**, **13**, **16**, in which the alkaline earth cations are replaced by  $\text{Cd}^{2+}$ ,  $\text{Zn}^{2+}$ ,  $\text{Pb}^{2+}$  and  $\text{Fe}^{3+}$ . A high number of water molecules and hydroxide moieties bound to intercalated metal cations are placed in between the layers, which are stacked above each other with an interlayer spacing of about 7 Å.<sup>[216,248]</sup>

It is important to note that Figure 7.10 is not based on structural refinements, e. g. by computational methods. Merely, the figure is a schematic representation of the obtained data discussed above.

Table 7.4. Parameters of 1-7 obtained from Mn-kedge EXAFS simulations.

Shell	K <sub>031</sub> -birm. (1)	Ca <sub>014</sub> -birm. (2)	Ca <sub>027</sub> -birm. (3)	St <sub>018</sub> -birm. (4)	St <sub>027</sub> -birm. (5)	Mg <sub>013</sub> -birm. (6)	Mg <sub>028</sub> -birm. (7)
Mn-O	R/Å	1.90/0.01	1.90/0.01	1.90/0.01	1.90/0.01	1.90/0.01	1.90/0.01
	N	4.9/0.3	4.5/0.4	5.1/0.3	4.7/0.3	4.6/0.3	4.9/0.3
Mn-O	$\sigma$ /Å	0.058/0.005	0.062/0.006	0.058/0.005	0.062/0.005	0.067/0.004	0.066/0.006
	R/Å	2.29/0.03	2.28/0.03	2.27/0.04	2.30/0.03	2.26/0.02	2.24/0.03
Mn-O	N	1.1/0.3	1.5/0.4	0.9/0.3	1.3/0.3	1.4/0.3	1.4/0.3
	$\sigma$ /Å	=	=	=	=	=	=
Mn-Mn	R/Å	2.86/0.01	2.87/0.02	2.87/0.01	2.86/0.02	2.86/0.01	2.88/0.01
	N	4.0/0.5	2.8/0.7	3.7/0.5	2.5/0.6	2.0/0.4	2.9/0.6
Mn-Mn	$\sigma$ /Å	0.063*	0.063*	0.063*	0.063*	0.063*	0.063*
	R/Å	2.99/0.02	2.98/0.07	3.01/0.04	2.97/0.09	2.99/0.06	2.99/0.06
Mn-Mn	N	1.8/0.5	0.8/0.7	1.0/0.5	0.6/0.6	0.5/0.4	0.9/0.6
	$\sigma$ /Å	=	=	=	=	=	=
Mn-Mn	R/Å	5.03/0.05	4.99/0.07	5.00/0.13	4.97/0.12	4.95/0.07	4.97/0.07
	N	1.6/1.4	1.1/1.6	0.6/1.5	0.6/1.3	0.8/1.0	1.5/1.5
Mn-Mn	$\sigma$ /Å	0.067*	0.067*	0.067*	0.067*	0.067*	0.067*
	R/Å				3.33/0.03	3.32/0.02	
Mn-Sr	N				0.5/0.3	0.5/0.3	
	$\sigma$ /Å				0.063*	0.063*	
	R <sub>F</sub> /%	13.8	21.6	16.4	14.7	13.6	20.5
							17.9

The parameters presented in the table were obtained by simulation of the  $k^3$ -weighted EXAFS spectra (N is the coordination number, R the absorber-backscatter distance and  $\sigma$  the Debye-Waller parameter). Estimated errors representing the 68 % confidence interval of the respective fit parameter are given in grey. The sum of the coordination numbers in the first two oxygen shells was fixed to 6. Debye-Waller parameters marked with \* were fixed for the longer Mn-Mn distance and for the Mn-Sr distance, those indicated by = were kept equal for the two oxygen shells and for the two short Mn-Mn distances. <sup>(223)</sup>

### 7.3 Birnessites vs. the OEC, a structural comparison

In M-birnessites, the Mn centers are coordinated by terminal or bridging oxido and hydroxido ligands in an octahedral fashion. Water molecules may also coordinate to manganese ions where open coordination sites are accessible. The oxides' layered, extensive  $\mu$ -O(H) bridged manganese network can be described as built up from interconnected, open cubane like  $\text{Mn}_3(\mu\text{-O})_4$  moieties. Some of the open corner positions are occupied by metal cations intercalated in between the M-birnessite layers, forming distorted, complete  $\text{MMn}_3(\mu\text{-O})_4$  cubanes (Figure 7.11, *left*). In case of the most active catalysts of this study, Ca-birnessites **2**, **14**, **25**, **34** and **35** (chapter 8), this cubane like moiety can be formulated as  $\text{CaMn}_3(\mu\text{-O})_4$ , with a mean manganese oxidation state between  $\text{Mn}^{3+}$  and  $\text{Mn}^{4+}$ .

Looking again at the structure of the OEC from this perspective, its  $\mu$ -oxido bridged calcium manganese cluster (*cf.* section 2.2.1) could also be described as a very small calcium manganese oxide particle embedded in a protein matrix.<sup>[103,283–285]</sup> The calcium and manganese ions are also arranged in a  $\text{CaMn}_3(\mu\text{-O})_4$  motif, with the fourth Mn bound to one edge of the distorted cubane via additional oxido bridges (Figure 7.11, *right*).<sup>[36]</sup> The Mn centers are cycling between oxidation states of  $\text{Mn}^{3+}$  and  $\text{Mn}^{4+}$  (*cf.* section 2.2.2).<sup>[26,29]</sup> The resemblance of these details is also reflected by similar XAS spectra of Ca-birnessites and the OEC, although of course certain differences exist.<sup>[56,215]</sup>

For example, the shortest Mn–Mn distance in the OEC is about 2.7 Å<sup>[64,286]</sup>, while the Mn–Mn distances found in M-birnessites are around 2.9 Å.<sup>[215,223]</sup> The different Mn–Mn vectors can be explained by variations of the  $\mu$ -O(H) bridging network of the Mn centers. The distance of 2.7 Å is characteristic for di- $\mu$ -O(H) bridged Mn ions with one or two unprotonated bridges.<sup>[287,288]</sup> The longer distance of about 2.9 Å can either be explained by the bridging of Mn ions by protonated oxido ligands or by the binding of each of the oxido bridges to three Mn centers.<sup>[289]</sup> Despite the difference in the length

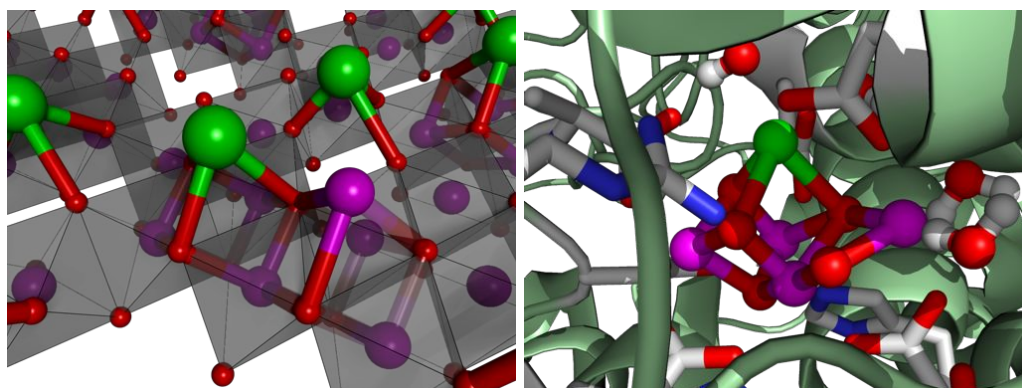


**Figure 7.11.** Comparison of a section of the M-birnessite structure (*left*) vs. the OEC (*right*). In both structures,  $\mu$ -O(H) bridged  $\text{Ca}^{2+}$  and  $\text{Mn}^{3+/4+}$  ions are forming distorted cubane like motifs (same color code as in Figure 7.10). In case of the OEC, a fourth Mn ion is bound to an edge of this cubane by additional  $\mu$ -oxido bridges. In M-birnessites, Mn ions in the interlayer space may be bound in  $\text{Mn}_4(\mu\text{-O})_4$  moieties. If an interlayer Mn ion is placed next to a  $\text{CaMn}_3(\mu\text{-O})_4$  cubane as shown in the foreground, a  $\text{CaMn}_4\text{O}_5$  cluster closely resembling the inorganic core of the OEC could be cut out of the oxide structure.<sup>[215,223]</sup> As before, the schematic representation of the M-birnessite's section is based on a layer of idealized  $\text{MnO}_6$  octahedra. The OEC is drawn using the coordinates from the structural analysis presented in<sup>[36]</sup>.

of the Mn–Mn vectors, these motifs are nevertheless very closely related. Mostly unprotonated di- $\mu$ -oxido bridges are probably only present in the OEC, while both structures contain  $\mu_2$ -OH and coordinatively saturated  $\mu_3$ -O groups.<sup>[215]</sup>

Another point to mention is the presence of clearly different but electronically strongly coupled manganese sites as parts of both M-birnessites and the OEC. In case of the OEC, it is mostly assumed that at least three Mn ions are involved in the accumulation of the oxidizing equivalents required for water-oxidation, while one Mn may only act as binding site for substrate water molecules.<sup>[26,29,36,215]</sup> We previously suggested that more ordered sections of the edge sharing  $\text{MnO}_6$  layers are acting as electronically coupled reservoirs of oxidizing equivalents, while the water-oxidation reaction itself takes place at vacancies close to the Ca binding sites or at the edges of  $\text{MnO}_6$  octahedra.<sup>[215]</sup> In short, M-birnessites resemble important features of PSII's  $\text{CaMn}_4\text{O}_5$  cluster, likely playing a key role for the activity in water-oxidation catalysis:<sup>[103,215]</sup>

- the mean oxidation state of the Mn ions is in between  $\text{Mn}^{3+}$  and  $\text{Mn}^{4+}$ , as thermodynamically required for the water-oxidation reaction (*cf.* Figure 4.3, section 4.2.2),
- open coordination sites in the layered structure of  $\text{MnO}_6$  octahedra can act as coordination sites for substrate water molecules to Mn, additional cations like  $\text{Ca}^{2+}$  bound to the layers also could act as binding and activation site,
- as a result of the low degree of order of the structures, some Mn ions show incomplete coordination spheres of oxido or hydroxido ligands. Thus, the formation of additional  $\mu$ -O bridges is possible, contributing to charge compensation and redox potential levelling,
- clearly different Mn sites are present in the oxides' structure. In various water-oxidation mechanisms suggested for the OEC, manganese centers accumulating oxidizing equivalents are involved, while O–O bond formation takes place at other Mn sites,
- and finally, the most active oxides contain  $\text{Ca}^{2+}$  ions, which are also playing a key role for the activity of the OEC even though their function in the bioinorganic catalytic cycle is not understood in detail yet (*cf.* section 2.2.2).

## 8 Phyllomanganates as water-oxidation catalysts

The investigation of the ability of M-birnessites **1-40** to act as water-oxidation catalysts was the central topic of the research project presented in this thesis. As described above, the identification of highly active catalysts for this reaction based on abundant materials is crucial to develop artificial photosynthetic processes for alternative energy production on a large scale (*cf.* chapter 3).

Following the composition of the OEC, our group was already earlier able to demonstrate that Ca-birnessites are promising candidates to catalyze the water-oxidation half reaction of an artificial photosynthetic process.<sup>[214,215]</sup> We already demonstrated in this initial work that these Ca-birnessites by far exceeded the catalytic activity of Mn oxides without any additional metal cations, but the role of the incorporated  $\text{Ca}^{2+}$  ions remained unsolved. In analogy to the function of the  $\text{Ca}^{2+}$  ion of the OEC, it was proposed that  $\text{Ca}^{2+}$  is functioning as binding and activation site for substrate water molecules. Starting at this point, the various birnessites discussed above were prepared in order to develop better understanding of water-oxidation catalyzed by mixed manganese oxides and in particular of the role of additional cations incorporated in the oxide structure. Thus, experiments on water-oxidation catalysis were carried out.

In general, it is possible to investigate the activity of water-oxidation catalysis electrochemically or by the use of suitable chemical oxidants. As birnessite electrodes were not prepared as part of this project, electrochemical water-oxidation experiments were not carried out. In the literature,  $\text{H}_2\text{O}_2$ ,  $\text{HSO}_5^-$  (oxone),  $\text{Ce}^{\text{IV}}$  and  $[\text{Ru}^{\text{III}}(\text{bpy})_3]^{3+}$  are discussed as potential oxidants to carry out oxygen evolution experiments.<sup>[169,170,173,214,290,291]</sup>

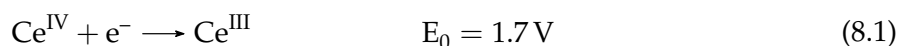
In a collaboration between Najafpour together with Kurz and the Messinger group from Umeå University, oxygen evolution catalyzed by Najafpour's Ca-Mn-oxide was investigated in more detail. Using  $^{18}\text{O}$ -enriched water and the oxidants listed above, the isotope composition of the  $\text{O}_2$  formed in the reaction of the oxides with the different oxidants were analyzed by membrane-inlet mass spectrometry (MIMS).<sup>[170]</sup> In this study, the authors clearly demonstrated that an observed oxygen evolution is not always necessarily resulting from water-oxidation. The oxygen evolved from the reaction of  $\text{H}_2\text{O}_2$  with the Ca-birnessite catalysts for instance, is resulting from the disproportionation of the peroxide. Thus, bulk water is not involved in the formation of the O–O bond. When  $\text{HSO}_5^-$  is employed as an oxidant, the authors were able to show that bulk water is participating in the O–O bond formation, but in such reactions only one oxygen atom originated from water, the other one from an oxygen transfer reaction from the oxone oxidant. In case of the single-electron oxidants  $\text{Ce}^{\text{IV}}$  and  $[\text{Ru}^{\text{III}}(\text{bpy})_3]^{3+}$ , it could be demonstrated that the atoms of the oxygen molecules evolved from the reactions of the oxidants with the birnessite catalysts both originated from bulk water.<sup>[170]</sup> Such reactions thus represent *true* water oxidation catalysis.

The requirements that have to be met by an oxidant to be used in experiments on water-oxidation catalysis can be formulated as follows. At first, the oxidant has to show a suitable potential for water-oxidation. Furthermore, the use of oxygen-transferring

reagents is only leading to a partially water-oxidation, thus non oxygen transferring oxidants are necessary. And to follow the fourfold one electron chemistry of the OEC, single-electron oxidants are required (*cf.* section 2.2.2). Hence, in the study presented herein,  $\text{Ce}^{\text{IV}}$  (section 8.1) as well as photochemically generated  $[\text{Ru}^{\text{III}}(\text{bpy})_3]^{3+}$  (section 8.2) were employed as oxidants.

## 8.1 Water-oxidation catalysis using $\text{Ce}^{\text{IV}}$ as oxidant

In order to investigate the capability of the synthetic M-birnessites **1-40** to act as water-oxidation catalysts, the single electron oxidant  $\text{Ce}^{\text{IV}}$  (i. e.  $(\text{NH}_4)_2\text{Ce}(\text{NO}_3)_6$ ) was used. Providing a potential of about +1.7 V *vs.* NHE in acidic solution<sup>[15]</sup> (eq. 8.1), the redox couple  $\text{Ce}^{\text{IV}}/\text{Ce}^{\text{III}}$  is suitable to drive the water-oxidation reaction.<sup>[170,171]</sup>



In our experiments, the M-birnessites **1-40** were suspended in 0.25 M solutions of  $\text{Ce}^{\text{IV}}$  in closed septum vials containing an atmosphere of air. A sample from the headspace of each septum vial was then injected into a GC in intervals of ten minutes to quantify the  $\text{O}_2$  product (for details see section 9.2.1).

To detect permanent gases like  $\text{O}_2$  and  $\text{N}_2$  as in case of our samples, a GC equipped with a molecular sieve column is usually used. In such a setup, the gas sample is transported through the mol sieve column by helium used as the carrier gas. Due to different interactions between  $\text{O}_2$  or  $\text{N}_2$  and the solid phase of the column, the gases are showing different retention times and are thus separated. The gas flow containing the column effluent (sample and carrier gas) is then analyzed by a thermal conductivity detector (TCD) against a reference flow only containing the carrier gas. By the difference

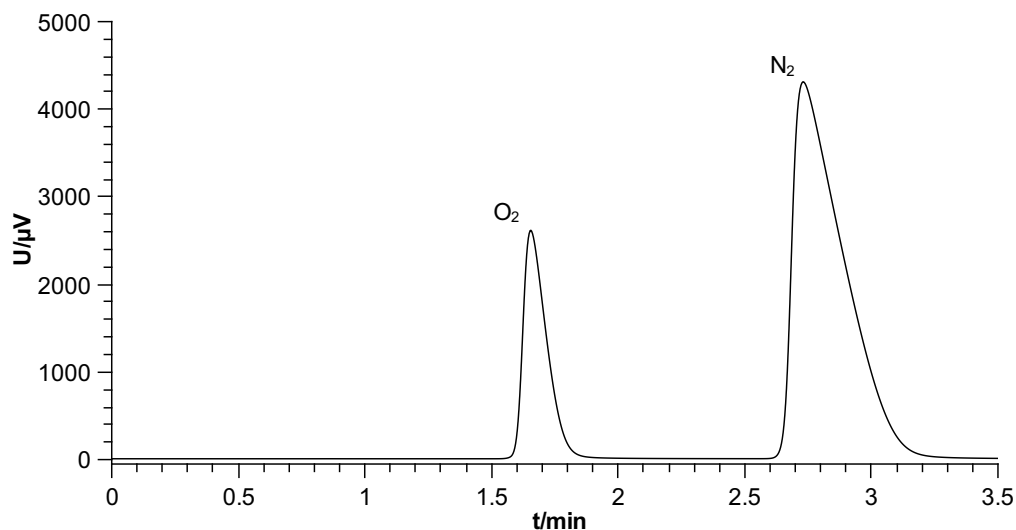


**Figure 8.1.** Exemplary GC plot. Due to different retention times on the GC columns,  $\text{O}_2$  and  $\text{N}_2$  are separated and can thus be detected individually. When one of the gases is reaching the TCD, differences in the thermal conductivity are inducing a voltage change which is recorded in dependence of time. The area under the respective curve is proportional to the amount of the distinct gas species. In our case, the evolved oxygen can then be quantified using the signal of  $\text{N}_2$  from air as a reference.

in thermal conductivity of the column effluent and the reference flow, a voltage change is induced in the TCD which is recorded *vs.* time (Figure 8.1). In this plot, the area under the curves is proportional to the amount of the detected gases. The results discussed in this section were then determined using the signal of  $N_2$  from air as a reference as its amount can be estimated from the septum vial's headspace volume and the universal gas constant (for details see section 9.2.1).

To be able to compare the results, the determined oxygen evolution rates have to be scaled versus a reference. Even as structural motifs present in the oxide materials have been elucidated, the catalytically active units of the birnessites are still completely unknown. Hence, the recorded oxygen evolution rates were calculated relative to the *catalyst mass*, the *surface area*, or the amount of *manganese ions*.

The reaction conditions in these experiments are limited by the strongly acidic pH, as  $Ce^{4+}$  ions precipitate as hydroxides in a reaction medium of  $pH > 3$ .<sup>[15]</sup> Thus, reference experiments were carried out using aqueous  $HNO_3$  at a pH of about 2 in order to make sure that oxygen evolution does not merely result from dissolving the Mn-oxides at the low pH of the catalytic mixture. In these reference experiments, no oxygen evolution could be detected (Figures 8.2, 8.4, 8.6 and 8.8).

### M-birnessites, prepared by direct synthesis

In the experiments using M-birnessites **1-13** as catalysts and  $Ce^{IV}$  as oxidant, all studied oxides showed activity in water-oxidation catalysis as oxygen evolution could be detected in all cases (Table 8.1). The  $Al_{0.02}$ -birnessite **10** was not probed, as the composition is relatively similar to  $Al_{0.03}$ -birnessite **11** and no significant amount of  $Al^{3+}$  ions is present in both structures.

The recorded oxygen evolution rates show different *performance rankings* depending on the kind of scaling method used. Per catalyst mass,  $Ca_{0.14}$ -birnessite **2** is showing the highest activity, followed by  $Ca_{0.27}$ -birnessite **3** and the Sr-birnessites **4** and **5**. The  $Mg_{0.13}$ -birnessite **6** and the  $Cd_{0.29}$ -birnessite **9** are showing the lowest activity for water-oxidation catalysis. The activities of the other materials are somewhere in between. This trend changes when the oxygen evolution rates are scaled to the surface area of the oxide materials. Then, the  $Zn_{0.20}$ -birnessite is showing the highest value, followed by  $Sr_{0.27}$ -birnessite **5**,  $K_{0.31}$ -birnessite **1** and  $Ca_{0.14}$ -birnessite **2**. Here,  $Mg_{0.28}$ -birnessite **7** and  $Cd_{0.29}$ -birnessite **9** are exhibiting the lowest activity. Scaled to the Mn content, **2** is again the most active catalyst and again it is followed by **3**, **4** and **5**. The Mg-birnessites **6** and **7** are showing the lowest activities.

Firstly, this comparison shows that the catalytic activity is depending on the method used for data analysis of the results. Furthermore, it seems that a calculation of the oxygen evolution rate per surface area is not reasonable in this case. In all experiments, about 5 mg of the respective oxides were weighed in (for sample weights, see appendix A.3). As the amount of catalyst employed in each experiment was thus relatively constant, the oxygen evolution rates scaled to the catalyst's mass is more or less corresponding to the absolute amount of evolved oxygen. Scaled to the catalyst mass, the  $Zn_{0.20}$ -birnessite **12** for instance shows a relatively low activity, comparable to that of  $Cd_{0.16}$ -birnessite **9** and about the half of  $Ca_{0.14}$ -birnessite **2**. But as **12** exhibits one of the lowest surface areas determined for all of the M-birnessites presented herein, its catalytic activity is scaled up out of proportion when the rate is calculated per  $m^2$ . As another extreme, the  $Ca_{0.27}$ -birnessite **3** is a quite active water-oxidation catalyst also showing a relatively large surface area. Calculating the activity of **3** per  $m^2$ , it is disproportionately

downscaled. The consideration of the activity in water-oxidation only calculated per m<sup>2</sup> surface area is thus misleading and has to be treated with caution.

The calculation of the catalytic activity per manganese ion seems to be the most reasonable method to scale the recorded oxygen evolution rates. Mn centers are definitively involved in the redox reaction steps of water-oxidation catalysis by the M-birnessites. However, it is not known how many Mn centers form a catalytic unit. The results are well corresponding to the values determined per catalyst mass. But when the manganese content is taken as a basis for the calculation of the rates, differences in the composition of the materials are considered as well. Thus, the analysis of the recorded oxygen evolution rates with respect to the manganese content will be discussed in more detail below (Figure 8.2). Also, comparisons of the rates per Mn to several other properties of the materials are given in order to identify trends in the catalytic activity.

In the plots of M-birnessites **1-13** of evolved oxygen per manganese ion *vs.* time (Figure 8.3), the dependency of the catalytic rate on the type of the additional cation is evident. Comparing the activity of the birnessites containing alkaline earth metal ions **2-7**, the observed trend dependent on the type of the cation can be clearly formulated as  $\text{Ca}^{2+} > \text{Sr}^{2+} > \text{Mg}^{2+}$ . The activity of the M-birnessites containing  $\text{K}^+$  (**1**),  $\text{Cd}^{2+}$  (**8, 9**),  $\text{Al}^{3+}$  (**11**),  $\text{Zn}^{2+}$  (**12**) and  $\text{Pb}^{2+}$  (**13**), respectively, is in between the activity of Sr<sub>0.27</sub>-birnessite **5** and Mg<sub>0.13</sub>-birnessite **6** (Figures 8.2 and 8.3, *a*).

The second, less distinct trend that can be observed from this set of M-birnessites is correlated to the concentration of the additional cations. Of the prepared Ca- (**2, 3**), Sr-

**Table 8.1. Catalytic activity of 1-13.**

Compound		evolved O <sub>2</sub> / μmol · g <sup>-1</sup> · h <sup>-1</sup> <sup>a</sup>	evolved O <sub>2</sub> / μmol · m <sup>-2</sup> · h <sup>-1</sup> <sup>b</sup>	evolved O <sub>2</sub> / mmol · mol(Mn) <sup>-1</sup> · h <sup>-1</sup> <sup>c</sup>
K <sub>0.31</sub> -birn.	(1)	4710	86	460
Ca <sub>0.14</sub> -birn.	(2)	8195	86	1120
Ca <sub>0.27</sub> -birn.	(3)	7055	31	880
Sr <sub>0.18</sub> -birn.	(4)	6885	66	730
Sr <sub>0.27</sub> -birn.	(5)	6160	88	530
Mg <sub>0.13</sub> -birn.	(6)	1905	25	250
Mg <sub>0.28</sub> -birn.	(7)	2500	19	220
Cd <sub>0.16</sub> -birn.	(8)	3865	70	410
Cd <sub>0.29</sub> -birn.	(9)	1860	25	320
Al <sub>0.03</sub> -birn.	(11)	3365	67	350
Zn <sub>0.20</sub> -birn. <sup>[224]</sup>	(12)	3800	127	470
Pb <sub>0.30</sub> -birn. <sup>[224]</sup>	(13)	2240	32	370

Oxygen evolution rates given in the table are rounded values obtained from experiments on water-oxidation using Ce<sup>IV</sup> as oxidant. The rates are scaled to <sup>a</sup> the employed catalyst's masses (appendix A.3), <sup>b</sup> their surface areas (Table 6.2) or <sup>c</sup> their molar manganese contents (Table A.5).

(4, 5), Mg- (6, 7) and Cd-birnessites (8, 9), the material exhibiting the minor amount of additional divalent metal cations incorporated in the structure is showing a higher catalytic activity (Figures 8.2 and 8.3, *a*). No further correlations of the catalytic activity of the respective M-birnessites to other determined parameters were found.

In a comparison of the activity in water-oxidation catalysis calculated per manganese ion to the specific surface area of 1-13, no relation can be observed (Figure 8.3, *b*). For instance  $Sr_{0.27}$ -birnessite 4 and  $Mg_{0.13}$ -birnessite 6 have similar surface areas but are showing a clearly different activity in water-oxidation. The same applies to  $Ca_{0.14}$ -birnessite 2,  $Sr_{0.27}$ -birnessite 4 and  $Mg_{0.28}$ -birnessite 7.

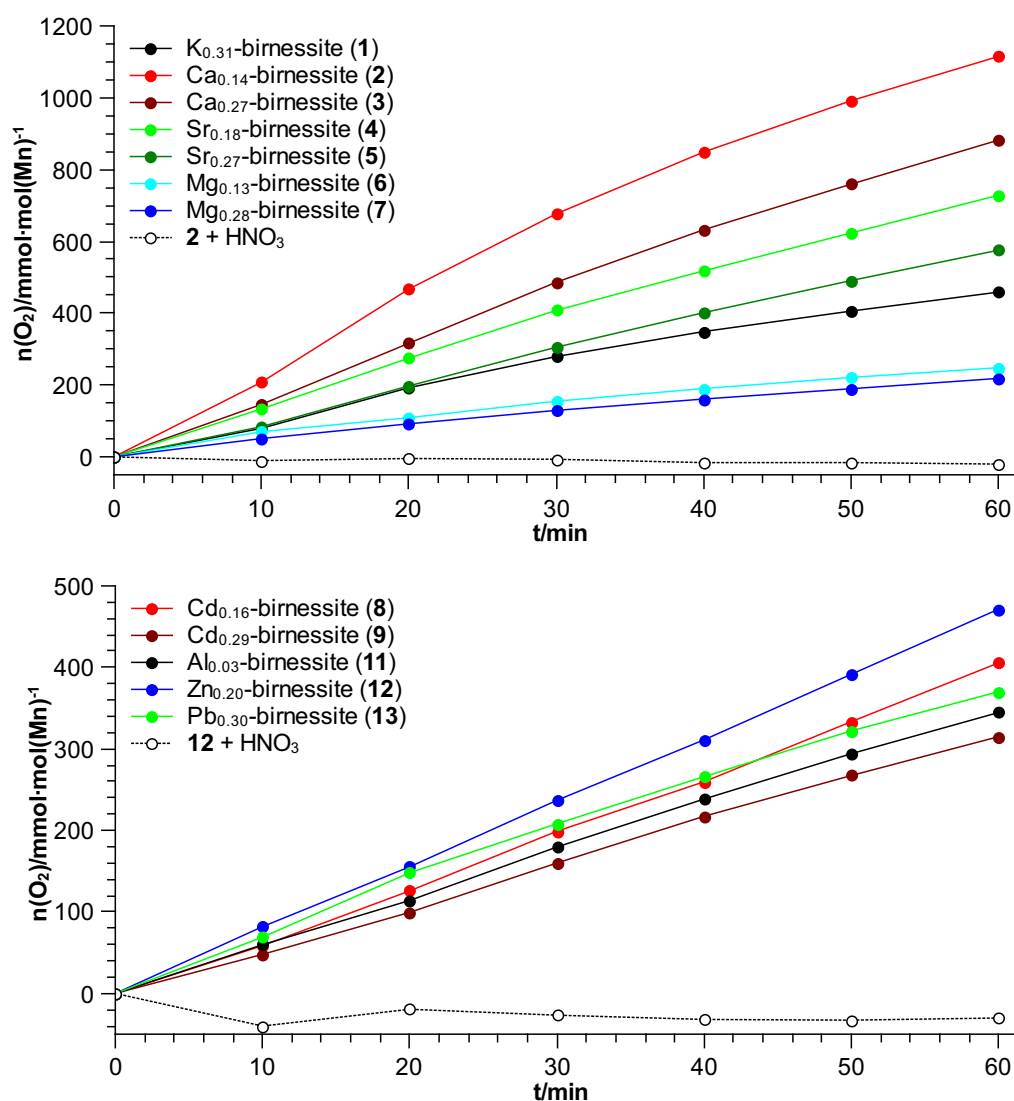


**Figure 8.2.** Oxygen evolution traces of M-birnessites 1-13. Each oxide sample ( $\sim 5$  mg) was weighed into a septum vial together with  $Ce^{IV}$  before 5 mL of  $H_2O$  were added to give an oxide suspension in a 0.25 M solution of  $Ce^{IV}$ . The progress of the reaction was then analyzed by headspace gas chromatography to detect and quantify the  $O_2$  product. No oxygen evolution could be detected in reference experiments, in which oxides 1-13 were suspended in  $HNO_3$  (pH 1.7), as shown for 2 and 12, respectively (dotted black traces).

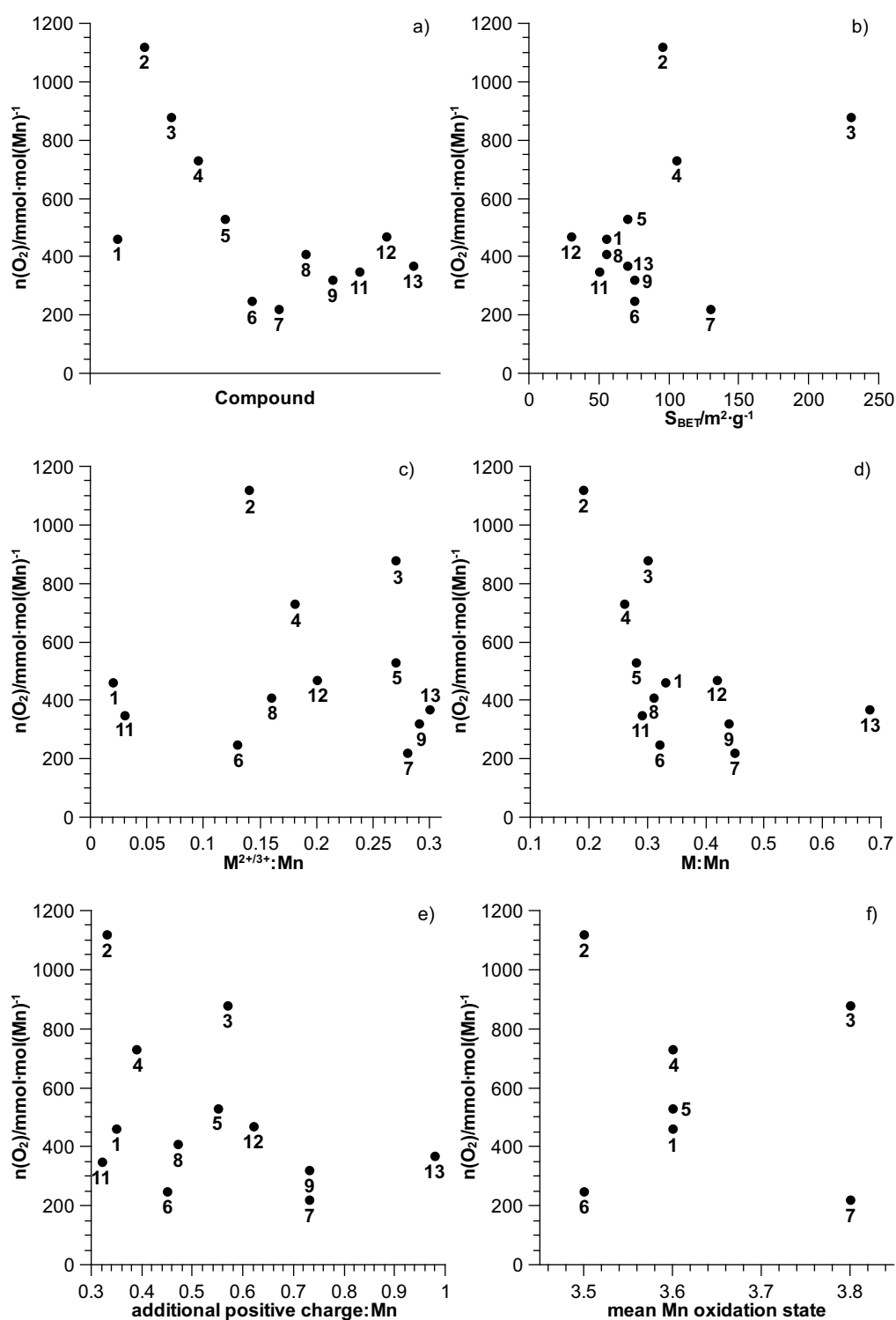


**Figure 8.3.** Catalytic activity of M-birnessites 1-13 calculated per Mn ion (a), compared to the specific surface area (b), the  $\text{M}^{2+/3+}:\text{Mn}$  ratio (c), the M:Mn ratio (d), positive charges present in the structure in addition to Mn ions (e) and the mean Mn oxidation state (f). Only correlations of the catalytic activity to the type and the concentration of the additional divalent metal cations yield trends which can be interpreted (a).

There are also oxides showing a similar amount of positive charges additional to the Mn ions but clearly different oxygen evolution rates (Figure 8.3, *c*). If only the amount of additional M<sup>2+/3+</sup> ions respective to the manganese content (Figure 8.3, *d*) or the ratio of all additional cations to manganese are compared to the activity (Figure 8.3, *e*), also no relation can be observed.

Even the mean Mn oxidation state seems not to play a key role, as values of 3.5 (**2**, **6**), 3.6 (**1**, **4**, **5**) and 3.8 (**3**, **7**) were determined, that are clearly not related to the catalytic activity of the studied materials (Figure 8.3, *f*). However, it has to be noted that an oxidation state of the manganese centers of the oxides between 3.5 and 4.0 is most likely necessary in order to catalyze the water-oxidation reaction at all.

### M-birnessites, prepared by ion exchange

In the experiments in which oxides **14-18** were probed for their ability to act as water-oxidation catalysts using Ce<sup>IV</sup> as oxidant, again all materials showed catalytic activity. As observed for M-birnessites **1-13**, the oxygen evolution rates are clearly different and trends are slightly dependent on the scaling method (Table 8.2). The oxygen evolution traces recorded for **14-18** are shown in Figure 8.4

The Ca<sub>ex</sub>-birnessite **14** is showing by far the highest catalytic activity, independent of the calculation method of the rates. Per catalyst mass as well as per manganese ion, the Fe<sub>ex</sub><sup>3+</sup>-birnessite **18** is showing the second highest activity, followed by the Mn<sub>ex</sub>-oxide **15**. Zn<sub>ex</sub>-birnessite **16** and Fe<sub>ex</sub><sup>2+</sup>-oxide **17** are showing the lowest activity per catalyst mass (**16**, **17**) or per manganese ion (**16**). As only traces of Mn were found to be present in the structure of **17** and its powder XRD pattern is likely indicating the formation of a FeO(OH) phase (*cf.* section 7.1), it is not reasonable to scale the activity of this Fe<sub>ex</sub><sup>2+</sup>-oxide material to the manganese content. It has to be noted that also the scaling per manganese ion of the activity of the Mn<sub>ex</sub>-oxide **15** might be misleading as a MnO(OH) phase has been identified from its powder XRD pattern. As discussed above, the absence of characteristic birnessite reflections in the pattern of **15** might indicate that only MnO(OH) has been formed, but it is also imaginable that an amorphous birnessite phase

**Table 8.2. Catalytic activity of 14-18.**<sup>(243)</sup>

Compound		n(O <sub>2</sub> )/ μmol · g <sup>-1</sup> · h <sup>-1</sup> <sup>a</sup>	n(O <sub>2</sub> )/ μmol · m <sup>-2</sup> · h <sup>-1</sup> <sup>b</sup>	n(O <sub>2</sub> )/ mmol · mol(Mn) <sup>-1</sup> · h <sup>-1</sup> <sup>c</sup>
Ca <sub>ex</sub> -birn. ( <b>14</b> )		9335	55	1100
Mn <sub>ex</sub> -oxide ( <b>15</b> )		2480	35	140
Zn <sub>ex</sub> -birn. ( <b>16</b> )		545	5	80
Fe <sub>ex</sub> <sup>2+</sup> -oxide ( <b>17</b> )		580	2	—
Fe <sub>ex</sub> <sup>3+</sup> -birn. ( <b>18</b> )		2925	7	480

Oxygen evolution rates given in the table are rounded values obtained from experiments on water-oxidation using Ce<sup>IV</sup> as oxidant. The rates are scaled to <sup>a</sup> the employed catalyst's mass (appendix A.3), <sup>b</sup> their surface area (Table 6.4) and <sup>c</sup> their manganese content (Table A.6). For **17**, a calculation of the oxygen evolution rate per Mn ion is not reasonable as only traces of Mn were found (*cf.* Table 6.3).

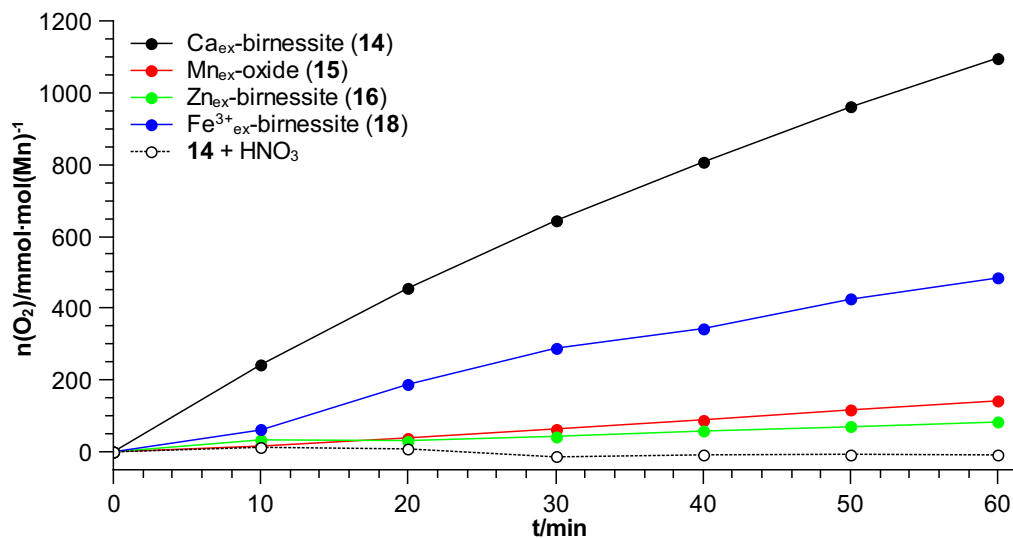


**Figure 8.4.** Oxygen evolution traces of ion exchange products **14**, **15**, **16** and **18**. Each oxide sample ( $\sim 5$  mg) was weighed into a septum vial together with  $\text{Ce}^{\text{IV}}$  before 5 mL of  $\text{H}_2\text{O}$  were added to give an oxide suspension in a 0.25 M solution of  $\text{Ce}^{\text{IV}}$ . The progress of the reaction was then analyzed by headspace gas chromatography to detect and quantify the  $\text{O}_2$  product. No oxygen evolution could be detected in reference experiments, in which **14**, **15**, **16** and **18** were suspended in  $\text{HNO}_3$  (pH 1.7), as shown for **14** (dotted black trace).

is present as well (*cf.* section 7.1). Based on the presented data it is thus not possible to assign the oxygen evolution rates calculated for **15** to a certain manganese oxide phase or to determine the activity of individual Mn centers. The investigation of the ability of a pure  $\text{MnO}(\text{OH})$  to act as water-oxidation catalyst would be very helpful but was not carried out in scope of this project.

Scaled to the specific surface area, the observed trend of the oxygen evolution rates changes. Again **14** is showing the highest activity, but here it is followed by **15**, **16** and **17**

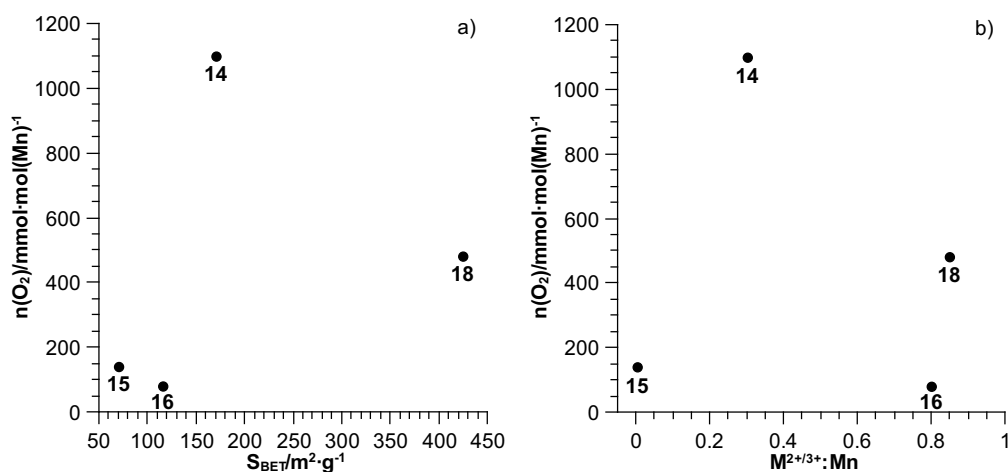


**Figure 8.5.** Catalytic activity of ion exchange products **14**, **15**, **16** and **18** compared to (a) the specific surface area and (b) the  $\text{M}^{2+/3+}:\text{Mn}$  ratio. No correlations can be observed.

are showing the lowest activity. Interestingly, the activity per surface area of **18**, which is showing the second highest activity calculated per catalyst mass or per manganese ion, is only negligible higher than that of **16**. A comparison of the catalytic activity calculated per Mn ion to the specific surface area of the oxide materials and the  $Mn^{2+/3+}$  content is again showing no correlation (Figure 8.5). A comparison of additional positive charges or the M:Mn ratio would be redundant and is thus not shown.

### K/Ca-birnessites with increasing $Ca^{2+}$ concentration

The K/Ca-birnessites **19-29** were prepared in order to investigate the influence of the concentration of  $Ca^{2+}$  ions incorporated in the birnessite structure on the activity in water-oxidation catalysis.

Firstly, oxygen evolution could be detected in all experiments using **19-29** as catalysts and  $Ce^{IV}$  as oxidant. I thus decided to carry out an additional experiment using the catalytically most active Ca-birnessites of this set. In this experiment, water of the river Rhine was used as reaction medium instead of deionized water, the other reaction parameters were not changed.

The oxygen evolution rates of all experiments were again calculated per employed catalyst mass, per specific surface area and per manganese ion (Table 8.3). The recorded oxygen evolution traces calculated per manganese ion are shown in Figure 8.6. With a

**Table 8.3. Catalytic activity of 19-29.**

Compound		evolved $O_2$ / $\mu\text{mol} \cdot \text{g}^{-1} \cdot \text{h}^{-1}$ <sup>a</sup>	evolved $O_2$ / $\mu\text{mol} \cdot \text{m}^{-2} \cdot \text{h}^{-1}$ <sup>b</sup>	evolved $O_2$ / $\text{mmol} \cdot \text{mol}(\text{Mn})^{-1} \cdot \text{h}^{-1}$ <sup>c</sup>
$K_{0.28}$ -birn. ( <b>19</b> )		2465	26	210
$Ca_{0.04}$ -birn. ( <b>20</b> )		7280	146	790
$Ca_{0.08}$ -birn. ( <b>21</b> )		7221	111	800
$Ca_{0.10}$ -birn. ( <b>22</b> )		4290	143	550
$Ca_{0.15}$ -birn. ( <b>23</b> )		5754	105	740
$Ca_{0.17}$ -birn. ( <b>24</b> )		7818	87	910
$Ca_{0.21}$ -birn. ( <b>25</b> )		9013	55	1050
$Ca_{0.21}$ -birn. <sup>d</sup> ( <b>25</b> )		8585	52	1000
$Ca_{0.28}$ -birn. ( <b>26</b> )		6680	38	800
$Ca_{0.36}$ -birn. ( <b>27</b> )		4650	19	570
$Ca_{0.54}$ -birn. ( <b>28</b> )		3380	12	480
$Ca_{0.67}$ -birn. ( <b>29</b> )		3205	14	480

Oxygen evolution rates given in the table are rounded values obtained from experiments on water-oxidation using  $Ce^{IV}$  as oxidant. The rates are scaled to <sup>a</sup> the employed catalyst's masses (appendix A.3), <sup>b</sup> their surface areas (Table 6.6) or <sup>c</sup> their molar manganese contents (Table A.7). <sup>d</sup> Instead of deionized  $H_2O$ , water of the river Rhine was used to carry out the experiment.

few exceptions (**20**, **21**, **26**) the observed trends of the catalytic activities calculated per mass and per manganese ion are consistent.  $\text{Ca}_{0.21}$ -birnessite **25** is showing the highest activity in water-oxidation catalysis, followed by  $\text{Ca}_{0.17}$ -birnessite **24**. Interestingly, when the experiment is carried out in Rhine water, the activity of **25** is only slightly decreased. Calculated per mass, the  $\text{Ca}_{0.04}$ - (**20**), the  $\text{Ca}_{0.08}$ - (**21**) and  $\text{Ca}_{0.28}$ -birnessite (**26**) are occupying the next places in the activity ranking. When the activity is calculated per manganese ion, **21** and **26** are showing the same relatively high activity, followed by **20**. Oxides **23**, **27**, **22**, **28** and **29** are showing a medium activity, again with the same gradations.  $\text{K}_{0.28}$ -birnessite **19** is the poorest catalyst of this set of oxide materials.

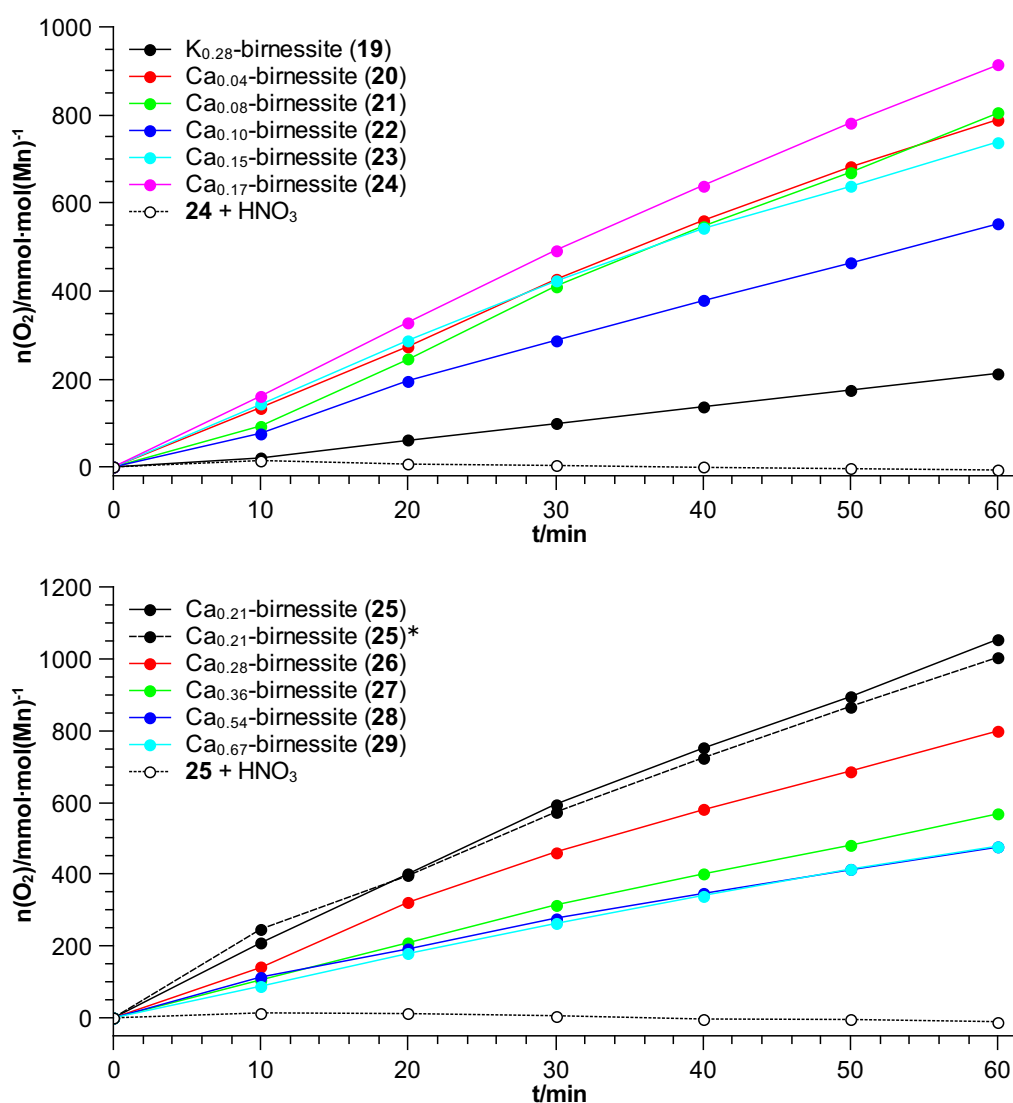


**Figure 8.6.** Oxygen evolution traces of M-birnessites **19-29**. Each oxide sample ( $\sim 5$  mg) was weighed into a septum vial together with  $\text{Ce}^{\text{IV}}$  before 5 mL of  $\text{H}_2\text{O}$  (\* water of the river Rhine) were added to give an oxide suspension in a 0.25 M solution of  $\text{Ce}^{\text{IV}}$ . The progress of the reaction was then analyzed by headspace gas chromatography to detect and quantify the  $\text{O}_2$  product. No oxygen evolution could be detected in reference experiments, in which oxides **19-29** were suspended in  $\text{HNO}_3$  (pH 1.7), as shown for **24** and **25**, respectively (dotted black traces).

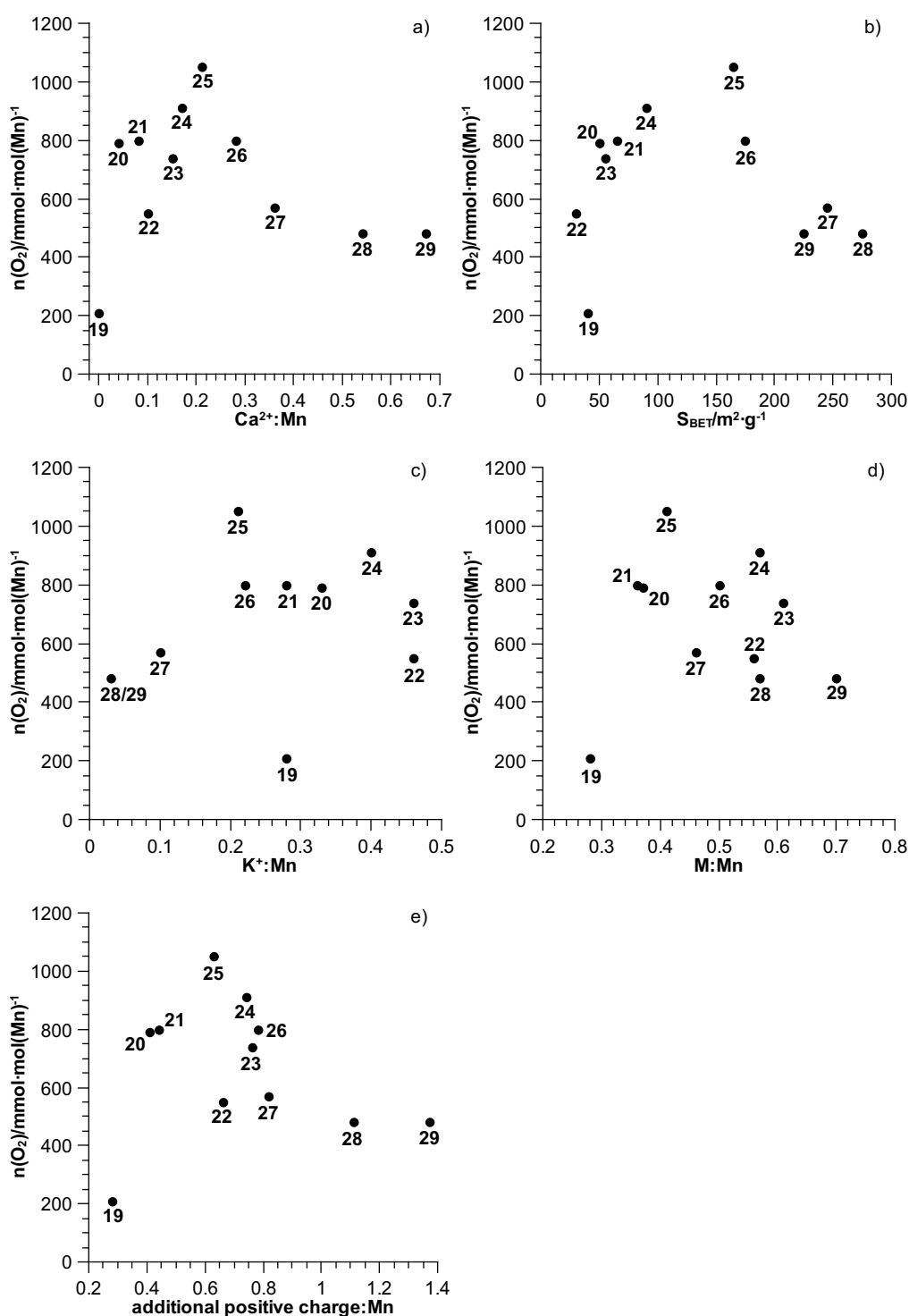


**Figure 8.7.** Catalytic activity of M-birnessites 19-29 calculated per Mn ion and compared to the  $Ca^{2+}:Mn$  ratio (a), the specific surface area (b), the  $K^+:Mn$  ratio (c), the  $M:Mn$  ratio (d) and positive charges present in the structure in addition to Mn ions (e). A correlation of the  $Ca^{2+}$  ion content and the surface area can be observed. As the surface area is related to the  $Ca^{2+}$  content, the observed correlation is a result of different amounts of  $Ca^{2+}$  incorporated in the oxide structures.

On the contrary, calculated per specific surface area, **20** is showing the highest activity, followed by **22** and **21**. Here, **28** is the material with the lowest activity. **19**, **20** and **22** are showing the smallest surface area. Their oxygen evolution rates are thus enlarged disproportionately. Hence, a scaling of the catalytic activity of the oxides **19-29** to the specific surface area is here not reasonable as well.

The catalyst ranking shows a trend in activity mainly correlated to the amount of  $\text{Ca}^{2+}$  ions incorporated in the birnessite structure. The birnessite showing the lowest catalytic activity is simultaneously the material which has been prepared without the addition of  $\text{Ca}^{2+}$  or other divalent metal ions. The presence of even small amounts of  $\text{Ca}^{2+}$  ions during the birnessite synthesis is leading to a significant increase in water-oxidation activity. This course progresses up to the medium  $\text{Ca}^{2+}$  concentration of  $\text{Ca}_{0.21}$ -birnessite **25** as the most active catalyst of this set.

When the amount of  $\text{Ca}^{2+}$  ions is further increased, the catalytic activity decreases to a medium level. In Figure 8.7, a), a plot of the water-oxidation activity calculated per manganese ion *vs.* the  $\text{Ca}^{2+}$  content of the samples, this trend is obvious. In addition, this figure clearly shows that **20** and **21** are showing a relatively high activity in respect to their quite low  $\text{Ca}^{2+}$  content.

A comparison of the activity per manganese and the specific surface area of the respective K/Ca-birnessites is also showing a correlation. With increasing surface area, the catalytic activity is also rising up to the most active oxide **25** which is showing a medium specific surface area. When the surface area is further enlarged, the catalytic activity is decreased. Considering also the correlation of the enlargement of the specific surface area with an increasing amount of  $\text{Ca}^{2+}$  ions incorporated in the structures found for oxides **19-29** (*cf.* chapter 6), the observed trend is attributable to the  $\text{Ca}^{2+}$  concentration as well and not to the surface area itself.

In Figure 8.7, c) - e), the catalytic activity per manganese ion of **19-29** is compared to the ratios of manganese to  $\text{K}^+$  ions, the sum of the metal ions additional to Mn and to additional charges originating from these cations. In all three cases, no correlation can be observed.

The fact that the catalytic activity of **25** is only slightly decreased in Rhine water is clearly showing that water-oxidation catalyzed by Ca-birnessites is even possible in non-purified water. This result is emphasizing the promising potential of these materials for a possible application in alternative energy production. Furthermore, this observation may indicate that the catalytic activity of synthetic birnessites may be optimized when deionized water as reaction medium is exchanged by a suitable buffer solution.

### **Ca-birnessites with increasing ripening time**

To study the influence of another synthetic parameter on the catalytic activity of Ca-birnessites, materials were prepared using the same  $\text{Ca}^{2+}$  ion concentration but varying ripening periods prior to the isolation of the catalyst material from the synthetic reaction mixture. In experiments on water-oxidation catalysis employing  $\text{Ce}^{\text{IV}}$  as oxidant, again all oxides showed catalytic activity. As expected from the results discussed above, the rates are again differing from each other.

The oxygen evolution rates were again calculated per employed catalyst mass, per specific surface area and per manganese ion (Table 8.4). Similar to the results discussed previously, the ranking of the catalyst's activity is dependent on the scaling method. Calculated per catalyst mass,  $\text{Ca}_{1\text{h}}$ -birnessite **31** is the most active catalyst, followed by  $\text{Ca}_{8\text{h}}$ -birnessite **34** and  $\text{Ca}_{0\text{h}}$ -birnessite **30**.  $\text{Ca}_{240\text{h}}$ -birnessite **40**,  $\text{Ca}_{12\text{h}}$ -birnessite **35** and

**Table 8.4. Catalytic activity of 30-40.**

Compound		evolved $O_2$ / $\mu\text{mol} \cdot \text{g}^{-1} \cdot \text{h}^{-1}$ <sup>a</sup>	evolved $O_2$ / $\mu\text{mol} \cdot \text{m}^{-2} \cdot \text{h}^{-1}$ <sup>b</sup>	evolved $O_2$ / $\text{mmol} \cdot \text{mol}(\text{Mn})^{-1} \cdot \text{h}^{-1}$ <sup>c</sup>
Ca <sub>0h</sub> -birn. (30)		8690	43	900
Ca <sub>1h</sub> -birn. (31)		9685	36	990
Ca <sub>2h</sub> -birn. (32)		6235	28	710
Ca <sub>4h</sub> -birn. (33)		7975	35	910
Ca <sub>8h</sub> -birn. (34)		8880	49	1170
Ca <sub>12h</sub> -birn. (35)		5215	47	1150
Ca <sub>24h</sub> -birn. (36)		6635	38	740
Ca <sub>48h</sub> -birn. (37)		8245	35	940
Ca <sub>120h</sub> -birn. (38)		7325	28	770
Ca <sub>168h</sub> -birn. (39)		5025	32	650
Ca <sub>240h</sub> -birn. (40)		5990	28	510

Oxygen evolution rates given in the table are rounded values obtained from experiments on water-oxidation using  $Ce^{IV}$  as oxidant. The rates are scaled to <sup>a</sup> the employed catalyst's masses (appendix A.3), <sup>b</sup> their surface areas (Table 6.8) or <sup>c</sup> their molar manganese contents (Table A.8).

Ca<sub>168h</sub>-birnessite **39** are at the lower end of the ranking. These results are not directly evidencing a trend in catalytic activity correlated to properties of the oxide materials. Only a relation to the ripening time could be considered. But as the activity of several materials is not following this trend, this conclusion is at least arguable.

Calculated per  $\text{m}^2$  surface area, again a trend related to the ripening time may be considered, as Ca<sub>8h</sub>-birnessite **34** and Ca<sub>12h</sub>-birnessite **35** are showing the highest activity. As both materials were prepared using a relatively short ripening period, this seems to be beneficial for catalytic activity. According to this, Ca<sub>168h</sub>-birnessite **39**, Ca<sub>120h</sub>-birnessite **38** and Ca<sub>240h</sub>-birnessite **40** are at the lower end of the activity ranking, indicating that longer ripening periods are resulting in a deactivation of the catalysts. However, similar to the oxygen evolution rates calculated per catalyst mass, outliers are also present here as oxides prepared with relatively short ripening periods are showing medium (**33**) or low activities (**32**).

The calculation of the oxygen evolution rates per manganese ion seems also to be the most reasonable method in case of Ca-birnessites **30-40** as the specific surface areas as well as the composition of the materials is varying (*cf.* section 6.4 and Table A.8). Comparing the oxygen evolution rates of **30-40** calculated per manganese ion (Figures 8.8 and 8.9, *a*), the previously discussed correlation to the ripening time is clearly visible. Up to a duration of eight to twelve hours (**34**, **35**) the activity in water-oxidation catalysis is increased. After that, the activity of the oxides is declining. But also here, outliers are present, as Ca<sub>0h</sub>-birnessites **30**, Ca<sub>1h</sub>-birnessites **31** and Ca<sub>24h</sub>-birnessites **36** are not exactly following this trend.

A comparison of the catalytic activity calculated per manganese ion with the specific surface area, the Ca:Mn molar ratio, the K:Mn molar ratio, the sum of additional metal cations per manganese as well as additional positive charges per manganese originating from the additional metal ions is showing no correlation (Figure 8.9, b-f).

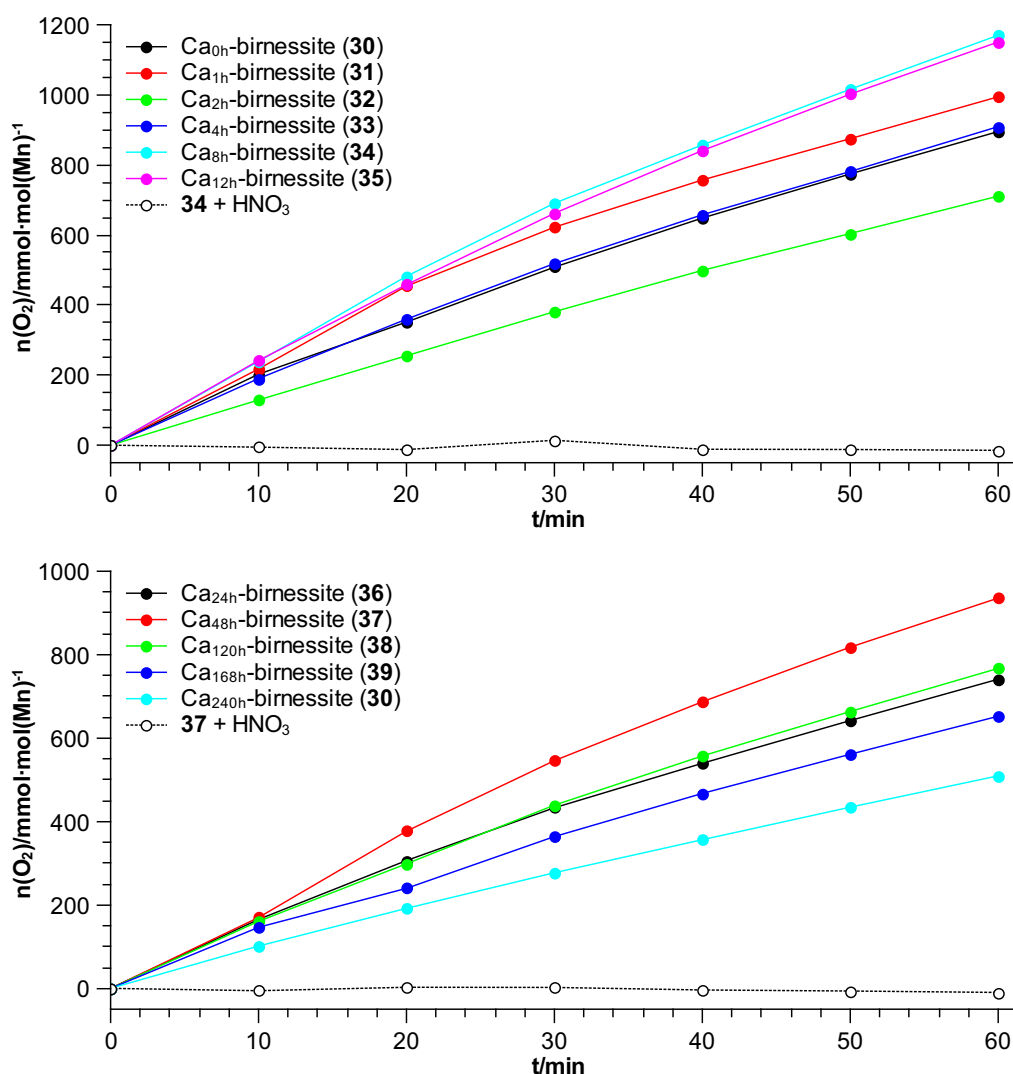


**Figure 8.8.** Oxygen evolution traces of M-birnessites **30-40**. Each oxide sample ( $\sim 5$  mg) was weighed into a septum vial together with  $\text{Ce}^{\text{IV}}$  before 5 mL of  $\text{H}_2\text{O}$  were added to give an oxide suspension in a 0.25 M solution of  $\text{Ce}^{\text{IV}}$ . The progress of the reaction was then analyzed by headspace gas chromatography to detect and quantify the  $\text{O}_2$  product. No oxygen evolution could be detected in reference experiments, in which oxides **30-40** were suspended in  $\text{HNO}_3$  (pH 1.7), as shown for **34** and **37**, respectively (dotted black traces).

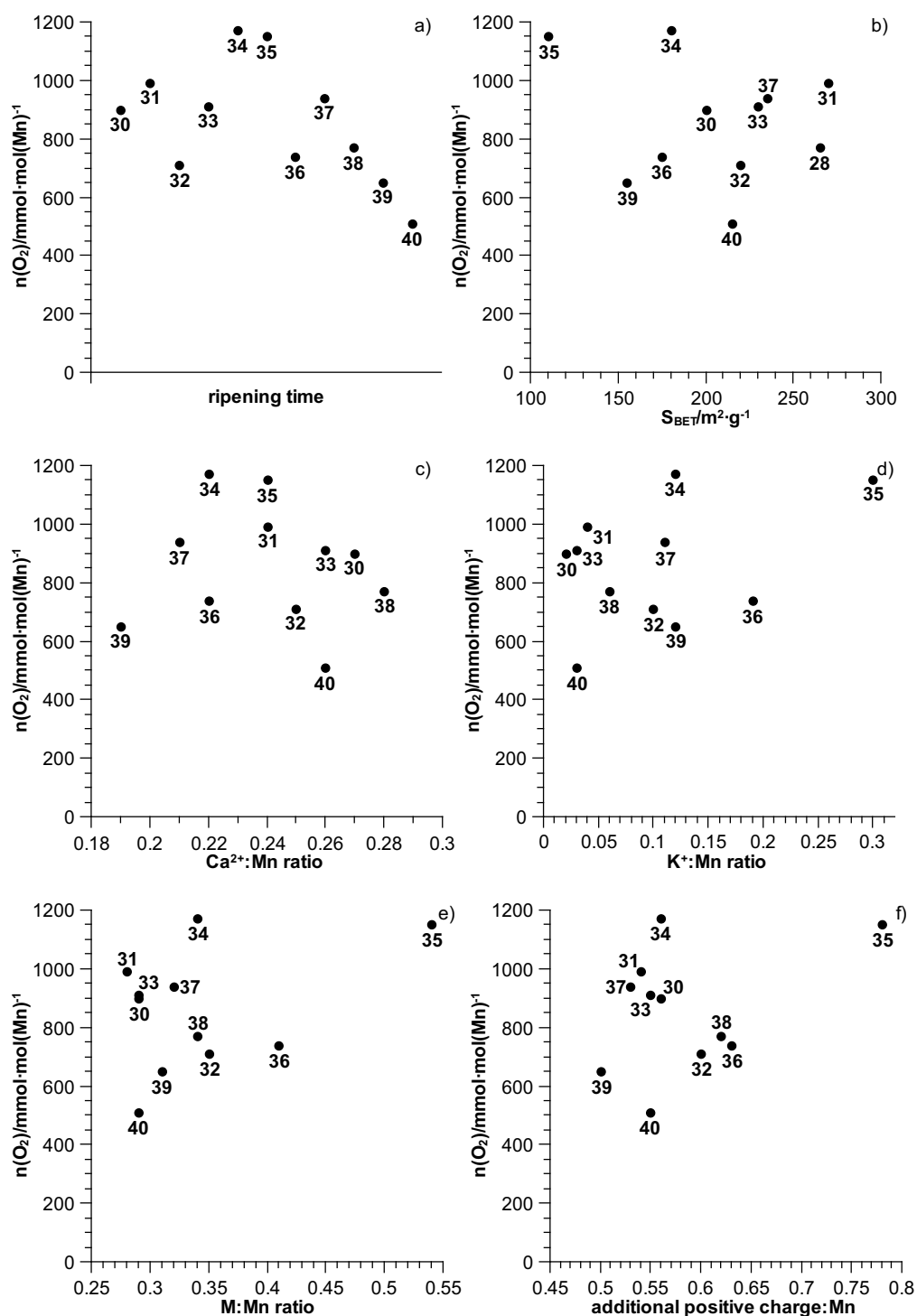


**Figure 8.9.** Catalytic activity of M-birnessites 30-40 calculated per Mn ion compared to the ripening time (a), the specific surface area (b), the  $\text{Ca}^{2+}:\text{Mn}$  ratio (c), the  $\text{K}^+:\text{Mn}$  ratio (d), the  $\text{M}:\text{Mn}$  ratio (e) and positive charges present in the structure in addition to Mn ions (f). Only a correlation of the catalytic activity to the ripening time can be observed (a).

### Concluding remarks on water-oxidation catalysis using Ce<sup>IV</sup> as oxidant

The first thing to mention is that all manganese oxide materials **1-40** (except of **10** which was not probed) are showing activity in water-oxidation catalysis in experiments using the single electron oxidant Ce<sup>IV</sup>. Amongst the studied materials, Ca-birnessites are the most active water-oxidation catalysts. Sr-birnessites are also showing a promising activity, while that of the studied Mg-, Cd-, Al-, Zn-, Pb- and Fe-birnessites is in all cases significantly lower. In general, the Mg-birnessites are showing the lowest activity. Thus, a correlation of the catalytic activity to the type of additional metal cations incorporated in the birnessite structure is evident. This trend can be formulated as  $\text{Ca}^{2+} > \text{Sr}^{2+} > \text{Mg}^{2+} / \text{Cd}^{2+} / \text{Al}^{3+} / \text{Zn}^{2+} / \text{Pb}^{2+} / \text{Fe}^{3+}$ . Furthermore, less distinct correlations between the ion concentration (especially Ca<sup>2+</sup>) as well as to the ripening period applied during the synthesis have been demonstrated. Overall, Ca<sub>0.14</sub>- (**2**), Ca<sub>ex</sub>- (**14**), Ca<sub>0.21</sub>- (**25**), Ca<sub>8h</sub>- (**34**) and Ca<sub>12h</sub>-birnessite (**35**) are the most active water-oxidation-catalysts.

In Table 8.5, an overview of some parameters of **2**, **14**, **25**, **34** and **35** is given. It is important to note that an extensive comparison of the catalytic activity of the materials is complicated as some properties are related to each other. If, for instance, the composition of the materials is changed, also the size of the surface area is affected. However, a rough comparison shows that the properties of the materials are similar, but definitely not identical. Ranging from 95 to 180 m<sup>2</sup> · g<sup>-1</sup>, the size of the specific surface area of **2**, **14**, **25**, **34** and **35** is not varying greatly and is in the midrange. None of the birnessites showing the largest specific surface areas are belonging to the most active catalysts. The M<sup>+</sup>:Mn molar ratios found for Ca-birnessites **2**, **14**, **25**, **34** and **35** are ranging from low to relatively high values. These comparisons are indicating that the amount of monovalent metal ions present in the oxide structures is most likely not playing a key role for the catalytic activity of the oxide materials.

Interestingly, also the Ca<sup>2+</sup>:Mn molar ratio found in the most active catalysts is varying in a range from 0.14 to 0.30. The amount of incorporated Ca<sup>2+</sup> ions in the Ca<sub>ex</sub>-birnessite **14** of 0.30 per Mn is considerably high compared to the most active catalyst of the set prepared with increasing Ca<sup>2+</sup> ion concentrations (**19-29**), Ca<sub>0.21</sub>-birnessite **25**. The Ca-birnessites containing Ca<sup>2+</sup> ions in similar amounts as **14** (**3**, **26**, **30**, **38**) are all less active in water-oxidation catalysis. Comparing these oxides with **14** in more detail, the most obvious difference is their preparation method. While **3**, **26**, **30** and **38** were synthesized in a direct approach (*cf.* sections 9.1.1, 9.1.3 and 9.1.4), **14** was prepared via ion exchange from a Ca-buserite precursor (*cf.* section 9.1.2).

Having a closer look to the oxygen evolution traces of **2**, **14**, **25**, **34** and **35** shown in Figures 8.2, 8.4, 8.6 and 8.8 it can be seen that the observed rates decrease slightly over the timescale of the experiment. In the initial study we already found that about 10 % of the total amount of Ca<sup>2+</sup> are removed from the birnessite structures under the same reaction conditions.<sup>[214]</sup> Recently, Najafpour *et al.* demonstrated that a Ca-birnessite which has been employed in experiments for water-oxidation can be reactivated by the treatment with a CaCl<sub>2</sub> solution.<sup>[292]</sup> Thus, removal of Ca<sup>2+</sup> ions during the water-oxidation experiment could explain the observed decline in catalytic activity.

The use of calcium containing buffers in future experiments on water-oxidation thus appears to be a promising approach in order to enhance long-term stability of the catalytic rates. In respect to a possible application in an artificial photosynthetic process for alternative energy production, also other reaction media than a calcium buffer or Rhine water have to be tested. Additionally, the results summarized above are giving impli-

**Table 8.5. Overview of parameters of 2, 14, 25, 34 and 35.**

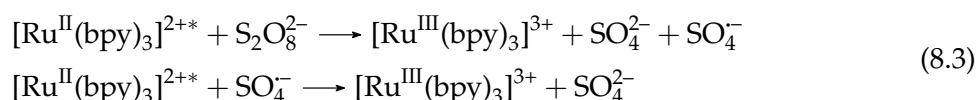
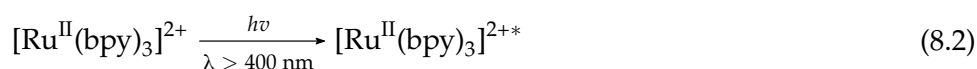
Compound		$n(\text{O}_2)/$ $\text{mmol} \cdot \text{mol}(\text{Mn})^{-1} \cdot \text{h}^{-1}$	surface area $\text{m}^2 \cdot \text{g}^{-1}$	$\text{Ca}^{2+}:\text{Mn}$ ratio	$\text{M}^+:\text{Mn}$ ratio
$\text{Ca}_{0.14}$ -birn.	(2)	1120	95	0.14	0.05
$\text{Ca}_{\text{ex}}$ -birn. <sup>[243]</sup>	(14)	1110	170	0.30	—
$\text{Ca}_{0.21}$ -birn.	(25)	1050	165	0.21	0.21
$\text{Ca}_{8\text{h}}$ -birn.	(34)	1170	180	0.22	0.12
$\text{Ca}_{12\text{h}}$ -birn.	(35)	1150	110	0.24	0.30

cations for optimizations of M-birnessites as water-oxidation catalysts as further modifications of the materials are showing a great potential to improve the catalytic performances. A combination of different  $\text{Ca}^{2+}$  concentrations, ion exchange steps and ripening times may lead to the formation of much more active Ca-birnessite catalysts. Also annealing steps should be included in future experiments, as Najafpour *et al.* already showed that heating the oxide materials to 400 °C is resulting in an increased activity in water-oxidation.<sup>[214]</sup> Additionally, the development of better electron-transfer-chains connecting the oxide materials as catalysts and the oxidant is crucial for applications in artificial photosynthesis. Of course, also the ability of M-birnessites to act as catalysts in light-driven water-oxidation is of general interest and has thus been focused on experiments of the following part of the project.

## 8.2 Water-oxidation catalysis using $(\text{Ru}^{\text{III}}(\text{bpy})_3)^{3+}$ as oxidant

In another series of oxygen evolution experiments, *in situ* generated  $[\text{Ru}^{\text{III}}(\text{bpy})_3]^{3+}$  was used as single electron oxidant. Providing a potential of  $\sim +1.3$  V *vs.* NHE<sup>[293]</sup>, this single-electron oxidant is also able to drive the water-oxidation reaction.<sup>[171,290,291]</sup> As mentioned above, it has also been shown that oxygen evolved in experiments using  $[\text{Ru}^{\text{III}}(\text{bpy})_3]^{3+}$  is entirely originating from water-oxidation.<sup>[170]</sup>

By the absorption of visible light ( $\lambda > 400$  nm),  $[\text{Ru}^{\text{II}}(\text{bpy})_3]^{2+}$  is transformed into its excited state,  $[\text{Ru}^{\text{II}}(\text{bpy})_3]^{2+*}$  (eq. 8.2).  $[\text{Ru}^{\text{II}}(\text{bpy})_3]^{2+*}$  can then be quenched either reductively or oxidatively, dependent on the applied reaction conditions. In the presence of suitable sacrificial electron acceptors like  $[\text{Co}^{\text{III}}(\text{NH}_3)_5\text{Cl}]^{2+}$  or  $\text{S}_2\text{O}_8^{2-}$ ,  $[\text{Ru}^{\text{II}}(\text{bpy})_3]^{2+*}$  is emitting an electron to the acceptor, forming the strong oxidant  $[\text{Ru}^{\text{III}}(\text{bpy})_3]^{3+}$  (eq. 8.3). The oxidizing equivalents required for water-oxidation then have to be accumulated by a fourfold oxidation (per  $\text{O}_2$  molecule) of the catalyst material by  $[\text{Ru}^{\text{III}}(\text{bpy})_3]^{3+}$ .



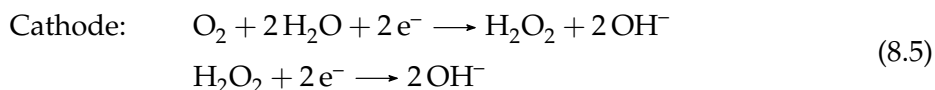
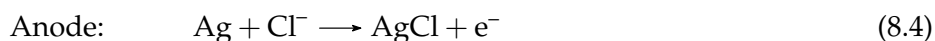
Water-oxidation catalysis under the use of photochemically generated  $[\text{Ru}^{\text{III}}(\text{bpy})_3]^{3+}$  is thus resembling the reaction sequence of photosynthetic water-oxidation within PSII. There, P680 is transformed into its excited state by the absorption of sunlight, which is then acting as initial electron donor, forming  $\text{P680}^+$ .  $\text{P680}^+$  is then re-reduced by an electron abstracted from the water-oxidation catalyst, the OEC (*cf.* section 2.1.3).

In contrast to the experiments using  $\text{Ce}^{\text{IV}}$  as an oxidant, a broader pH range ( $\text{pH} \leq 5$ ) can be applied by the use of different buffers.<sup>[171,290]</sup> But the buffer conditions are strongly influencing the oxygen evolution rate. Using colloidal  $\text{IrO}_2$  as catalyst for water-oxidation, Hara *et al.* screened several buffer systems ( $\text{pH}$  4.5-5.8) and investigated oxygen evolution as well as the decomposition of the photosensitizer.<sup>[290]</sup> They reported that the decomposition reaction via nucleophilic attack of  $\text{H}_2\text{O}$  on the bpy ligand and the formation of  $\text{bpyOH}$  occurs faster in phosphate buffers. Thus, Hara *et al.* used  $\text{SiF}_6^{2-}$  containing buffes, as  $\text{SiF}_6^{2-}$  and its hydrolysis products are very weak nucleophiles.<sup>[290]</sup>

In  $\text{Na}_2\text{SiF}_6/\text{NaHCO}_3$  buffer at  $\text{pH} \sim 5$ , the authors could improve the lifetime of the ruthenium photosensitizer and the turnover number of its reaction cycle (*i. e.* the reactions given in eqs. 8.2 and 8.3).<sup>[290]</sup> But even if the decomposition of the photosensitizer is not competing kinetically with oxygen evolution, it remains to be an issue. Furthermore, the amount of evolved oxygen is still relatively low compared to experiments using  $\text{Ce}^{\text{IV}}$  and is thus difficult to quantify by headspace gas chromatography.

However, experiments on water-oxidation catalysis were carried out using  $\text{Ca}_{0.14}$ - (1),  $\text{Ca}_{0.27}$ - (3),  $\text{Sr}_{0.18}$ - (4),  $\text{Mg}_{0.13}$ - (6) and  $\text{Ca}_{0.21}$ -birnessite (25) as well as commercial  $\text{RuO}_2$  as catalysts and photochemically generated  $[\text{Ru}^{\text{III}}(\text{bpy})_3]^{3+}$  as the oxidant. For the catalytic runs, a  $\text{Na}_2\text{SiF}_6/\text{NaHCO}_3$  buffer solution ( $\text{pH} \sim 5$ ) was added in the dark to a solid mixture of the oxide powders and  $[\text{Ru}^{\text{II}}(\text{bpy})_3]^{2+}$  (for details see section 9.2.2). Prior to the irradiation with visible light, the resulting suspensions were purged with  $\text{N}_2$ . Oxygen evolution was detected using a Clark type electrode placed in the reaction vessel.

The Clark electrode was originally designed to measure the oxygen content of blood continuously.<sup>[294]</sup> It consists of two polarized electrodes, a cathode (usually Pt) and an anode (here Ag/AgCl). The electrodes are separated from the sample solution by a gas permeable membrane (here silicone). When oxygen is present in the sample solution, it diffuses through the membrane to the cathode where it is stepwise reduced (eq. 8.5), while  $\text{Ag}^0$  from the anode is oxidized to  $\text{Ag}^+$  (eq. 8.4).



The resulting current is proportional to the  $\text{O}_2$  concentration in the sample solution. When the Clark electrode is calibrated, *e. g.* by measuring the current of  $\text{O}_2$  saturated and Ar or  $\text{N}_2$  purged  $\text{H}_2\text{O}$  in addition to the sample solution, it is possible to determine the  $\text{O}_2$  concentration of the aqueous solution under investigation. The oxygen evolution rates can then be obtained from the slope of the plot of evolved oxygen *vs.* time (for details see section 9.2.2).

In the experiments carried out and evaluated in this way, all of the studied oxide materials showed activity in water-oxidation catalysis (Figure 8.10 and Table 8.6).  $\text{RuO}_2$  was probed as a reference because in the literature it is often reported as highly active water-oxidation catalyst.<sup>[122-124,150,155,195]</sup> Actually, here it is also the most active catalyst

among the studied oxide materials showing an oxygen evolution rate about six times higher than the most active birnessite.  $\text{Ca}_{0.21}$ -birnessite **25** is the most active manganese oxide catalyst. It also was one of the most active catalysts in the water-oxidation experiments using  $\text{Ce}^{\text{IV}}$  as oxidant (cf. Table 8.5). Interestingly, the activity of  $\text{Ca}_{0.14}$ -birnessite **1**, also one of the most active catalysts in water-oxidation experiments using  $\text{Ce}^{\text{IV}}$ , is only on the midrange. In the cerium experiments, the  $\text{Ca}_{0.27}$ -birnessite **3** also showed good activity in water-oxidation catalysis, but was less active than **2** (cf. Table 8.1). In the experiments here, when  $[\text{Ru}^{\text{III}}(\text{bpy})_3]^{3+}$  was used, the ranking of the activity of **2** and **3** has switched. As more than a year passed between the cerium and the ruthenium experiments, the activity of **2** was again investigated as described in section 8.1, showing similar results as the initial experiments. Thus, the lower activity can not be assigned to a deactivation of the material through aging, e. g. by alterations of the birnessite. Thus, the changed trend might be explained for example by a pH dependence of the catalytic activity. The influence of other reaction conditions may also play an important role.

However, the general trend observed in the  $\text{Ce}^{\text{IV}}$  water-oxidation experiments carried out using **1-13** as catalysts is also found here for the photocatalytic reactions. Comparing the M-birnessites containing  $\text{Ca}^{2+}$  (**2**, **3**, **25**),  $\text{Sr}^{2+}$  (**4**) and  $\text{Mg}^{2+}$  (**6**), respectively, the trend in activity can be formulated as  $\text{Ca}^{2+} > \text{Sr}^{2+} > \text{Mg}^{2+}$ . While the  $\text{Sr}_{0.18}$ -birnessite **4** is showing a medium activity, the oxygen evolution rate of the  $\text{Mg}_{0.13}$ -birnessite **6** is only slightly above the detection limit.

Furthermore, the oxygen evolution traces given in Figure 8.10 demonstrate that  $\text{RuO}_2$

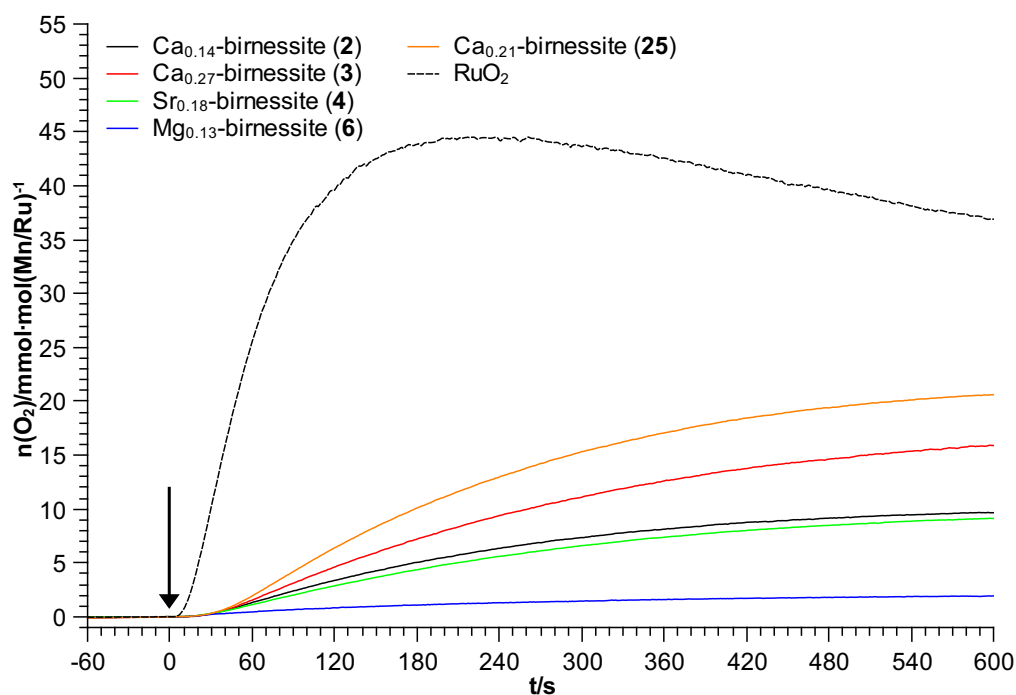


**Figure 8.10.** Oxygen evolution traces of M-birnessites **2**, **3**, **4**, **6**, **25** and  $\text{RuO}_2$ . In the dark, 10 mL of a  $\text{Na}_2\text{SiF}_6/\text{NaHCO}_3$  buffer (pH 5.2) were added to a mixture of the oxide sample ( $\sim 5$  mg),  $(\text{Ru}^{\text{II}}(\text{bpy})_3)^{2+}$  ( $\sim 7.5$  mg) and  $\text{K}_2\text{S}_2\text{O}_8$  ( $\sim 27$  mg). After purging the reaction mixture in the closed reaction vessel, light was switched on (indicated by the arrow). The progress of the reaction was then analyzed by a Clark electrode to detect and quantify the  $\text{O}_2$  product.

**Table 8.6. Oxygen evolution rates of 2, 3, 4, 6, 25 and RuO<sub>2</sub>.**

Compound		$n(\text{O}_2)/$ $\mu\text{mol} \cdot \text{mol}(\text{Mn})^{-1} \cdot \text{s}^{-1}$
Ca <sub>0.14</sub> -birn.	(2)	34
Ca <sub>0.27</sub> -birn.	(3)	51
Sr <sub>0.18</sub> -birn.	(4)	29
Mg <sub>0.13</sub> -birn.	(6)	6
Ca <sub>0.21</sub> -birn.	(25)	75
RuO <sub>2</sub>		415

Oxygen evolution rates given in the table are rounded values obtained from experiments on water-oxidation using the photochemically generated single electron oxidant  $(\text{Ru}^{\text{III}}(\text{bpy})_3)^{3+}$ . The rates are scaled to the manganese content of the oxides (Table A.8).

is not only showing a higher oxygen evolution rate, the entire course of the reaction is accelerated. Water-oxidation already started ten seconds after the beginning of illumination of the suspension. After about three minutes the reaction was over. The decay of the detected amount of O<sub>2</sub> is resulting from equilibration with the headspace, which was purged with N<sub>2</sub> during the whole reaction. The oxygen evolution rates of the birnessites 2, 3, 4, 6 and 25 are showing a similar, but much slower reaction course. Using these materials as water-oxidation catalysts, oxygen evolution started about thirty seconds after the beginning of illumination. A decay of the detected amount of O<sub>2</sub> could not be observed for the first ten to fifteen minutes of illumination. In order to investigate this observation in more detail, it would be necessary to study kinetics of the water-oxidation reaction catalyzed by M-birnessites and RuO<sub>2</sub>.

### 8.3 Birnessites vs. the OEC, a comparison of the catalytic activity

First of all, one should keep in mind that a comparison of the mechanisms of water-oxidation catalysis of oxide powders to that of the active site of the PSII metalloenzyme is of course only possible in a restricted manner. PSII contains not only the CaMn<sub>4</sub>O<sub>5</sub> cluster as its active site for water-oxidation, but also channels for proton management and the transport of H<sub>2</sub>O and O<sub>2</sub>, repair mechanisms and, particularly, an amazingly optimized and elaborate electron-transfer chain (*cf.* section 2.2). In other words, water-oxidation catalyzed by PSII is a strictly regulated and directed sequence of reactions.<sup>[26,28,29,64,65]</sup> Water-oxidation catalyzed by birnessites on the contrary is initialized by redox processes occurring between birnessite particles and randomly diffusing Ce<sup>IV</sup> ions and  $[\text{Ru}^{\text{III}}(\text{bpy})_3]^{3+}$  molecules, respectively.

The differences are reflected in the extremely divergent oxygen evolution rates found for PSII in comparison to the described test system for catalysis by birnessites. Water-oxidation catalyzed by the most active birnessites proceeds with the formation of about 1.2 oxygen molecules per manganese ion and hour ( $\sim 3 \cdot 10^{-4} \text{ s}^{-1}$ ). Showing a turnover

frequency of about  $400 \text{ s}^{-1}$  ( $100 \text{ s}^{-1}$  per manganese)<sup>[29]</sup>, oxygen evolution catalyzed by the OEC is faster by a factor of approximately  $3 \cdot 10^5$ . Thus, the absolute turnover frequencies of PSII and the prepared oxide materials can hardly be compared.

However, as described in the introductory part, the reactivity of the OEC is strongly dependent on the presence of  $\text{Ca}^{2+}$  ions (*cf.* section 2.2.2). If calcium is removed from the OEC or exchanged by  $\text{Mg}^{2+}$ , the water-oxidation reaction is inhibited.<sup>[84–89]</sup> In contrast, the substitution with  $\text{Sr}^{2+}$  is resulting in the restoration of the activity of the protein, though at a lower reaction rate.<sup>[84–86,90]</sup> Thus, a ranking of the catalytic activity of the OEC dependent on the type of the alkaline earth cation can be formulated as  $\text{Ca}^{2+} > \text{Sr}^{2+} \gg \text{Mg}^{2+}$ .<sup>[84,86]</sup> Interestingly, this trend is identical to the results of the activity studies on synthetic birnessites containing alkaline earth cations carried out here, regardless whether  $\text{Ce}^{\text{IV}}$  or  $[\text{Ru}(\text{bpy})_3]^{3+}$  were used as oxidants at pH values of 2 or 5, respectively (*cf.* sections 8.1 and 8.2).<sup>[223]</sup>

To be able to discuss the influence of alkaline earth cations on the catalytic activity in more detail, relative oxygen evolution rates for the respective M-birnessites from this work are compared with those for the  $\text{Ca}^{2+}$ ,  $\text{Sr}^{2+}$ ,  $\text{Mg}^{2+}$  and  $\text{Na}^+$  reactivated OEC reported in the literature (Figure 8.11). Two different datasets for reactivated PSII are shown (green bars).<sup>[84,86]</sup> In each case the activity of the  $\text{Ca}^{2+}$  reactivated enzyme was set to 100 %. On the oxides' side, the activity of  $\text{Ca}_{8\text{h}}$ -birnessite **34**,  $\text{Sr}_{0.18}$ -birnessite **4** and  $\text{Mg}_{0.13}$ -birnessite **6** is shown (dark brown bars). These materials were selected as they are the most active catalysts containing the respective alkaline earth cations in the experiments using  $\text{Ce}^{\text{IV}}$  as oxidant. In addition, the activity of  $\text{K}_{0.28}$ -birnessite **19** is shown as this oxide has been prepared in the absence of alkaline earth cations (or any other additional divalent metal ions). Furthermore, relative oxygen evolution rates of  $\text{Ca}_{0.21}$ -birnessite **25**,  $\text{Sr}_{0.18}$ -birnessite **4** and  $\text{Mg}_{0.13}$ -birnessite **6** are given, determined using photochemically generated  $[\text{Ru}^{\text{III}}(\text{bpy})_3]^{3+}$  as oxidant (light brown bars). As a birnessite free of alkaline earth cations was not probed in photochemical water-oxidation experiments, such data cannot be shown. According to the data of PSII, the activity of the selected M-birnessites is shown relative to the activity of the respective Ca-birnessites, which was set to 100 %.

The differences between the relative oxygen evolution rates of the OEC and the M-birnessites containing the different alkaline earth cations are showing striking similarities. Not only the general trends mentioned above, but also the quantitative comparisons are rather consistent. But differences between the datasets cannot be denied. It is important to note that the catalytic activities observed for the  $\text{Ca}^{2+}$  depleted, not reactivated OEC (activity of Na-OEC in Figure 8.11) and for the  $\text{Mg}^{2+}$  exchanged enzyme could originate from a number of PSII ensembles for which  $\text{Ca}^{2+}$  removal was incomplete.<sup>[86]</sup> As already mentioned, the removal of  $\text{Ca}^{2+}$  or its substitution with  $\text{Mg}^{2+}$  ions results in a virtually complete inactivation of the enzyme. In contrast, Mg- and K-birnessites are at least slightly to moderately active water-oxidation catalysts. So, PSII seems to react more pronounced to cation substitution than the M-birnessites. But this is no surprise, as small changes can have a strong impact in biological systems and the OEC is optimized to bind  $\text{Ca}^{2+}$ .

Nevertheless, the presented results are indicating possible similarities in the role of the alkaline earth cations for both, M-birnessites and the OEC. According to the structural similarities of the M-birnessites containing the respective alkaline earth cations (section 7.2) and of  $\text{Ca}^{2+}$  and  $\text{Sr}^{2+}$  containing OEC as demonstrated by Cox *et al.*<sup>[91]</sup>, a sheer structural role seems to be very unlikely. Rather, the results are indicating a functional role

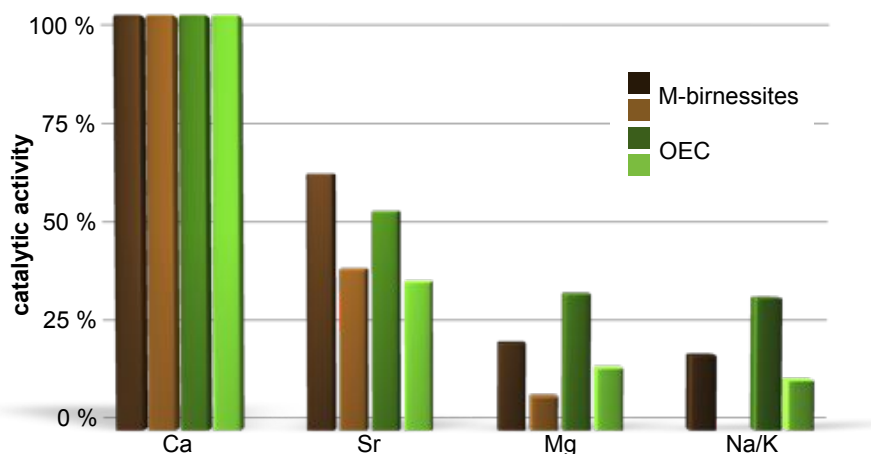


**Figure 8.11.** Relative catalytic activities of M-birnessites **34**, **4**, **6** and **19** determined using  $\text{Ce}^{\text{IV}}$  as oxidant (dark brown) and of **25**, **4** and **6** determined using photochemically generated  $(\text{Ru}^{\text{III}}(\text{bpy})_3)^{3+}$  as oxidant (light brown, activity of **34** and **25**, respectively, was set to 100 %) in comparison to  $\text{Ca}^{2+}$  depleted PSII, reactivated with  $\text{Ca}^{2+}$ ,  $\text{Sr}^{2+}$ ,  $\text{Mg}^{2+}$  or  $\text{Na}^+$  solutions (dark green<sup>[84]</sup> and light green<sup>[86]</sup>, activity of Ca-reactivated PSII was set to 100%).

of  $\text{Ca}^{2+}$  (and also  $\text{Sr}^{2+}$ ) in water-oxidation catalysis. Together with common structural motifs found for M-birnessites and the OEC (*cf.* section 7.3), the similarities found in the relative catalytic activities are indicating possible similarities in the water-oxidation mechanism for both, M-birnessites and the OEC.<sup>[223]</sup>

For PSII's  $\text{CaMn}_4\text{O}_5$  cluster, it has been suggested that  $\text{Ca}^{2+}$  may act as binding and activation site for substrate water.<sup>[36,79,80,95–97]</sup> The same function is also imaginable for birnessites.<sup>[215,223]</sup> Thus, the  $\text{Ca}^{2+}$  ions are probably involved in the O–O bond formation step in both catalytic systems (*cf.* sections 2.2.2 and 8.4). Furthermore,  $\mu$ -oxido or  $\mu$ -hydroxido bridges have been proposed to play a key role in proton management at the OEC. To accumulate the required redox equivalents, PCET is essential.<sup>[28,29,64–66]</sup> The protein environment is of course also playing a crucial role in the abstraction and transport of protons in biological water-oxidation.<sup>[25–29]</sup> In M-birnessites such a network of organic residues is not present. But  $\mu$ -oxido and  $\mu$ -hydroxido bridges of the oxide structure could be actively involved in water-oxidation catalysis.<sup>[223]</sup> The  $\mu$ -O bridges are probably required for proton abstraction from substrate water. Deprotonation of  $\mu$ -OH bridges could contribute to the necessary charge compensation for the accumulation of several oxidation equivalents before O–O bond formation occurs. In addition, the oxido bridges may play a key role in multi-step long-distance proton transfer within and at the surface of the synthetic catalysts and may thus substitute for proton channels of PSII's protein matrix.<sup>[223]</sup>

## 8.4 Possible mechanisms for the O–O bond formation

The similarities of structural motifs and of the relative oxygen evolution rates between the OEC and M-birnessites, and also the possible similarities in their water-oxidation mechanisms are raising the question if scenarios proposed for the O–O bond formation step in water-oxidation catalyzed by the OEC can be adopted to our synthetic manganese oxide catalysts as well.

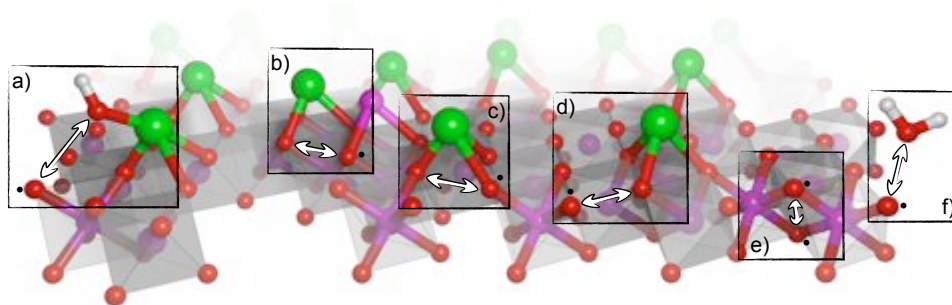


**Figure 8.12.** Possible routes for O–O coupling in water-oxidation catalyzed by M-birnessites adopted from mechanistic proposals for the OEC (color code as in Figure 7.10). a) Ca (or Sr) is acting as binding and activation site for a nucleophilic attack by hydroxide to a terminal oxyl radical. Terminal or bridging oxygens are also discussed to be involved in schemes for the O–O bond formation, where always one oxygen may be present as an oxyl radical. Here, the O–O bond may form between two bridging oxygens, activated by Ca (b), a  $\mu_2$ - and a  $\mu_3$ -O<sup>2-</sup>, both bound to Ca (c), one terminal and one  $\mu_3$ -oxygen (d), or between two  $\mu_2$ -oxygen atoms of the oxide layer (e). Furthermore, a mechanism where substrate water is directly coupled to a terminal oxyl radical (f) can be considered.

For the OEC, it is mostly assumed that oxygen evolution takes place via the formation of a peroxide intermediate as the rate-limiting step.<sup>[26,29]</sup> In the various mechanistic scenarios that are under discussion (*cf.* section 2.2.2), bridging or terminal O<sup>2-</sup> or O<sup>-</sup> ligands are considered to be involved in the formation of the transition state. OH<sup>-</sup> or H<sub>2</sub>O molecules in vicinity of the OEC could also play a key role in the pathway leading towards oxygen evolution.<sup>[28,29,64–66]</sup> Ca<sup>2+</sup> as Lewis acid could act as binding and/or activation site.<sup>[36,79,80,95–97]</sup>

As discussed previously, the structural motifs necessary for these reaction pathways were also identified to be present in layered manganese oxides (*cf.* sections 7.2 and 7.3). Interestingly, these motifs are most likely in a suitable orientation to facilitate the O–O bond formation in scenarios similar to those suggested for the OEC (*cf.* Figure 2.10).<sup>[26,29]</sup> Therefore it is proposed herein that mechanistic concepts for O–O bond formation developed for the OEC could indeed be adopted to the water-oxidation reaction catalyzed by M-birnessites as well.<sup>[223]</sup>

Substrate water molecules, probably partially deprotonated in form of hydroxides, could be bound by Ca<sup>2+</sup> (or Sr<sup>2+</sup> respectively) and activated for a nucleophilic attack on a terminal O<sup>-</sup> ligand of the manganese oxide layer (Figure 8.12, route a).<sup>[26,29,32,79–81]</sup> Also a direct coupling of an outer sphere substrate water or hydroxide to a terminal oxyl radical can be considered without the activation by Ca<sup>2+</sup> (Figure 8.12, route f).<sup>[77,82,83]</sup> Not only mechanistic scenarios in which H<sub>2</sub>O or OH<sup>-</sup> molecules are involved in O–O coupling can be adopted from the OEC. Scenarios in which the O–O bond is formed between terminal and bridging ligands are also feasible. In these mechanistic proposals, always one oxygen may be present as an oxyl radical. So, the peroxide intermediate is possibly formed from two bridging oxido ligands<sup>[49,78]</sup> (Figure 8.12, route e), of which one could be activated by Ca<sup>2+</sup> (Figure 8.12, route b).<sup>[223]</sup> Alternatively, O–O coupling could occur between a bridging oxido and a terminal oxyl ligand. In such mechanistic schemes, both<sup>[55]</sup> (Figure 8.12, route c) or only one of the ligands<sup>[25]</sup> (Figure 8.12, route d) may be bound and activated by Ca<sup>2+</sup> ions within the birnessite structure.

Based on the results presented in this thesis, none of the mechanisms shown in Figure 8.12 can be completely ruled out. But the differences in the relative activities of the vari-

ous birnessites are indicating that routes in which  $\text{Ca}^{2+}$  (or also  $\text{Sr}^{2+}$ ) is actively involved (*a-d*) are more likely than Mn-only routes (*e* and *f*). If exchange rates of terminal or bridging oxido or oxyl ligands of the oxides were accessible, a more detailed discussion of the mechanistic schemes including these motifs would be possible. In the literature, exchange rates can be found for terminal oxido ligands of Mn porphyrins or for bridging oxido ligands of multi centered Mn complexes. In these studies it has been shown that the exchange of terminal oxido ligands in porphyrins is fast, while the exchange of bridging ligands in the multinuclear complexes is slow.<sup>[295–299]</sup>

However, it is important to note that the schemes for O–O coupling shown in Figure 8.12 are only hypotheses for a reaction step that may occur in water-oxidation catalyzed by the OEC and M-birnessites as well. No further investigations e. g. by computational methods have been carried out so far.

## 9 Experimental

### 9.1 Synthesis of M-Birnessites

#### 9.1.1 Synthesis of M-birnessites 1-13

Following a previously established route<sup>[217]</sup> M-birnessites **1-13** were synthesized by comproportionation reactions of  $\text{Mn}^{2+}$  and  $\text{MnO}_4^-$  in the presence of  $\text{K}^+$  or  $\text{Na}^+$  respectively, and  $\text{Ca}^{2+}$  (**1, 2, 3**),  $\text{Sr}^{2+}$  (**4, 5**),  $\text{Mg}^{2+}$  (**6, 7**),  $\text{Cd}^{2+}$  (**8, 9**),  $\text{Al}^{3+}$  (**10, 11**),  $\text{Zn}^{2+}$  (**12**) or  $\text{Pb}^{2+}$  (**13**). For the preparation of **1-11** the following three solutions were prepared:

- 1) In a 250 mL flask, KOH or NaOH respectively, were dissolved in 30 mL  $\text{H}_2\text{O}$ , see Table 9.1 for the weight of the hydroxide taken.
- 2)  $\text{Mn}(\text{AcO})_2$  and the respective  $\text{M}^{2+/3+}$  salt were dissolved in 30 mL  $\text{H}_2\text{O}$ , see Table 9.1 for the amount of respective metal salts taken.
- 3) 948 mg (6 mmol)  $\text{KMnO}_4$  were dissolved in 100 mL  $\text{H}_2\text{O}$ .

The three solutions were slowly combined as follows: 2) was added drop-wise within 10 min under vigorous stirring to 1), resulting in an off-white to light brown suspension. Subsequently, 3) was added drop-wise to the suspension of 1) and 2) in 30 min under vigorous stirring.

The obtained dark brown suspensions were then treated differently. The suspensions of **1-7** were stirred for 72 h at 40 °C. Then, the precipitate of each approach was filtered off and washed stepwise with 1 L  $\text{H}_2\text{O}$ , before it was dried at 65 °C over a period of 16 h. The dried product was ground into a fine powder using pestle and mortar.

**8-11** were directly processed after precipitating. Each of the suspensions of **8-11** was centrifuged for 5 min. at 5000 rpm. The supernatant was discarded. The precipitate was suspended in  $\text{H}_2\text{O}$  and again centrifuged for 5 min. at 5000 rpm. This washing procedure was repeated two times. Afterwards the precipitate was dried at 65 °C over a period of 48 h. The dried product was ground to fine powder using pestle and mortar.

The  $\text{Zn}^{2+}$ - (**12**) and  $\text{Pb}^{2+}$ -birnessite (**13**) was synthesized by Michael Poschmann as part of his bachelor's thesis.<sup>[224]</sup> The preparation of **12** and **13** was carried out in analogy to the synthesis of **8-11**. The following solutions were prepared:

- 1) In a 250 mL flask, 14.0 g (250 mmol) KOH were dissolved in 50 mL  $\text{H}_2\text{O}$ .
- 2)  $\text{Mn}(\text{AcO})_2$  and  $\text{Zn}(\text{AcO})_2$  or  $\text{Pb}(\text{AcO})_2$  respectively were dissolved in 50 mL  $\text{H}_2\text{O}$ , see Table 9.1 for the amount of respective metal salts taken.
- 3) 948 mg (6 mmol)  $\text{KMnO}_4$  were dissolved in 150 mL  $\text{H}_2\text{O}$ .

The solutions were combined as described above. The obtained precipitates were directly processed after the addition of 3). Each suspension of **12** and **13** was centrifuged for 5 min. at 5000 rpm. The supernatant was discarded. The precipitate was suspended

in H<sub>2</sub>O and again centrifuged for 5 min. at 5000 rpm. This washing procedure was repeated two times. Afterwards the precipitate was dried at 65 °C over a period of 48 to 72 h. The dried product was ground into a fine powder using pestle and mortar.

**Table 9.1. Amount of educts used for the synthesis of 1-13.**

		Solution 1)	Solution 2)
K <sub>0.31</sub> -birn.	(1)	14.0 g (250 mmol) KOH	3.92 g (16 mmol) Mn(AcO) <sub>2</sub> · 4 H <sub>2</sub> O + 56 mg (0.3 mmol) Ca(AcO) <sub>2</sub> · H <sub>2</sub> O
Ca <sub>0.14</sub> -birn.	(2)	10.0 g (250 mmol) NaOH	3.92 g (16 mmol) Mn(AcO) <sub>2</sub> · 4 H <sub>2</sub> O + 564 mg (3.2 mmol) Ca(AcO) <sub>2</sub> · H <sub>2</sub> O
Ca <sub>0.27</sub> -birn.	(3)	14.0 g (250 mmol) KOH	3.92 g (16 mmol) Mn(AcO) <sub>2</sub> · 4 H <sub>2</sub> O + 1.13 g (6.4 mmol) Ca(AcO) <sub>2</sub> · H <sub>2</sub> O
Sr <sub>0.18</sub> -birn.	(4)	14.0 g (250 mmol) KOH	3.92 g (16 mmol) Mn(AcO) <sub>2</sub> · 4 H <sub>2</sub> O + 677 mg (3.2 mmol) Sr(NO <sub>3</sub> ) <sub>2</sub>
Sr <sub>0.27</sub> -birn.	(5)	14.0 g (250 mmol) KOH	3.92 g (16 mmol) Mn(AcO) <sub>2</sub> · 4 H <sub>2</sub> O + 1.35 g (6.4 mmol) Sr(NO <sub>3</sub> ) <sub>2</sub>
Mg <sub>0.13</sub> -birn.	(6)	10.0 g (250 mmol) NaOH	3.92 g (16 mmol) Mn(AcO) <sub>2</sub> · 4 H <sub>2</sub> O + 686 mg (3.2 mmol) Mg(AcO) <sub>2</sub> · 4 H <sub>2</sub> O
Mg <sub>0.28</sub> -birn.	(7)	14.0 g (250 mmol) KOH	3.92 g (16 mmol) Mn(AcO) <sub>2</sub> · 4 H <sub>2</sub> O + 1.37 g (6.4 mmol) Mg(AcO) <sub>2</sub> · 4 H <sub>2</sub> O
Cd <sub>0.16</sub> -birn.	(8)	14.0 g (250 mmol) KOH	3.92 g (16 mmol) Mn(AcO) <sub>2</sub> · 4 H <sub>2</sub> O + 853 mg (3.2 mmol) Cd(AcO) <sub>2</sub> · 2 H <sub>2</sub> O
Cd <sub>0.29</sub> -birn.	(9)	14.0 g (250 mmol) KOH	3.92 g (16 mmol) Mn(AcO) <sub>2</sub> · 4 H <sub>2</sub> O + 1.71 g (6.4 mmol) Cd(AcO) <sub>2</sub> · 2 H <sub>2</sub> O
Al <sub>0.02</sub> -birn.	(10)	14.0 g (250 mmol) KOH	3.92 g (16 mmol) Mn(AcO) <sub>2</sub> · 4 H <sub>2</sub> O + 1.20 g (3.2 mmol) Al(NO <sub>3</sub> ) <sub>3</sub> · 9 H <sub>2</sub> O
Al <sub>0.03</sub> -birn.	(11)	14.0 g (250 mmol) KOH	3.92 g (16 mmol) Mn(AcO) <sub>2</sub> · 4 H <sub>2</sub> O + 1.40 g (6.4 mmol) Al(NO <sub>3</sub> ) <sub>3</sub> · 9 H <sub>2</sub> O
Zn <sub>0.20</sub> -birn. <sup>[224]</sup>	(12)	14.0 g (250 mmol) KOH	3.92 g (16 mmol) Mn(AcO) <sub>2</sub> · 4 H <sub>2</sub> O + 1.04 g (4.7 mmol) Zn(AcO) <sub>2</sub> · 2 H <sub>2</sub> O
Pb <sub>0.30</sub> -birn. <sup>[224]</sup>	(13)	14.0 g (250 mmol) KOH	3.92 g (16 mmol) Mn(AcO) <sub>2</sub> · 4 H <sub>2</sub> O + 1.82 g (4.8 mmol) Pb(AcO) <sub>2</sub> · 3 H <sub>2</sub> O

### 9.1.2 Synthesis of oxides 14-18

Based on the synthesis route published by Luo *et al.*<sup>[217]</sup>, M-birnessites **14-18** were prepared via ion exchange experiments starting with a CaMn-oxide, synthesized by the comproportionation of  $\text{Mn}^{2+}$  and  $\text{MnO}_4^-$  in presence of  $\text{Ca}^{2+}$ . The preparation of the CaMn-oxide and **14-18** was carried out by Thorben Reinert as part of his advanced inorganic chemistry lab course (MNF-chem 1004 A).<sup>[243]</sup>

#### Synthesis of the CaMn-oxide as precursor

7.84 g (32.0 mmol)  $\text{Mn}(\text{AcO})_2 \cdot 4\text{H}_2\text{O}$  and 2.26 g (12.8 mmol)  $\text{Ca}(\text{AcO})_2 \cdot \text{H}_2\text{O}$  were dissolved in 60 mL  $\text{H}_2\text{O}$  in a 1 L flask. A solution of 28.0 g (500 mmol) KOH in 60 mL  $\text{H}_2\text{O}$  was added drop-wise over a period of 20 min. under vigorous stirring to the solution of  $\text{Mn}(\text{AcO})_2$  and  $\text{Ca}(\text{AcO})_2$  using a dropping funnel. Afterwards, 1.90 g (12.0 mmol)  $\text{KMnO}_4$  were dissolved in 200 mL  $\text{H}_2\text{O}$ . This solution was also added to the previously combined solutions under vigorous stirring using a dropping funnel. The dark brown precipitate was centrifuged for 5 min. at 5000 rpm. The supernatant was discarded and the obtained slurry was used in ion exchange experiments without further processing.

#### Ion exchange experiments

To prepare the final M-birnessites **14-18**, ion exchange experiments were carried out by stirring the previously synthesized CaMn-oxide in solutions of distinct metal chlorides. For this, 200 mmol of  $\text{Ca}^{\text{II}}$ ,  $\text{Mn}^{\text{II}}$ ,  $\text{Zn}^{\text{II}}$ ,  $\text{Fe}^{\text{II}}$  and  $\text{Fe}^{\text{III}}$  chloride, respectively (see Table 9.2), were dissolved in 200 mL  $\text{H}_2\text{O}$ . The CaMn-oxide slurry obtained in the previous step for the oxide synthesis was separated into 5 equal portions and added to these solutions of the metal chlorides. The thus obtained suspensions were stirred over night. The solid of each approach was then centrifuged for 5 min. at 5000 rpm. The supernatant was discarded. The precipitate was suspended in  $\text{H}_2\text{O}$  and again centrifuged for 5 min. at 5000 rpm. This washing procedure was repeated two times. Then, the precipitate was dried at 65 °C over a period of 16 h. The dried products were ground into a fine powder using pestle and mortar.

**Table 9.2. Amount of metal chlorides used for the synthesis of 14-18.**<sup>(243)</sup>

Weight and type of metal chlorides used				
$\text{Ca}_{\text{ex}}$ -birnessite	(14)	4.40 g	(200 mmol)	$\text{CaCl}_2 \cdot 6\text{H}_2\text{O}$
$\text{Mn}_{\text{ex}}$ -birnessite	(15)	3.96 g	(200 mmol)	$\text{MnCl}_2 \cdot 4\text{H}_2\text{O}$
$\text{Zn}_{\text{ex}}$ -birnessite	(16)	2.73 g	(200 mmol)	$\text{ZnCl}_2$
$\text{Fe}_{\text{ex}}^{2+}$ -oxide	(17)	3.78 g	(200 mmol)	$\text{FeCl}_2 \cdot 4\text{H}_2\text{O}$
$\text{Fe}_{\text{ex}}^{3+}$ -birnessite	(18)	5.40 g	(200 mmol)	$\text{FeCl}_3 \cdot 6\text{H}_2\text{O}$

### 9.1.3 Synthesis of K/Ca-birnessites 19-29

K/Ca-birnessites **19-29** with increasing  $\text{Ca}^{2+}$  concentrations were also prepared following the route described above.<sup>[217]</sup> Three solutions were prepared where the amount of  $\text{Ca}(\text{AcO})_2$  was successive increased:

- 1) 14.4 g (250 mmol) KOH were dissolved in 30 mL  $\text{H}_2\text{O}$ .
- 2) 3.92 g (16 mmol)  $\text{Mn}(\text{AcO})_2$  and 0 - 2.82 g (0 - 16 mmol)  $\text{Ca}(\text{AcO})_2$  were dissolved in 30 mL  $\text{H}_2\text{O}$ , see Table 9.3 for the amount of  $\text{Ca}(\text{AcO})_2$  used.
- 3) 948 mg (6 mmol)  $\text{KMnO}_4$  were dissolved in 100 mL  $\text{H}_2\text{O}$ .

The three solutions were slowly combined as follows: 2) was added drop-wise within 10 min under vigorous stirring to 1), resulting in an off-white to light brown suspension. Subsequently, 3) was added drop-wise to the suspension of 1) and 2) in 30 min under vigorous stirring. Each of the suspensions of **19-29** was centrifuged for 5 min. at 5000 rpm. The supernatant was discarded. The precipitate was suspended in  $\text{H}_2\text{O}$  and again centrifuged for 5 min. at 5000 rpm. This washing procedure was repeated two times. Afterwards the precipitate was dried at 65 °C over a period of 48 h. The dried product was ground into a fine powder using pestle and mortar.

**Table 9.3. Amount of  $\text{Ca}(\text{AcO})_2$  used for the synthesis of 19-29.**

		m (n) $\text{Ca}(\text{AcO})_2 \cdot \text{H}_2\text{O}$	$\text{Ca}^{2+}:\text{Mn}^{2+}$ ratio
$\text{K}_{0.28}$ -birnessite	(19)	—	0.00
$\text{Ca}_{0.04}$ -birnessite	(20)	141 mg (0.8 mmol)	0.05
$\text{Ca}_{0.08}$ -birnessite	(21)	282 mg (1.6 mmol)	0.10
$\text{Ca}_{0.10}$ -birnessite	(22)	423 mg (2.4 mmol)	0.15
$\text{Ca}_{0.15}$ -birnessite	(23)	564 mg (3.2 mmol)	0.20
$\text{Ca}_{0.17}$ -birnessite	(24)	705 mg (4.0 mmol)	0.25
$\text{Ca}_{0.21}$ -birnessite	(25)	846 mg (4.8 mmol)	0.30
$\text{Ca}_{0.28}$ -birnessite	(26)	1.13 g (6.4 mmol)	0.40
$\text{Ca}_{0.36}$ -birnessite	(27)	1.41 g (8.0 mmol)	0.50
$\text{Ca}_{0.54}$ -birnessite	(28)	2.11 g (12 mmol)	0.75
$\text{Ca}_{0.67}$ -birnessite	(29)	2.82 g (16 mmol)	1.00

### 9.1.4 Synthesis of Ca-birnessites 30-40

The syntheses of Ca-birnessites **30-40** were carried out in analogy to the previously described syntheses of M-birnessites **1-29**, but with increasing ripening time. Therefore, three solutions were prepared:

- 1) 14.0 g (250 mmol) KOH were dissolved in 30 mL H<sub>2</sub>O.
- 2) 3.92 g (16.0 mmol) Mn(AcO)<sub>2</sub> and 1.13 g (6.40 mmol) Ca(AcO)<sub>2</sub> were dissolved in 30 mL H<sub>2</sub>O.
- 3) 948 mg (6.00 mmol) KMnO<sub>4</sub> were dissolved in 100 mL H<sub>2</sub>O.

The three solutions were slowly combined as follows. 2) was added drop-wise within 10 min under vigorous stirring to 1), resulting in an off-white to light brown suspension. Subsequently, 3) was added drop-wise to the suspension of 1) and 2) in 30 min under vigorous stirring. After the addition of 3) to the formed suspension of solution 1) and 2), the reaction batch was stirred at 20 °C (**30-35**) and 40 °C respectively (**36-40**) for a period of 0 to 240 h (see Table 9.4). After ripening, each of the suspensions of **30-40** was centrifuged for 5 min. at 5000 rpm. The supernatant was discarded. The precipitate was suspended in H<sub>2</sub>O and again centrifuged for 5 min. at 5000 rpm. This washing procedure was repeated two times. Afterwards the precipitate was dried at 65 °C over a period of 48 h. The dried product was ground into a fine powder using pestle and mortar.

**Table 9.4. Ripening times and temperatures for the preparation of 30-40.**

		Time/h	Temperature/°C
Ca <sub>0h</sub> -birnessite	(30)	0	20
Ca <sub>1h</sub> -birnessite	(31)	1	20
Ca <sub>2h</sub> -birnessite	(32)	2	20
Ca <sub>4h</sub> -birnessite	(33)	4	20
Ca <sub>8h</sub> -birnessite	(34)	8	20
Ca <sub>12h</sub> -birnessite	(35)	12	20
Ca <sub>24h</sub> -birnessite	(36)	24	40
Ca <sub>48h</sub> -birnessite	(37)	48	40
Ca <sub>120h</sub> -birnessite	(38)	120	40
Ca <sub>168h</sub> -birnessite	(39)	168	40
Ca <sub>240h</sub> -birnessite	(40)	240	40

## 9.2 Water-oxidation catalysis

### 9.2.1 Water-oxidation catalysis using $\text{Ce}^{\text{IV}}$ as oxidant

To carry out the water-oxidation experiments, about 5 mg ( $\sim 30\text{-}60\ \mu\text{mol}$  Mn, see appendix A.3 for precise values) of oxides **1-40** and 685 mg (1.25 mmol)  $(\text{NH}_4)_2\text{Ce}(\text{NO}_3)_6$  were weighed into 20 mL septum vials. After the addition of 5 mL of deionized  $\text{H}_2\text{O}$ , the vials were capped immediately using gas tight, teflon coated butyl rubber septa (Figure 9.1). The mixtures were treated in the ultrasonic bath for several seconds to ensure the suspension of the oxide samples and to immediately dissolve the  $\text{Ce}^{\text{IV}}$  powders.

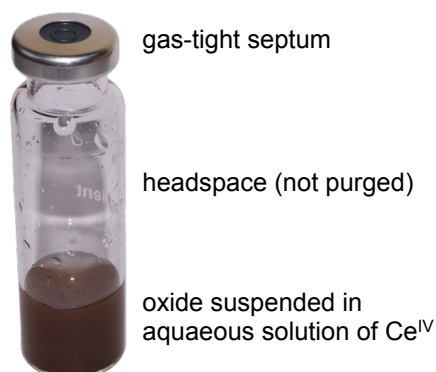


**Figure 9.1.** Septum vial for headspace gas chromatography as a reaction vessel for water-oxidation catalysis.

After the ultrasonic treatment, headspace gas chromatography was immediately started. Gas samples from the vial's headspace were injected to a HP 6890 Series GC System equipped with a 8 ft x 1/8 in 5 Å molsieve column (Supelco) via a HP 7694 Headspace Sampler equipped with a 1 mL sample-loop (Figure 9.2), using helium 4.6 as carrier gas. The gases  $\text{O}_2$  and  $\text{N}_2$  were recorded by a thermal conductivity detector.



**Figure 9.2.** Headspace sampler (*left*) for the automatic injection of gas samples from the headspace of the septum vials into the GC (*right*).

Six headspace extractions out of a single septum vial were injected in intervals of 10 min. The following settings were used for the extraction of headspace gas samples:

- multiple headspace extraction value was set to 6,
- the vial equilibration time was set to 8.6 min,
- pressurize time was set to 0.10 min,
- loop fill time was set to 0.20 min,
- loop equilibration time was set to 0.10 min
- the injection time was set to 1.0 min, giving an overall cycle time of 10 min and an overall time of 1 h for each measurement.

The following temperature settings were used:

- oven temperature (headspace sampler): 40°C (lowest temperature adjustable),
- sample loop temperature (headspace sampler): 50°C,
- transfer line temperature (headspace sampler): 65°C,
- oven temperature (GC): 70°C.

Due to automatic pressurization of the septum vials before every single measurement, the headspace gas to analyze is diluted with carrier gas. In addition, leakage may occur after the first puncture of the septa by the headspace sampler needle in multiple headspace extraction mode. Thus, the detected values for O<sub>2</sub> and N<sub>2</sub> were corrected by a factor calculated from repeating the experiments as described above, but with only one headspace extraction at the end of the interval of 1 h (for calculations see below). All measurements described here were carried out for three times for each oxide (in case of 14-18 each measurement was repeated two times).

### **Water-oxidation catalysis using Ce<sup>IV</sup> as oxidant, carried out in Rhine water**

In addition to the water-oxidation experiments carried out in deionized H<sub>2</sub>O, using oxides 1-40 as catalysts and Ce<sup>IV</sup> as oxidant, the activity of 25 was probed in water of the river Rhine as reaction medium. Apart from the replacement of deionized H<sub>2</sub>O by Rhine water, the measurements were carried out as described above.

Rhine water was taken directly from the river in Cologne. The water was filtered through a folded filter in order to remove floating particles. No further purification was carried out.

About 5 mg (~ 45 μmol Mn) of Ca<sub>0.21</sub>-birnessite 25 (see appendix A.3, Table A.33) and 685 mg (1.25 mmol) (NH<sub>4</sub>)<sub>2</sub>Ce(NO<sub>3</sub>)<sub>6</sub> were weighed into 20 mL septum vials. After the addition of 5 mL of the filtered Rhine water, the septum vials were closed with gas tight, teflon coated, butyl rubber septa. The reaction mixture was then treated in an ultrasonic bath for several seconds. Subsequent, headspace gas chromatography was performed as described above. The experiments were carried out three times with six extractions every 10 min and three times with one extraction after 1 h.

### Reference measurements

In reference experiments, about 5 mg of oxides **1-40** were placed in 20 mL septum vials. 5 mL aqueous HNO<sub>3</sub> (pH=1.7) were added to the oxide powders. The septum vials were closed with teflon coated butyl rubber septa before the samples were treated in the ultrasonic bath for several seconds. The vials' headspace was then probed in intervals of 10 min as described above.

### Calculation of oxygen evolution rates

The headspace of the septum vials was not purged and is thus containing air at the start of the experiments. The amount of evolved O<sub>2</sub> was then calculated based on the signals of N<sub>2</sub> from air. The corresponding amount of oxygen from air was also calculated and subtracted for every measurement. The amount of air as well as of N<sub>2</sub> and O<sub>2</sub> in the headspace of the septum vials can be estimated from the ideal gas law:<sup>[250]</sup>

$$n = \frac{pV}{RT} \quad (9.1)$$

Assuming standard conditions for temperature ( $T=273.15$  K) and pressure ( $p=101325$  Pa)<sup>[250]</sup> and using the universal gas constant ( $R=8.31451$  J K<sup>-1</sup> mol<sup>-1</sup>)<sup>[250]</sup> and the headspace volume above the reaction mixture of  $V=16.4$  mL, the amount of air can be calculated to be  $n(\text{air})=0.73$  mmol. Considering the percentage of N<sub>2</sub> (~ 79 %) and O<sub>2</sub> (~ 21 %) in air, values of  $n(\text{N}_2)=0.58$  mmol and  $n(\text{O}_2)=0.15$  mmol can be calculated. From these numbers, the amount of evolved oxygen (O<sub>2</sub><sup>ev</sup>) can be determined from the areas under the peaks in the GC curve corresponding to the analyzed gases N<sub>2</sub> and O<sub>2</sub> (cf. Figure 8.1):

$$n(\text{O}_2^{\text{ev}}) = 0.58 \text{ mmol} \cdot \frac{\text{area}(\text{O}_2)}{\text{area}(\text{N}_2)} - 0.15 \text{ mmol} \quad (9.2)$$

If more than one gas sample is extracted from a septum vial, corrections of the determined amount of evolved oxygen are required. The vials are pressurized with the carrier gas (He) before the sample loop of the headspace sampler is filled with the extracted gas. This means that the air (and also the evolved oxygen) is diluted when several extractions are performed, as the pressurizing step is repeated for every measurement. As the used headspace sampler was equipped with a 1 mL sample loop, I assumed that a sample volume of 1 mL is extracted in each measurement and the same amount of He is injected to the vial. This 1 mL is about 6.1 % of the total headspace volume. Thus, the N<sub>2</sub> signal in the second measurement should be 93.9 %, that of the third one 88.2 %, of the fourth one 82.8 %, of the fifth one 77.8 % and of the sixth one 73.0 % of the initial N<sub>2</sub> signal. These factors were included in the calculation of the evolved oxygen in the respective extraction step.

Unfortunately, the reproducibility of multiple headspace extractions from the same septum vial is limited due to leakage after first puncture of the septum. Thus, additional measurements were carried out with only one headspace extraction (and thus only one puncture of the septum) after an interval of 1 h. By division of the value determined (after first correction) for the evolved oxygen after 1 h from the multiple headspace extraction by the determined value after 1 h from single extraction, a scaling factor was obtained. This scaling factor was then used for a final correction of the amount of evolved oxygen. This amount of evolved oxygen was then scaled to the specific surface area derived from nitrogen absorption/desorption isotherms, employed catalyst mass and to the manganese content as determined by AAS.

### 9.2.2 Water-oxidation catalysis using $(\text{Ru}^{\text{III}}(\text{bpy})_3)^{3+}$ as oxidant

In these water-oxidation experiments, photochemically generated  $(\text{Ru}^{\text{III}}(\text{bpy})_3)^{3+}$  was used as oxidant. Therefore, suspensions of M-birnessites **2**, **3**, **4**, **6**, **25** and commercial  $\text{RuO}_2$  (Sigma Aldrich) in a buffer solution containing  $(\text{Ru}^{\text{II}}(\text{bpy})_3)^{2+}$  were irradiated with visible light, resulting in the *in situ* generation of the oxidant.

7.5 mg (10  $\mu\text{mol}$ )  $(\text{Ru}^{\text{II}}(\text{bpy}))\text{Cl}_2$ , 27 mg (0.1 mmol)  $\text{K}_2\text{S}_2\text{O}_8$  and 71 mg (0.5 mmol)  $\text{Na}_2\text{SO}_4$  were added to about 5 mg of the respective oxide powder (Table 9.5) in a Metrohm vessel, originally designed for electrochemistry (Figure 9.3, *left*). 10 mL of a  $\text{Na}_2\text{SiF}_6/\text{NaHCO}_3$  buffer (pH = 5.2) were added to the powders in the dark and the reaction vessel was closed with the appropriate Metrohm cap. The openings of the cap were closed with rubber septa. The reaction mixture was purged with  $\text{N}_2$  in the dark.

The  $\text{O}_2$  concentration in solution was recorded using a Unisense OX-500 Microsensor connected to a Microsensor Monometer. Purging of the reaction mixture with  $\text{N}_2$  was performed until a minimal oxygen concentration was recorded. After purging of the suspensions, irradiation was started, while the headspace of the reaction vessel was permanently purged with a minimum flow of  $\text{N}_2$ . The reaction mixtures were irradiated using a slide projector equipped with a 250 W halogen bulb and a 85 mm f2.7 lens (no cut-off filter was used) positioned at  $\sim 30$  cm distance from the reaction vessel. The oxygen concentrations were recorded for at least 10 min. Each experiment was repeated once (*cf.* appendix A.4). Prior to each set of experiments, the oxygen sensor was calibrated in air saturated and  $\text{N}_2$  purged water in order to determine signals corresponding to maximum and minimum oxygen concentrations in solution (see below).

The  $\text{Na}_2\text{SiF}_6/\text{NaHCO}_3$  buffer solution was prepared according to Hara *et al.*<sup>[290]</sup> 16.4 g (87 mmol)  $\text{Na}_2\text{SiF}_6$  and 9.5 g (113 mmol)  $\text{NaHCO}_3$  (molar ratio of 1.0:1.3) were dissolved in 250 mL  $\text{H}_2\text{O}$ . Prior to the first use of the buffer, the solution was ripened over night at room temperature. The pH value was determined to 5.2.



**Figure 9.3.** Reaction vessel (*left*) and slide projector as light source (*right*) for experiments on water-oxidation catalysis using photochemically generated  $(\text{Ru}^{\text{III}}(\text{bpy})_3)^{3+}$ .

**Table 9.5. Amount of oxide powders used in the water-oxidation experiments**

		m/mg	(n/ $\mu$ mol)
Ca <sub>0.14</sub> -birnessite	(2)	5.2	(38.22)
		5.0	(36.75)
Ca <sub>0.27</sub> -birnessite	(3)	4.9	(39.20)
		4.9	(39.20)
Sr <sub>0.18</sub> -birnessite	(4)	5.0	(47.25)
		5.0	(47.25)
Mg <sub>0.13</sub> -birnessite	(6)	4.9	(37.63)
		5.1	(39.17)
Ca <sub>0.21</sub> -birnessite	(25)	5.0	(42.75)
		5.0	(42.75)
RuO <sub>2</sub>		4.9	(32.44)
		5.2	(34.42)

### Calculation of oxygen evolution rates

The Unisense OX-500 Microsensor is basically a Clark type electrode. Thus, a current proportional to the O<sub>2</sub> concentration in solution is recorded. Via calibration measurements at known O<sub>2</sub> concentrations, the unknown O<sub>2</sub> concentration of a sample solution can be determined by measuring the current.

A two-point calibration was carried out as the O<sub>2</sub> concentration was measured in air saturated H<sub>2</sub>O and in N<sub>2</sub> purged H<sub>2</sub>O. The current measured in case of N<sub>2</sub> purged H<sub>2</sub>O was set to a O<sub>2</sub> concentration of 0.0  $\mu$ mol · L<sup>-1</sup> in the software provided by Unisense (SensorTrace Basic). In this software, a value of c(O<sub>2</sub>) = 289.9  $\mu$ mol · L<sup>-1</sup> was preset for air saturated, deionized H<sub>2</sub>O. This value can be calculated from Henry's law:<sup>[250]</sup>

$$x_{\text{O}_2} = \frac{p_{\text{O}_2}}{K_{\text{O}_2}} \quad (9.3)$$

$x_{\text{O}_2}$  is the mole fraction of O<sub>2</sub>,  $p_{\text{O}_2}$  is the partial pressure of O<sub>2</sub> above the solution and  $K_{\text{O}_2}$  is the Henry constant of O<sub>2</sub>.<sup>[250]</sup> Applying this two-point calibration to the recorded, O<sub>2</sub> dependent current, the concentration of evolved O<sub>2</sub> can be derived from the measurement.

The oxygen evolved per Mn ion (or Ru ion) can be calculated from the O<sub>2</sub> concentration determined as described, the volume of the reaction mixture (10 mL) and the manganese (or ruthenium) content of the respective catalyst. Oxygen evolution rates can be estimated by linear regression of the plot of evolved O<sub>2</sub> *vs.* time. The oxygen evolution rates of M-birnessites **2**, **3**, **4**, **6** and **25** given in Table 8.6 were determined from the slope of the curve at 60-120 s and the value given for RuO<sub>2</sub> was determined from the slope of the curve at 30-90 s.

## 9.3 Physical Measurements

### Atomic absorption spectroscopy

Manganese AAS was performed on an AAnalyst spectrometer system by PerkinElmer. Prior to the analysis, about 10 mg of oxides 1-40 were carefully weighed, suspended in 3 mL of a mixture of concentrated HNO<sub>3</sub> and 30 % H<sub>2</sub>O<sub>2</sub> in a ratio of 2:1. The mixtures were left at room temperature over night. The obtained clear solutions were then diluted with H<sub>2</sub>O to 50 mL. 1 mL of the diluted solution was again diluted to 50 mL and then analyzed by AAS.

### Energy dispersive X-ray spectroscopy

EDX analysis of 1-29 was realized at a Philips ESEM XL30 microscope equipped with an EDAX detector. EDX analysis of 30-40 was carried out using a ZEISS ULTRA plus microscope equipped with an Oxford Instruments PentaFET Precision x-act detector. The compositions given in Tables 6.1, 6.3, 6.5 and 6.7 are the result of averaging multiple independent measurements from a given sample.

### Infrared spectroscopy

ATR IR spectra of the solid oxide powders of 1-40 were obtained using a Bruker Alpha P spectrometer. The spectra shown in Figures 6.5, 6.6, 6.9, 6.13 and 6.17 are averaged from 100 single recordings. Baseline corrections of the IR spectra were performed using the software OPUS provided by Bruker.

### Nitrogen adsorption/desorption

N<sub>2</sub> physisorption measurements were performed using a BelsorpMAX (1, 2, 6, 7) and a BelsorpMINI instrument (3-5 and 8-40), respectively. Prior to the analysis, the samples were activated for 2 h at 120 °C and 10<sup>-2</sup> kPa in order to remove adsorbed water. The isotherms were analyzed according to BET theory in order to determine the specific surface areas of the oxide powders. Therefore, the Belsorp Adsorption/Desorption Data Analysis Software was used.

### Scanning electron microscopy

SEM images of oxides 1-7, 12 and 13 were taken using a Philips ESEM XL30 microscope. Images of oxides 19, 22, 25, 29 and 30-40 were taken using a ZEISS ULTRA plus equipped with an in-lens detector.

### Thermogravimetric analysis

Thermogravimetric analyses of M-birnessites 1-7 were carried out using a Netzsch STA 429DT - TG device. The samples were heated to 1000 °C at a rate of 4 °C · min<sup>-1</sup> in an airflow (75 mL min<sup>-1</sup>) in Al<sub>2</sub>O<sub>3</sub> crucibles. The thermogravimetric data were corrected for buoyancy and current effects.

### **X-ray absorption spectroscopy**

XAS of M-birnessites **1-7** was performed at the Mn K-edges at the BESSY synchrotron (Helmholtz-Zentrum Berlin, Germany). The measurements were acquired in transmission mode at the KMC-1 bending-magnet beamline at 20 K in a cryostat (Oxford-Danfysik) with a liquid helium flow system.

### **X-ray powder diffractometry**

The X-ray powder patterns of **1-40** were measured in reflection geometry using a PANalytical X'Pert PRO instrument. The background was subtracted from the recorded XRD patterns using the software PANalytical X'Pert HighScore.

## 10 Conclusion

Various mixed manganese oxides that differ in their elemental compositions and morphologies were synthesized. A detailed analysis showed that the prepared manganese oxide materials feature an amorphous birnessite-like structure, build up from layers of edge-sharing  $\text{MnO}_6$  octahedra with a large number of layer defects. Additional cations are intercalated in between the layers of the phyllosulfates.

It has been demonstrated that M-birnessites containing  $\text{K}^+$ ,  $\text{Ca}^{2+}$ ,  $\text{Sr}^{2+}$ ,  $\text{Mg}^{2+}$ ,  $\text{Cd}^{2+}$ ,  $\text{Al}^{3+}$ ,  $\text{Zn}^{2+}$ ,  $\text{Pb}^{2+}$  or  $\text{Fe}^{3+}$  can be obtained from comproportionation reactions either directly or via ion exchange. However, it was shown that it is not possible to incorporate  $\text{Mn}^{2+}$  or  $\text{Fe}^{2+}$  ions in the birnessite structure via ion exchange. Instead, redox reactions occur resulting in the formation of  $\text{Mn}^{\text{III}}\text{O}(\text{OH})$  and  $\text{Fe}^{\text{III}}\text{O}(\text{OH})$  phases, respectively. EDX analyses of the prepared M-birnessites showed that the oxide composition can be controlled by the metal ion ratio used in the synthesis. Ca-, Sr- and Mg-birnessites were prepared with different amounts of intercalated alkaline earth cations. The  $\text{M}^{2+}:\text{Mn}$  molar ratios found in these oxides were similar to the ion ratios used in the syntheses. Even for high  $\text{Ca}^{2+}$  concentrations, the  $\text{M}^{2+}:\text{Mn}$  molar ratios used in the syntheses and found in the oxides were virtually identical.

SEM images and  $\text{N}_2$  adsorption/desorption isotherms showed that the morphology of the oxide particles is influenced by their compositions. If higher amounts of  $\text{M}^{2+}$  ions are incorporated in the oxide structures, smaller particles are formed which also show larger specific surface areas. These results were confirmed by the recorded XRD patterns. In these patterns, the intensity of the characteristic birnessite reflections is decreased with increasing  $\text{M}^{2+}$  ion concentrations. This effect can be observed for the K/Ca-birnessites **19-29**, which were synthesized in the presence of increasing amounts of  $\text{Ca}^{2+}$ .

X-ray absorption spectra of the Ca-, Sr-, and Mg-birnessites **1-7** measured at the Mn K-edge revealed an insight into structural details. XANES spectra showed that the mean oxidation state of the Mn centers of the M-birnessites **1-7** is in between 3.5 and 4.0. EXAFS spectra showed peaks corresponding to structural motifs analogous to previously studied birnessite catalysts.<sup>[215]</sup> The  $\text{Ca}^{2+}$ ,  $\text{Sr}^{2+}$  and  $\text{Mg}^{2+}$  ions are forming corners of complete  $\text{M}^{2+}\text{Mn}_3(\mu\text{-O})_4$  or incomplete  $\text{M}^{2+}\text{Mn}_2(\mu\text{-O})_4$  cubane like units. Additionally, the  $\text{M}^{2+}$  cations are found above defects in the  $\text{MnO}_6$  layers, where they are bound in a triple corner sharing  $\text{M}^{2+}\text{O}_x$  fashion.  $\text{Mn}^{2+/3+}$  ions could also be present in between the oxide layers, probably forming  $\text{Mn}_4(\mu\text{-O})_4$  cubanes.

Oxygen evolution experiments carried out using oxides **1-40** as catalysts clearly demonstrated that M-birnessites are promising candidates to catalyze the water-oxidation reaction. Furthermore, the experiments (carried out using  $\text{Ce}^{\text{IV}}$  as well as photochemically generated  $[\text{Ru}^{\text{III}}(\text{bpy})_3]^{3+}$  as oxidants) show differences in the reactivity for the various M-birnessites depending on the type of the intercalated metal cations. A catalytic activity trend can be formulated as  $\text{Ca}^{2+} > \text{Sr}^{2+} > \text{Mg}^{2+}/\text{Cd}^{2+}/\text{Al}^{3+}/\text{Zn}^{2+}/\text{Pb}^{2+}$ . But also less distinct correlations between the ion concentration (especially  $\text{Ca}^{2+}$ ) as well as

to the ripening period applied during the syntheses were detected. Strikingly, the observed trend correlated to the type of the intercalated cations is in a good agreement with the order of oxygen evolution rates observed for the native OEC and its  $\text{Sr}^{2+}$  and  $\text{Mg}^{2+}$  substituted forms.

M-birnessites are not only resembling trends in catalytic activity observed for the OEC, also similar structural motifs are found:

- Mn ions in oxidation states of  $\text{Mn}^{3+}$  and  $\text{Mn}^{4+}$  are interconnected by  $\mu$ -oxido and  $\mu$ -hydroxido bridges,
- open coordination sites are present, which may act as binding sites for substrate water molecules,
- some Mn ions show incomplete coordination spheres of oxido or hydroxido ligands, likely contributing to charge compensation and redox potential levelling via the formation of additional  $\mu$ -O bridges,
- clearly different Mn sites could either be involved in accumulation of oxidizing equivalents or in O–O bond formation (or both),
- $\text{Ca}^{2+}$  ions are required to reach maximal catalytic activity.

Thus, it is suggested that  $\text{Ca}^{2+}$  could have a similar function in catalysis for both systems and that O–O bond formation mechanisms proposed for water-oxidation catalyzed by the OEC may be adopted to M-birnessites. In these mechanistic scenarios,  $\text{Ca}^{2+}$  is suggested to act as binding and activation site for substrate water molecules.

In addition, the results presented above are supporting previously proposed requirements which have to be met by Mn based compounds to act as water-oxidation catalyst:

- a multinuclear ( $\geq \text{Mn}_4$ )  $\mu$ -O(H) bridged manganese core is necessary,
- redox potential leveling is crucial, deprotonation of  $\mu$ -OH, or proton abstraction by  $\mu$ -O moieties may occur,
- the  $\mu$ -O(H) core has to be stabilized in order to facilitate the necessary changes in geometry related to changes of the oxidation state,
- open coordination sites are necessary to bind and activate substrate  $\text{H}_2\text{O}$  molecules.

In summary, the presented findings show that M-birnessites are outstanding OEC model compounds as they mimic the structure and the function of the OEC as well as the key role  $\text{Ca}^{2+}$  cations are playing for activity in water-oxidation catalysis to achieve maximum catalytic rates. As M-birnessites are composed of cheap and abundant elements, these materials are also promising candidates to catalyze the water-oxidation half-reaction in an artificial photosynthetic process.

Of course, in this case the use of oxidants like  $\text{Ce}^{\text{IV}}$  or  $[\text{Ru}^{\text{III}}(\text{bpy})_3]^{3+}$  is no option to drive the water-oxidation reaction. Rather, integrated devices have to be developed, in which M-birnessites are e. g. coupled to multi-junction semiconductors or DSCs based on abundant materials in order to achieve light-driven water-splitting. A fundamental step towards this target is the preparation of catalytically active birnessite electrodes which could then be coupled to the light-harvesting units. Thus, the deposition of

---

birnessite-like manganese oxides on electrode materials is already under investigation in the Kurz Group. In addition, first promising results towards this end were recently published by other research teams.<sup>[131–133]</sup>

If such integrated devices for light-driven water-splitting could in the end be set up with high solar to fuel conversion efficiencies, this would be a major breakthrough for alternative energy production on a large scale.



## References

- [1] N. S. Lewis and D. G. Nocera, Powering the planet: Chemical challenges in solar energy utilization, *Proc. Natl. Acad. Sci. U.S.A.*, **2006**, *103*, 15729.
- [2] N. Armaroli and V. Balzani, The Future of Energy Supply: Challenges and Opportunities, *Angew. Chem. Int. Ed.*, **2007**, *46*, 52.
- [3] D. G. Nocera, Chemistry of Personalized Solar Energy, *Inorg. Chem.*, **2009**, *48*, 10001.
- [4] D. G. Nocera, "Fast food" energy, *Energy Environ. Sci.*, **2010**, *3*, 993.
- [5] N. Armaroli and V. Balzani, *Energy for a Sustainable World*, Wiley-VCH, Weinheim, **2010**.
- [6] G. Ciamician, The photochemistry of the future, *Science*, **1912**, *36*, 385.
- [7] BP, Historical Data, <http://www.bp.com/statisticalreview>, **2012**.
- [8] Original data were given in Million tonnes oil equivalent (Mtoe; 1 Mtoe  $\sim$  12 TWh, 1 TWh =  $10^{12}$  Wh). With 8760 h per year, global primary energy consumption in 1965 is given as  $(3750 \text{ Mtoe} \cdot 12 \text{ TWh/Mtoe}) \cdot 8760 \text{ h}^{-1} = 5.14 \text{ TW}$ , in 2010 as  $(11977.8 \text{ Mtoe} \cdot 12 \text{ TWh/Mtoe}) \cdot 8760 \text{ h}^{-1} = 16.41 \text{ TW}$ . Data and conversion factors for energy units are given in<sup>[7]</sup>.
- [9] REN21, Renewables 2012 Global Status Report, **2012**.
- [10] BP, BP Statistical Review of World Energy, **2011**.
- [11] *Final energy*: energy as consumed by end users, energy consumed by the energy sector itself (e. g. for delivery and transformation) is excluded.
- [12] R. F. Keeling, S. C. Piper, A. F. Bollenbacher and W. S. J., Atmospheric Carbon Dioxide Record from Mauna Loa, <http://cdiac.esd.ornl.gov/trends/co2/sio-mlo.html>, **2009**.
- [13] K. W. Thoning, K. D. R. and A. Crotwell, Atmospheric Carbon Dioxide Dry Air Mole Fractions from quasi-continuous measurements at Barrow, Alaska; Mauna Loa, Hawaii; American Samoa; and South Pole, 1973-2010, <ftp://ftp.cmdl.noaa.gov/ccg/co2/in-situ>, **2011**.
- [14] R. F. Keeling, S. C. Piper, A. F. Bollenbacher and W. S. J., Atmospheric Carbon Dioxide Record from the South Pole, <http://cdiac.esd.ornl.gov/trends/co2/sio-spl.html>, **2008**.
- [15] A. F. Holleman, E. Wiberg and N. Wiberg, *Lehrbuch der Anorganischen Chemie*, de-Gruyter, Berlin, **1995**.
- [16] *Primary energy*: energy sources found directly in form of their feedstocks without further conversion or transformation processing.
- [17] United Nations Framework Convention on Climate Change, <http://unfccc.int>.
- [18] European Commission DG CLIMA, Climate Change Factsheet, <http://ec.europa.eu/clima/publications>, **2012**.
- [19] R. E. Blankenship, *Molecular Mechanisms of Photosynthesis*, Blackwell Science, Oxford, **2002**.
- [20] L. Taiz and E. Zeiger, *Plant Physiology*, Sinauer Associates, Inc., Sunderland, **2010**.

- [21] N. Nelson and A. Ben-Shem, The complex architecture of oxygenic photosynthesis, *Nat. Rev. Mol. Cell Biol.*, **2004**, *5*, 971.
- [22] B. M. Griffin, J. Schott and B. Schink, Nitrite, an Electron Donor for Anoxygenic Photosynthesis, *Science*, **2007**, *316*, 1870.
- [23] J. T. Beatty, J. Overmann, M. T. Lince, A. K. Manske, A. S. Lang, R. E. Blankenship, C. L. Van Dover, T. A. Martinson and F. G. Plumley, An obligately photosynthetic bacterial anaerobe from a deep-sea hydrothermal vent, *Proc. Natl. Acad. Sci. U.S.A.*, **2005**, *102*, 9306.
- [24] J. Barber, Photosynthetic energy conversion: natural and artificial, *Chem. Soc. Rev.*, **2009**, *38*, 185.
- [25] J. Messinger, Evaluation of different mechanistic proposals for water oxidation in photosynthesis on the basis of  $Mn_4OCa$  structures for the catalytic site and spectroscopic data, *Phys. Chem. Chem. Phys.*, **2004**, *6*, 4764.
- [26] J. P. McEvoy and G. W. Brudvig, Water-Splitting Chemistry of Photosystem II, *Chem. Rev.*, **2006**, *106*, 4455.
- [27] W. Lubitz, E. J. Reijerse and J. Messinger, Solar Water-Splitting into  $H_2$  and  $O_2$ : Design Principles of Photosystem II and Hydrogenases, *Energy Environ. Sci.*, **2008**, *1*, 15.
- [28] H. Dau and M. Haumann, The manganese complex of photosystem II in its reaction cycle – Basic framework and possible realization at the atomic level, *Coord. Chem. Rev.*, **2008**, *252*, 273.
- [29] H. Dau, C. Limberg, T. Reier, M. Risch, S. Roggan and P. Strasser, The Mechanism of Water Oxidation: From Electrolysis via Homogeneous to Biological Catalysis, *ChemCatChem*, **2010**, *2*, 724.
- [30] M. Calvin, Forty years of photosynthesis and related activities, *Photosynth. Res.*, **1989**, *21*, 3.
- [31] *Nobel Lectures, Chemistry 1942-1962*, Elsevier Publishing Company, Amsterdam, **1964**.
- [32] K. N. Ferreira, T. M. Iverson, K. Maghlaoui, J. Barber and S. Iwata, Architecture of the Photosynthetic Oxygen-Evolving Center, *Science*, **2004**, *303*, 1831.
- [33] B. Loll, J. Kern, W. Saenger, A. Zouni and J. Biesiadka, Towards complete cofactor arrangement in the 3.0 Å resolution structure of photosystem II, *Nature*, **2005**, *438*, 1040.
- [34] A. Guskov, J. Kern, A. Gabdulkhakov, M. Broser, A. Zouni and W. Saenger, Cyanobacterial photosystem II at 2.9-Å resolution and the role of quinones, lipids, channels and chloride, *Nat. Struct. Mol. Biol.*, **2009**, *16*, 334.
- [35] N. Kamiya and J.-R. Shen, Crystal structure of oxygen-evolving photosystem II from *Thermosynechococcus vulcanus* at 3.7-Å resolution, *Proc. Natl. Acad. Sci. U.S.A.*, **2003**, *100*, 98.
- [36] Y. Umena, K. Kawakami, J.-R. Shen and N. Kamiya, Crystal structure of oxygen-evolving photosystem II at a resolution of 1.9 Å, *Nature*, **2011**, *473*, 55.
- [37] J.-L. Soret, Analyse spectrale: Sur le spectre d'absorption du sang dans la partie violette et ultra-violette, *C. R. Acad. Sci.*, **1883**, *97*, 1269.
- [38] F. Scandola, C. Chiorboli, A. Prodi, E. Iengo and E. Alessio, Photophysical properties of metal-mediated assemblies of porphyrins, *Coord. Chem. Rev.*, **2006**, *250*, 1471.

- [39] P. D. Laible, R. S. Knox and T. G. Owens, Detailed Balance in Förster-Dexter Excitation Transfer and Its Application to Photosynthesis, *J. Phys. Chem. B*, **1998**, *102*, 1641.
- [40] I. N. Serdiuk, N. R. Zaccai and J. Zaccai, *Methods in Molecular Biophysics: Structure, Dynamics, Function*, Cambridge University Press, **2007**.
- [41] C. R. Cantor and P. R. Schimmel, *Biophysical Chemistry: Part II: Techniques for the Study of Biological Structure and Function: Techniques for the Study of Biological Structure and Function*, W. H. Freeman, San Francisco, **1980**.
- [42] T. Förster, Zwischenmolekulare Energiewanderung und Fluoreszenz, *Ann. Phys.*, **1948**, *437*, 55.
- [43] J. W. Verhoeven, Glossary of terms used in photochemistry, *Pure Appl. Chem.*, **1996**, *68*, 2223.
- [44] D. L. Dexter, A Theory of Sensitized Luminescence in Solids, *J. Chem. Phys.*, **1953**, *21*, 836.
- [45] J. W. Murray and J. Barber, Structural characteristics of channels and pathways in photosystem II including the identification of an oxygen channel, *J. Struct. Biol.*, **2007**, *159*, 228.
- [46] R. E. Blankenship and R. C. Prince, Excited-state redox potentials and the Z scheme of photosynthesis, *Trends in Biochemical Sciences*, **1985**, *10*, 382.
- [47] F. Rappaport, M. Guergova-Kuras, P. J. Nixon, B. A. Diner and J. Lavergne, Kinetics and Pathways of Charge Recombination in Photosystem II, *Biochemistry*, **2002**, *41*, 8518.
- [48] M. Grabolle and H. Dau, Energetics of primary and secondary electron transfer in Photosystem II membrane particles of spinach revisited on basis of recombination-fluorescence measurements, *Biochim. Biophys. Acta, Bioenerg.*, **2005**, *1708*, 209.
- [49] V. K. Yachandra, K. Sauer and M. P. Klein, Manganese Cluster in Photosynthesis: Where Plants Oxidize Water to Dioxygen, *Chem. Rev.*, **1996**, *96*, 2927.
- [50] J. Yano, J. Kern, K. Sauer, M. J. Latimer, Y. Pushkar, J. Biesiadka, B. Loll, W. Saenger, J. Messinger, A. Zouni and V. K. Yachandra, Where water is oxidized to dioxygen: Structure of the photosynthetic Mn<sub>4</sub>Ca cluster, *Science*, **2006**, *314*, 821.
- [51] J. Yano and V. K. Yachandra, Where water is oxidized to dioxygen: Structure of the photosynthetic Mn<sub>4</sub>Ca cluster from X-ray spectroscopy, *Inorg. Chem.*, **2008**, *47*, 1711.
- [52] C. W. Hoganson and G. T. Babcock, A Metalloradical Mechanism for the Generation of Oxygen from Water in Photosynthesis, *Science*, **1997**, *277*, 1953.
- [53] C. Tommos and G. T. Babcock, Proton and hydrogen currents in photosynthetic water oxidation., *Biochim. Biophys. Acta*, **2000**, *1458*, 199.
- [54] J. Yano, J. Kern, K.-D. Irrgang, M. J. Latimer, U. Bergmann, P. Glatzel, Y. Pushkar, J. Biesiadka, B. Loll, K. Sauer, J. Messinger, A. Zouni and V. K. Yachandra, X-ray damage to the Mn<sub>4</sub>Ca complex in single crystals of photosystem II: A case study for metalloprotein crystallography, *Proc. Natl. Acad. Sci. U.S.A.*, **2005**, *102*, 12047.
- [55] P. E. M. Siegbahn, Structures and Energetics for O<sub>2</sub> Formation in Photosystem II, *Acc. Chem. Res.*, **2009**, *42*, 1871.
- [56] H. Dau, A. Grundmeier, P. Lojka and M. Haumann, On the structure of the manganese complex of photosystem II: extended-range EXAFS data and specific atomic-resolution models for four S-states, *Philos. Trans. R. Soc. London, Ser. B*, **2008**,

- 363, 1237.
- [57] J. W. Murray, K. Maghlaoui, J. Kargul, N. Ishida, T.-L. Lai, A. W. Rutherford, M. Sugiura, A. Boussac and J. Barber, X-ray crystallography identifies two chloride binding sites in the oxygen evolving centre of Photosystem II, *Energy Environ. Sci.*, **2008**, *1*, 161.
- [58] K. Kawakami, Y. Umena, N. Kamiya and J.-R. Shen, Location of chloride and its possible functions in oxygen-evolving photosystem II revealed by X-ray crystallography, *Proc. Natl. Acad. Sci. U.S.A.*, **2009**, *106*, 8567.
- [59] F. M. Ho and S. Styring, Access channels and methanol binding site to the CaMn<sub>4</sub> cluster in Photosystem II based on solvent accessibility simulations, with implications for substrate water access., *Biochim. Biophys. Acta*, **2008**, *1777*, 140.
- [60] F. M. Ho, Structural and mechanistic investigations of photosystem II through computational methods, *Biochim. Biophys. Acta, Bioenerg.*, **2012**, *1817*, 106.
- [61] F. M. Ho, Uncovering channels in photosystem II by computer modelling: current progress, future prospects, and lessons from analogous systems, *Photosynth. Res.*, **2008**, *98*, 503.
- [62] P. Joliot and A. Joliot, A polarographic method for detection of oxygen production and reduction of Hill reagent by isolated chloroplasts, *Biochim. Biophys. Acta, Bioenerg.*, **1968**, *153*, 625.
- [63] B. Kok, B. Forbush and M. McGloin, Cooperation of Charges in Photosynthetic O<sub>2</sub> Evolution – I. A Linear Four Step Mechanism, *Photochem. Photobiol.*, **1970**, *11*, 457.
- [64] M. Haumann, C. Müller, P. Liebisch, L. Iuzzolino, J. Dittmer, M. Grabolle, T. Neisius, W. Meyer-Klaucke and H. Dau, Structural and oxidation state changes of the photosystem II manganese complex in four transitions of the water oxidation cycle (S<sub>0</sub> → S<sub>1</sub>, S<sub>1</sub> → S<sub>2</sub>, S<sub>2</sub> → S<sub>3</sub>, and S<sub>3,4</sub> → S<sub>0</sub>) characterized by X-ray absorption spectroscopy at 20 K and room temperature, *Biochemistry*, **2005**, *44*, 1894.
- [65] H. Dau and M. Haumann, Considerations on the mechanism of photosynthetic water oxidation - dual role of oxo-bridges between Mn ions in (i) redox-potential maintenance and (ii) proton abstraction from substrate water, *Photosynth. Res.*, **2005**, *84*, 325.
- [66] P. E. M. Siegbahn, Mechanisms for proton release during water oxidation in the S<sub>2</sub> to S<sub>3</sub> and S<sub>3</sub> to S<sub>4</sub> transitions in photosystem II, *Phys. Chem. Chem. Phys.*, **2012**, *14*, 4849.
- [67] H. Dau and M. Haumann, Eight steps preceding O-O bond formation in oxygenic photosynthesis—a basic reaction cycle of the Photosystem II manganese complex, *Biochim. Biophys. Acta, Bioenerg.*, **2007**, *1767*, 472.
- [68] H. Dau and M. Haumann, Time-resolved X-ray spectroscopy leads to an extension of the classical S-state cycle model of photosynthetic oxygen evolution, *Photosynth. Res.*, **2007**, *92*, 327.
- [69] I. Zaharieva, J. M. Wichmann and H. Dau, Thermodynamic Limitations of Photosynthetic Water Oxidation at High Proton Concentrations, *J. Biol. Chem.*, **2011**, *286*, 18222.
- [70] A. Klauss, M. Haumann and H. Dau, Alternating electron and proton transfer steps in photosynthetic water oxidation, *Proc. Natl. Acad. Sci. U.S.A.*, **2012**, *109*, 16035.
- [71] T. A. Ono, T. Noguchi, Y. Inoue, M. Kusunoki, T. Matsushita and H. Oyanagi, X-ray Detection of the Period-Four Cycling of the Manganese Cluster in Photo-

- synthetic Water Oxidizing Enzyme, *Science*, **1992**, 258, 1335.
- [72] L. Iuzzolino, J. Dittmer, W. Dörner, W. Meyer-Klaucke and H. Dau, X-ray absorption spectroscopy on layered photosystem II membrane particles suggests manganese-centered oxidation of the oxygen-evolving complex for the  $S_0$ - $S_1$ ,  $S_1$ - $S_2$ , and  $S_2$ - $S_3$  transitions of the water oxidation cycle, *Biochemistry*, **1998**, 37, 17112.
- [73] H. Dau, P. Liebisch and M. Haumann, X-ray absorption spectroscopy to analyze nuclear geometry and electronic structure of biological metal centers—potential and questions examined with special focus on the tetra-nuclear manganese complex of oxygenic photosynthesis, *Anal. Bioanal. Chem.*, **2003**, 376, 562.
- [74] T. A. Roelofs, W. Liang, M. J. Latimer, R. M. Cinco, A. Rompel, J. C. Andrews, K. Sauer, V. K. Yachandra and M. P. Klein, Oxidation states of the manganese cluster during the flash-induced S-state cycle of the photosynthetic oxygen-evolving complex., *Proc. Natl. Acad. Sci. U.S.A.*, **1996**, 93, 3335.
- [75] W. Liang, T. A. Roelofs, R. M. Cinco, A. Rompel, M. J. Latimer, W. O. Yu, K. Sauer, M. P. Klein and V. K. Yachandra, Structural Change of the Mn Cluster during the  $S_2 \rightarrow S_3$  State Transition of the Oxygen-Evolving Complex of Photosystem II. Does It Reflect the Onset of Water/Substrate Oxidation? Determination by Mn X-ray Absorption Spectroscopy, *J. Am. Chem. Soc.*, **2000**, 122, 3399.
- [76] J. Messinger, J. H. Robblee, U. Bergmann, C. Fernandez, P. Glatzel, H. Visser, R. M. Cinco, K. L. McFarlane, E. Bellacchio, S. A. Pizarro, S. P. Cramer, K. Sauer, M. P. Klein and V. K. Yachandra, Absence of Mn-centered oxidation in the  $S_2 \rightarrow S_3$  transition: implications for the mechanism of photosynthetic water oxidation, *J. Am. Chem. Soc.*, **2001**, 123, 7804.
- [77] H. Dau, L. Iuzzolino and J. Dittmer, The tetra-manganese complex of photosystem II during its redox cycle: X-ray absorption results and mechanistic implications, *Biochim. Biophys. Acta, Bioenerg.*, **2001**, 1503, 24.
- [78] W. Ruettinger, M. Yagi, K. Wolf, S. Bernasek and G. C. Dismukes,  $O_2$  Evolution from the Manganese Oxo Cubane Core  $Mn_4O_4^{6+}$ : A Molecular Mimic of the Photosynthetic Water Oxidation Enzyme?, *J. Am. Chem. Soc.*, **2000**, 122, 10353.
- [79] V. L. Pecoraro, M. J. Baldwin, M. T. Caudle, W. Y. Hsieh and N. A. Law, A proposal for water oxidation in photosystem II, *Pure Appl. Chem.*, **1998**, 70, 925.
- [80] J. S. Vrettos, J. Limburg and G. W. Brudvig, Mechanism of photosynthetic water oxidation: combining biophysical studies of photosystem II with inorganic model chemistry, *Biochim. Biophys. Acta, Bioenerg.*, **2001**, 1503, 229.
- [81] J. P. McEvoy, J. A. Gascon, V. S. Batista and G. W. Brudvig, The mechanism of photosynthetic water splitting, *Photochem. Photobiol. Sci.*, **2005**, 4.
- [82] J. Messinger, M. Badger and T. Wydrzynski, Detection of one slowly exchanging substrate water molecule in the  $S_3$  state of photosystem II, *Proc. Natl. Acad. Sci. U.S.A.*, **1995**, 92, 3209.
- [83] W. Hillier and T. Wydrzynski, Oxygen ligand exchange at metal sites implications for the  $O_2$  evolving mechanism of photosystem II, *Biochim. Biophys. Acta, Bioenerg.*, **2001**, 1503, 197.
- [84] D. F. Ghanotakis, G. T. Babcock and C. F. Yocum, Calcium reconstitutes high rates of oxygen evolution in polypeptide depleted Photosystem II preparations, *FEBS Lett.*, **1984**, 167, 127.
- [85] A. Boussac and A. W. Rutherford, Nature of the Inhibition of the Oxygen-Evolving Enzyme of Photosystem II Induced by NaCl Washing and Reversed by the Addi-

- tion of  $\text{Ca}^{2+}$  or  $\text{Sr}^{2+}$ , *Biochemistry*, **1988**, *27*, 3476.
- [86] T.-a. Ono and Y. Inoue, Discrete extraction of the Ca atom functional for  $\text{O}_2$  evolution in higher plant photosystem II by a simple low pH treatment, *FEBS Lett.*, **1988**, *227*, 147.
- [87] M. Miyao and N. Murata, Calcium ions can be substituted for the 24-kDa polypeptide in photosynthetic oxygen evolution, *FEBS Lett.*, **1984**, *168*, 118.
- [88] A. Boussac, J. L. Zimmermann and A. W. Rutherford, EPR signals from modified charge accumulation states of the oxygen-evolving enzyme in calcium-deficient photosystem II, *Biochemistry*, **1989**, *28*, 8984.
- [89] A. Boussac, J.-L. Zimmermann and A. W. Rutherford, Factors influencing the formation of modified  $\text{S}_2$  EPR signal and the  $\text{S}_3$  EPR signal in  $\text{Ca}^{2+}$ -depleted photosystem II, *FEBS Lett.*, **1990**, *277*, 69.
- [90] A. Boussac, F. Rappaport, P. Carrier, J. M. Verbavatz, R. Gobin, D. Kirilovsky, A. W. Rutherford and M. Sugiura, Biosynthetic  $\text{Ca}^{2+}/\text{Sr}^{2+}$  exchange in the photosystem II oxygen-evolving enzyme of *Thermosynechococcus elongatus*, *J. Biol. Chem.*, **2004**, *279*, 22809.
- [91] N. Cox, L. Rapatskiy, J.-H. Su, D. A. Pantazis, M. Sugiura, L. Kulik, P. Dorlet, A. W. Rutherford, F. Neese, A. Boussac, W. Lubitz and J. Messinger, Effect of  $\text{Ca}^{2+}/\text{Sr}^{2+}$  Substitution on the Electronic Structure of the Oxygen-Evolving Complex of Photosystem II: A Combined Multifrequency EPR,  $^{55}\text{Mn}$ -ENDOR, and DFT Study of the  $\text{S}_2$  State, *J. Am. Chem. Soc.*, **2011**, *133*, 3635.
- [92] J. M. Peloquin, K. A. Campbell, D. W. Randall, M. A. Evanchik, V. L. Pecoraro, W. H. Armstrong and R. D. Britt,  $^{55}\text{Mn}$  ENDOR of the  $\text{S}_2$ -State Multiline EPR Signal of Photosystem II: Implications on the Structure of the Tetranuclear Mn Cluster, *J. Am. Chem. Soc.*, **2000**, *122*, 10926.
- [93] L. V. Kulik, B. Epel, W. Lubitz and J. Messinger,  $^{55}\text{Mn}$  pulse ENDOR at 34 GHz of the  $\text{S}_0$  and  $\text{S}_2$  states of the oxygen-evolving complex in photosystem II., *J. Am. Chem. Soc.*, **2005**, *127*, 2392.
- [94] L. Kulik, B. Epel, J. Messinger and W. Lubitz, Pulse EPR,  $^{55}\text{Mn}$ -ENDOR and ELDOR-detected NMR of the  $\text{S}_2$ -state of the oxygen evolving complex in photosystem II., *Photosynth. Res.*, **2005**, *84*, 347.
- [95] J. P. McEvoy and G. W. Brudvig, Structure-based mechanism of photosynthetic water oxidation, *Phys. Chem. Chem. Phys.*, **2004**, *6*, 4754.
- [96] C. F. Yocum, The calcium and chloride requirements of the  $\text{O}_2$  evolving complex, *Coord. Chem. Rev.*, **2008**, *252*, 296.
- [97] V. K. Yachandra and J. Yano, Calcium in the oxygen-evolving complex: Structural and mechanistic role determined by X-ray spectroscopy, *J. Photochem. Photobiol., B*, **2011**, *104*, 51.
- [98] M. Kirch, J.-M. Lehn and J.-P. Sauvage, Hydrogen Generation by Visible Light Irradiation of Aqueous Solutions of Metal Complexes. An approach to the photochemical conversion and storage of solar energy, *Helv. Chim. Acta*, **1979**, *62*, 1345.
- [99] E. S. Andreiadis, M. Chavarot-Kerlidou, M. Fontecave and V. Artero, Artificial Photosynthesis: From Molecular Catalysts for Light-driven Water Splitting to Photoelectrochemical Cells, *Photochem. Photobiol.*, **2011**, *87*, 946.
- [100] S. Styring, Artificial photosynthesis for solar fuels, *Faraday Discuss.*, **2012**, *155*, 357.
- [101] C. W. Cady, R. H. Crabtree and G. W. Brudvig, Functional models for the oxygen-evolving complex of photosystem II, *Coord. Chem. Rev.*, **2008**, *252*, 444.

- [102] K. Maeda, A. Xiong, T. Yoshinaga, T. Ikeda, N. Sakamoto, T. Hisatomi, M. Takashima, D. Lu, M. Kanehara, T. Setoyama, T. Teranishi and K. Domen, Photocatalytic Overall Water Splitting Promoted by Two Different Cocatalysts for Hydrogen and Oxygen Evolution under Visible Light, *Angew. Chem.*, **2010**, *122*, 4190.
- [103] M. Wiechen, H.-M. Berends and P. Kurz, Water oxidation catalysed by manganese compounds: from complexes to 'biomimetic rocks', *Dalton Trans.*, **2012**, *41*, 21.
- [104] C. H. Hamann, A. Hamnett and W. Vielstich, *Electrochemistry*, Wiley-VCH, Weinheim, **2007**.
- [105] J. Rossmeisl, A. Logadottir and J. K. Nørskov, Electrolysis of water on (oxidized) metal surfaces, *Chem. Phys.*, **2005**, *319*, 178.
- [106] J. Rossmeisl, Z.-W. Qu, H. Zhu, G.-J. Kroes and J. K. Nørskov, Electrolysis of water on oxide surfaces, *J. Electroanal. Chem.*, **2007**, *607*, 83.
- [107] J. O. Bockris, Hydrogen economy in the future, *Int. J. Hydrogen Energy*, **1999**, *24*, 1.
- [108] V. Balzani, A. Credi and M. Venturi, Photochemical conversion of solar energy, *ChemSusChem*, **2008**, *1*, 26.
- [109] M. G. Walter, E. L. Warren, J. R. McKone, S. W. Boettcher, Q. Mi, E. A. Santori and N. S. Lewis, Solar Water Splitting Cells, *Chem. Rev.*, **2010**, *110*, 6446.
- [110] K. Maeda and K. Domen, Photocatalytic Water Splitting: Recent Progress and Future Challenges, *J. Phys. Chem. Lett.*, **2010**, *1*, 2655.
- [111] A. Kudo and Y. Miseki, Heterogeneous photocatalyst materials for water splitting, *Chem. Soc. Rev.*, **2009**, *38*, 253.
- [112] A. Kudo, Z-scheme photocatalyst systems for water splitting under visible light irradiation, *MRS Bulletin*, **2011**, *36*, 32.
- [113] K. Maeda, A. Xiong, T. Yoshinaga, T. Ikeda, N. Sakamoto, T. Hisatomi, M. Takashima, D. Lu, M. Kanehara, T. Setoyama, T. Teranishi and K. Domen, Photocatalytic Overall Water Splitting Promoted by Two Different Cocatalysts for Hydrogen and Oxygen Evolution under Visible Light, *Angew. Chem. Int. Ed.*, **2010**, *49*, 4096.
- [114] K. Maeda and K. Domen, Oxynitride materials for solar water splitting, *MRS Bull.*, **2011**, *36*, 25.
- [115] A. P. Troostwijk and J. R. Deiman, *Obs. Phys.*, **1789**, *35*, 369.
- [116] R. de Levie, The electrolysis of water, *J. Electroanal. Chem.*, **1999**, *476*, 92.
- [117] H. Cavendish, *Phil. Trans.*, **1784**, *74*, 119.
- [118] S. Trasatti, 1799 - 1999: Alessandro Volta's 'Electric Pile' Two hundred years, but it doesn't seem like it, *J. Electroanal. Chem.*, **1999**, *460*, 1.
- [119] S. Trasatti, Water electrolysis: who first?, *J. Electroanal. Chem.*, **1999**, *476*, 90.
- [120] A. W. Hofmann, *Introduction to Modern Chemistry: Experimental and Theoretic*, Walton and Maberly, London, **1866**.
- [121] I. C. Man, H.-Y. Su, F. Calle-Vallejo, H. A. Hansen, J. I. Martínez, N. G. Inoglu, J. Kitchin, T. F. Jaramillo, J. K. Nørskov and J. Rossmeisl, Universality in Oxygen Evolution Electrocatalysis on Oxide Surfaces, *Chemcatchem*, **2011**, *3*, 1159.
- [122] L. da Silva, V. Alves, M. da Silva, S. Trasatti and J. Boodts, Oxygen evolution in acid solution on IrO<sub>2</sub> + TiO<sub>2</sub> ceramic films. A study by impedance, voltammetry and SEM, *Electrochim. Acta*, **1997**, *42*, 271.
- [123] T. Lassali, S. D. Castro and J. Boodts, Structural, morphological and surface prop-

- erties as a function of composition of Ru+Ti+Pt mixed-oxide electrodes, *Electrochim. Acta*, **1998**, *43*, 2515.
- [124] S. Song, H. Zhang, X. Ma, Z. Shao, R. T. Baker and B. Yi, Electrochemical investigation of electrocatalysts for the oxygen evolution reaction in PEM water electrolyzers, *Int. J. Hydrogen Energy*, **2008**, *33*, 4955.
- [125] K. Zeng and D. Zhang, Recent progress in alkaline water electrolysis for hydrogen production and applications, *Prog. Energy Combust. Sci.*, **2010**, *36*, 307.
- [126] P. Millet, R. Ngameni, S. Grigoriev, N. Mbemba, F. Brisset, A. Ranjbari and C. Etiévant, PEM water electrolyzers: From electrocatalysis to stack development, *Int. J. Hydrogen Energy*, **2010**, *35*, 5043.
- [127] M. W. Kanan and D. G. Nocera, In situ formation of an oxygen-evolving catalyst in neutral water containing phosphate and  $\text{Co}^{2+}$ , *Science*, **2008**, *321*, 1072.
- [128] M. Risch, V. Khare, I. Zaharieva, L. Gerencser, P. Chernev and H. Dau, Cobalt-oxo core of a water-oxidizing catalyst film, *J. Am. Chem. Soc.*, **2009**, *131*, 6936.
- [129] M. W. Kanan, J. Yano, Y. Surendranath, M. Dincă, V. K. Yachandra and D. G. Nocera, Structure and valency of a cobalt-phosphate water oxidation catalyst determined by in situ X-ray spectroscopy, *J. Am. Chem. Soc.*, **2010**, *132*, 13692.
- [130] J. J. H. Pijpers, M. T. Winkler, Y. Surendranath, T. Buonassisi and D. G. Nocera, Light-induced water oxidation at silicon electrodes functionalized with a cobalt oxygen-evolving catalyst, *Proc. Natl. Acad. Sci. U.S.A.*, **2011**, *108*, 10056.
- [131] R. K. Hocking, R. Brimblecombe, L.-Y. Chang, A. Singh, M. H. Cheah, C. Glover, W. H. Casey and L. Spiccia, Water-oxidation catalysis by manganese in a geochemical-like cycle, *Nat. Chem.*, **2011**, *3*, 461.
- [132] B. A. Pinaud, Z. Chen, D. N. Abram and T. F. Jaramillo, Thin Films of Sodium Birnessite-Type  $\text{MnO}_2$ : Optical Properties, Electronic Band Structure, and Solar Photoelectrochemistry, *J. Phys. Chem. C*, **2011**, *115*, 11830.
- [133] I. Zaharieva, P. Chernev, M. Risch, K. Klingan, M. Kohlhoff, A. Fischer and H. Dau, Electrosynthesis, functional, and structural characterization of a water-oxidizing manganese oxide, *Energy Environ. Sci.*, **2012**, *5*, 7081.
- [134] M. Dincă, Y. Surendranath and D. G. Nocera, Nickel-borate oxygen-evolving catalyst that functions under benign conditions, *Proc. Natl. Acad. Sci. U.S.A.*, **2010**, *107*, 10337.
- [135] M. Risch, K. Klingan, J. Heidkamp, D. Ehrenberg, P. Chernev, I. Zaharieva and H. Dau, Nickel-oxido structure of a water-oxidizing catalyst film, *Chem. Commun.*, **2011**, *47*, 11912.
- [136] S. Y. Reece, J. A. Hamel, K. Sung, T. D. Jarvi, A. J. Esswein, J. J. H. Pijpers and D. G. Nocera, Wireless Solar Water Splitting Using Silicon-Based Semiconductors and Earth-Abundant Catalysts, *Science*, **2011**, *334*, 645.
- [137] D. G. Nocera, The Artificial Leaf, *Acc. Chem. Res.*, **2012**, *45*, 767.
- [138] A. Paracchino, V. Laporte, K. Sivula, M. Grätzel and E. Thimsen, Highly active oxide photocathode for photoelectrochemical water reduction, *Nat. Mater.*, **2011**, *10*, 456.
- [139] KLIMARETTER.INFO, <http://www.klimaretter.info/energie/nachricht/9730-windstrom-zu-jeder-zeit>.
- [140] J. R. Hook and H. E. Hall, *Solid State Physics*, John Wiley & Sons, Chichester, **1991**.
- [141] B. O'Regan and M. Gratzel, A low-cost, high-efficiency solar cell based on dye-

- sensitized colloidal TiO<sub>2</sub> films, *Nature*, **1991**, 353, 737.
- [142] M. Grätzel, Recent Advances in Sensitized Mesoscopic Solar Cells, *Acc. Chem. Res.*, **2009**, 42, 1788.
- [143] B. C. O'Regan and J. R. Durrant, Kinetic and Energetic Paradigms for Dye-Sensitized Solar Cells: Moving from the Ideal to the Real, *Acc. Chem. Res.*, **2009**, 42, 1799.
- [144] A. Hagfeldt, G. Boschloo, L. Sun, L. Kloo and H. Pettersson, Dye-Sensitized Solar Cells, *Chem. Rev.*, **2010**, 110, 6595.
- [145] M. K. Nazeeruddin, E. Baranoff and M. Grätzel, Dye-sensitized solar cells: A brief overview, *Sol. Energy*, **2011**, 85, 1172.
- [146] A. Fujishima and K. Honda, Electrochemical Photolysis of Water at a Semiconductor Electrode, *Nature*, **1972**, 238, 37.
- [147] H. Yoneyama, H. Sakamoto and H. Tamura, A Photo-electrochemical cell with production of hydrogen and oxygen by a cell reaction, *Electrochimica Acta*, **1975**, 20, 341.
- [148] A. J. Nozik, p-n photoelectrolysis cells, *Applied Physics Letters*, **1976**, 29, 150.
- [149] R. C. Kainthla, B. Zelenay and J. O. Bockris, Significant Efficiency Increase in Self-Driven Photoelectrochemical Cell for Water Photoelectrolysis, *J. Electrochem. Soc.*, **1987**, 134, 841.
- [150] G. H. Lin, M. Kapur, R. C. Kainthla and J. O. Bockris, One step method to produce hydrogen by a triple stack amorphous silicon solar cell, *Appl. Phys. Lett.*, **1989**, 55, 386.
- [151] A. Delahoy, S. Gau, O. Murphy, M. Kapur and J. Bockris, A one-unit photovoltaic electrolysis system based on a triple stack of amorphous silicon (pin) cells, *Int. J. Hydrogen Energy*, **1985**, 10, 113.
- [152] A. Appleby, A. Delahoy, S. Gau, O. Murphy, M. Kapur and J. Bockris, An amorphous silicon-based one-unit photovoltaic electrolyzer, *Energy*, **1985**, 10, 871.
- [153] Y. Sakai, S. Sugahara, M. Matsumura, Y. Nakato and H. Tsubomura, Photoelectrochemical water splitting by tandem type and heterojunction amorphous silicon electrodes, *Can. J. Chem.*, **1988**, 66, 1853.
- [154] R. E. Rocheleau, E. L. Miller and A. Misra, High-Efficiency Photoelectrochemical Hydrogen Production Using Multijunction Amorphous Silicon Photoelectrodes, *Energy Fuels*, **1998**, 12, 3.
- [155] S. Licht, B. Wang, S. Mukerji, T. Soga, M. Umeno and H. Tributsch, Efficient Solar Water Splitting, Exemplified by RuO<sub>2</sub>-Catalyzed AlGaAs/Si Photoelectrolysis, *J. Phys. Chem. B*, **2000**, 104, 8920.
- [156] O. Khaselev and J. A. Turner, A Monolithic Photovoltaic-Photoelectrochemical Device for Hydrogen Production via Water Splitting, *Science*, **1998**, 280, 425.
- [157] O. Khaselev, A. Bansal and J. A. Turner, High-efficiency integrated multijunction photovoltaic/electrolysis systems for hydrogen production, *Int. J. Hydrogen Energy*, **2001**, 26, 127.
- [158] R. Brimblecombe, A. Koo, G. C. Dismukes, G. F. Swiegers and L. Spiccia, A Tandem Water-Splitting Device Based on a Bio-inspired Manganese Catalyst, *ChemSusChem*, **2010**, 3, 1146.
- [159] R. Brimblecombe, A. Koo, G. C. Dismukes, G. F. Swiegers and L. Spiccia, Solar Driven Water Oxidation by a Bioinspired Manganese Molecular Catalyst, *J. Am.*

- Chem. Soc.*, **2010**, *132*, 2892.
- [160] S.-H. A. Lee, Y. Zhao, E. A. Hernandez-Pagan, L. Blasdel, W. J. Youngblood and T. E. Mallouk, Electron transfer kinetics in water splitting dye-sensitized solar cells based on core-shell oxide electrodes, *Faraday Discuss.*, **2012**, *155*, 165.
- [161] L. Li, L. Duan, F. Wen, C. Li, M. Wang, A. Hagfeldt and L. Sun, Visible light driven hydrogen production from a photo-active cathode based on a molecular catalyst and organic dye-sensitized p-type nanostructured NiO, *Chem. Commun.*, **2012**, *48*, 988.
- [162] R. Abe, K. Shinmei, K. Hara and B. Ohtani, Robust dye-sensitized overall water splitting system with two-step photoexcitation of coumarin dyes and metal oxide semiconductors, *Chem. Commun.*, **2009**, *46*, 3577.
- [163] K. Takanabe, K. Kamata, X. Wang, M. Antonietti, J. Kubota and K. Domen, Photocatalytic hydrogen evolution on dye-sensitized mesoporous carbon nitride photocatalyst with magnesium phthalocyanine, *Phys. Chem. Chem. Phys.*, **2010**, *12*, 13020.
- [164] M. Yagi and M. Kaneko, Molecular Catalysts for Water Oxidation, *Chem. Rev.*, **2001**, *101*, 21.
- [165] S. Mukhopadhyay, S. K. Mandal, S. Bhaduri and W. H. Armstrong, Manganese clusters with relevance to photosystem II, *Chem. Rev.*, **2004**, *104*, 3981.
- [166] C. S. Mullins and V. L. Pecoraro, Reflections on small molecule manganese models that seek to mimic photosynthetic water oxidation chemistry, *Coord. Chem. Rev.*, **2008**, *252*, 416.
- [167] M.-N. Collomb and A. Deronzier, Electro- and Photoinduced Formation and Transformation of Oxido-Bridged Multinuclear Mn Complexes, *Eur. J. Inorg. Chem.*, **2009**, *2009*, 2025.
- [168] H.-M. Berends, *Manganese compounds as catalysts for water oxidation and as CO releasing molecules*, Ph.D. thesis, Christian-Albrechts-Universität zu Kiel, **2011**.
- [169] H.-M. Berends, A.-M. Manke, C. Näther, F. Tucek and P. Kurz, A manganese oxido complex bearing facially coordinating trispyridyl ligands - is coordination geometry crucial for water oxidation catalysis?, *Dalton Trans.*, **2012**, *41*, 6215.
- [170] D. Shevela, S. Koroidov, M. M. Najafpour, J. Messinger and P. Kurz, Calcium Manganese Oxides as Oxygen Evolution Catalysts: O<sub>2</sub> Formation Pathways Indicated by <sup>18</sup>O-Labeling Studies, *Chem. Eur. J.*, **2011**, *17*, 5415.
- [171] A. R. Parent, R. H. Crabtree and G. W. Brudvig, Comparison of primary oxidants for water-oxidation catalysis, *Chem. Soc. Rev.*, **2013**, *42*, 2247.
- [172] R. Ramaraj, A. Kira and M. Kaneko, Heterogeneous Water Oxidation by a Dinuclear Manganese Complex, *Chem. Lett.*, **1987**, *16*, 261.
- [173] H.-M. Berends, T. Homburg, I. Kunz and P. Kurz, K10 montmorillonite supported manganese catalysts for the oxidation of water to dioxygen, *Appl. Clay Sci.*, **2011**, *53*, 174.
- [174] T. Homburg, *Manganbasierte Wasseroxidationskatalysatoren auf Montmorillonit*, BSc thesis, Christian-Albrechts-Universität zu Kiel, **2010**.
- [175] E. A. Karlsson, B.-L. Lee, T. Åkermark, E. V. Johnston, M. D. Kärkäs, J. Sun, Ö. Hansson, J.-E. Bäckvall and B. Åkermark, Photosensitized Water Oxidation by Use of a Bioinspired Manganese Catalyst, *Angew. Chem. Int. Ed.*, **2011**, *50*, 11715.
- [176] W. F. Ruettinger, C. Campana and G. C. Dismukes, Synthesis and characterization of Mn<sub>4</sub>O<sub>4</sub>L<sub>6</sub> complexes with cubane-like core structure: A new class of models of

- the active site of the photosynthetic water oxidase, *J. Am. Chem. Soc.*, **1997**, *119*, 6670.
- [177] M. Yagi, K. V. Wolf, P. J. Baesjou, S. L. Bernasek and G. C. Dismukes, Selective Photoproduction of O<sub>2</sub> from the Mn<sub>4</sub>O<sub>4</sub> Cubane Core: A Structural and Functional Model for the Photosynthetic Water-Oxidizing Complex, *Angew. Chem. Int. Ed.*, **2001**, *40*, 2925.
- [178] R. Brimblecombe, G. Swiegers, G. Dismukes and L. Spiccia, Sustained Water Oxidation Photocatalysis by a Bioinspired Manganese Cluster, *Angew. Chem. Int. Ed.*, **2008**, *47*, 7335.
- [179] L. Flamigni, J.-P. Collin and J.-P. Sauvage, Iridium Terpyridine Complexes as Functional Assembling Units in Arrays for the Conversion of Light Energy, *Acc. Chem. Res.*, **2008**, *41*, 857.
- [180] J. J. Concepcion, J. W. Jurss, M. K. Brennaman, P. G. Hoertz, A. O. T. Patrocinio, N. Y. Murakami Iha, J. L. Templeton and T. J. Meyer, Making Oxygen with Ruthenium Complexes, *Acc. Chem. Res.*, **2009**, *42*, 1954.
- [181] S. Romain, L. Vigara and A. Llobet, Oxygen-Oxygen Bond Formation Pathways Promoted by Ruthenium Complexes, *Acc. Chem. Res.*, **2009**, *42*, 1944.
- [182] J. J. Concepcion, M.-K. Tsai, J. T. Muckerman and T. J. Meyer, Mechanism of Water Oxidation by Single-Site Ruthenium Complex Catalysts, *J. Am. Chem. Soc.*, **2010**, *132*, 1545.
- [183] V. Artero, M. Chavarot-Kerlidou and M. Fontecave, Splitting Water with Cobalt, *Angew. Chem. Int. Ed.*, **2011**, *50*, 7238.
- [184] S. W. Gersten, G. J. Samuels and T. J. Meyer, Catalytic oxidation of water by an oxo-bridged ruthenium dimer, *J. Am. Chem. Soc.*, **1982**, *104*, 4029.
- [185] J. A. Gilbert, D. S. Eggleston, W. R. Murphy, D. A. Geselowitz, S. W. Gersten, D. J. Hodgson and T. J. Meyer, Structure and redox properties of the water-oxidation catalyst [(bpy)<sub>2</sub>(OH<sub>2</sub>)RuORu(OH<sub>2</sub>)(bpy)<sub>2</sub>]<sup>4+</sup>, *J. Am. Chem. Soc.*, **1985**, *107*, 3855.
- [186] F. Liu, J. J. Concepcion, J. W. Jurss, T. Cardolaccia, J. L. Templeton and T. J. Meyer, Mechanisms of Water Oxidation from the Blue Dimer to Photosystem II, *Inorg. Chem.*, **2008**, *47*, 1727.
- [187] L. Duan, A. Fischer, Y. Xu and L. Sun, Isolated Seven-Coordinate Ru(IV) Dimer Complex with [HOHOH]<sup>-</sup> Bridging Ligand as an Intermediate for Catalytic Water Oxidation, *J. Am. Chem. Soc.*, **2009**, *131*, 10397.
- [188] Y. V. Geletii, C. Besson, Y. Hou, Q. Yin, D. G. Musaev, D. Quiñonero, R. Cao, K. I. Hardcastle, A. Proust, P. Kögerler and C. L. Hill, Structural, Physicochemical, and Reactivity Properties of an All-Inorganic, Highly Active Tetra-ruthenium Homogeneous Catalyst for Water Oxidation, *J. Am. Chem. Soc.*, **2009**, *131*, 17360.
- [189] L. Duan, F. Bozoglian, S. Mandal, B. Stewart, T. Privalov, A. Llobet and L. Sun, A molecular ruthenium catalyst with water-oxidation activity comparable to that of photosystem II, *Nat. Chem.*, **2012**, *4*, 418.
- [190] Q. Yin, J. M. Tan, C. Besson, Y. V. Geletii, D. G. Musaev, A. E. Kuznetsov, Z. Luo, K. I. Hardcastle and C. L. Hill, A Fast Soluble Carbon-Free Molecular Water Oxidation Catalyst Based on Abundant Metals, *Science*, **2010**, *328*, 342.
- [191] Y. Geletii, B. Botar, P. Kögerler, D. Hillesheim, D. Musaev and C. Hill, An All-Inorganic, Stable, and Highly Active Tetra-ruthenium Homogeneous Catalyst for Water Oxidation, *Angew. Chem. Int. Ed.*, **2008**, *47*, 3896.
- [192] A. Sartorel, M. Carraro, G. Scorrano, R. D. Zorzi, S. Geremia, N. D.

- McDaniel, S. Bernhard and M. Bonchio, Polyoxometalate Embedding of a Tetraruthenium(IV)-oxo-core by Template-Directed Metalation of  $[\gamma\text{-SiW}_{10}\text{O}_{36}]^{8-}$ : A Totally Inorganic Oxygen-Evolving Catalyst, *J. Am. Chem. Soc.*, **2008**, *130*, 5006.
- [193] A. Sartorel, P. Miró, E. Salvadori, S. Romain, M. Carraro, G. Scorrano, M. D. Valentin, A. Llobet, C. Bo and M. Bonchio, Water Oxidation at a Tetraruthenate Core Stabilized by Polyoxometalate Ligands: Experimental and Computational Evidence To Trace the Competent Intermediates, *J. Am. Chem. Soc.*, **2009**, *131*, 16051.
- [194] Y. V. Geletii, Z. Huang, Y. Hou, D. G. Musaev, T. Lian and C. L. Hill, Homogeneous Light-Driven Water Oxidation Catalyzed by a Tetraruthenium Complex with All Inorganic Ligands, *J. Am. Chem. Soc.*, **2009**, *131*, 7522.
- [195] A. Harriman, I. J. Pickering, J. M. Thomas and P. A. Christensen, Metal oxides as heterogeneous catalysts for oxygen evolution under photochemical conditions, *J. Chem. Soc., Faraday Trans. 1 F*, **1988**, *84*, 2795.
- [196] D. A. Lutterman, Y. Surendranath and D. G. Nocera, A Self-Healing Oxygen-Evolving Catalyst, *J. Am. Chem. Soc.*, **2009**, *131*, 3838.
- [197] Y. Surendranath, M. Dinca and D. G. Nocera, Electrolyte-Dependent Electrosynthesis and Activity of Cobalt-Based Water Oxidation Catalysts, *J. Am. Chem. Soc.*, **2009**, *131*, 2615.
- [198] J. B. Gerken, J. G. McAlpin, J. Y. C. Chen, M. L. Rigsby, W. H. Casey, R. D. Britt and S. S. Stahl, Electrochemical Water Oxidation with Cobalt-Based Electrocatalysts from pH 0-14: The Thermodynamic Basis for Catalyst Structure, Stability, and Activity, *J. Am. Chem. Soc.*, **2011**, *133*, 14431.
- [199] M. Risch, K. Klingan, F. Ringleb, P. Chernev, I. Zaharieva, A. Fischer and H. Dau, Water Oxidation by Electrodeposited Cobalt Oxides—Role of Anions and Redox-Inert Cations in Structure and Function of the Amorphous Catalyst, *ChemSusChem*, **2012**, *5*, 542.
- [200] M. W. Kanan, Y. Surendranath and D. G. Nocera, Cobalt-phosphate oxygen-evolving compound, *Chem. Soc. Rev.*, **2009**, *38*, 109.
- [201] E. M. P. Steinmiller and K.-S. Choi, Photochemical deposition of cobalt-based oxygen evolving catalyst on a semiconductor photoanode for solar oxygen production, *Proc. Natl. Acad. Sci. U.S.A.*, **2009**, *106*, 20633.
- [202] D. K. Zhong, J. Sun, H. Inumaru and D. R. Gamelin, Solar Water Oxidation by Composite Catalyst/ $\alpha\text{-Fe}_2\text{O}_3$  Photoanodes, *J. Am. Chem. Soc.*, **2009**, *131*, 6086.
- [203] D. K. Zhong and D. R. Gamelin, Photoelectrochemical Water Oxidation by Cobalt Catalyst (“Co-Pi”)/ $\alpha\text{-Fe}_2\text{O}_3$  Composite Photoanodes: Oxygen Evolution and Resolution of a Kinetic Bottleneck, *J. Am. Chem. Soc.*, **2010**, *132*, 4202.
- [204] M. Barroso, A. J. Cowan, S. R. Pendlebury, M. Grätzel, D. R. Klug and J. R. Durrant, The Role of Cobalt Phosphate in Enhancing the Photocatalytic Activity of  $\alpha\text{-Fe}_2\text{O}_3$  toward Water Oxidation, *J. Am. Chem. Soc.*, **2011**, *133*, 14868.
- [205] M. Risch, F. Ringleb, V. Khare, P. Chernev, I. Zaharieva and H. Dau, Characterisation of a water-oxidizing Co-film by XAFS, *J. Phys. Conf. Ser.*, **2009**, *190*, 012167.
- [206] K. Sun, N. Park, Z. Sun, J. Zhou, J. Wang, X. Pang, S. Shen, S. Y. Noh, Y. Jing, S. Jin, P. K. L. Yu and D. Wang, Nickel oxide functionalized silicon for efficient photo-oxidation of water, *Energy Environ. Sci.*, **2012**, *5*, 7872.
- [207] M. Morita, C. Iwakura and H. Tamura, Anodic Characteristics of Manganese-Dioxide Electrodes Prepared by Thermal-Decomposition of Manganese Nitrate,

- Electrochim. Acta*, **1977**, *22*, 325.
- [208] M. Morita, C. Iwakura and H. Tamura, The anodic characteristics of massive manganese oxide electrode, *Electrochim. Acta*, **1979**, *24*, 357.
- [209] S. Trasatti, Electrocatalysis by oxides – Attempt at a unifying approach, *J. Electroanal. Chem. Interfacial Electrochem.*, **1980**, *111*, 125.
- [210] Y. Matsumoto and E. Sato, Electrocatalytic properties of transition metal oxides for oxygen evolution reaction, *Mater. Chem. Phys.*, **1986**, *14*, 397.
- [211] D. G. Brookins, *Eh-pH Diagrams for Geochemistry*, Springer, Berlin, Heidelberg, **1988**.
- [212] N. Takeno, Atlas of Eh-pH diagrams, Geological Survey of Japan Open File Report No.419, [www.gsj.jp/data/openfile/no0419/openfile419e.pdf](http://www.gsj.jp/data/openfile/no0419/openfile419e.pdf), **2005**.
- [213] V. Y. Shafirovich, N. K. Khannanov and A. E. Shilov, Inorganic models of photosystem II of plant photosynthesis. Catalytic and photocatalytic oxidation of water with participation of manganese compounds, *J. Inorg. Biochem.*, **1981**, *15*, 113.
- [214] M. Najafpour, T. Ehrenberg, M. Wiechen and P. Kurz, Calcium Manganese(III) Oxides ( $\text{CaMn}_2\text{O}_4 \cdot x \text{H}_2\text{O}$ ) as Biomimetic Oxygen-Evolving Catalysts, *Angew. Chem. Int. Ed.*, **2010**, *49*, 2233.
- [215] I. Zaharieva, M. M. Najafpour, M. Wiechen, M. Haumann, P. Kurz and H. Dau, Synthetic manganese-calcium oxides mimic the water-oxidizing complex of photosynthesis functionally and structurally, *Energy Environ. Sci.*, **2011**, *4*, 2400.
- [216] J. E. Post, Manganese oxide minerals: Crystal structures and economic and environmental significance, *Proc. Natl. Acad. Sci. U.S.A.*, **1999**, *96*, 3447.
- [217] J. Luo, Q. Zhang, A. Huang, O. Giraldo and S. L. Suib, Double-Aging Method for Preparation of Stabilized Na-Buserite and Transformations to Todorokites Incorporated with Various Metals, *Inorg. Chem.*, **1999**, *38*, 6106.
- [218] J. Luo, Q. Zhang and S. L. Suib, Mechanistic and kinetic studies of crystallization of birnessite, *Inorg. Chem.*, **2000**, *39*, 741.
- [219] S. Brunauer, P. H. Emmett and E. Teller, Adsorption of Gases in Multimolecular Layers, *J. Am. Chem. Soc.*, **1938**, *60*, 309.
- [220] S. Brunauer, L. S. Deming, W. E. Deming and E. Teller, On a Theory of the van der Waals Adsorption of Gases, *J. Am. Chem. Soc.*, **1940**, *62*, 1723.
- [221] K. Sing, D. Everett, R. Haul, L. Moscou, R. Pierotti, J. Rouquerol and T. Siemieniowska, Reporting physisorption data for gas/solid systems with special reference to the determination of surface area and porosity, *Pure Appl. Chem.*, **1985**, *57*, 603.
- [222] J. Rouquerol, D. Avnir, C. Fairbridge, D. Everett, J. Haynes, N. Pernicone, J. Ramsay, K. Sing and K. Unger, Recommendations for the characterization of porous solids, *Pure Appl. Chem.*, **1994**, *66*, 1739.
- [223] M. Wiechen, I. Zaharieva, H. Dau and P. Kurz, Layered manganese oxides for water-oxidation: alkaline earth cations influence catalytic activity in a photosystem II-like fashion, *Chem. Sci.*, **2012**, *3*, 2330.
- [224] M. Poschmann, *Wasseroxidationskatalyse mit "biomimetischen" Oxiden – Variation des Birnessitsystems*, BSc thesis, Christian-Albrechts-Universität zu Kiel, **2011**.
- [225] A. Elmchaouri and R. Mahboub, Effects of preadsorption of organic amine on Al-PILCs structures, *Colloids Surf., A*, **2005**, *259*, 135.
- [226] A. Gil, M. Vicente and S. Korili, Effect of the Si/Al ratio on the structure and

- surface properties of silica-alumina-pillared clays, *J. Catal.*, **2005**, *229*, 119.
- [227] B. Mishra and G. R. Rao, Cerium Containing Al- and Zr-Pillared Clays: Promoting Effect of Cerium (III) Ions on Structural and Catalytic Properties, *J. Porous Mater.*, **2005**, *12*, 171.
- [228] A. Gil, M. A. Vicente and S. A. Korili, Effect of the nature and structure of pillared clays in the catalytic behaviour of supported manganese oxide, *Catal. Today*, **2006**, *112*, 117.
- [229] S. Zuo and R. Zhou, Influence of synthesis condition on pore structure of Al pillared clays and supported Pd catalysts for deep oxidation of benzene, *Microporous Mesoporous Mater.*, **2008**, *113*, 472.
- [230] M. P. Gashti and S. Eslami, Structural, optical and electromagnetic properties of aluminum–clay nanocomposites, *Superlattices Microstruct.*, **2012**, *51*, 135.
- [231] H. Cui, L. You, X. Feng, W. Tan, G. Qiu and F. Liu, Factors Governing the Formation of Lithiophorite at Atmospheric Pressure, *Clays Clay Miner.*, **2009**, *57*, 353.
- [232] A. Manceau, B. Lanson and V. A. Drits, Structure of heavy metal sorbed birnessite. Part III: Results from powder and polarized extended X-ray absorption fine structure spectroscopy, *Geochim. Cosmochim. Acta*, **2002**, *66*, 2639.
- [233] B. M. Tebo, J. R. Bargar, B. G. Clement, G. J. Dick, K. J. Murray, D. Parker, R. Verity and S. M. Webb, Biogenic manganese oxides: Properties and mechanisms of formation, *Annu. Rev. Earth Planet. Sci.*, **2004**, *32*, 287.
- [234] D. C. Golden, C. C. Chen and J. B. Dixon, Synthesis of todorokite, *Science*, **1986**, *231*, 717.
- [235] R. M. Potter and G. R. Rossman, The tetravalent manganese oxides: identification, hydration, and structural relationships by infrared spectroscopy, *Am. Mineral.*, **1979**, *64*, 1199.
- [236] X.-M. Shen and A. Clearfield, Phase transitions and ion exchange behavior of electrolytically prepared manganese dioxide, *J. Solid State Chem.*, **1986**, *64*, 270.
- [237] Q. Feng, Y. Miyai, H. Kanoh and K. Ooi, Li<sup>+</sup> extraction/insertion with spinel-type lithium manganese oxides. Characterization of redox-type and ion-exchange-type sites, *Langmuir*, **1992**, *8*, 1861.
- [238] J. Luo, A. Huang, S. H. Park, S. L. Suib and C.-L. O'Young, Crystallization of Sodium-Birnessite and Accompanied Phase Transformation, *Chem. Mater.*, **1998**, *10*, 1561.
- [239] L. Kang, M. Zhang, Z.-H. Liu and K. Ooi, IR spectra of manganese oxides with either layered or tunnel structures, *Spectrochim. Acta, Part A*, **2007**, *67*, 864.
- [240] D. S. Yang and M. K. Wang, Syntheses and Characterization of Well-Crystallized Birnessite, *Chem. Mater.*, **2001**, *13*, 2589.
- [241] C. Julien, M. Massot and C. Poinignon, Lattice vibrations of manganese oxides: Part I. Periodic structures, *Spectrochim. Acta, Part A*, **2004**, *60*, 689.
- [242] D. C. Golden, C. C. Chen and J. B. Dixon, Transformation of Birnessite to Buserite, Todorokite, and Manganite Under Mild Hydrothermal Treatment, *Clays Clay Miner.*, **1987**, *35*, 271.
- [243] T. Reinert, *Darstellung und Charakterisierung "biomimetischer Steine" zur Nachahmung des OEC im Photosystem II*, Internship report (MNF-chem 1004 A), Christian-Albrechts-Universität zu Kiel, **2012**.
- [244] G. S. R. Krishnamurti and P. M. Huang, The Catalytic Role of Birnessite in the

- Transformation of Iron, *Can. J. Soil Sci.*, **1987**, *67*, 533.
- [245] F. J. Ewing, The Crystal Structure of Lepidocrocite, *J. Chem. Phys.*, **1935**, *3*, 420.
- [246] D. G. Lewis and F. V. C., Infrared Absorption of Surface Hydroxyl Groups and Lattice Vibrations in Lepidocrocite ( $\gamma$ -FeOOH) and Boehmite ( $\gamma$ -AlOOH), *Clay Miner.*, **1986**, *21*, 93.
- [247] H. Dachs, Neutronen- und Röntgenuntersuchungen am Manganit, MnOOH, *Z. Kristallogr., Kristallgeom., Kristallphys., Kristallchem.*, **1963**, *118*, 303.
- [248] J. E. Post and D. R. Veblen, Crystal-Structure Determinations of Synthetic Sodium, Magnesium, and Potassium Birnessite Using TEM and the Rietveld Method, *Am. Mineral.*, **1990**, *75*, 477.
- [249] D. W. Oscarson, P. M. Huang and L. W. K., Role of Manganese in the Oxidation of Arsenite by Freshwater Lake Sediments, *Clays Clay Miner.*, **1981**, *29*, 219.
- [250] P. W. Atkins, *Physikalische Chemie*, Wiley-VCH, Weinheim, **2001**.
- [251] H. M. Rietveld, A profile refinement method for nuclear and magnetic structures, *J. Appl. Crystallogr.*, **1969**, *2*, 65.
- [252] R. A. Young, *The Rietveld Method*, Oxford University Press, Oxford, **1993**.
- [253] M. Villalobos, B. Toner, J. Bargar and G. Sposito, Characterization of the manganese oxide produced by *Pseudomonas putida* strain MnB1, *Geochim. Cosmochim. Acta*, **2003**, *67*, 2649.
- [254] S. M. Webb, B. M. Tebo and J. R. Bargar, Structural characterization of biogenic Mn oxides produced in seawater by the marine *bacillus sp.* strain SG-1, *Am. Mineral.*, **2005**, *90*, 1342.
- [255] T. G. Spiro, J. R. Bargar, G. Sposito and B. M. Tebo, Bacteriogenic manganese oxides, *Acc. Chem. Res.*, **2010**, *43*, 2.
- [256] B. Lanson, V. A. Drits, E. Silvester and A. Manceau, Structure of H-exchanged hexagonal birnessite and its mechanism of formation from Na-rich monoclinic busserite at low pH, *Am. Mineral.*, **2000**, *85*, 826.
- [257] V. A. Drits, E. Silvester, A. I. Gorshkov and A. Manceau, Structure of synthetic monoclinic Na-rich birnessite and hexagonal birnessite: I. Results from X-ray diffraction and selected-area electron diffraction, *Am. Mineral.*, **1997**, *82*, 946.
- [258] B. Lanson, V. A. Drits, Q. Feng and A. Manceau, Structure of synthetic Na-birnessite: Evidence for a triclinic one-layer unit cell, *Am. Mineral.*, **2002**, *87*, 1662.
- [259] A. C. Gaillot, D. Flot, V. A. Drits, A. Manceau, M. Burghammer and B. Lanson, Structure of synthetic K-rich birnessite obtained by high-temperature decomposition of KMnO<sub>4</sub>. I. Two-layer polytype from 800 degrees C experiment, *Chem. Mater.*, **2003**, *15*, 4666.
- [260] A. C. Gaillot, V. A. Drits, A. Plancon and B. Lanson, Structure of synthetic K-rich birnessites obtained by high-temperature decomposition of KMnO<sub>4</sub>. 2. Phase and structural heterogeneities, *Chem. Mater.*, **2004**, *16*, 1890.
- [261] A. C. Gaillot, B. Lanson and V. A. Drits, Structure of birnessite obtained from decomposition of permanganate under soft hydrothermal conditions. 1. Chemical and structural evolution as a function of temperature, *Chem. Mater.*, **2005**, *17*, 2959.
- [262] O. P. Bricker, Some stability relations in the system Mn-O<sub>2</sub>-H<sub>2</sub>O at 25 ° and one atmosphere total pressure, *Am. Mineral.*, **1965**, *50*, 1296.
- [263] V. Borodin, V. Lyutin, V. Ilyukhin and N. Belov, Isomorphic series of calcite-otavite, *Dokl. Akad. Nauk SSSR*, **1979**, *245*, 1099.

- [264] H. F. McMurdie, M. C. Morris, E. H. Evans, B. Paretzkin, W. Wong-Ng, L. Ettliger and C. R. Hubbard, Standard X-Ray Diffraction Powder Patterns from the JCPDS Research Associateship, *Powder Diffr.*, **1986**, *1*, 64.
- [265] M. I. Baneyeva and S. V. Popova, A study of zink hydroxide at high pressures and temperatures, *Geochem. Int.*, **1969**, *6*, 807.
- [266] B. L. Dubey and N. Tiwari, Solid-State Reaction between Zinc Hydroxide and 8-Quinolinol, *Bull. Chem. Soc. Jpn.*, **1992**, *65*, 495.
- [267] J. D. Hanawalt, H. W. Rinn and L. K. Frevel, Chemical Analysis by X-Ray Diffraction, *Ind. Eng. Chem., Anal. Ed.*, **1938**, *10*, 457.
- [268] F. Jellinek, On barium manganate and some related compounds, *J. Inorg. Nucl. Chem.*, **1960**, *13*, 329.
- [269] H. I. Schlesinger and H. B. Siems, The Solubility Product of Barium Manganate and the Equilibrium Between Manganate and Permanganate Ions, *J. Am. Chem. Soc.*, **1924**, *46*, 1965.
- [270] V. A. Drits, B. Lanson and A. C. Gaillot, Birnessite polytype systematics and identification by powder X-ray diffraction, *Am. Mineral.*, **2007**, *92*, 771.
- [271] R. Sass, R. Vidale and J. Donohue, Interatomic Distances and Thermal Anisotropy in Sodium Nitrate and Calcite, *Acta Cryst.*, **1957**, *10*, 567.
- [272] G. W. Brindley (Editor), *Crystal structures of clay minerals and their x-ray identification*, Mineralog. Soc., London, **1951**.
- [273] B. Teo, *EXAFS: Basic principles and data analysis*, Springer Verlag, Berlin, Germany, **1986**, pc.
- [274] M. Newville, *Fundamentals of XAFS*, Consortium for Advanced Radiation Sources, Chicago, **2004**.
- [275] L. S. Kau, D. J. Spira-Solomon, J. E. Penner-Hahn, K. O. Hodgson and E. I. Solomon, X-ray absorption edge determination of the oxidation state and coordination number of copper. Application to the type 3 site in *Rhus vernicifera* laccase and its reaction with oxygen, *J. Am. Chem. Soc.*, **1987**, *109*, 6433.
- [276] R. W. G. Wyckoff, *Crystal Structures 1*, Interscience Publishers, New York, **1963**.
- [277] R. E. Pacalo and E. K. Graham, Pressure and temperature dependence of the elastic properties of synthetic MnO, *Phys. Chem. Miner.*, **1991**, *18*, 69.
- [278] S. Geller, Structures of  $\alpha$ -Mn<sub>2</sub>O<sub>3</sub>, (Mn<sub>0.983</sub>Fe<sub>0.017</sub>)<sub>2</sub>O<sub>3</sub> and (Mn<sub>0.37</sub>Fe<sub>0.63</sub>)<sub>2</sub>O<sub>3</sub> and relation to magnetic ordering, *Acta Cryst.*, **1971**, *B27*, 821.
- [279] M. Villalobos, B. Lanson, A. Manceau, B. Toner and G. Sposito, Structural model for the biogenic Mn oxide produced by *Pseudomonas putida*, *Am. Mineral.*, **2006**, *91*, 489.
- [280] G. C. Dismukes, R. Brimblecombe, G. A. N. Felton, R. S. Pryadun, J. E. Sheats, L. Spiccia and G. F. Swiegers, Development of bioinspired Mn<sub>4</sub>O<sub>4</sub>-cubane water oxidation catalysts: Lessons from photosynthesis, *Acc. Chem. Res.*, **2009**, *42*, 1935.
- [281] Y. Takahashi, A. Manceau, N. Geoffroy, M. A. Marcus and A. Usui, Chemical and structural control of the partitioning of Co, Ce, and Pb in marine ferromanganese oxides, *Geochim. Cosmochim. Acta*, **2007**, *71*, 984.
- [282] B. Toner, A. Manceau, S. M. Webb and G. Sposito, Zinc sorption to biogenic hexagonal-birnessite particles within a hydrated bacterial biofilm, *Geochim. Cosmochim. Acta*, **2006**, *70*, 27.
- [283] K. Sauer and V. K. Yachandra, A possible evolutionary origin for the Mn<sub>4</sub> cluster

- of the photosynthetic water oxidation complex from natural MnO<sub>2</sub> precipitates in the early ocean, *Proc. Natl. Acad. Sci. U.S.A.*, **2002**, *99*, 8631.
- [284] L. Spiccia and W. H. Casey, Synthesis of experimental models for molecular inorganic geochemistry - A review with examples, *Geochim. Cosmochim. Acta*, **2007**, *71*, 5590.
- [285] F. A. Armstrong, Why did nature choose manganese to make oxygen?, *Philos. Trans. R. Soc. London, Ser. B*, **2008**, *363*, 1263.
- [286] V. K. Yachandra, R. D. Guiles, A. McDermott, R. D. Britt, S. L. Dexheimer, K. Sauer and M. P. Klein, The state of manganese in the photosynthetic apparatus: 4. Structure of the manganese complex in Photosystem II studied using EXAFS spectroscopy. The S<sub>1</sub> state of the O<sub>2</sub>-evolving Photosystem II complex from spinach, *Biochim. Biophys. Acta, Bioenerg.*, **1986**, *850*, 324.
- [287] K. Wieghardt, The Active Sites in Manganese-Containing Metalloproteins and Inorganic Model Complexes, *Angew. Chem. Int. Ed.*, **1989**, *28*, 1153.
- [288] H. Dau, P. Liebisch and M. Haumann, The structure of the manganese complex of Photosystem II in its dark-stable S<sub>1</sub>-state—EXAFS results in relation to recent crystallographic data, *Phys. Chem. Chem. Phys.*, **2004**, *6*, 4781.
- [289] M. J. Baldwin and V. L. Pecoraro, Energetics of Proton-Coupled Electron Transfer in High-Valent Mn<sub>2</sub>(μ-O)<sub>2</sub> Systems: Models for Water Oxidation by the Oxygen-Evolving Complex of Photosystem II, *J. Am. Chem. Soc.*, **1996**, *118*, 11325.
- [290] M. Hara, C. C. Waraksa, J. T. Lean, B. A. Lewis and T. E. Mallouk, Photocatalytic water oxidation in a buffered tris(2,2'-bipyridyl)ruthenium complex-colloidal IrO<sub>2</sub> system, *J. Phys. Chem. A*, **2000**, *104*, 5275.
- [291] M. Hara and T. E. Mallouk, Photocatalytic water oxidation by Nafion-stabilized iridium oxide colloids, *Chem. Commun.*, **2000**, 1903.
- [292] M. M. Najafpour, S. Nayeri and B. Pashaei, Nano-size amorphous calcium-manganese oxide as an efficient and biomimetic water oxidizing catalyst for artificial photosynthesis: back to manganese, *Dalton Trans.*, **2011**, *40*, 9374.
- [293] G. J. Kavarnos, *Fundamentals of Photoinduced Electron Transfer*, Wiley-VCH, Weinheim, **1993**.
- [294] L. C. Clark, R. Wolf, D. Granger and Z. Taylor, Continuous Recording of Blood Oxygen Tensions by Polarography, *J. Appl. Physiol.*, **1953**, *6*, 189.
- [295] M. Pitie, J. Bernadou and B. Meunier, Oxidation at Carbon-1' of DNA Deoxyriboses by the Mn-TMPyP/KHSO<sub>5</sub> System Results from a Cytochrome P-450-type Hydroxylation Reaction, *J. Am. Chem. Soc.*, **1995**, *117*, 2935.
- [296] J. T. Groves, J. Lee and S. S. Marla, Detection and Characterization of an Oxomanganese(V) Porphyrin Complex by Rapid-Mixing Stopped-Flow Spectrophotometry, *J. Am. Chem. Soc.*, **1997**, *119*, 6269.
- [297] M. J. Baldwin, N. A. Law, T. L. Stemmler, J. W. Kampf, J. E. Penner-Hahn and V. L. Pecoraro, Reactivity of [ $\{\text{Mn}^{\text{IV}}(\text{salpn})\}_2(\mu\text{-O},\mu\text{-OCH}_3)\text{]}^+$  and [ $\{\text{Mn}^{\text{IV}}(\text{salpn})\}_2(\mu\text{-O},\mu\text{-OH})\text{]}^+$ : Effects of Proton Lability and Hydrogen Bonding, *Inorg. Chem.*, **1999**, *38*, 4801.
- [298] R. Tagore, Chen, R. H. Crabtree and G. W. Brudvig, Determination of μ-Oxo Exchange Rates in Di-μ-Oxo Dimanganese Complexes by Electrospray Ionization Mass Spectrometry, *J. Am. Chem. Soc.*, **2006**, *128*, 9457.
- [299] C. A. Ohlin, R. Brimblecombe, L. Spiccia and W. H. Casey, Oxygen isotopic exchange in an Mn<sup>III</sup>Mn<sub>3</sub><sup>IV</sup>-oxo cubane, *Dalton Trans.*, **2009**, 5278.



# Appendix

## A.1 Overview of the prepared samples

**Table A.1. Overview of directly synthesized M-birnessites.**

		lab. code	synthesis	composition	oxygen evol.
K <sub>0.31</sub> -birnessite	(1)	MW 23	p. 123	pp. 55, 159	pp. 102, 161
Ca <sub>0.14</sub> -birnessite	(2)	MW 22	p. 123	pp. 55, 159	pp. 102, 117, 162, 201
Ca <sub>0.27</sub> -birnessite	(3)	MW 37	p. 123	pp. 55, 159	pp. 102, 117, 163, 201
Sr <sub>0.18</sub> -birnessite	(4)	MW 35	p. 123	pp. 55, 159	pp. 102, 117, 164, 202
Sr <sub>0.27</sub> -birnessite	(5)	MW 36	p. 123	pp. 55, 159	pp. 102, 165
Mg <sub>0.13</sub> -birnessite	(6)	MW 28	p. 123	pp. 55, 159	pp. 102, 117, 166, 202
Mg <sub>0.28</sub> -birnessite	(7)	MW 29	p. 123	pp. 55, 159	pp. 102, 167
Cd <sub>0.16</sub> -birnessite	(8)	MW 60	p. 123	pp. 55, 159	pp. 102, 168
Cd <sub>0.29</sub> -birnessite	(9)	MW 61	p. 123	pp. 55, 159	pp. 102, 169
Al <sub>0.02</sub> -birnessite	(10)	MW 62	p. 123	pp. 55, 159	—
Al <sub>0.03</sub> -birnessite	(11)	MW 63	p. 123	pp. 55, 159	pp. 102, 170
Zn <sub>0.20</sub> -birnessite <sup>[224]</sup>	(12)	MP 1	p. 123	pp. 55, 159	pp. 102, 171
Pb <sub>0.30</sub> -birnessite <sup>[224]</sup>	(13)	MP 2	p. 123	pp. 55, 159	pp. 102, 172

**Table A.2. Overview of M-birnessites prepared by ion exchange.<sup>(243)</sup>**

		lab. code	synthesis	composition	oxygen evol.
Ca <sub>ex</sub> -birnessite	(14)	TR 1	p. 125	pp. 65, 159	pp. 105, 173
Mn <sub>ex</sub> -birnessite	(15)	TR 2	p. 125	pp. 65, 159	pp. 105, 174
Zn <sub>ex</sub> -birnessite	(16)	TR 3	p. 125	pp. 65, 159	pp. 105, 175
Fe <sub>ex</sub> <sup>2+</sup> -oxide	(17)	TR 4	p. 125	pp. 65, 159	pp. 105, 176
Fe <sub>ex</sub> <sup>3+</sup> -birnessite	(18)	TR 5	p. 125	pp. 65, 159	pp. 105, 177

**Table A.3. Overview of K/Ca-birnessites with increasing Ca<sup>2+</sup> concentration.**

		lab. code	synthesis	composition	oxygen evol.
K <sub>0.28</sub> -birnessite	(19)	MW 49	p. 126	pp. 70, 160	pp. 107, 178
Ca <sub>0.04</sub> -birnessite	(20)	MW 59	p. 126	pp. 70, 160	pp. 107, 179
Ca <sub>0.08</sub> -birnessite	(21)	MW 50	p. 126	pp. 70, 160	pp. 107, 180
Ca <sub>0.10</sub> -birnessite	(22)	MW 51	p. 126	pp. 70, 160	pp. 107, 181
Ca <sub>0.15</sub> -birnessite	(23)	MW 52	p. 126	pp. 70, 160	pp. 107, 182
Ca <sub>0.17</sub> -birnessite	(24)	MW 53	p. 126	pp. 70, 160	pp. 107, 183
Ca <sub>0.21</sub> -birnessite	(25)	MW 54	p. 126	pp. 70, 160	pp. 111, 117, 184, 203
Ca <sub>0.28</sub> -birnessite	(26)	MW 55	p. 126	pp. 70, 160	pp. 107, 186
Ca <sub>0.36</sub> -birnessite	(27)	MW 56	p. 126	pp. 70, 160	pp. 107, 187
Ca <sub>0.54</sub> -birnessite	(28)	MW 57	p. 126	pp. 70, 160	pp. 107, 188
Ca <sub>0.67</sub> -birnessite	(29)	MW 58	p. 126	pp. 70, 160	pp. 107, 189

**Table A.4. Overview of Ca-birnessites with increasing ripening time.**

		lab. code	synthesis	composition	oxygen evol.
Ca <sub>0h</sub> -birnessite	(30)	MW 38	p. 127	pp. 76, 160	pp. 111, 190
Ca <sub>1h</sub> -birnessite	(31)	MW 39	p. 127	pp. 76, 160	pp. 111, 191
Ca <sub>2h</sub> -birnessite	(32)	MW 40	p. 127	pp. 76, 160	pp. 111, 192
Ca <sub>4h</sub> -birnessite	(33)	MW 41	p. 127	pp. 76, 160	pp. 111, 193
Ca <sub>8h</sub> -birnessite	(34)	MW 42	p. 127	pp. 76, 160	pp. 111, 194
Ca <sub>12h</sub> -birnessite	(35)	MW 43	p. 127	pp. 76, 160	pp. 111, 195
Ca <sub>24h</sub> -birnessite	(36)	MW 44	p. 127	pp. 76, 160	pp. 111, 196
Ca <sub>48h</sub> -birnessite	(37)	MW 45	p. 127	pp. 76, 160	pp. 111, 197
Ca <sub>120h</sub> -birnessite	(38)	MW 46	p. 127	pp. 76, 160	pp. 111, 198
Ca <sub>168h</sub> -birnessite	(39)	MW 47	p. 127	pp. 76, 160	pp. 111, 199
Ca <sub>240h</sub> -birnessite	(40)	MW 48	p. 127	pp. 76, 160	pp. 111, 200

## A.2 Atomic absorption spectroscopy data

**Table A.5. AAS results of directly synthesized M-birnessites.**

		initial sample weight/mg	$\beta_{\text{AAS}}(\text{Mn})/$ $\text{mg} \cdot \text{L}^{-1}$	Mn content/ $\mu\text{mol} \cdot \text{mg}(\text{sample})^{-1}$
K <sub>0.31</sub> -birnessite	(1)	9.6	4.335	10.27
Ca <sub>0.14</sub> -birnessite	(2)	9.8	3.168	7.35
Ca <sub>0.27</sub> -birnessite	(3)	10.4	1.829	8.00
Sr <sub>0.18</sub> -birnessite	(4)	9.7	2.005	9.45
Sr <sub>0.27</sub> -birnessite	(5)	9.7	2.269	10.70
Mg <sub>0.13</sub> -birnessite	(6)	14.4	4.860	7.68
Mg <sub>0.28</sub> -birnessite	(7)	10.0	5.030	11.44
Cd <sub>0.16</sub> -birnessite	(8)	10.6	2.221	9.53
Cd <sub>0.29</sub> -birnessite	(9)	15.3	1.986	5.91
Al <sub>0.02</sub> -birnessite	(10)	20.3	2.245	5.03
Al <sub>0.03</sub> -birnessite	(11)	11.4	2.445	9.76
Zn <sub>0.20</sub> -birnessite	(12)	5.4	3.182	8.06
Pb <sub>0.30</sub> -birnessite	(13)	6.4	3.415	6.05

**Table A.6. AAS results of M-birnessites prepared by ion exchange.**

		initial sample weight/mg	$\beta_{\text{AAS}}(\text{Mn})/$ $\text{mg} \cdot \text{L}^{-1}$	Mn content/ $\mu\text{mol} \cdot \text{mg}(\text{sample})^{-1}$
Ca <sub>ex</sub> -birnessite	(14)	9.5	1.77	8.51
Mn <sub>ex</sub> -birnessite	(15)	11.6	4.47	17.49
Zn <sub>ex</sub> -birnessite	(16)	16.0	2.30	6.54
Fe <sub>ex</sub> <sup>2+</sup> -oxide	(17)	9.3	0.01	0.05
Fe <sub>ex</sub> <sup>3+</sup> -birnessite	(18)	11.8	1.57	6.04

**Table A.7. AAS results of K/Ca-birnessites with increasing Ca<sup>2+</sup> concentration.**

		initial sample weight/mg	$\beta_{\text{AAS}}(\text{Mn})/$ $\text{mg} \cdot \text{L}^{-1}$	Mn content/ $\mu\text{mol} \cdot \text{mg}(\text{sample})^{-1}$
K <sub>0.28</sub> -birnessite	(19)	12.6	3.209	11.59
Ca <sub>0.04</sub> -birnessite	(20)	16.3	3.302	9.22
Ca <sub>0.08</sub> -birnessite	(21)	9.6	1.895	8.98
Ca <sub>0.10</sub> -birnessite	(22)	13.3	2.268	7.76
Ca <sub>0.15</sub> -birnessite	(23)	10.6	1.815	7.79
Ca <sub>0.17</sub> -birnessite	(24)	11.1	2.089	8.56
Ca <sub>0.21</sub> -birnessite	(25)	10.6	1.992	8.55
Ca <sub>0.28</sub> -birnessite	(26)	9.7	1.783	8.36
Ca <sub>0.36</sub> -birnessite	(27)	10.2	1.834	8.18
Ca <sub>0.54</sub> -birnessite	(28)	10.3	1.609	7.11
Ca <sub>0.67</sub> -birnessite	(29)	9.7	1.429	6.70

**Table A.8. AAS results of Ca-birnessites with increasing ripening time.**

		initial sample weight/mg	$\beta_{\text{AAS}}(\text{Mn})/$ $\text{mg} \cdot \text{L}^{-1}$	Mn content/ $\mu\text{mol} \cdot \text{mg}(\text{sample})^{-1}$
Ca <sub>0h</sub> -birnessite	(30)	10.0	2.141	9.71
Ca <sub>1h</sub> -birnessite	(31)	10.0	2.136	9.74
Ca <sub>2h</sub> -birnessite	(32)	9.7	1.870	8.77
Ca <sub>4h</sub> -birnessite	(33)	11.4	2.128	8.77
Ca <sub>8h</sub> -birnessite	(34)	10.5	1.750	7.59
Ca <sub>12h</sub> -birnessite	(35)	10.9	1.085	4.53
Ca <sub>24h</sub> -birnessite	(36)	10.1	1.994	8.95
Ca <sub>48h</sub> -birnessite	(37)	10.9	2.104	8.81
Ca <sub>120h</sub> -birnessite	(38)	11.0	2.307	9.55
Ca <sub>168h</sub> -birnessite	(39)	12.9	2.188	7.70
Ca <sub>240h</sub> -birnessite	(40)	9.9	2.556	11.76

## A.3 Headspace gas chromatography data

Table A.9. Results of headspace gas chromatography of K<sub>0.31</sub>-birnessite (1).

	t/min	area (O <sub>2</sub> )/ $\mu\text{V} \cdot \text{s}$	area (N <sub>2</sub> )/ $\mu\text{V} \cdot \text{s}$	O <sub>2</sub> /%	N <sub>2</sub> /%
Vial 1 <sup>a</sup> 5.2 mg of <b>1</b> (53.40 $\mu\text{mol Mn}$ )	10	16278.5	59503.7	21.5	78.5
	20	13814.7	48752.5	22.1	77.9
	30	12302.5	42175.3	22.6	77.4
	40	10880.0	36280.5	23.1	76.9
	50	8381.0	27245.1	23.5	76.5
	60	7879.8	24908.2	24.0	76.0
Vial 2 <sup>a</sup> 4.9 mg of <b>1</b> (50.32 $\mu\text{mol Mn}$ )	10	16305.2	59756.9	21.4	78.6
	20	14432.0	51210.1	22.0	78.0
	30	12286.9	42372.4	22.5	77.5
	40	10838.1	36404.6	22.9	77.1
	50	9608.1	31450.3	23.4	76.6
	60	8499.2	27103.3	23.9	76.1
Vial 3 <sup>a</sup> 5.6 mg of <b>1</b> (57.51 $\mu\text{mol Mn}$ )	10	15295.0	55995.1	21.5	78.5
	20	14103.0	49574.9	22.1	77.9
	30	12599.1	42475.7	22.9	77.1
	40	11051.9	35945.0	23.5	76.5
	50	9718.3	30593.6	24.1	75.9
	60	8628.8	26311.5	24.7	75.3
Vial 4 <sup>b</sup> 5.1 mg of <b>1</b> (52.38 $\mu\text{mol Mn}$ )	60	12039.8	39050.7	23.6	76.4
Vial 5 <sup>b</sup> 5.1 mg of <b>1</b> (52.38 $\mu\text{mol Mn}$ )	60	15273.1	50013.0	23.4	76.6
Vial 6 <sup>b</sup> 5.2 mg of <b>1</b> (53.40 $\mu\text{mol Mn}$ )	60	15406.3	49810.8	23.6	76.4
Vial 7 <sup>c</sup> 6.6 mg of <b>1</b> (67.78 $\mu\text{mol Mn}$ )	10	12805.2	48174.9	21.0	79.0
	20	7164.5	27077.2	20.9	79.1
	30	5662.5	21459.5	20.9	79.1
	40	6318.8	23895.7	20.9	79.1
	50	5335.7	20182.2	20.9	79.1
	60	4472.5	16926.5	20.9	79.1

<sup>a</sup> The oxide sample was suspended in 5 mL of a 0.25 M Ce<sup>IV</sup> solution in a septum vial. Over a period of 60 min. a gas sample of the headspace of the septum vial was injected every 10 min. to the GC.

<sup>b</sup> The oxide sample was suspended in 5 mL of a 0.25 M Ce<sup>IV</sup> solution in a septum vial. After 60 min. a single gas sample of the headspace of the septum vial was injected to the GC.

<sup>c</sup> The oxide sample was suspended in 5 mL HNO<sub>3</sub> (pH  $\approx$  1.7). Over a period of 60 min. a gas sample of the headspace of the septum vial was injected every 10 min. to the GC.

**Table A.10. Results of headspace gas chromatography of Ca<sub>0.14</sub>-birnessite (2).**

	t/min	area (O <sub>2</sub> )/ $\mu\text{V} \cdot \text{s}$	area (N <sub>2</sub> )/ $\mu\text{V} \cdot \text{s}$	O <sub>2</sub> /%	N <sub>2</sub> /%
Vial 1 <sup>a</sup> 5.3 mg of 2 (38.96 $\mu\text{mol}$ Mn)	10	16893.1	60191.4	21.9	78.1
	20	15423.9	51307.9	23.1	76.9
	30	14004.2	43962.3	24.2	75.8
	40	12674.1	37764.0	25.1	74.9
	50	11060.7	31398.5	26.1	73.9
	60	10062.5	27262.8	27.0	73.0
Vial 2 <sup>a</sup> 5.1 mg of 2 (37.49 $\mu\text{mol}$ Mn)	10	16859.2	60371.7	21.8	78.2
	20	15240.4	51100.4	23.0	77.0
	30	13728.0	43481.1	24.0	76.0
	40	12483.1	37567.4	24.9	75.1
	50	10235.8	29408.6	25.8	74.2
	60	8462.8	23254.5	26.7	73.3
Vial 3 <sup>a</sup> 4.9 mg of 2 (36.02 $\mu\text{mol}$ Mn)	10	16022.8	57629.8	21.8	78.2
	20	14518.6	49099.4	22.8	77.2
	30	13034.1	41655.4	23.8	76.2
	40	11787.9	35774.9	24.8	75.2
	50	10671.9	30856.5	25.7	74.3
	60	9599.7	26503.6	26.6	73.4
Vial 4 <sup>b</sup> 4.9 mg of 2 (36.02 $\mu\text{mol}$ Mn)	60	15731.4	46734.3	25.2	74.8
Vial 5 <sup>b</sup> 5.8 mg of 2 (42.63 $\mu\text{mol}$ Mn)	60	15878.9	46360.9	25.5	74.5
Vial 6 <sup>b</sup> 5.0 mg of 2 (36.75 $\mu\text{mol}$ Mn)	60	16313.6	47965.4	25.4	74.6
Vial 7 <sup>c</sup> 5.1 mg of 2 (37.49 $\mu\text{mol}$ Mn)	10	8668.5	32721.2	20.9	79.1
	20	9516.7	35861.4	21.0	79.0
	30	8166.8	30791.3	21.0	79.0
	40	6858.2	25888.8	20.9	79.1
	50	5762.3	21781.2	20.9	79.1
	60	4848.1	18345.5	20.9	79.1

<sup>a</sup> The oxide sample was suspended in 5 mL of a 0.25 M Ce<sup>IV</sup> solution in a septum vial. Over a period of 60 min. a gas sample of the headspace of the septum vial was injected every 10 min. to the GC.

<sup>b</sup> The oxide sample was suspended in 5 mL of a 0.25 M Ce<sup>IV</sup> solution in a septum vial. After 60 min. a single gas sample of the headspace of the septum vial was injected to the GC.

<sup>c</sup> The oxide sample was suspended in 5 mL HNO<sub>3</sub> (pH  $\approx$  1.7). Over a period of 60 min. a gas sample of the headspace of the septum vial was injected every 10 min. to the GC.

**Table A.11. Results of headspace gas chromatography of Ca<sub>0.27</sub>-birnessite (3).**

	t/min	area (O <sub>2</sub> )/ $\mu\text{V} \cdot \text{s}$	area (N <sub>2</sub> )/ $\mu\text{V} \cdot \text{s}$	O <sub>2</sub> /%	N <sub>2</sub> /%
Vial 1 <sup>a</sup> 5.9 mg of <b>3</b> (39.20 $\mu\text{mol Mn}$ )	10	13358.6	48510.9	21.6	78.4
	20	9198.8	31492.3	22.6	77.4
	30	9605.9	31014.2	23.6	76.4
	40	7083.0	21604.7	24.7	75.3
	50	5456.2	15797.1	25.7	74.3
	60	5927.7	16241.8	26.7	73.3
Vial 2 <sup>a</sup> 5.0 mg of <b>3</b> (40.00 $\mu\text{mol Mn}$ )	10	8966.9	32426.4	21.7	78.3
	20	6693.1	22924.7	22.6	77.4
	30	6817.8	22185.9	23.5	76.5
	40	7112.8	21970.1	24.5	75.5
	50	6169.4	18074.5	25.4	74.6
	60	5408.1	15025.3	26.5	73.5
Vial 3 <sup>a</sup> 5.1 mg of <b>3</b> (40.80 $\mu\text{mol Mn}$ )	10	13282.1	48146.9	21.6	78.4
	20	11645.6	39490.2	22.8	77.2
	30	10270	32722.3	23.9	76.1
	40	6780.6	20509.9	24.8	75.2
	50	7327.7	21120.5	25.8	74.2
	60	6433.2	17639	26.7	73.3
Vial 4 <sup>b</sup> 5.6 mg of <b>3</b> (47.25 $\mu\text{mol Mn}$ )	60	15799.2	48693.3	24.5	75.5
Vial 5 <sup>b</sup> 5.4 mg of <b>3</b> (49.14 $\mu\text{mol Mn}$ )	60	16138.6	48181.6	25.1	74.9
Vial 6 <sup>b</sup> 5.3 mg of <b>3</b> (49.14 $\mu\text{mol Mn}$ )	60	14872.5	44190.5	25.2	74.8
Vial 7 <sup>c</sup> 5.5 mg of <b>3</b> (48.35 $\mu\text{mol Mn}$ )	10	12610.3	47433.5	21.0	79.0
	20	11383.6	42802.2	21.0	79.0
	30	7795.0	29393.0	21.0	79.0
	40	7165.3	27038.0	20.9	79.1
	50	5852.4	22111.2	20.9	79.1
	60	5009.0	18942.7	20.9	79.1

<sup>a</sup> The oxide sample was suspended in 5 mL of a 0.25 M Ce<sup>IV</sup> solution in a septum vial. Over a period of 60 min. a gas sample of the headspace of the septum vial was injected every 10 min. to the GC.

<sup>b</sup> The oxide sample was suspended in 5 mL of a 0.25 M Ce<sup>IV</sup> solution in a septum vial. After 60 min. a single gas sample of the headspace of the septum vial was injected to the GC.

<sup>c</sup> The oxide sample was suspended in 5 mL HNO<sub>3</sub> (pH  $\approx$  1.7). Over a period of 60 min. a gas sample of the headspace of the septum vial was injected every 10 min. to the GC.

**Table A.12. Results of headspace gas chromatography of Sr<sub>0.18</sub>-birnessite (4).**

	t/min	area (O <sub>2</sub> )/ $\mu\text{V} \cdot \text{s}$	area (N <sub>2</sub> )/ $\mu\text{V} \cdot \text{s}$	O <sub>2</sub> /%	N <sub>2</sub> /%
Vial 1 <sup>a</sup> 4.8 mg of 4 (45.36 $\mu\text{mol Mn}$ )	10	10857.6	39357.8	21.6	78.4
	20	11087.1	37709.8	22.7	77.3
	30	8004.3	25667.8	23.8	76.2
	40	8090.3	24594.3	24.8	75.2
	50	7163.6	20606.2	25.8	74.2
	60	6330.7	17230.5	26.9	73.1
Vial 2 <sup>a</sup> 5.2 mg of 4 (49.14 $\mu\text{mol Mn}$ )	10	13353	48086.4	21.7	78.3
	20	11707.9	39544.4	22.8	77.2
	30	10149.5	32440.1	23.8	76.2
	40	6342.2	19257.8	24.8	75.2
	50	7192.5	20752.7	25.7	74.3
	60	6146.2	16783.6	26.8	73.2
Vial 3 <sup>a</sup> 5.1 mg of 4 (48.20 $\mu\text{mol Mn}$ )	10	13400.0	48387.1	21.7	78.3
	20	11685.9	39627.1	22.8	77.2
	30	9835.5	31626.8	23.7	76.3
	40	4961.3	15216.4	24.6	75.4
	50	5272.3	15384.1	25.5	74.5
	60	2957.0	8172.2	26.6	73.4
Vial 4 <sup>b</sup> 5.0 mg of 4 (47.25 $\mu\text{mol Mn}$ )	60	13005.3	39758.6	24.6	75.4
Vial 5 <sup>b</sup> 5.2 mg of 4 (49.14 $\mu\text{mol Mn}$ )	60	15754.5	48363.2	24.5	75.5
Vial 6 <sup>b</sup> 5.2 mg of 4 (49.14 $\mu\text{mol Mn}$ )	60	7546.6	22970.6	24.7	75.3
Vial 7 <sup>c</sup> 5.3 mg of 4 (50.09 $\mu\text{mol Mn}$ )	10	13391.9	50339.5	21.0	79.0
	20	9894.4	37282.6	21.0	79.0
	30	8567.2	32292.8	21.0	79.0
	40	4496.5	17046.6	20.9	79.1
	50	5490.5	20783.0	20.9	79.1
	60	4655.6	17631.4	20.9	79.1

<sup>a</sup> The oxide sample was suspended in 5 mL of a 0.25 M Ce<sup>IV</sup> solution in a septum vial. Over a period of 60 min. a gas sample of the headspace of the septum vial was injected every 10 min. to the GC.

<sup>b</sup> The oxide sample was suspended in 5 mL of a 0.25 M Ce<sup>IV</sup> solution in a septum vial. After 60 min. a single gas sample of the headspace of the septum vial was injected to the GC.

<sup>c</sup> The oxide sample was suspended in 5 mL HNO<sub>3</sub> (pH  $\approx$  1.7). Over a period of 60 min. a gas sample of the headspace of the septum vial was injected every 10 min. to the GC.

**Table A.13. Results of headspace gas chromatography of Sr<sub>0.27</sub>-birnessite (5).**

	t/min	area (O <sub>2</sub> )/ $\mu\text{V} \cdot \text{s}$	area (N <sub>2</sub> )/ $\mu\text{V} \cdot \text{s}$	O <sub>2</sub> /%	N <sub>2</sub> /%
Vial 1 <sup>a</sup> 5.5 mg of 5 (58.85 $\mu\text{mol Mn}$ )	10	12706.8	46447.0	21.5	78.5
	20	11045.9	38398.1	22.3	77.7
	30	9490.6	31464.4	23.2	76.8
	40	8124.2	25726.3	24.0	76.0
	50	7141.1	21570.9	24.9	75.1
	60	6009.3	17322.7	25.8	74.2
Vial 2 <sup>a</sup> 5.6 mg of 5 (59.92 $\mu\text{mol Mn}$ )	10	12957.0	47025.2	21.6	78.4
	20	11234.7	38360.6	22.7	77.3
	30	9607.3	31004.8	23.7	76.3
	40	8523.7	26021.2	24.7	75.3
	50	7392.2	21393.0	25.7	74.3
	60	6554.9	17946.5	26.8	73.2
Vial 3 <sup>a</sup> 5.0 mg of 5 (53.50 $\mu\text{mol Mn}$ )	10	10591.5	38732.9	21.5	78.5
	20	10731.1	37232.2	22.4	77.6
	30	9187.3	30294.5	23.3	76.7
	40	8048.5	25276.6	24.2	75.8
	50	6612.2	19753.0	25.1	74.9
	60	6051.6	17178.1	26.1	73.9
Vial 4 <sup>b</sup> 5.2 mg of 5 (55.64 $\mu\text{mol Mn}$ )	60	12822.9	39819.4	24.4	75.6
Vial 5 <sup>b</sup> 5.4 mg of 5 (57.78 $\mu\text{mol Mn}$ )	60	15502.8	48125.4	24.4	75.6
Vial 6 <sup>b</sup> 5.0 mg of 5 (53.50 $\mu\text{mol Mn}$ )	60	11030.0	34531.6	24.2	75.8
Vial 7 <sup>c</sup> 6.0 mg of 5 (64.2 $\mu\text{mol Mn}$ )	10	8585.1	32437	20.9	79.1
	20	10003.5	37695.4	21.0	79.0
	30	7913.8	29834.3	21.0	79.0
	40	7165.5	27030.1	21.0	79.0
	50	6036.4	22793.7	20.9	79.1
	60	4999.1	18901.3	20.9	79.1

<sup>a</sup> The oxide sample was suspended in 5 mL of a 0.25 M Ce<sup>IV</sup> solution in a septum vial. Over a period of 60 min. a gas sample of the headspace of the septum vial was injected every 10 min. to the GC.

<sup>b</sup> The oxide sample was suspended in 5 mL of a 0.25 M Ce<sup>IV</sup> solution in a septum vial. After 60 min. a single gas sample of the headspace of the septum vial was injected to the GC.

<sup>c</sup> The oxide sample was suspended in 5 mL HNO<sub>3</sub> (pH  $\approx$  1.7). Over a period of 60 min. a gas sample of the headspace of the septum vial was injected every 10 min. to the GC.

**Table A.14. Results of headspace gas chromatography of Mg<sub>0.13</sub>-birnessite (6).**

	t/min	area (O <sub>2</sub> )/ $\mu\text{V} \cdot \text{s}$	area (N <sub>2</sub> )/ $\mu\text{V} \cdot \text{s}$	O <sub>2</sub> /%	N <sub>2</sub> /%
Vial 1 <sup>a</sup> 4.9 mg of <b>6</b> (37.63 $\mu\text{mol Mn}$ )	10	17042.0	62913.4	21.3	78.7
	20	15263.3	55210.4	21.7	78.3
	30	13285.3	47102.4	22.0	78.0
	40	11826.6	41191.2	22.3	77.7
	50	10329.4	35297.6	22.6	77.4
	60	9072.1	30466.3	22.9	77.1
Vial 2 <sup>a</sup> 7.4 mg of <b>6</b> (56.83 $\mu\text{mol Mn}$ )	10	17131.7	62968.0	21.4	78.6
	20	15381.3	55004.0	21.9	78.1
	30	13728.8	47866.9	22.3	77.7
	40	12264.6	41792.1	22.7	77.3
	50	10909.2	36433.4	23.0	77.0
	60	9436.0	30859.8	23.4	76.6
Vial 3 <sup>a</sup> 5.7 mg of <b>6</b> (43.78 $\mu\text{mol Mn}$ )	10	17127.9	63189.3	21.3	78.7
	20	14982.0	54078.0	21.7	78.3
	30	13320.3	47133.0	22.0	78.0
	40	11904.2	41410.2	22.3	77.7
	50	10275.5	35121.3	22.6	77.4
	60	9133.8	30635.8	23.0	77.0
Vial 4 <sup>b</sup> 5.7 mg of <b>6</b> (43.78 $\mu\text{mol Mn}$ )	60	13858.5	47886.7	22.4	77.6
Vial 5 <sup>b</sup> 5.2 mg of <b>6</b> (39.94 $\mu\text{mol Mn}$ )	60	10720.5	38125.2	21.9	78.1
Vial 6 <sup>b</sup> 6.3 mg of <b>6</b> (48.38 $\mu\text{mol Mn}$ )	60	14005.7	49405.5	22.1	77.9
Vial 7 <sup>c</sup> 4.8 mg of <b>6</b> (36.86 $\mu\text{mol Mn}$ )	10	14041.0	52764.7	21.0	79.0
	20	11789.7	44330.6	21.0	79.0
	30	9872.5	37180.8	21.0	79.0
	40	8278.1	31230.2	21.0	79.0
	50	6972.0	26308.4	20.9	79.1
	60	5827.4	22028.6	20.9	79.1

<sup>a</sup> The oxide sample was suspended in 5 mL of a 0.25 M Ce<sup>IV</sup> solution in a septum vial. Over a period of 60 min. a gas sample of the headspace of the septum vial was injected every 10 min. to the GC.

<sup>b</sup> The oxide sample was suspended in 5 mL of a 0.25 M Ce<sup>IV</sup> solution in a septum vial. After 60 min. a single gas sample of the headspace of the septum vial was injected to the GC.

<sup>c</sup> The oxide sample was suspended in 5 mL HNO<sub>3</sub> (pH  $\approx$  1.7). Over a period of 60 min. a gas sample of the headspace of the septum vial was injected every 10 min. to the GC.

**Table A.15. Results of headspace gas chromatography of Mg<sub>0.28</sub>-birnessite (7).**

	t/min	area (O <sub>2</sub> )/ $\mu\text{V} \cdot \text{s}$	area (N <sub>2</sub> )/ $\mu\text{V} \cdot \text{s}$	O <sub>2</sub> /%	N <sub>2</sub> /%
Vial 1 <sup>a</sup> 5.0 mg of 7 (57.20 $\mu\text{mol Mn}$ )	10	15977.0	58994.8	21.3	78.7
	20	14422.2	52169.2	21.7	78.3
	30	12731.8	45228.8	22.0	78.0
	40	11201.6	39141.0	22.3	77.7
	50	9923.5	34163.1	22.5	77.5
	60	8804.6	29859.5	22.8	77.2
Vial 2 <sup>a</sup> 5.2 mg of 7 (59.49 $\mu\text{mol Mn}$ )	10	17041.9	62697.0	21.4	78.6
	20	15213.4	54732.1	21.8	78.2
	30	13617.1	48091.9	22.1	77.9
	40	11747.3	40807.8	22.4	77.6
	50	10375.8	35477.8	22.6	77.4
	60	9006.3	30290.6	22.9	77.1
Vial 3 <sup>a</sup> 4.8 mg of 7 (54.91 $\mu\text{mol Mn}$ )	10	11754.2	43528.1	21.3	78.7
	20	10847.4	39337.1	21.6	78.4
	30	9215.7	32749.0	22.0	78.0
	40	7794.6	27171.9	22.3	77.7
	50	6619.2	22630.5	22.6	77.4
	60	5559.9	18627.9	23.0	77.0
Vial 4 <sup>b</sup> 5.2 mg of 7 (59.49 $\mu\text{mol Mn}$ )	60	14247.1	49245.7	22.4	77.6
Vial 5 <sup>b</sup> 5.5 mg of 7 (62.92 $\mu\text{mol Mn}$ )	60	14259.4	48887.2	22.6	77.4
Vial 6 <sup>b</sup> 5.5 mg of 7 (62.92 $\mu\text{mol Mn}$ )	60	14066.2	9100.9	22.3	77.7
Vial 7 <sup>c</sup> 5.0 mg of 7 (57.20 $\mu\text{mol Mn}$ )	10	14194.2	53311.6	21.0	79.0
	20	9696.5	36551.0	21.0	79.0
	30	9009.3	33981.9	21.0	79.0
	40	7782.9	29348.9	21.0	79.0
	50	6531.4	24667.9	20.9	79.1
	60	5089.5	19268.4	20.9	79.1

<sup>a</sup> The oxide sample was suspended in 5 mL of a 0.25 M Ce<sup>IV</sup> solution in a septum vial. Over a period of 60 min. a gas sample of the headspace of the septum vial was injected every 10 min. to the GC.

<sup>b</sup> The oxide sample was suspended in 5 mL of a 0.25 M Ce<sup>IV</sup> solution in a septum vial. After 60 min. a single gas sample of the headspace of the septum vial was injected to the GC.

<sup>c</sup> The oxide sample was suspended in 5 mL HNO<sub>3</sub> (pH  $\approx$  1.7). Over a period of 60 min. a gas sample of the headspace of the septum vial was injected every 10 min. to the GC.

**Table A.16. Results of headspace gas chromatography of Cd<sub>0.16</sub>-birnessite (8).**

	t/min	area (O <sub>2</sub> )/ $\mu\text{V} \cdot \text{s}$	area (N <sub>2</sub> )/ $\mu\text{V} \cdot \text{s}$	O <sub>2</sub> /%	N <sub>2</sub> /%
Vial 1 <sup>a</sup> 6.0 mg of 8 (57.18 $\mu\text{mol Mn}$ )	10	10634.8	39528.4	21.2	78.8
	20	8723.7	31229.0	21.8	78.2
	30	6321.3	21861.0	22.4	77.6
	40	183.8	622.3	22.8	77.2
	50	3412.7	10997.2	23.7	76.3
	60	3858.9	11790.3	24.7	75.3
Vial 2 <sup>a</sup> 5.3 mg of 8 (50.51 $\mu\text{mol Mn}$ )	10	9641.6	35613.3	21.3	78.7
	20	10417.5	36979.2	22.0	78.0
	30	6442.2	22130.5	22.5	77.5
	40	7092.4	23467.5	23.2	76.8
	50	5977.1	19044.3	23.9	76.1
	60	4867.1	14927.9	24.6	75.4
Vial 3 <sup>a</sup> 4.8 mg of 8 (45.74 $\mu\text{mol Mn}$ )	10	13621.3	49947.2	21.4	78.6
	20	4928.4	17591.9	21.9	78.1
	30	7038.1	24199.1	22.5	77.5
	40	6909.4	22896.1	23.2	76.8
	50	5724.6	18274.6	23.9	76.1
	60	4877.3	14961.8	24.6	75.4
Vial 4 <sup>b</sup> 5.9 mg of 8 (56.23 $\mu\text{mol Mn}$ )	60	9303.4	30766.7	23.2	76.8
Vial 5 <sup>b</sup> 5.3 mg of 8 (50.51 $\mu\text{mol Mn}$ )	60	11377.2	37891.6	23.1	76.9
Vial 6 <sup>b</sup> 4.8 mg of 8 (45.74 $\mu\text{mol Mn}$ )	60	11044.5	36673.5	22.3	76.9
Vial 7 <sup>c</sup> 5.4 mg of 8 (51.46 $\mu\text{mol Mn}$ )	10	9903.7	37224.9	21.0	79.0
	20	8399.3	31589.3	21.0	79.0
	30	7827.0	29430.7	21.0	79.0
	40	4244.7	16031.5	20.9	79.1
	50	2920.9	11058.1	20.9	79.1
	60	3701.4	13986.8	20.9	79.1

<sup>a</sup> The oxide sample was suspended in 5 mL of a 0.25 M Ce<sup>IV</sup> solution in a septum vial. Over a period of 60 min. a gas sample of the headspace of the septum vial was injected every 10 min. to the GC.

<sup>b</sup> The oxide sample was suspended in 5 mL of a 0.25 M Ce<sup>IV</sup> solution in a septum vial. After 60 min. a single gas sample of the headspace of the septum vial was injected to the GC.

<sup>c</sup> The oxide sample was suspended in 5 mL HNO<sub>3</sub> (pH  $\approx$  1.7). Over a period of 60 min. a gas sample of the headspace of the septum vial was injected every 10 min. to the GC.

**Table A.17. Results of headspace gas chromatography of Cd<sub>0.29</sub>-birnessite (9).**

	t/min	area (O <sub>2</sub> )/ $\mu\text{V} \cdot \text{s}$	area (N <sub>2</sub> )/ $\mu\text{V} \cdot \text{s}$	O <sub>2</sub> /%	N <sub>2</sub> /%
Vial 1 <sup>a</sup> 6.6 mg of <b>9</b> (30.01 $\mu\text{mol Mn}$ )	10	12525.6	46685.0	21.2	78.8
	20	7175.8	26349.2	21.4	78.6
	30	7069.3	25408.8	21.8	78.2
	40	6848.2	24060.8	22.2	77.8
	50	5782.8	19875.0	22.5	77.5
	60	4743.6	15935.0	22.9	77.1
Vial 2 <sup>a</sup> 4.8 mg of <b>9</b> (28.37 $\mu\text{mol Mn}$ )	10	13686.8	50966.1	21.2	78.8
	20	8897.6	32687.4	21.4	78.6
	30	7834.4	28300.2	21.7	78.3
	40	7000.1	24829.2	22.0	78.0
	50	5853.6	20378.8	22.3	77.7
	60	4048.2	13842.2	22.6	77.4
Vial 3 <sup>a</sup> 5.2 mg of <b>9</b> (30.73 $\mu\text{mol Mn}$ )	10	13776.7	51298.2	21.2	78.8
	20	11455.8	41887.3	21.5	78.5
	30	9401.9	33833.1	21.7	78.3
	40	7591.6	26881.7	22.0	78.0
	50	5071.4	17683.1	22.3	77.7
	60	4436.4	15185.6	22.6	77.4
Vial 4 <sup>b</sup> 5.7 mg of <b>9</b> (33.69 $\mu\text{mol Mn}$ )	60	9688.2	34256.4	22.0	78.0
Vial 5 <sup>b</sup> 5.3 mg of <b>9</b> (31.32 $\mu\text{mol Mn}$ )	60	12957.2	45743.8	22.1	77.9
Vial 6 <sup>b</sup> 4.8 mg of <b>9</b> (28.37 $\mu\text{mol Mn}$ )	60	13666.6	48446.3	22.0	78.0
Vial 7 <sup>c</sup> 6.9 mg of <b>9</b> (40.78 $\mu\text{mol Mn}$ )	10	12290.5	46099.0	21.0	79.0
	20	9512.1	35732.9	21.0	79.0
	30	8312.5	31242.6	21.0	79.0
	40	6849.3	25766.1	21.0	79.0
	50	5606.0	21127.6	21.0	79.0
	60	2318.2	8781.6	20.9	79.1

<sup>a</sup> The oxide sample was suspended in 5 mL of a 0.25 M Ce<sup>IV</sup> solution in a septum vial. Over a period of 60 min. a gas sample of the headspace of the septum vial was injected every 10 min. to the GC.

<sup>b</sup> The oxide sample was suspended in 5 mL of a 0.25 M Ce<sup>IV</sup> solution in a septum vial. After 60 min. a single gas sample of the headspace of the septum vial was injected to the GC.

<sup>c</sup> The oxide sample was suspended in 5 mL HNO<sub>3</sub> (pH  $\approx$  1.7). Over a period of 60 min. a gas sample of the headspace of the septum vial was injected every 10 min. to the GC.

**Table A.18. Results of headspace gas chromatography of Al<sub>0.03</sub>-birnessite (11).**

	t/min	area (O <sub>2</sub> )/ $\mu\text{V} \cdot \text{s}$	area (N <sub>2</sub> )/ $\mu\text{V} \cdot \text{s}$	O <sub>2</sub> /%	N <sub>2</sub> /%
Vial 1 <sup>a</sup> 5.3 mg of <b>11</b> (51.73 $\mu\text{mol Mn}$ )	10	7259.7	26754.8	21.3	78.7
	20	10029.2	35397.1	22.1	77.9
	30	8710.3	29481.7	22.8	77.2
	40	7416.7	24126.1	23.5	76.5
	50	4418.3	13832.9	24.2	75.8
	60	4986.0	14962.3	25.0	75.0
Vial 2 <sup>a</sup> 5.7 mg of <b>11</b> (55.63 $\mu\text{mol Mn}$ )	10	11386.7	41893.3	21.4	78.6
	20	10514.3	37304.4	22.0	78.0
	30	7534.4	25778.7	22.6	77.4
	40	7229.8	23821.7	23.3	76.6
	50	6269.8	19818.6	24.0	76.0
	60	2467.8	7515.1	24.7	75.3
Vial 3 <sup>a</sup> 5.2 mg of <b>11</b> (50.75 $\mu\text{mol Mn}$ )	10	8155.1	30127.7	21.3	78.7
	20	9172.4	32707.9	21.9	79.1
	30	8487.4	29220.2	22.5	77.5
	40	7155.4	23795.5	23.1	76.9
	50	6040.7	19380.2	23.8	76.2
	60	3323.9	10291.7	24.4	75.6
Vial 4 <sup>b</sup> 5.7 mg of <b>11</b> (55.63 $\mu\text{mol Mn}$ )	60	5868.8	19984.3	22.7	77.3
Vial 5 <sup>b</sup> 5.1 mg of <b>11</b> (49.78 $\mu\text{mol Mn}$ )	60	14202.7	47928.0	22.9	77.1
Vial 6 <sup>b</sup> 5.1 mg of <b>11</b> (49.78 $\mu\text{mol Mn}$ )	60	14442.6	48235.4	23.0	77.0
Vial 7 <sup>c</sup> 6.2 mg of <b>11</b> (60.51 $\mu\text{mol Mn}$ )	10	13207.6	49489.4	21.1	78.9
	20	10886.6	40813.1	21.1	78.9
	30	9050.9	33982.4	21.0	79.0
	40	6044.6	22777.6	21.0	79.0
	50	3974.7	15023.7	20.9	79.1
	60	2950.9	11170.6	20.9	79.1

<sup>a</sup> The oxide sample was suspended in 5 mL of a 0.25 M Ce<sup>IV</sup> solution in a septum vial. Over a period of 60 min. a gas sample of the headspace of the septum vial was injected every 10 min. to the GC.

<sup>b</sup> The oxide sample was suspended in 5 mL of a 0.25 M Ce<sup>IV</sup> solution in a septum vial. After 60 min. a single gas sample of the headspace of the septum vial was injected to the GC.

<sup>c</sup> The oxide sample was suspended in 5 mL HNO<sub>3</sub> (pH  $\approx$  1.7). Over a period of 60 min. a gas sample of the headspace of the septum vial was injected every 10 min. to the GC.

**Table A.19. Results of headspace gas chromatography of Zn<sub>0.20</sub>-birnessite (12).**

	t/min	area (O <sub>2</sub> )/ $\mu\text{V} \cdot \text{s}$	area (N <sub>2</sub> )/ $\mu\text{V} \cdot \text{s}$	O <sub>2</sub> /%	N <sub>2</sub> /%
Vial 1 <sup>a</sup> 5.6 mg of <b>12</b> (45.14 $\mu\text{mol Mn}$ )	10	11268.0	41482.6	21.4	78.6
	20	9971.6	35640.2	21.9	78.1
	30	5452.4	18950.1	22.3	77.7
	40	6917.8	23252.8	22.9	77.1
	50	5567.9	18028.2	23.6	76.4
	60	5012.7	15631.2	24.3	75.7
Vial 2 <sup>a</sup> 5.3 mg of <b>12</b> (42.72 $\mu\text{mol Mn}$ )	10	12126	44586.1	21.4	78.6
	20	9376.1	33325.4	22.0	78.0
	30	8985.4	30814.3	22.6	77.4
	40	7727.9	25588.1	23.2	76.8
	50	5697.8	18199.6	23.8	76.2
	60	5410.0	16621.9	24.6	75.4
Vial 3 <sup>a</sup> 5.7 mg of <b>12</b> (45.95 $\mu\text{mol Mn}$ )	10	13221.7	48461.8	21.4	78.6
	20	7306.5	25909.8	22.0	78.0
	30	7483.1	25603.3	22.6	77.4
	40	2318.3	7686.7	23.2	76.8
	50	3886.0	12355.1	23.9	76.1
	60	3214.9	9754.9	24.8	75.2
Vial 4 <sup>b</sup> 6.0 mg of <b>12</b> (48.37 $\mu\text{mol Mn}$ )	60	14521.2	47853.3	23.3	76.7
Vial 5 <sup>b</sup> 5.0 mg of <b>12</b> (40.30 $\mu\text{mol Mn}$ )	60	14324.5	47825.9	23.0	77.0
Vial 6 <sup>b</sup> 5.3 mg of <b>12</b> (42.72 $\mu\text{mol Mn}$ )	60	11702.5	38829.3	23.2	76.8
Vial 7 <sup>c</sup> 4.8 mg of <b>12</b> (38.69 $\mu\text{mol Mn}$ )	10	7717.2	29287.3	20.9	79.1
	20	9923.9	37533.6	20.9	79.1
	30	6341.4	24081.6	20.8	79.2
	40	5693.8	21650.5	20.8	79.2
	50	5231.3	19904.8	20.8	79.2
	60	4332.4	16482.9	20.8	79.2

<sup>a</sup> The oxide sample was suspended in 5 mL of a 0.25 M Ce<sup>IV</sup> solution in a septum vial. Over a period of 60 min. a gas sample of the headspace of the septum vial was injected every 10 min. to the GC.

<sup>b</sup> The oxide sample was suspended in 5 mL of a 0.25 M Ce<sup>IV</sup> solution in a septum vial. After 60 min. a single gas sample of the headspace of the septum vial was injected to the GC.

<sup>c</sup> The oxide sample was suspended in 5 mL HNO<sub>3</sub> (pH  $\approx$  1.7). Over a period of 60 min. a gas sample of the headspace of the septum vial was injected every 10 min. to the GC.

**Table A.20. Results of headspace gas chromatography of Pb<sub>0.30</sub>-birnessite (13).**

	t/min	area (O <sub>2</sub> )/ $\mu\text{V} \cdot \text{s}$	area (N <sub>2</sub> )/ $\mu\text{V} \cdot \text{s}$	O <sub>2</sub> /%	N <sub>2</sub> /%
Vial 1 <sup>a</sup> 6.3 mg of <b>13</b> (38.12 $\mu\text{mol Mn}$ )	10	5646.3	21056.7	21.1	78.9
	20	9033	32809.5	21.6	78.4
	30	7593.5	26932.5	22.0	78.0
	40	4694.6	16312.8	22.3	77.7
	50	5317.4	18014.3	22.8	77.2
	60	3696.5	12204.1	23.2	76.8
Vial 2 <sup>a</sup> 5.4 mg of <b>13</b> (32.68 $\mu\text{mol Mn}$ )	10	11250.5	41706	21.2	78.8
	20	9232.3	33504.4	21.6	78.4
	30	4316.8	15433.9	21.9	78.1
	40	6455.2	22554.7	22.3	77.7
	50	5537.2	18881	22.7	77.3
	60	4266.9	14211	23.1	76.9
Vial 3 <sup>a</sup> 4.8 mg of <b>13</b> (29.05 $\mu\text{mol Mn}$ )	10	13150.9	48534	21.3	78.7
	20	11064.5	39825.8	21.7	78.3
	30	8700.3	30626.9	22.1	77.9
	40	5703.9	19610.9	22.5	77.5
	50	5547.3	18592.7	23.0	77.0
	60	5066.9	16527	23.5	76.5
Vial 4 <sup>b</sup> 4.7 mg of <b>13</b> (28.44 $\mu\text{mol Mn}$ )	60	13433.8	47211.9	22.2	77.8
Vial 5 <sup>b</sup> 5.6 mg of <b>13</b> (33.89 $\mu\text{mol Mn}$ )	60	12233.4	42563.9	22.3	77.7
Vial 6 <sup>b</sup> 5.3 mg of <b>13</b> (32.07 $\mu\text{mol Mn}$ )	60	13690.2	47888.7	22.2	77.8
Vial 7 <sup>c</sup> 4.9 mg of <b>13</b> (29.65 $\mu\text{mol Mn}$ )	10	13526.1	50913.3	21.0	79.0
	20	11177.3	42122.4	21.0	79.0
	30	7909.1	29926.7	20.9	79.1
	40	5721.2	21732.4	20.8	79.2
	50	5322.3	20195.2	20.9	79.1
	60	4630.6	17585.0	20.8	79.2

<sup>a</sup> The oxide sample was suspended in 5 mL of a 0.25 M Ce<sup>IV</sup> solution in a septum vial. Over a period of 60 min. a gas sample of the headspace of the septum vial was injected every 10 min. to the GC.

<sup>b</sup> The oxide sample was suspended in 5 mL of a 0.25 M Ce<sup>IV</sup> solution in a septum vial. After 60 min. a single gas sample of the headspace of the septum vial was injected to the GC.

<sup>c</sup> The oxide sample was suspended in 5 mL HNO<sub>3</sub> (pH  $\approx$  1.7). Over a period of 60 min. a gas sample of the headspace of the septum vial was injected every 10 min. to the GC.

**Table A.21. Results of headspace gas chromatography of Ca<sub>ex</sub>-birnessite (14).**

	t/min	area (O <sub>2</sub> )/ $\mu\text{V} \cdot \text{s}$	area (N <sub>2</sub> )/ $\mu\text{V} \cdot \text{s}$	O <sub>2</sub> /%	N <sub>2</sub> /%
Vial 1 <sup>a</sup> 5.1 mg of <b>14</b> (43.40 $\mu\text{mol Mn}$ )	10	14679.6	51184.9	22.3	77.7
	20	13043.5	41838.5	23.8	76.2
	30	9072.4	27286.1	25.0	75.0
	40	9357.2	26528.0	26.1	73.9
	50	8261.2	22046.4	27.3	72.7
	60	6744.6	16999.4	28.4	71.6
Vial 2 <sup>a</sup> 5.1 mg of <b>14</b> (43.40 $\mu\text{mol Mn}$ )	10	9906.5	35219.8	22.0	78.0
	20	6558.2	21712.5	23.2	76.8
	30	7399.5	22933.8	24.4	75.6
	40	7731.5	22489.5	25.6	74.4
	50	6901.7	18863.7	26.8	73.2
	60	6152.2	15815.1	28.0	72.0
Vial 3 <sup>b</sup> 5.1 mg of <b>14</b> (43.40 $\mu\text{mol Mn}$ )	60	16577.9	47696.9	25.8	74.2
Vial 4 <sup>b</sup> 5.7 mg of <b>14</b> (48.51 $\mu\text{mol Mn}$ )	60	17620.4	49152.1	26.4	73.6
Vial 5 <sup>c</sup> 4.8 mg of <b>14</b> (40.848 $\mu\text{mol Mn}$ )	10	13006.6	48766.6	21.1	78.9
	20	10299.0	38654.9	21.0	79.0
	30	4529.1	17110.6	20.9	79.1
	40	6202.2	23394.9	21.0	79.0
	50	5217.8	19674.4	21.0	79.0
	60	4337.5	16368.8	20.9	79.1

<sup>a</sup> The oxide sample was suspended in 5 mL of a 0.25 M Ce<sup>IV</sup> solution in a septum vial. Over a period of 60 min. a gas sample of the headspace of the septum vial was injected every 10 min. to the GC.

<sup>b</sup> The oxide sample was suspended in 5 mL of a 0.25 M Ce<sup>IV</sup> solution in a septum vial. After 60 min. a single gas sample of the headspace of the septum vial was injected to the GC.

<sup>c</sup> The oxide sample was suspended in 5 mL HNO<sub>3</sub> (pH  $\approx$  1.7). Over a period of 60 min. a gas sample of the headspace of the septum vial was injected every 10 min. to the GC.

**Table A.22. Results of headspace gas chromatography of Mn<sub>ex</sub>-birnessite (15).**

	t/min	area (O <sub>2</sub> )/ $\mu\text{V} \cdot \text{s}$	area (N <sub>2</sub> )/ $\mu\text{V} \cdot \text{s}$	O <sub>2</sub> /%	N <sub>2</sub> /%
Vial 1 <sup>a</sup> 5.1 mg of <b>15</b> (89.20 $\mu\text{mol Mn}$ )	10	13714.7	51130.9	21.1	78.9
	20	11597.5	42336.2	21.5	78.5
	30	9816.3	35022.8	21.9	78.1
	40	7570.8	26362.5	22.3	77.7
	50	6857.1	23201.4	22.8	77.2
	60	4274.4	14057.8	23.3	76.7
Vial 2 <sup>a</sup> 5.0 mg of <b>15</b> (87.45 $\mu\text{mol Mn}$ )	10	13824.1	51519.9	21.2	78.8
	20	11707.8	42707.3	21.5	78.5
	30	8587.2	30660.4	21.9	78.1
	40	8104.0	28215.6	22.3	77.7
	50	6833.0	23108.7	22.8	77.2
	60	5795.9	19021.5	23.4	76.6
Vial 3 <sup>b</sup> 5.2 mg of <b>15</b> (90.95 $\mu\text{mol Mn}$ )	60	10991.7	38139.5	22.4	77.6
Vial 4 <sup>b</sup> 5.4 mg of <b>15</b> (94.45 $\mu\text{mol Mn}$ )	60	13139.8	45472.8	22.4	77.6
Vial 5 <sup>c</sup> 5.3 mg of <b>15</b> (92.70 $\mu\text{mol Mn}$ )	10	13138.4	49263.9	21.1	78.9
	20	10939.3	41040.8	21.0	79.0
	30	5807.4	21907.2	21.0	79.0
	40	3564.0	13501.9	20.9	79.1
	50	3765.5	14251.3	20.9	79.1
	60	4026.5	15209.6	20.9	79.1

<sup>a</sup> The oxide sample was suspended in 5 mL of a 0.25 M Ce<sup>IV</sup> solution in a septum vial. Over a period of 60 min. a gas sample of the headspace of the septum vial was injected every 10 min. to the GC.

<sup>b</sup> The oxide sample was suspended in 5 mL of a 0.25 M Ce<sup>IV</sup> solution in a septum vial. After 60 min. a single gas sample of the headspace of the septum vial was injected to the GC.

<sup>c</sup> The oxide sample was suspended in 5 mL HNO<sub>3</sub> (pH  $\approx$  1.7). Over a period of 60 min. a gas sample of the headspace of the septum vial was injected every 10 min. to the GC.

**Table A.23. Results of headspace gas chromatography of Zn<sub>ex</sub>-birnessite (16).**

	t/min	area (O <sub>2</sub> )/ $\mu\text{V} \cdot \text{s}$	area (N <sub>2</sub> )/ $\mu\text{V} \cdot \text{s}$	O <sub>2</sub> /%	N <sub>2</sub> /%
Vial 1 <sup>a</sup> 6.9 mg of <b>16</b> (45.13 $\mu\text{mol Mn}$ )	10	13518.6	50482.9	21.1	78.9
	20	10873.5	40105.8	21.3	78.7
	30	8838.0	32298.8	21.5	78.5
	40	7434.3	26851.0	21.7	78.3
	50	6243.0	22264.9	21.9	78.1
	60	5250.0	18488.5	22.1	77.9
Vial 2 <sup>a</sup> 5.0 mg of <b>16</b> (32.70 $\mu\text{mol Mn}$ )	10	13474.1	50244.1	21.1	78.9
	20	11086.9	40831.3	21.4	78.6
	30	7781.9	28383.6	21.5	78.5
	40	7407.1	26664.3	21.7	78.3
	50	4999.1	17799.5	21.9	78.1
	60	4987.7	17489.9	22.2	77.8
Vial 3 <sup>b</sup> 5.2 mg of <b>16</b> (34.01 $\mu\text{mol Mn}$ )	60	8007.4	29737.8	21.2	78.8
Vial 4 <sup>b</sup> 5.6 mg of <b>16</b> (36.63 $\mu\text{mol Mn}$ )	60	14173.2	51986.8	21.4	78.6
Vial 5 <sup>c</sup> 6.1 mg of <b>16</b> (39.89 $\mu\text{mol Mn}$ )	10	13108.6	49124.2	21.1	78.9
	20	10883.6	40815.6	21.1	78.9
	30	6497.5	24482.6	21.0	79.0
	40	6865.8	25854.6	21.0	79.0
	50	5752.2	21670.2	21.0	79.0
	60	4670.4	17616.0	21.0	79.0

<sup>a</sup> The oxide sample was suspended in 5 mL of a 0.25 M Ce<sup>IV</sup> solution in a septum vial. Over a period of 60 min. a gas sample of the headspace of the septum vial was injected every 10 min. to the GC.

<sup>b</sup> The oxide sample was suspended in 5 mL of a 0.25 M Ce<sup>IV</sup> solution in a septum vial. After 60 min. a single gas sample of the headspace of the septum vial was injected to the GC.

<sup>c</sup> The oxide sample was suspended in 5 mL HNO<sub>3</sub> (pH  $\approx$  1.7). Over a period of 60 min. a gas sample of the headspace of the septum vial was injected every 10 min. to the GC.

**Table A.24. Results of headspace gas chromatography of Fe<sub>ex</sub><sup>2+</sup>-oxide (17).**

	t/min	area (O <sub>2</sub> )/ $\mu\text{V} \cdot \text{s}$	area (N <sub>2</sub> )/ $\mu\text{V} \cdot \text{s}$	O <sub>2</sub> /%	N <sub>2</sub> /%
Vial 1 <sup>a</sup> 5.4 mg of 17 (0.27 $\mu\text{mol}$ Mn)	10	13461.4	51374.4	20.8	79.2
	20	11241.1	42417.4	20.9	79.1
	30	9387.8	35050.1	21.1	78.9
	40	7838.8	28993.2	21.3	78.7
	50	6590.0	24169.2	21.4	78.6
	60	5548.4	20187.8	21.6	78.4
Vial 2 <sup>a</sup> 7.5 mg of 17 (0.38 $\mu\text{mol}$ Mn)	10	9809.8	37376.5	20.8	79.2
	20	10435.7	39279.7	21.0	79.0
	30	7191.8	26856.8	21.1	78.9
	40	5892.0	21795.0	21.3	78.7
	50	2300.2	855.4	21.2	78.8
	60	4034.8	14660.2	21.6	78.4
Vial 3 <sup>b</sup> 6.2 mg of 17 (0.31 $\mu\text{mol}$ Mn)	60	12658.2	46984.8	21.2	78.8
Vial 4 <sup>b</sup> 5.7 mg of 17 (0.29 $\mu\text{mol}$ Mn)	60	13489.1	49238.2	21.5	78.5
Vial 5 <sup>c</sup> 5.6 mg of 17 (0.28 $\mu\text{mol}$ Mn)	10	5204.3	19678.1	20.9	79.1
	20	9112.4	34263.0	21.0	79.0
	30	4552.6	17196.2	20.9	79.1
	40	5706.9	21518.9	21.0	79.0
	50	4830.8	18213.5	21.0	79.0
	60	4033.9	15227.7	20.9	79.1

<sup>a</sup> The oxide sample was suspended in 5 mL of a 0.25 M Ce<sup>IV</sup> solution in a septum vial. Over a period of 60 min. a gas sample of the headspace of the septum vial was injected every 10 min. to the GC.

<sup>b</sup> The oxide sample was suspended in 5 mL of a 0.25 M Ce<sup>IV</sup> solution in a septum vial. After 60 min. a single gas sample of the headspace of the septum vial was injected to the GC.

<sup>c</sup> The oxide sample was suspended in 5 mL HNO<sub>3</sub> (pH  $\approx$  1.7). Over a period of 60 min. a gas sample of the headspace of the septum vial was injected every 10 min. to the GC.

**Table A.25. Results of headspace gas chromatography of Fe<sup>3+</sup><sub>ex</sub>-birnessite (18).**

	t/min	area (O <sub>2</sub> )/ $\mu\text{V} \cdot \text{s}$	area (N <sub>2</sub> )/ $\mu\text{V} \cdot \text{s}$	O <sub>2</sub> /%	N <sub>2</sub> /%
Vial 1 <sup>a</sup> 5.5 mg of <b>18</b> (33.22 $\mu\text{mol Mn}$ )	10	12859.9	47864.7	21.2	78.8
	20	11436.9	41155.5	21.7	78.3
	30	9679.5	33874.5	22.2	77.8
	40	8231.4	28106.2	22.7	77.3
	50	7028.6	23439.5	23.1	76.9
	60	5979.8	19447.9	23.5	76.5
Vial 2 <sup>a</sup> 5.0 mg of <b>18</b> (30.20 $\mu\text{mol Mn}$ )	10	13736.2	50952.1	21.2	78.8
	20	11710.7	42008.4	21.8	78.2
	30	9946.9	34683.5	22.3	77.7
	40	4019.5	13824.8	22.5	77.5
	50	6181.3	20593.8	23.1	76.9
	60	3764.3	12254.8	23.5	76.5
Vial 3 <sup>b</sup> 5.1 mg of <b>18</b> (30.80 $\mu\text{mol Mn}$ )	60	14513.6	50755.1	22.2	77.8
Vial 4 <sup>b</sup> 5.3 mg of <b>18</b> (32.01 $\mu\text{mol Mn}$ )	60	15159.2	50780.4	23.0	77.0
Vial 5 <sup>c</sup> 5.2 mg of <b>18</b> (31.41 $\mu\text{mol Mn}$ )	10	13112.3	49139.6	21.1	78.9
	20	7916.7	29781.1	21.0	79.0
	30	8308.2	31234.8	21.0	79.0
	40	6896.6	25957.4	21.0	79.0
	50	5760.3	21699.1	21.0	79.0
	60	4009.1	15137.8	20.9	79.1

<sup>a</sup> The oxide sample was suspended in 5 mL of a 0.25 M Ce<sup>IV</sup> solution in a septum vial. Over a period of 60 min. a gas sample of the headspace of the septum vial was injected every 10 min. to the GC.

<sup>b</sup> The oxide sample was suspended in 5 mL of a 0.25 M Ce<sup>IV</sup> solution in a septum vial. After 60 min. a single gas sample of the headspace of the septum vial was injected to the GC.

<sup>c</sup> The oxide sample was suspended in 5 mL HNO<sub>3</sub> (pH  $\approx$  1.7). Over a period of 60 min. a gas sample of the headspace of the septum vial was injected every 10 min. to the GC.

**Table A.26. Results of headspace gas chromatography of K<sub>0.28</sub>-birnessite (19).**

	t/min	area (O <sub>2</sub> )/ $\mu\text{V} \cdot \text{s}$	area (N <sub>2</sub> )/ $\mu\text{V} \cdot \text{s}$	O <sub>2</sub> /%	N <sub>2</sub> /%
Vial 1 <sup>a</sup> 6.4 mg of <b>19</b> (74.18 $\mu\text{mol Mn}$ )	10	13362.8	49140.6	21.4	78.6
	20	8755.8	31289.1	21.9	78.1
	30	5913.6	20557.2	22.3	77.7
	40	6041.7	20312.8	22.9	77.1
	50	5937.2	19254.9	23.6	76.4
	60	2597.5	8126.6	24.2	75.8
Vial 2 <sup>a</sup> 7.7 mg of <b>19</b> (89.24 $\mu\text{mol Mn}$ )	10	13081.2	48751.9	21.2	78.8
	20	10702.2	38625.1	21.7	78.3
	30	6512.7	22888.9	22.2	77.8
	40	6038.6	20605.3	22.7	77.3
	50	5886.0	19421.2	23.3	76.7
	60	5001.2	15937.8	23.9	76.1
Vial 3 <sup>a</sup> 4.9 mg of <b>19</b> (56.79 $\mu\text{mol Mn}$ )	10	7071.6	26624.3	21.0	79.0
	20	7099.3	26067.7	21.4	78.6
	30	7009.5	25082.8	21.8	78.2
	40	5999.3	20903.5	22.3	77.7
	50	4532.5	15373.3	22.8	77.2
	60	4195.4	13774.3	23.3	76.7
Vial 4 <sup>b</sup> 4.9 mg of <b>19</b> (56.79 $\mu\text{mol Mn}$ )	60	13569.3	47296.8	22.3	77.7
Vial 5 <sup>b</sup> 5.3 mg of <b>19</b> (61.43 $\mu\text{mol Mn}$ )	60	13802.3	47753.9	22.4	77.6
Vial 6 <sup>b</sup> 6.1 mg of <b>19</b> (70.70 $\mu\text{mol Mn}$ )	60	13642.4	46896.0	22.5	77.5
Vial 7 <sup>c</sup> 5.9 mg of <b>19</b> (68.38 $\mu\text{mol Mn}$ )	10	9693.4	36484.4	21.0	79.0
	20	10239.1	38480.7	21.0	79.0
	30	8581.9	32266.5	21.0	79.0
	40	5356.8	20222.0	20.9	79.1
	50	4590.9	17354.7	20.9	79.1
	60	3797.0	14368.1	20.9	79.1

<sup>a</sup> The oxide sample was suspended in 5 mL of a 0.25 M Ce<sup>IV</sup> solution in a septum vial. Over a period of 60 min. a gas sample of the headspace of the septum vial was injected every 10 min. to the GC.

<sup>b</sup> The oxide sample was suspended in 5 mL of a 0.25 M Ce<sup>IV</sup> solution in a septum vial. After 60 min. a single gas sample of the headspace of the septum vial was injected to the GC.

<sup>c</sup> The oxide sample was suspended in 5 mL HNO<sub>3</sub> (pH  $\approx$  1.7). Over a period of 60 min. a gas sample of the headspace of the septum vial was injected every 10 min. to the GC.

**Table A.27. Results of headspace gas chromatography of Ca<sub>0.04</sub>-birnessite (20).**

	t/min	area (O <sub>2</sub> )/ $\mu\text{V} \cdot \text{s}$	area (N <sub>2</sub> )/ $\mu\text{V} \cdot \text{s}$	O <sub>2</sub> /%	N <sub>2</sub> /%
Vial 1 <sup>a</sup> 6.9 mg of <b>20</b> (63.62 $\mu\text{mol Mn}$ )	10	11511.6	40850.1	22.0	78.0
	20	7256.0	23757.0	23.4	76.6
	30	9038.1	27315.6	24.9	75.1
	40	8097.1	22662.7	26.3	73.7
	50	7090.5	18449.7	27.8	72.2
	60	4649.5	11278.6	29.2	70.8
Vial 2 <sup>a</sup> 5.3 mg of <b>20</b> (48.87 $\mu\text{mol Mn}$ )	10	5824.6	21000.1	21.7	78.3
	20	8098.8	27107.9	23.0	77.0
	30	8586.2	26740.6	24.3	75.7
	40	7429.5	21635.1	25.6	74.4
	50	6598.8	17977.6	26.9	73.1
	60	4738.1	12124.0	28.1	71.9
Vial 3 <sup>a</sup> 4.9 mg of <b>20</b> (45.18 $\mu\text{mol Mn}$ )	10	10727.0	38935.5	21.6	78.4
	20	11174.4	38197.3	22.6	77.4
	30	9725.4	31393.5	23.7	76.3
	40	8450.9	25847.8	24.6	75.4
	50	7274.4	21119.1	25.6	74.4
	60	6258.6	17272.0	26.6	73.4
Vial 4 <sup>b</sup> 5.7 mg of <b>20</b> (52.55 $\mu\text{mol Mn}$ )	60	9902.6	29190.7	25.3	74.7
Vial 5 <sup>b</sup> 5.5 mg of <b>20</b> (50.71 $\mu\text{mol Mn}$ )	60	15771.9	47151.8	25.1	74.9
Vial 6 <sup>b</sup> 5.6 mg of <b>20</b> (51.63 $\mu\text{mol Mn}$ )	60	7686.4	22926.7	25.1	74.9
Vial 7 <sup>c</sup> 5.4 mg of <b>20</b> (49.79 $\mu\text{mol Mn}$ )	10	13049.5	48906.3	21.1	78.9
	20	10501.1	39394.8	21.0	79.0
	30	8653.6	32505.1	21.0	79.0
	40	6965.8	26208.5	21.0	79.0
	50	5856.2	22065.8	21.0	79.0
	60	3151.2	11917.7	20.9	79.1

<sup>a</sup> The oxide sample was suspended in 5 mL of a 0.25 M Ce<sup>IV</sup> solution in a septum vial. Over a period of 60 min. a gas sample of the headspace of the septum vial was injected every 10 min. to the GC.

<sup>b</sup> The oxide sample was suspended in 5 mL of a 0.25 M Ce<sup>IV</sup> solution in a septum vial. After 60 min. a single gas sample of the headspace of the septum vial was injected to the GC.

<sup>c</sup> The oxide sample was suspended in 5 mL HNO<sub>3</sub> (pH  $\approx$  1.7). Over a period of 60 min. a gas sample of the headspace of the septum vial was injected every 10 min. to the GC.

**Table A.28. Results of headspace gas chromatography of Ca<sub>0.08</sub>-birnessite (21).**

	t/min	area (O <sub>2</sub> )/ $\mu\text{V} \cdot \text{s}$	area (N <sub>2</sub> )/ $\mu\text{V} \cdot \text{s}$	O <sub>2</sub> /%	N <sub>2</sub> /%
Vial 1 <sup>a</sup> 6.3 mg of <b>21</b> (56.57 $\mu\text{mol Mn}$ )	10	5867.3	20876.0	21.9	78.1
	20	3296.0	10821.3	23.3	76.7
	30	8115.1	24471.4	24.9	75.1
	40	5725.5	15931.6	26.4	73.6
	50	4269.9	11036.3	27.9	72.1
	60	3799.5	9109.9	29.4	70.6
Vial 2 <sup>a</sup> 4.8 mg of <b>21</b> (43.10 $\mu\text{mol Mn}$ )	10	12946.2	48203.5	21.2	78.8
	20	6453.3	22586.9	22.2	77.8
	30	6062.1	19749.6	23.5	76.5
	40	6165.1	18880.7	24.6	75.4
	50	5055.8	14589.3	25.7	74.3
	60	4449.9	12062.1	26.9	73.1
Vial 3 <sup>a</sup> 4.9 mg of <b>21</b> (44.00 $\mu\text{mol Mn}$ )	10	11279.8	41397.8	21.4	78.6
	20	10991.1	37449.2	22.7	77.3
	30	8460.0	27078.1	23.8	76.2
	40	5088.6	15453.1	24.8	75.2
	50	3617.0	10407.8	25.8	74.2
	60	5050.2	13530.8	27.2	72.8
Vial 4 <sup>b</sup> 5.0 mg of <b>21</b> (44.90 $\mu\text{mol Mn}$ )	60	13569.3	47296.8	22.3	77.7
Vial 5 <sup>b</sup> 5.6 mg of <b>21</b> (50.29 $\mu\text{mol Mn}$ )	60	13802.3	47753.9	22.4	77.6
Vial 6 <sup>b</sup> 5.3 mg of <b>21</b> (47.59 $\mu\text{mol Mn}$ )	60	13642.4	46896.0	22.5	77.5
Vial 7 <sup>c</sup> 5.0 mg of <b>21</b> (44.90 $\mu\text{mol Mn}$ )	10	13323.3	49952.1	21.1	78.9
	20	11075.9	41541.6	21.1	78.9
	30	9196.9	34554.5	21.0	79.0
	40	7523.6	28312.2	21.0	79.0
	50	4926.1	18600.9	20.9	79.1
	60	3351.0	12684.2	20.9	79.1

<sup>a</sup> The oxide sample was suspended in 5 mL of a 0.25 M Ce<sup>IV</sup> solution in a septum vial. Over a period of 60 min. a gas sample of the headspace of the septum vial was injected every 10 min. to the GC.

<sup>b</sup> The oxide sample was suspended in 5 mL of a 0.25 M Ce<sup>IV</sup> solution in a septum vial. After 60 min. a single gas sample of the headspace of the septum vial was injected to the GC.

<sup>c</sup> The oxide sample was suspended in 5 mL HNO<sub>3</sub> (pH  $\approx$  1.7). Over a period of 60 min. a gas sample of the headspace of the septum vial was injected every 10 min. to the GC.

**Table A.29. Results of headspace gas chromatography of Ca<sub>0.10</sub>-birnessite (22).**

	t/min	area (O <sub>2</sub> )/ $\mu\text{V} \cdot \text{s}$	area (N <sub>2</sub> )/ $\mu\text{V} \cdot \text{s}$	O <sub>2</sub> /%	N <sub>2</sub> /%
Vial 1 <sup>a</sup> 5.1 mg of <b>22</b> (39.58 $\mu\text{mol Mn}$ )	10	11870.1	43817.9	21.3	78.7
	20	10899.7	38072.2	22.3	77.7
	30	3553.1	12063.8	22.8	77.2
	40	3978.0	12905.4	23.6	76.4
	50	4272.3	13167.8	24.5	75.5
	60	3663.9	10721.4	25.5	74.5
Vial 2 <sup>a</sup> 4.9 mg of <b>22</b> (38.02 $\mu\text{mol Mn}$ )	10	12353.5	45695.9	21.3	78.7
	20	10721.5	37794.3	22.1	77.9
	30	9177.5	31048.2	22.8	77.2
	40	7898.1	25704.6	23.5	76.5
	50	4895.2	15417.5	24.1	75.9
	60	4344.9	13152.5	24.8	75.2
Vial 3 <sup>a</sup> 4.9 mg of <b>22</b> (38.02 $\mu\text{mol Mn}$ )	10	13185.8	48554.9	21.4	78.6
	20	11071.3	38986.7	22.1	77.9
	30	9520.6	32232.6	22.8	77.2
	40	6632.2	21736.4	23.4	76.6
	50	5528.4	17467.2	24.0	76.0
	60	5456 .0	16541.4	24.8	75.2
Vial 4 <sup>b</sup> 5.7 mg of <b>22</b> (44.23 $\mu\text{mol Mn}$ )	60	14709.1	47684.9	23.6	76.4
Vial 5 <sup>b</sup> 5.8 mg of <b>22</b> (45.01 $\mu\text{mol Mn}$ )	60	14725.3	47443.6	23.7	76.3
Vial 6 <sup>b</sup> 6.0 mg of <b>22</b> (46.56 $\mu\text{mol Mn}$ )	60	14726.3	47763.6	23.6	76.4
Vial 7 <sup>c</sup> 5.5 mg of <b>22</b> (42.68 $\mu\text{mol Mn}$ )	10	13087.1	49066.4	21.1	78.9
	20	10783.9	40453.8	21.0	79.0
	30	8949 .0	33611.3	21.0	79.0
	40	5972.7	22515.2	21.0	79.0
	50	2370.1	8983.7	20.9	79.1
	60	4151.5	15689.5	20.9	79.1

<sup>a</sup> The oxide sample was suspended in 5 mL of a 0.25 M Ce<sup>IV</sup> solution in a septum vial. Over a period of 60 min. a gas sample of the headspace of the septum vial was injected every 10 min. to the GC.

<sup>b</sup> The oxide sample was suspended in 5 mL of a 0.25 M Ce<sup>IV</sup> solution in a septum vial. After 60 min. a single gas sample of the headspace of the septum vial was injected to the GC.

<sup>c</sup> The oxide sample was suspended in 5 mL HNO<sub>3</sub> (pH  $\approx$  1.7). Over a period of 60 min. a gas sample of the headspace of the septum vial was injected every 10 min. to the GC.

**Table A.30. Results of headspace gas chromatography of Ca<sub>0.15</sub>-birnessite (23).**

	t/min	area (O <sub>2</sub> )/ $\mu\text{V} \cdot \text{s}$	area (N <sub>2</sub> )/ $\mu\text{V} \cdot \text{s}$	O <sub>2</sub> /%	N <sub>2</sub> /%
Vial 1 <sup>a</sup> 5.6 mg of <b>23</b> (43.62 $\mu\text{mol Mn}$ )	10	13326.4	47956.8	21.7	78.3
	20	11725.1	39428.3	22.9	77.1
	30	10186.2	32295.9	24.0	76.0
	40	8761.7	26292.4	25.0	75.0
	50	7636.1	21784.6	26.0	74.0
	60	6613.6	17964.8	26.9	73.1
Vial 2 <sup>a</sup> 5.0 mg of <b>23</b> (38.95 $\mu\text{mol Mn}$ )	10	13427.3	48628.5	21.6	78.4
	20	11734.6	39928.9	22.7	77.3
	30	7946.9	25765.9	23.6	76.4
	40	8101.2	24982.0	24.5	75.5
	50	4875.9	14381.0	25.3	74.7
	60	5598.6	15660.4	26.3	73.7
Vial 3 <sup>a</sup> 5.4 mg of <b>23</b> (42.07 $\mu\text{mol Mn}$ )	10	7675.1	27996.5	21.5	78.5
	20	10241.4	35033.9	22.6	77.4
	30	7447.5	24160.2	23.6	76.4
	40	7407.8	22870.4	24.5	75.5
	50	4502.7	13308.3	25.3	74.7
	60	5163.8	14502.9	26.3	73.7
Vial 4 <sup>b</sup> 5.0 mg of <b>23</b> (38.95 $\mu\text{mol Mn}$ )	60	9459.9	29916.4	24.0	76.0
Vial 5 <sup>b</sup> 4.9 mg of <b>23</b> (38.17 $\mu\text{mol Mn}$ )	60	9086.4	28758.9	24.0	76.0
Vial 6 <sup>b</sup> 6.1 mg of <b>23</b> (47.52 $\mu\text{mol Mn}$ )	60	15257.8	47078.3	24.5	75.5
Vial 7 <sup>c</sup> 5.2 mg of <b>23</b> (40.51 $\mu\text{mol Mn}$ )	10	12779.8	47918.0	21.1	78.9
	20	10527.7	39500.0	21.0	79.0
	30	7724.4	29073.2	21.0	79.0
	40	7052.2	26458.5	21.0	79.0
	50	4697.7	17744.7	20.9	79.1
	60	4628.8	17478.6	20.9	79.1

<sup>a</sup> The oxide sample was suspended in 5 mL of a 0.25 M Ce<sup>IV</sup> solution in a septum vial. Over a period of 60 min. a gas sample of the headspace of the septum vial was injected every 10 min. to the GC.

<sup>b</sup> The oxide sample was suspended in 5 mL of a 0.25 M Ce<sup>IV</sup> solution in a septum vial. After 60 min. a single gas sample of the headspace of the septum vial was injected to the GC.

<sup>c</sup> The oxide sample was suspended in 5 mL HNO<sub>3</sub> (pH  $\approx$  1.7). Over a period of 60 min. a gas sample of the headspace of the septum vial was injected every 10 min. to the GC.

**Table A.31. Results of headspace gas chromatography of Ca<sub>0.17</sub>-birnessite (24).**

	t/min	area (O <sub>2</sub> )/ $\mu\text{V} \cdot \text{s}$	area (N <sub>2</sub> )/ $\mu\text{V} \cdot \text{s}$	O <sub>2</sub> /%	N <sub>2</sub> /%
Vial 1 <sup>a</sup> 5.6 mg of <b>24</b> (43.62 $\mu\text{mol Mn}$ )	10	12614.2	44700.2	22.0	78.0
	20	11599.5	37825.9	23.5	76.5
	30	8911.4	27182.5	24.7	75.3
	40	8550.2	24453.9	25.9	74.1
	50	7458.5	19998.2	27.2	72.8
	60	6379.4	16065.2	28.4	71.6
Vial 2 <sup>a</sup> 5.0 mg of <b>24</b> (38.95 $\mu\text{mol Mn}$ )	10	12938.6	46807.1	21.7	78.3
	20	11142.0	37337.0	23.0	77.0
	30	8679.6	27138.0	24.2	75.8
	40	6964.0	20494.8	25.4	74.6
	50	6899.0	19068.1	26.6	73.4
	60	6034.0	15647.6	27.8	72.2
Vial 3 <sup>a</sup> 5.4 mg of <b>24</b> (42.07 $\mu\text{mol Mn}$ )	10	7902.6	28284.7	21.8	78.2
	20	5810.2	19322.5	23.1	76.9
	30	5080.9	15769.6	24.4	75.6
	40	5698.7	16442.5	25.7	74.3
	50	4081.3	10935.4	27.2	72.8
	60	2657.2	6626.9	28.6	71.4
Vial 4 <sup>b</sup> 4.8 mg of <b>24</b> (41.09 $\mu\text{mol Mn}$ )	60	15622.7	47205.0	24.9	75.1
Vial 5 <sup>b</sup> 5.2 mg of <b>24</b> (44.51 $\mu\text{mol Mn}$ )	60	15798.8	47002.0	25.2	74.8
Vial 6 <sup>b</sup> 5.1 mg of <b>24</b> (43.66 $\mu\text{mol Mn}$ )	60	15751.7	47079.6	25.1	74.9
Vial 7 <sup>c</sup> 4.9 mg of <b>24</b> (41.94 $\mu\text{mol Mn}$ )	10	13278.7	49755.1	21.1	78.9
	20	9812.9	36845.4	21.0	79.0
	30	8728.8	32802.1	21.0	79.0
	40	7140.3	26869.3	21.0	79.0
	50	5864.8	22093.3	21.0	79.0
	60	4843.4	18267.6	21.0	79.0

<sup>a</sup> The oxide sample was suspended in 5 mL of a 0.25 M Ce<sup>IV</sup> solution in a septum vial. Over a period of 60 min. a gas sample of the headspace of the septum vial was injected every 10 min. to the GC.

<sup>b</sup> The oxide sample was suspended in 5 mL of a 0.25 M Ce<sup>IV</sup> solution in a septum vial. After 60 min. a single gas sample of the headspace of the septum vial was injected to the GC.

<sup>c</sup> The oxide sample was suspended in 5 mL HNO<sub>3</sub> (pH  $\approx$  1.7). Over a period of 60 min. a gas sample of the headspace of the septum vial was injected every 10 min. to the GC.

**Table A.32. Results of headspace gas chromatography of Ca<sub>0.21</sub>-birnessite (25).**

	t/min	area (O <sub>2</sub> )/ $\mu\text{V} \cdot \text{s}$	area (N <sub>2</sub> )/ $\mu\text{V} \cdot \text{s}$	O <sub>2</sub> /%	N <sub>2</sub> /%
Vial 1 <sup>a</sup> 5.1 mg of <b>25</b> (43.61 $\mu\text{mol Mn}$ )	10	12483.4	44248.5	22.0	78.0
	20	8661.0	28388.8	23.4	76.6
	30	9409.4	28759.5	24.7	75.3
	40	4675.9	13459.3	25.8	74.2
	50	6523.7	17607.5	27.0	73.0
	60	5777.2	14547.1	28.4	71.6
Vial 2 <sup>a</sup> 4.8 mg of <b>25</b> (41.04 $\mu\text{mol Mn}$ )	10	10437.7	37373.0	21.8	78.2
	20	11418.6	37974.4	23.1	76.9
	30	8339.9	26123.8	24.2	75.8
	40	5163.3	15372.2	25.1	74.9
	50	2116.4	6010.4	26.0	74.0
	60	3078.9	8197.8	27.3	72.7
Vial 3 <sup>a</sup> 5.4 mg of <b>25</b> (46.17 $\mu\text{mol Mn}$ )	10	9453.8	33346.7	22.1	77.9
	20	5398.9	17483.1	23.6	76.4
	30	8638.4	25689.4	25.2	74.8
	40	7319.6	20143.1	26.7	73.3
	50	6781.7	17336.5	28.1	71.9
	60	4715.7	11184.4	29.7	70.3
Vial 4 <sup>b</sup> 6.3 mg of <b>25</b> (53.87 $\mu\text{mol Mn}$ )	60	16760.0	47529.3	26.1	73.9
Vial 5 <sup>b</sup> 5.5 mg of <b>25</b> (47.03 $\mu\text{mol Mn}$ )	60	16530.2	46434.8	26.3	73.7
Vial 6 <sup>b</sup> 4.8 mg of <b>25</b> (41.04 $\mu\text{mol Mn}$ )	60	16103.6	46610.3	25.7	74.3
Vial 7 <sup>c</sup> 5.0 mg of <b>25</b> (42.75 $\mu\text{mol Mn}$ )	10	13161.2	49319.9	21.1	78.9
	20	10927.5	40963.9	21.1	78.9
	30	9029.8	33904.9	21.0	79.0
	40	6634.0	24983.3	21.0	79.0
	50	5925.3	22326.1	21.0	79.0
	60	4047.8	15289.0	20.9	79.1

<sup>a</sup> The oxide sample was suspended in 5 mL of a 0.25 M Ce<sup>IV</sup> solution in a septum vial. Over a period of 60 min. a gas sample of the headspace of the septum vial was injected every 10 min. to the GC.

<sup>b</sup> The oxide sample was suspended in 5 mL of a 0.25 M Ce<sup>IV</sup> solution in a septum vial. After 60 min. a single gas sample of the headspace of the septum vial was injected to the GC.

<sup>c</sup> The oxide sample was suspended in 5 mL HNO<sub>3</sub> (pH  $\approx$  1.7). Over a period of 60 min. a gas sample of the headspace of the septum vial was injected every 10 min. to the GC.

**Table A.33. Results of headspace gas chromatography of Ca<sub>0.21</sub>-birnessite (25) in water of the river Rhine.**

	t/min	area (O <sub>2</sub> )/ $\mu\text{V} \cdot \text{s}$	area (N <sub>2</sub> )/ $\mu\text{V} \cdot \text{s}$	O <sub>2</sub> /%	N <sub>2</sub> /%
Vial 1 <sup>a</sup> 5.0 mg of <b>25</b> (42.75 $\mu\text{mol Mn}$ )	10	13625.1	47223.2	22.4	77.6
	20	8670.9	27506.6	24.0	76.0
	30	8352.7	24716.4	25.3	74.7
	40	4436.1	12310.6	26.5	73.5
	50	4754.2	12361.1	27.8	72.2
	60	5487.2	13288.4	29.2	70.8
Vial 2 <sup>a</sup> 5.2 mg of <b>25</b> (44.46 $\mu\text{mol Mn}$ )	10	13352.8	47189.1	22.1	77.9
	20	5105.4	16725.4	23.4	76.6
	30	8465.3	25780.2	24.7	75.3
	40	7671.0	21771.8	26.1	73.9
	50	6634.6	17541.8	27.4	72.6
	60	2710.1	6677.1	28.9	71.1
Vial 3 <sup>a</sup> 6.2 mg of <b>25</b> (53.01 $\mu\text{mol Mn}$ )	10	7958.3	27902.6	22.2	77.8
	20	10982.7	34715.9	24.0	76.0
	30	9903.7	28594.0	25.7	74.3
	40	8674.7	23156.0	27.3	72.7
	50	7641.2	18898.8	28.8	71.2
	60	6629.7	15278.8	30.3	69.7
Vial 4 <sup>b</sup> 5.0 mg of <b>25</b> (42.75 $\mu\text{mol Mn}$ )	60	15390.4	44807.8	25.6	74.4
Vial 5 <sup>b</sup> 5.3 mg of <b>25</b> (45.32 $\mu\text{mol Mn}$ )	60	15645.2	45957.1	25.4	74.6
Vial 6 <sup>b</sup> 5.5 mg of <b>25</b> (47.03 $\mu\text{mol Mn}$ )	60	12018.4	34539.6	25.8	74.2

<sup>a</sup> The oxide sample was suspended in a septum vial in a solution of 685 mg (1.25 mmol) (NH<sub>4</sub>)<sub>2</sub>Ce<sup>IV</sup>(NO<sub>3</sub>)<sub>6</sub> in 5mL water of the river Rhine. Over a period of 60 min. a gas sample of the headspace of the septum vial was injected every 10 min. to the GC.

<sup>b</sup> The oxide sample was suspended in a septum vial in a solution of 685 mg (1.25 mmol) (NH<sub>4</sub>)<sub>2</sub>Ce<sup>IV</sup>(NO<sub>3</sub>)<sub>6</sub> in 5mL water of the river Rhine. After 60 min. a single gas sample of the headspace of the septum vial was injected to the GC.

**Table A.34. Results of headspace gas chromatography of Ca<sub>0.28</sub>-birnessite (26).**

	t/min	area (O <sub>2</sub> )/ $\mu\text{V} \cdot \text{s}$	area (N <sub>2</sub> )/ $\mu\text{V} \cdot \text{s}$	O <sub>2</sub> /%	N <sub>2</sub> /%
Vial 1 <sup>a</sup> 5.8 mg of <b>26</b> (48.49 $\mu\text{mol Mn}$ )	10	8876.6	31955.5	21.7	78.3
	20	10765.1	36325.1	22.9	77.1
	30	9177.1	29271.8	23.9	76.1
	40	5487.3	16686.8	24.7	75.3
	50	4379.4	12691.9	25.7	74.3
	60	5126.5	14056.5	26.7	73.3
Vial 2 <sup>a</sup> 5.7 mg of <b>26</b> (47.65 $\mu\text{mol Mn}$ )	10	13498.0	49036.5	21.6	78.4
	20	11713.2	40333.0	22.5	77.5
	30	10068.8	33052.8	23.3	76.7
	40	8713.9	27364.1	24.2	75.8
	50	6153.3	18516.8	24.9	75.1
	60	5971.6	17160.6	25.8	74.2
Vial 3 <sup>a</sup> 5.3 mg of <b>26</b> (44.31 $\mu\text{mol Mn}$ )	10	13564.6	48727.8	21.7	78.3
	20	11889.5	40345.9	22.9	77.1
	30	7183.6	23330.2	23.9	76.1
	40	7391.4	22963.1	24.7	75.3
	50	6800.8	20180.9	25.7	74.3
	60	5901.0	16702.9	26.7	73.3
Vial 4 <sup>b</sup> 5.2 mg of <b>26</b> (43.47 $\mu\text{mol Mn}$ )	60	15644.6	47680.1	24.7	75.3
Vial 5 <sup>b</sup> 5.4 mg of <b>26</b> (45.14 $\mu\text{mol Mn}$ )	60	15296.1	47223.5	24.5	75.5
Vial 6 <sup>b</sup> 5.2 mg of <b>26</b> (43.47 $\mu\text{mol Mn}$ )	60	15643.6	47719.5	24.7	75.3
Vial 7 <sup>c</sup> 5.7 mg of <b>26</b> (47.65 $\mu\text{mol Mn}$ )	10	10586.9	39813.0	21.0	79.0
	20	10126.6	38057.5	21.0	79.0
	30	6736.2	25385.7	21.0	79.0
	40	2333.9	8856.0	20.9	79.1
	50	4618.4	17458.2	20.9	79.1
	60	3911.8	14781.4	20.9	79.1

<sup>a</sup> The oxide sample was suspended in 5 mL of a 0.25 M Ce<sup>IV</sup> solution in a septum vial. Over a period of 60 min. a gas sample of the headspace of the septum vial was injected every 10 min. to the GC.

<sup>b</sup> The oxide sample was suspended in 5 mL of a 0.25 M Ce<sup>IV</sup> solution in a septum vial. After 60 min. a single gas sample of the headspace of the septum vial was injected to the GC.

<sup>c</sup> The oxide sample was suspended in 5 mL HNO<sub>3</sub> (pH  $\approx$  1.7). Over a period of 60 min. a gas sample of the headspace of the septum vial was injected every 10 min. to the GC.

**Table A.35. Results of headspace gas chromatography of Ca<sub>0.36</sub>-birnessite (27).**

	t/min	area (O <sub>2</sub> )/μV · s	area (N <sub>2</sub> )/μV · s	O <sub>2</sub> /%	N <sub>2</sub> /%
Vial 1 <sup>a</sup> 5.1 mg of 27 (41.72 μmol Mn)	10	13411.4	48812.3	21.6	78.4
	20	11600.2	40342.4	22.3	77.7
	30	10005.5	33387.4	23.1	76.9
	40	8630.5	27717.9	23.7	76.3
	50	7470.8	23087.8	24.4	75.6
	60	6482.9	19276.9	25.2	74.8
Vial 2 <sup>a</sup> 5.3 mg of 27 (43.35 μmol Mn)	10	13179.0	48671.4	21.3	78.7
	20	11085.4	39552.6	21.9	78.1
	30	9299.6	32105.4	22.5	77.5
	40	7888.4	26417.1	23.0	77.0
	50	2653.0	8649.2	23.5	76.5
	60	4896.3	15305.5	24.2	75.8
Vial 3 <sup>a</sup> 5.3 mg of 27 (43.35 μmol Mn)	10	13393.1	48634.7	21.6	78.4
	20	8351.5	28912.4	22.4	77.6
	30	9193.8	30352.3	23.2	76.8
	40	4689.5	14835.1	24.0	76.0
	50	6231.8	18800.6	24.9	75.1
	60	4173.7	11988.1	25.8	74.2
Vial 4 <sup>b</sup> 5.0 mg of 27 (40.90 μmol Mn)	60	13220.1	43075.2	23.5	76.5
Vial 5 <sup>b</sup> 5.1 mg of 27 (41.72 μmol Mn)	60	14938.4	48286.2	23.6	76.4
Vial 6 <sup>b</sup> 5.6 mg of 27 (45.81 μmol Mn)	60	11408.5	37155.3	23.5	76.5
Vial 7 <sup>c</sup> 4.9 mg of 27 (40.08 μmol Mn)	10	13181.1	49416.7	21.1	78.9
	20	10704.7	40162.5	21.0	79.0
	30	7728.4	29080.0	21.0	79.0
	40	7000.7	26358.7	21.0	79.0
	50	5876.9	22143.9	21.0	79.0
	60	3898.8	14725.1	20.9	78.9

<sup>a</sup> The oxide sample was suspended in 5 mL of a 0.25 M Ce<sup>IV</sup> solution in a septum vial. Over a period of 60 min. a gas sample of the headspace of the septum vial was injected every 10 min. to the GC.

<sup>b</sup> The oxide sample was suspended in 5 mL of a 0.25 M Ce<sup>IV</sup> solution in a septum vial. After 60 min. a single gas sample of the headspace of the septum vial was injected to the GC.

<sup>c</sup> The oxide sample was suspended in 5 mL HNO<sub>3</sub> (pH ≈ 1.7). Over a period of 60 min. a gas sample of the headspace of the septum vial was injected every 10 min. to the GC.

**Table A.36. Results of headspace gas chromatography of Ca<sub>0.54</sub>-birnessite (28).**

	t/min	area (O <sub>2</sub> )/μV · s	area (N <sub>2</sub> )/μV · s	O <sub>2</sub> /%	N <sub>2</sub> /%
Vial 1 <sup>a</sup> 5.2 mg of <b>28</b> (36.97 μmol Mn)	10	13189.3	48161.5	21.5	78.5
	20	11329.8	39855.0	22.1	77.9
	30	9478.1	32312.1	22.7	77.3
	40	7823.9	25896.0	23.2	76.8
	50	6752.2	21690.3	23.7	76.3
	60	5716.2	17804.6	24.3	75.7
Vial 2 <sup>a</sup> 4.8 mg of <b>28</b> (34.13 μmol Mn)	10	13152.2	48081.7	21.5	78.5
	20	11233.8	39496.8	22.1	77.9
	30	9609.5	32689.9	22.7	77.3
	40	5669.7	18776.9	23.2	76.8
	50	6361.7	20411.6	23.8	76.2
	60	5454.8	16904.2	24.4	75.6
Vial 3 <sup>a</sup> 5.0 mg of <b>28</b> (35.55 μmol Mn)	10	10327.9	37873.1	21.4	78.6
	20	7918.0	28007.8	22.0	78.0
	30	8393.9	28622.4	22.7	77.3
	40	7273.5	23949.9	23.3	76.7
	50	6268.8	19941.1	23.9	76.1
	60	5425.2	16665.8	24.6	75.4
Vial 4 <sup>b</sup> 5.0 mg of <b>28</b> (35.55 μmol Mn)	60	12604.4	42518.8	22.9	77.1
Vial 5 <sup>b</sup> 5.6 mg of <b>28</b> (39.82 μmol Mn)	60	10305.5	34373.2	23.1	76.9
Vial 6 <sup>b</sup> 5.5 mg of <b>28</b> (39.11 μmol Mn)	60	10660.6	36109.3	22.8	77.2
Vial 7 <sup>c</sup> 6.0 mg of <b>28</b> (42.66 μmol Mn)	10	13143.2	49269.6	21.1	78.9
	20	10904.7	40887.7	21.1	78.9
	30	8701.3	32678.8	21.0	79.0
	40	7214.4	27135.2	21.0	79.0
	50	5973.5	22496.5	21.0	79.0
	60	4921.0	18560.6	21.0	79.0

<sup>a</sup> The oxide sample was suspended in 5 mL of a 0.25 M Ce<sup>IV</sup> solution in a septum vial. Over a period of 60 min. a gas sample of the headspace of the septum vial was injected every 10 min. to the GC.

<sup>b</sup> The oxide sample was suspended in 5 mL of a 0.25 M Ce<sup>IV</sup> solution in a septum vial. After 60 min. a single gas sample of the headspace of the septum vial was injected to the GC.

<sup>c</sup> The oxide sample was suspended in 5 mL HNO<sub>3</sub> (pH ≈ 1.7). Over a period of 60 min. a gas sample of the headspace of the septum vial was injected every 10 min. to the GC.

**Table A.37. Results of headspace gas chromatography of Ca<sub>0.67</sub>-birnessite (29).**

	t/min	area (O <sub>2</sub> )/ $\mu\text{V} \cdot \text{s}$	area (N <sub>2</sub> )/ $\mu\text{V} \cdot \text{s}$	O <sub>2</sub> /%	N <sub>2</sub> /%
Vial 1 <sup>a</sup> 5.1 mg of <b>29</b> (34.17 $\mu\text{mol}$ Mn)	10	13096.2	48263.4	21.3	78.7
	20	8010.6	28836.5	21.7	78.3
	30	8661.5	30403.4	22.2	77.8
	40	7453.0	25536.4	22.6	77.4
	50	6317.1	21149.5	23.0	77.0
	60	5397.9	17632.9	23.4	76.6
Vial 2 <sup>a</sup> 5.6 mg of <b>29</b> (37.52 $\mu\text{mol}$ Mn)	10	12372.4	45733.0	21.3	78.7
	20	10683.4	38380.4	21.8	78.2
	30	9097.8	31787.0	22.3	77.7
	40	7779.3	26429.7	22.7	77.3
	50	6664.7	22011.4	23.2	76.8
	60	2690.8	8678.4	23.7	76.3
Vial 3 <sup>a</sup> 5.4 mg of <b>29</b> (36.18 $\mu\text{mol}$ Mn)	10	13214.9	48585.5	21.4	78.6
	20	11313.9	40297.3	21.9	78.1
	30	6436.5	22352.1	22.4	77.6
	40	5715.9	19285.7	22.9	77.1
	50	6035.8	19710.1	23.4	76.6
	60	5265.4	16623.8	24.1	75.9
Vial 4 <sup>b</sup> 5.1 mg of <b>29</b> (34.17 $\mu\text{mol}$ Mn)	60	13065.3	44187.4	22.8	77.2
Vial 5 <sup>b</sup> 5.2 mg of <b>29</b> (34.84 $\mu\text{mol}$ Mn)	60	13195.4	45247.7	22.6	77.4
Vial 6 <sup>b</sup> 5.6 mg of <b>29</b> (37.52 $\mu\text{mol}$ Mn)	60	14497.8	48590.8	23.0	77.0
Vial 7 <sup>c</sup> 5.0 mg of <b>29</b> (33.5 $\mu\text{mol}$ Mn)	10	13070.9	48982.4	21.1	78.9
	20	10236.0	38407.7	21.0	79.0
	30	8389.2	31527.6	21.0	79.0
	40	6422.0	24182.4	21.0	79.0
	50	5493.1	20701.0	21.0	79.0
	60	4520.6	17062.7	20.9	79.1

<sup>a</sup> The oxide sample was suspended in 5 mL of a 0.25 M Ce<sup>IV</sup> solution in a septum vial. Over a period of 60 min. a gas sample of the headspace of the septum vial was injected every 10 min. to the GC.

<sup>b</sup> The oxide sample was suspended in 5 mL of a 0.25 M Ce<sup>IV</sup> solution in a septum vial. After 60 min. a single gas sample of the headspace of the septum vial was injected to the GC.

<sup>c</sup> The oxide sample was suspended in 5 mL HNO<sub>3</sub> (pH  $\approx$  1.7). Over a period of 60 min. a gas sample of the headspace of the septum vial was injected every 10 min. to the GC.

**Table A.38. Results of headspace gas chromatography of Ca<sub>0h</sub>-birnessite (30).**

	t/min	area (O <sub>2</sub> )/μV · s	area (N <sub>2</sub> )/μV · s	O <sub>2</sub> /%	N <sub>2</sub> /%
Vial 1 <sup>a</sup> 5.0 mg of <b>30</b> (48.55 μmol Mn)	10	13164.3	46305.3	22.1	77.9
	20	5644.3	18420.9	23.5	76.5
	30	8962.5	27298.5	24.7	75.3
	40	7481.3	21289.7	26.0	74.0
	50	6909.7	18455.4	27.2	72.8
	60	6144.7	15385.8	28.5	71.5
Vial 2 <sup>a</sup> 5.7 mg of <b>30</b> (55.35 μmol Mn)	10	12964.5	45713.0	22.1	77.9
	20	6997.5	22866.5	23.4	76.6
	30	9169.2	27909.1	24.7	75.3
	40	6528.1	18633.8	25.9	74.1
	50	6849.8	18374.8	27.2	72.8
	60	5781.6	14537.1	28.5	71.5
Vial 3 <sup>a</sup> 4.9 mg of <b>30</b> (47.58 μmol Mn)	10	9699.1	34337.8	22.0	78.0
	20	8595.7	28324.6	23.3	76.7
	30	7716.0	23878.6	24.4	75.6
	40	7797.7	22692.3	25.6	74.4
	50	6759.3	18495.1	26.8	73.2
	60	6003.8	15454.2	28.0	72.0
Vial 4 <sup>b</sup> 4.8 mg of <b>30</b> (46.61 μmol Mn)	60	15788.3	46482.1	25.4	74.6
Vial 5 <sup>b</sup> 5.0 mg of <b>30</b> (48.55 μmol Mn)	60	15346.4	45956.2	25.0	75.0
Vial 6 <sup>b</sup> 5.5 mg of <b>30</b> (53.41 μmol Mn)	60	16766.7	47318.3	26.2	73.8
Vial 7 <sup>c</sup> 4.8 mg of <b>30</b> (46.61 μmol Mn)	10	12125.7	45680.9	21.0	79.0
	20	8319.2	31430.0	21.0	79.0
	30	7947.0	29989.6	21.0	79.0
	40	5535.5	20953.6	20.9	79.1
	50	4449.1	16864.5	20.9	79.1
	60	4277.4	16199.1	20.9	79.1

<sup>a</sup> The oxide sample was suspended in 5 mL of a 0.25 M Ce<sup>IV</sup> solution in a septum vial. Over a period of 60 min. a gas sample of the headspace of the septum vial was injected every 10 min. to the GC.

<sup>b</sup> The oxide sample was suspended in 5 mL of a 0.25 M Ce<sup>IV</sup> solution in a septum vial. After 60 min. a single gas sample of the headspace of the septum vial was injected to the GC.

<sup>c</sup> The oxide sample was suspended in 5 mL HNO<sub>3</sub> (pH ≈ 1.7). Over a period of 60 min. a gas sample of the headspace of the septum vial was injected every 10 min. to the GC.

**Table A.39. Results of headspace gas chromatography of Ca<sub>1h</sub>-birnessite (31).**

	t/min	area (O <sub>2</sub> )/ $\mu\text{V} \cdot \text{s}$	area (N <sub>2</sub> )/ $\mu\text{V} \cdot \text{s}$	O <sub>2</sub> /%	N <sub>2</sub> /%
Vial 1 <sup>a</sup> 4.9 mg of <b>31</b> (47.73 $\mu\text{mol Mn}$ )	10	13631.7	48064.5	22.1	77.9
	20	11593.0	37960.3	23.4	76.6
	30	9694.1	29991.2	24.4	75.6
	40	8959.5	26281.2	25.4	74.6
	50	7047.1	19607.8	26.4	73.6
	60	6673.2	17577.5	27.5	72.5
Vial 2 <sup>a</sup> 5.7 mg of <b>31</b> (55.52 $\mu\text{mol Mn}$ )	10	14062.2	48833.6	22.4	77.6
	20	12618.9	40170.5	23.9	76.1
	30	11175.3	33212.6	25.2	74.8
	40	9800.2	27511.2	26.3	73.7
	50	8502.5	22608.0	27.3	72.7
	60	7434.0	18718.5	28.4	71.6
Vial 3 <sup>a</sup> 6.5 mg of <b>31</b> (63.31 $\mu\text{mol Mn}$ )	10	12337.2	42775.5	22.4	77.6
	20	9196.4	29160.7	24.0	76.0
	30	9859.0	29131.9	25.3	74.7
	40	7020.8	19486.9	26.5	73.5
	50	2820.0	7388.5	27.6	72.4
	60	5207.7	12772.5	29.0	71.0
Vial 4 <sup>b</sup> 5.2 mg of <b>31</b> (50.65 $\mu\text{mol Mn}$ )	60	13275.9	37421.9	26.2	73.8
Vial 5 <sup>b</sup> 5.0 mg of <b>31</b> (48.70 $\mu\text{mol Mn}$ )	60	15942.6	46210.6	25.7	74.3
Vial 6 <sup>b</sup> 5.0 mg of <b>31</b> (48.70 $\mu\text{mol Mn}$ )	60	13907.9	39467.5	26.1	73.9
Vial 7 <sup>c</sup> 5.3 mg of <b>31</b> (51.62 $\mu\text{mol Mn}$ )	10	13077.1	49065.8	21.0	79.0
	20	10794.7	40527.9	21.0	79.0
	30	8974.8	33748.0	21.0	79.0
	40	7461.3	28101.6	21.0	79.0
	50	6167.6	23254.3	21.0	79.0
	60	4986.0	18822.3	20.9	79.1

<sup>a</sup> The oxide sample was suspended in 5 mL of a 0.25 M Ce<sup>IV</sup> solution in a septum vial. Over a period of 60 min. a gas sample of the headspace of the septum vial was injected every 10 min. to the GC.

<sup>b</sup> The oxide sample was suspended in 5 mL of a 0.25 M Ce<sup>IV</sup> solution in a septum vial. After 60 min. a single gas sample of the headspace of the septum vial was injected to the GC.

<sup>c</sup> The oxide sample was suspended in 5 mL HNO<sub>3</sub> (pH  $\approx$  1.7). Over a period of 60 min. a gas sample of the headspace of the septum vial was injected every 10 min. to the GC.

**Table A.40. Results of headspace gas chromatography of Ca<sub>2h</sub>-birnessite (32).**

	t/min	area (O <sub>2</sub> )/ $\mu\text{V} \cdot \text{s}$	area (N <sub>2</sub> )/ $\mu\text{V} \cdot \text{s}$	O <sub>2</sub> /%	N <sub>2</sub> /%
Vial 1 <sup>a</sup> 5.2 mg of <b>32</b> (45.60 $\mu\text{mol Mn}$ )	10	7007.6	25424.9	21.6	78.4
	20	10591.1	35956.3	22.8	77.2
	30	5798.3	18613.0	23.8	76.2
	40	6936.9	21045.7	24.8	75.2
	50	5832.8	16735.3	25.8	74.2
	60	2232.5	6067.4	26.9	73.1
Vial 2 <sup>a</sup> 5.1 mg of <b>32</b> (44.73 $\mu\text{mol Mn}$ )	10	13018.7	47270.0	21.6	78.4
	20	11082.9	38164.4	22.5	77.5
	30	6219.1	20482.6	23.3	76.7
	40	7512.4	23582.1	24.2	75.8
	50	6595.5	19704.7	25.1	74.9
	60	5695.3	16190.3	26.0	74.0
Vial 3 <sup>a</sup> 4.8 mg of <b>32</b> (42.10 $\mu\text{mol Mn}$ )	10	8006.9	29016.4	21.6	78.4
	20	10776.1	36640.5	22.7	77.3
	30	9337.9	29937.9	23.8	76.2
	40	7675.2	23257.8	24.8	75.2
	50	2318.2	6675.0	25.8	74.2
	60	4911.4	13285.1	27.0	73.0
Vial 4 <sup>b</sup> 5.5 mg of <b>32</b> (48.24 $\mu\text{mol Mn}$ )	60	15165.0	46974.3	24.4	75.6
Vial 5 <sup>b</sup> 5.1 mg of <b>32</b> (44.73 $\mu\text{mol Mn}$ )	60	2936.9	9173.9	24.3	75.7
Vial 6 <sup>b</sup> 4.9 mg of <b>32</b> (42.97 $\mu\text{mol Mn}$ )	60	12765.6	39725.5	24.3	75.7
Vial 7 <sup>c</sup> 5.2 mg of <b>32</b> (45.60 $\mu\text{mol Mn}$ )	10	10190.8	38328.1	21.0	79.0
	20	9874.5	37105.8	21.0	79.0
	30	8043.4	30251.2	21.0	79.0
	40	6654.6	25068.3	21.0	79.0
	50	1576.3	5983.7	20.9	79.1
	60	2728.5	10346.2	20.9	79.1

<sup>a</sup> The oxide sample was suspended in 5 mL of a 0.25 M Ce<sup>IV</sup> solution in a septum vial. Over a period of 60 min. a gas sample of the headspace of the septum vial was injected every 10 min. to the GC.

<sup>b</sup> The oxide sample was suspended in 5 mL of a 0.25 M Ce<sup>IV</sup> solution in a septum vial. After 60 min. a single gas sample of the headspace of the septum vial was injected to the GC.

<sup>c</sup> The oxide sample was suspended in 5 mL HNO<sub>3</sub> (pH  $\approx$  1.7). Over a period of 60 min. a gas sample of the headspace of the septum vial was injected every 10 min. to the GC.

**Table A.41. Results of headspace gas chromatography of Ca<sub>4h</sub>-birnessite (33).**

	t/min	area (O <sub>2</sub> )/ $\mu\text{V} \cdot \text{s}$	area (N <sub>2</sub> )/ $\mu\text{V} \cdot \text{s}$	O <sub>2</sub> /%	N <sub>2</sub> /%
Vial 1 <sup>a</sup> 4.9 mg of <b>33</b> (42.97 $\mu\text{mol Mn}$ )	10	13138.4	46487.3	22.0	78.0
	20	6773.8	22240.8	23.3	76.7
	30	9219.8	28375.5	24.5	75.5
	40	7948.4	23044.9	25.6	74.4
	50	5151.1	14116.8	26.7	73.3
	60	5782.4	14949.2	27.9	72.1
Vial 2 <sup>a</sup> 6.5 mg of <b>33</b> (57.01 $\mu\text{mol Mn}$ )	10	6461.3	22911.1	22.0	78.0
	20	10595.1	34495.3	23.5	76.5
	30	9476.4	28582.4	24.9	75.1
	40	8338.7	23535.5	26.2	73.8
	50	7228.2	19153.1	27.4	72.6
	60	5694.4	14148.1	28.7	71.3
Vial 3 <sup>a</sup> 5.1 mg of <b>33</b> (44.73 $\mu\text{mol Mn}$ )	10	13198.3	47180.3	21.9	78.1
	20	10005.9	33560.7	23.0	77.0
	30	7439.6	23694.5	23.9	76.1
	40	5234.4	15769.3	24.9	75.1
	50	2130.3	6073.4	26.0	74.0
	60	3804.6	10165.6	27.2	72.8
Vial 4 <sup>b</sup> 5.3 mg of <b>33</b> (46.48 $\mu\text{mol Mn}$ )	60	16249.1	47754.9	25.4	74.6
Vial 5 <sup>b</sup> 6.4 mg of <b>33</b> (56.13 $\mu\text{mol Mn}$ )	60	16380.0	47581.2	25.6	74.4
Vial 6 <sup>b</sup> 4.9 mg of <b>33</b> (42.97 $\mu\text{mol Mn}$ )	60	16213.8	47732.4	25.4	74.6
Vial 7 <sup>c</sup> 5.3 mg of <b>33</b> (46.48 $\mu\text{mol Mn}$ )	10	12348.3	46335.9	21.0	79.0
	20	10025.2	37647.7	21.0	79.0
	30	8294.2	31195.9	21.0	79.0
	40	6776.9	25522.0	21.0	79.0
	50	2710.5	10265.2	20.9	79.1
	60	3325.8	12596.4	20.9	79.1

<sup>a</sup> The oxide sample was suspended in 5 mL of a 0.25 M Ce<sup>IV</sup> solution in a septum vial. Over a period of 60 min. a gas sample of the headspace of the septum vial was injected every 10 min. to the GC.

<sup>b</sup> The oxide sample was suspended in 5 mL of a 0.25 M Ce<sup>IV</sup> solution in a septum vial. After 60 min. a single gas sample of the headspace of the septum vial was injected to the GC.

<sup>c</sup> The oxide sample was suspended in 5 mL HNO<sub>3</sub> (pH  $\approx$  1.7). Over a period of 60 min. a gas sample of the headspace of the septum vial was injected every 10 min. to the GC.

**Table A.42. Results of headspace gas chromatography of Ca<sub>8n</sub>-birnessite (34).**

	t/min	area (O <sub>2</sub> )/μV · s	area (N <sub>2</sub> )/μV · s	O <sub>2</sub> /%	N <sub>2</sub> /%
Vial 1 <sup>a</sup> 5.7 mg of <b>34</b> (43.26 μmol Mn)	10	6400.1	22477.8	22.2	77.8
	20	10912.6	35089.8	23.7	76.3
	30	9688.6	28873.6	25.1	74.9
	40	6969.1	19393.8	26.4	73.6
	50	6602.4	17173.3	27.8	72.2
	60	6303.9	15282.0	29.2	70.8
Vial 2 <sup>a</sup> 6.2 mg of <b>34</b> (47.06 μmol Mn)	10	14082.9	49092.4	22.3	77.7
	20	12677.3	40368.9	23.9	76.1
	30	11214.8	33178.4	25.3	74.7
	40	9776.9	27216.6	26.4	73.6
	50	8635.6	22661.5	27.6	72.4
	60	7628.7	18918.7	28.7	71.3
Vial 3 <sup>a</sup> 7.0 mg of <b>34</b> (53.13 μmol Mn)	10	13929.8	48908.3	22.2	77.8
	20	12421.3	40087.4	23.7	76.3
	30	8683.1	26035.7	25.0	75.0
	40	4885.5	13729.4	26.2	73.8
	50	5943.8	15568.4	27.6	72.4
	60	6207.4	15101.9	29.1	70.9
Vial 4 <sup>b</sup> 5.0 mg of <b>34</b> (37.95 μmol Mn)	60	14387.5	41823.2	25.6	74.4
Vial 5 <sup>b</sup> 5.0 mg of <b>34</b> (37.95 μmol Mn)	60	16614.5	48623.7	25.5	74.5
Vial 6 <sup>b</sup> 5.3 mg of <b>34</b> (40.23 μmol Mn)	60	16859.9	48626.0	25.7	74.3
Vial 7 <sup>c</sup> 5.1 mg of <b>34</b> (38.71 μmol Mn)	10	9425.3	35507.5	21.0	79.0
	20	7201.6	27183.2	20.9	79.1
	30	7861.1	29454.8	21.0	79.0
	40	5421.4	20466.8	20.9	79.1
	50	5106.1	19285.7	20.9	79.1
	60	3637.8	13754.6	20.9	79.1

<sup>a</sup> The oxide sample was suspended in 5 mL of a 0.25 M Ce<sup>IV</sup> solution in a septum vial. Over a period of 60 min. a gas sample of the headspace of the septum vial was injected every 10 min. to the GC.

<sup>b</sup> The oxide sample was suspended in 5 mL of a 0.25 M Ce<sup>IV</sup> solution in a septum vial. After 60 min. a single gas sample of the headspace of the septum vial was injected to the GC.

<sup>c</sup> The oxide sample was suspended in 5 mL HNO<sub>3</sub> (pH ≈ 1.7). Over a period of 60 min. a gas sample of the headspace of the septum vial was injected every 10 min. to the GC.

**Table A.43. Results of headspace gas chromatography of Ca<sub>12h</sub>-birnessite (35).**

	t/min	area (O <sub>2</sub> )/ $\mu\text{V} \cdot \text{s}$	area (N <sub>2</sub> )/ $\mu\text{V} \cdot \text{s}$	O <sub>2</sub> /%	N <sub>2</sub> /%
Vial 1 <sup>a</sup> 5.4 mg of 35 (24.46 $\mu\text{mol}$ Mn)	10	11445.1	41294.5	21.7	78.3
	20	7859.6	26980.0	22.6	77.4
	30	9127.2	29834.3	23.4	76.6
	40	7788.1	24220.6	24.3	75.7
	50	6846.1	20330.6	25.2	74.8
	60	5088.1	14439.6	26.1	73.9
Vial 2 <sup>a</sup> 6.2 mg of 35 (28.09 $\mu\text{mol}$ Mn)	10	10351.9	37494.9	21.6	78.4
	20	11198.4	38497.2	22.5	77.5
	30	9752.5	32015.2	23.3	76.7
	40	7830.4	24570.6	24.2	75.8
	50	7150.7	21501.7	25.0	75.0
	60	5485.9	15789.2	25.8	74.2
Vial 3 <sup>a</sup> 5.0 mg of 35 (22.65 $\mu\text{mol}$ Mn)	10	13558.3	49221.7	21.6	78.4
	20	11777.6	40825.0	22.4	77.6
	30	9530.1	31799.9	23.1	76.9
	40	7638.4	24637.8	23.7	76.3
	50	6985.6	21698.2	24.4	75.6
	60	5662.7	16919.2	25.1	74.9
Vial 4 <sup>b</sup> 5.1 mg of 35 (23.10 $\mu\text{mol}$ Mn)	60	14451.9	45831.2	24.0	76.0
Vial 5 <sup>b</sup> 5.2 mg of 35 (23.56 $\mu\text{mol}$ Mn)	60	14512.4	46320.5	23.9	76.1
Vial 6 <sup>b</sup> 5.2 mg of 35 (23.56 $\mu\text{mol}$ Mn)	60	15599.9	50564.3	23.6	76.4
Vial 7 <sup>c</sup> 4.9 mg of 35 (22.20 $\mu\text{mol}$ Mn)	10	12936.6	48533.7	21.0	79.0
	20	6378.6	24065.4	21.0	79.0
	30	7765.2	29249.5	21.0	79.0
	40	5270.5	19895.2	20.9	79.1
	50	5042.7	19037.5	20.9	79.1
	60	4236.9	16000.6	20.9	79.1

<sup>a</sup> The oxide sample was suspended in 5 mL of a 0.25 M Ce<sup>IV</sup> solution in a septum vial. Over a period of 60 min. a gas sample of the headspace of the septum vial was injected every 10 min. to the GC.

<sup>b</sup> The oxide sample was suspended in 5 mL of a 0.25 M Ce<sup>IV</sup> solution in a septum vial. After 60 min. a single gas sample of the headspace of the septum vial was injected to the GC.

<sup>c</sup> The oxide sample was suspended in 5 mL HNO<sub>3</sub> (pH  $\approx$  1.7). Over a period of 60 min. a gas sample of the headspace of the septum vial was injected every 10 min. to the GC.

**Table A.44. Results of headspace gas chromatography of Ca<sub>24h</sub>-birnessite (36).**

	t/min	area (O <sub>2</sub> )/μV · s	area (N <sub>2</sub> )/μV · s	O <sub>2</sub> /%	N <sub>2</sub> /%
Vial 1 <sup>a</sup> 5.3 mg of <b>36</b> (47.44 μmol Mn)	10	10730.2	38773.3	21.7	78.3
	20	11119.2	37889.5	22.7	77.3
	30	7664.0	24873.9	23.6	76.4
	40	7978.5	24735.9	24.4	75.6
	50	6875.4	20327.2	25.3	74.7
	60	5238.0	14782.1	26.2	73.8
Vial 2 <sup>a</sup> 4.9 mg of <b>36</b> (43.86 μmol Mn)	10	13524.4	48387.5	21.8	78.2
	20	11814.4	39746.9	22.9	77.1
	30	8745.4	28023.4	23.8	76.2
	40	3136.5	9662.3	24.5	75.5
	50	6311.4	18536.7	25.4	74.6
	60	4817.0	13433.4	26.4	73.6
Vial 3 <sup>a</sup> 5.1 mg of <b>36</b> (45.65 μmol Mn)	10	12076.4	43095.3	21.9	78.1
	20	9867.3	33057.6	23.0	77.0
	30	9668.4	30659.0	24.0	76.0
	40	7754.9	23239.7	25.0	75.0
	50	4536.5	12918.7	26.0	74.0
	60	4176.8	11283.2	27.0	73.0
Vial 4 <sup>b</sup> 5.7 mg of <b>36</b> (51.02 μmol Mn)	60	13462.8	41268.1	24.6	75.4
Vial 5 <sup>b</sup> 4.9 mg of <b>36</b> (43.86 μmol Mn)	60	16081.3	49210.5	24.6	75.4
Vial 6 <sup>b</sup> 4.9 mg of <b>36</b> (43.86 μmol Mn)	60	13143.9	40873.3	24.3	75.7
Vial 7 <sup>c</sup> 4.9 mg of <b>36</b> (43.86 μmol Mn)	10	13221.5	49568.3	21.1	78.9
	20	8075.9	30395.4	21.0	79.0
	30	8364.3	31463.0	21.0	79.0
	40	6962.9	26214.7	21.0	79.0
	50	5648.9	21295.8	21.0	79.0
	60	4465.6	16858.0	20.9	79.1

<sup>a</sup> The oxide sample was suspended in 5 mL of a 0.25 M Ce<sup>IV</sup> solution in a septum vial. Over a period of 60 min. a gas sample of the headspace of the septum vial was injected every 10 min. to the GC.

<sup>b</sup> The oxide sample was suspended in 5 mL of a 0.25 M Ce<sup>IV</sup> solution in a septum vial. After 60 min. a single gas sample of the headspace of the septum vial was injected to the GC.

<sup>c</sup> The oxide sample was suspended in 5 mL HNO<sub>3</sub> (pH ≈ 1.7). Over a period of 60 min. a gas sample of the headspace of the septum vial was injected every 10 min. to the GC.

**Table A.45. Results of headspace gas chromatography of Ca<sub>48h</sub>-birnessite (37).**

	t/min	area (O <sub>2</sub> )/ $\mu\text{V} \cdot \text{s}$	area (N <sub>2</sub> )/ $\mu\text{V} \cdot \text{s}$	O <sub>2</sub> /%	N <sub>2</sub> /%
Vial 1 <sup>a</sup> 5.0 mg of 37 (44.05 $\mu\text{mol}$ Mn)	10	13667.1	48480.6	22.0	78.0
	20	11982.8	39387.7	23.3	76.7
	30	8260.0	25500.1	24.5	75.5
	40	8423.3	24481.7	25.6	74.4
	50	7361.2	20152.4	26.8	73.2
	60	4428.2	11418.7	27.9	72.1
Vial 2 <sup>a</sup> 5.0 mg of 37 (44.05 $\mu\text{mol}$ Mn)	10	13653.5	49503.1	21.6	78.4
	20	11843.2	40079.2	22.8	77.2
	30	10244.3	32715.1	23.8	76.2
	40	8925.5	27024.8	24.8	75.2
	50	7805.0	22432.3	25.8	74.2
	60	5607.6	15350.9	26.8	73.2
Vial 3 <sup>a</sup> 5.2 mg of 37 (45.81 $\mu\text{mol}$ Mn)	10	14079.7	50452.3	21.8	78.2
	20	12308.6	41183.5	23.0	77.0
	30	10703.1	33828.1	24.0	76.0
	40	8610.9	25926.8	24.9	75.1
	50	7821.6	22397.2	25.9	74.1
	60	6856.3	18675.5	26.9	73.1
Vial 4 <sup>b</sup> 5.0 mg of 37 (44.05 $\mu\text{mol}$ Mn)	60	15412.4	45160.9	25.4	74.6
Vial 5 <sup>b</sup> 5.5 mg of 37 (48.46 $\mu\text{mol}$ Mn)	60	16756.7	48677.3	25.6	74.4
Vial 6 <sup>b</sup> 6.6 mg of 37 (58.15 $\mu\text{mol}$ Mn)	60	17105.0	48262.7	26.2	73.8
Vial 7 <sup>c</sup> 5.1 mg of 37 (44.93 $\mu\text{mol}$ Mn)	10	8486.9	31973.1	21.0	79.0
	20	9756.4	36677.0	21.0	79.0
	30	8094.4	30431.6	21.0	79.0
	40	6627.3	24960.8	21.0	79.0
	50	5536.0	20868.9	21.0	79.0
	60	4478.6	16905.4	20.9	79.1

<sup>a</sup> The oxide sample was suspended in 5 mL of a 0.25 M Ce<sup>IV</sup> solution in a septum vial. Over a period of 60 min. a gas sample of the headspace of the septum vial was injected every 10 min. to the GC.

<sup>b</sup> The oxide sample was suspended in 5 mL of a 0.25 M Ce<sup>IV</sup> solution in a septum vial. After 60 min. a single gas sample of the headspace of the septum vial was injected to the GC.

<sup>c</sup> The oxide sample was suspended in 5 mL HNO<sub>3</sub> (pH  $\approx$  1.7). Over a period of 60 min. a gas sample of the headspace of the septum vial was injected every 10 min. to the GC.

**Table A.46. Results of headspace gas chromatography of Ca<sub>120h</sub>-birnessite (38).**

	t/min	area (O <sub>2</sub> )/ $\mu\text{V} \cdot \text{s}$	area (N <sub>2</sub> )/ $\mu\text{V} \cdot \text{s}$	O <sub>2</sub> /%	N <sub>2</sub> /%
Vial 1 <sup>a</sup> 5.6 mg of <b>38</b> (53.48 $\mu\text{mol Mn}$ )	10	13592.8	48392.4	21.9	78.1
	20	11986.6	39735.7	23.2	76.8
	30	10357.5	32419.2	24.2	75.8
	40	8305.5	24687.3	25.2	74.8
	50	7567.7	21375.6	26.1	73.9
	60	6697.4	17940.2	27.2	72.8
Vial 2 <sup>a</sup> 4.9 mg of <b>38</b> (46.80 $\mu\text{mol Mn}$ )	10	942.3	3426.9	21.6	78.4
	20	4898.5	16744.3	22.6	77.4
	30	7291.6	23346.9	23.8	76.2
	40	6560.8	19718.0	25.0	75.0
	50	5742.8	16270.9	26.1	73.9
	60	5021.0	13392.9	27.3	72.7
Vial 3 <sup>a</sup> 5.7 mg of <b>38</b> (54.44 $\mu\text{mol Mn}$ )	10	13157.9	46132.3	22.2	77.8
	20	11962.5	38540.7	23.7	76.3
	30	8730.8	26240.2	25.0	75.0
	40	6940.7	19641.3	26.1	73.9
	50	7357.8	19585.4	27.3	72.7
	60	5958.2	14897.0	28.6	71.4
Vial 4 <sup>b</sup> 5.2 mg of <b>38</b> (49.66 $\mu\text{mol Mn}$ )	60	16362.3	49019.1	25.0	75.0
Vial 5 <sup>b</sup> 4.9 mg of <b>38</b> (46.80 $\mu\text{mol Mn}$ )	60	12593.0	38290.6	24.7	75.3
Vial 6 <sup>b</sup> 6.5 mg of <b>38</b> (62.08 $\mu\text{mol Mn}$ )	60	16740.4	48625.2	25.6	74.4
Vial 7 <sup>c</sup> 5.4 mg of <b>38</b> (51.57 $\mu\text{mol Mn}$ )	10	13332.2	49972.6	21.1	78.9
	20	11092.4	41592.2	21.1	78.9
	30	9193.2	34528.9	21.0	79.0
	40	7406.2	27864.2	21.0	79.0
	50	4800.8	18120.3	20.9	79.1
	60	4703.3	17752.2	20.9	79.1

<sup>a</sup> The oxide sample was suspended in 5 mL of a 0.25 M Ce<sup>IV</sup> solution in a septum vial. Over a period of 60 min. a gas sample of the headspace of the septum vial was injected every 10 min. to the GC.

<sup>b</sup> The oxide sample was suspended in 5 mL of a 0.25 M Ce<sup>IV</sup> solution in a septum vial. After 60 min. a single gas sample of the headspace of the septum vial was injected to the GC.

<sup>c</sup> The oxide sample was suspended in 5 mL HNO<sub>3</sub> (pH  $\approx$  1.7). Over a period of 60 min. a gas sample of the headspace of the septum vial was injected every 10 min. to the GC.

**Table A.47. Results of headspace gas chromatography of Ca<sub>168h</sub>-birnessite (39).**

	t/min	area (O <sub>2</sub> )/ $\mu\text{V} \cdot \text{s}$	area (N <sub>2</sub> )/ $\mu\text{V} \cdot \text{s}$	O <sub>2</sub> /%	N <sub>2</sub> /%
Vial 1 <sup>a</sup> 5.8 mg of <b>39</b> (44.66 $\mu\text{mol}$ Mn)	10	7111.9	25621.7	21.7	78.3
	20	10692.7	36038.3	22.9	77.1
	30	9517.6	30157.1	24.0	76.0
	40	8275.6	24816.9	25.0	75.0
	50	7076.2	20087.9	26.0	74.0
	60	6276.5	16851.8	27.1	72.9
Vial 2 <sup>a</sup> 6.5 mg of <b>39</b> (50.05 $\mu\text{mol}$ Mn)	10	8796.1	31589.3	21.8	78.2
	20	10919.2	36621.6	23.0	77.0
	30	9678.2	30491.8	24.1	75.9
	40	8368.2	24917.5	25.1	74.9
	50	6226.8	17572.3	26.2	73.8
	60	4653.9	12425.7	27.2	72.8
Vial 3 <sup>a</sup> 5.1 mg of <b>39</b> (39.27 $\mu\text{mol}$ Mn)	10	8617.5	31290.9	21.6	78.4
	20	9704.7	33266.4	22.6	77.4
	30	9353.9	30336.0	23.6	76.4
	40	8047.2	24776.6	24.5	75.5
	50	6848.6	20018.9	25.5	74.5
	60	5861.7	16225.4	26.5	73.5
Vial 4 <sup>b</sup> 9.4 mg of <b>39</b> (72.38 $\mu\text{mol}$ Mn)	60	11297.0	33788.0	25.1	74.9
Vial 5 <sup>b</sup> 5.2 mg of <b>39</b> (40.04 $\mu\text{mol}$ Mn)	60	13608.9	43034.8	24.0	76.0
Vial 6 <sup>b</sup> 5.5 mg of <b>39</b> (42.35 $\mu\text{mol}$ Mn)	60	13608.9	39409.0	24.0	76.0
Vial 7 <sup>c</sup> 4.9 mg of <b>39</b> (37.73 $\mu\text{mol}$ Mn)	10	8731.5	32878.5	21.0	79.0
	20	9956.2	37410.0	21.0	79.0
	30	5053.6	19085.1	20.9	79.1
	40	5741.0	21656.3	21.0	79.0
	50	4928.5	18593.6	21.0	79.0
	60	3918.7	14798.1	20.9	79.1

<sup>a</sup> The oxide sample was suspended in 5 mL of a 0.25 M Ce<sup>IV</sup> solution in a septum vial. Over a period of 60 min. a gas sample of the headspace of the septum vial was injected every 10 min. to the GC.

<sup>b</sup> The oxide sample was suspended in 5 mL of a 0.25 M Ce<sup>IV</sup> solution in a septum vial. After 60 min. a single gas sample of the headspace of the septum vial was injected to the GC.

<sup>c</sup> The oxide sample was suspended in 5 mL HNO<sub>3</sub> (pH  $\approx$  1.7). Over a period of 60 min. a gas sample of the headspace of the septum vial was injected every 10 min. to the GC.

**Table A.48. Results of headspace gas chromatography of Ca<sub>240h</sub>-birnessite (40).**

	t/min	area (O <sub>2</sub> )/ $\mu\text{V} \cdot \text{s}$	area (N <sub>2</sub> )/ $\mu\text{V} \cdot \text{s}$	O <sub>2</sub> /%	N <sub>2</sub> /%
Vial 1 <sup>a</sup> 5.1 mg of <b>40</b> (59.98 $\mu\text{mol Mn}$ )	10	13461.0	48703.2	21.7	78.3
	20	11774.3	40576.3	22.5	77.5
	30	10169.8	33578.3	23.2	76.8
	40	8812.9	27943.7	24.0	76.0
	50	7258.4	22093.9	24.7	75.3
	60	6510.8	19006.9	25.5	74.5
Vial 2 <sup>a</sup> 5.3 mg of <b>40</b> (62.33 $\mu\text{mol Mn}$ )	10	13372.9	48406.5	21.6	78.4
	20	11549.2	39793.0	22.5	77.5
	30	9391.4	30938.7	23.3	76.7
	40	8374.5	26429.3	24.1	75.9
	50	7368.8	22219.5	24.9	75.1
	60	6091.3	17468.7	25.9	74.1
Vial 3 <sup>a</sup> 5.7 mg of <b>40</b> (67.03 $\mu\text{mol Mn}$ )	10	13465.5	48430.3	21.8	78.2
	20	6587.8	22516.2	22.6	77.4
	30	6613.0	21516.6	23.5	76.5
	40	7433.9	22900.2	24.5	75.5
	50	6657.7	19329.6	25.6	74.4
	60	5218.7	14294.8	26.7	73.3
Vial 4 <sup>b</sup> 5.2 mg of <b>40</b> (61.15 $\mu\text{mol Mn}$ )	60	15554.6	49721.5	23.8	76.2
Vial 5 <sup>b</sup> 5.0 mg of <b>40</b> (58.80 $\mu\text{mol Mn}$ )	60	15262.7	48080.3	24.1	75.9
Vial 6 <sup>b</sup> 5.1 mg of <b>40</b> (59.98 $\mu\text{mol Mn}$ )	60	16080.2	49385.6	24.6	75.4
Vial 7 <sup>c</sup> 5.5 mg of <b>40</b> (64.68 $\mu\text{mol Mn}$ )	10	4226.1	16034.6	20.9	79.1
	20	9272.2	34896.8	21.0	79.0
	30	7799.1	29337.7	21.0	79.0
	40	6455.0	24315.8	21.0	79.0
	50	5383.5	20300.6	21.0	79.0
	60	4497.5	16977.6	20.9	79.1

<sup>a</sup> The oxide sample was suspended in 5 mL of a 0.25 M Ce<sup>IV</sup> solution in a septum vial. Over a period of 60 min. a gas sample of the headspace of the septum vial was injected every 10 min. to the GC.

<sup>b</sup> The oxide sample was suspended in 5 mL of a 0.25 M Ce<sup>IV</sup> solution in a septum vial. After 60 min. a single gas sample of the headspace of the septum vial was injected to the GC.

<sup>c</sup> The oxide sample was suspended in 5 mL HNO<sub>3</sub> (pH  $\approx$  1.7). Over a period of 60 min. a gas sample of the headspace of the septum vial was injected every 10 min. to the GC.

## A.4 Oxygen-evolution traces detected in water-oxidation experiments using $(Ru^{III}(bpy)_3)^{3+}$ as oxidant

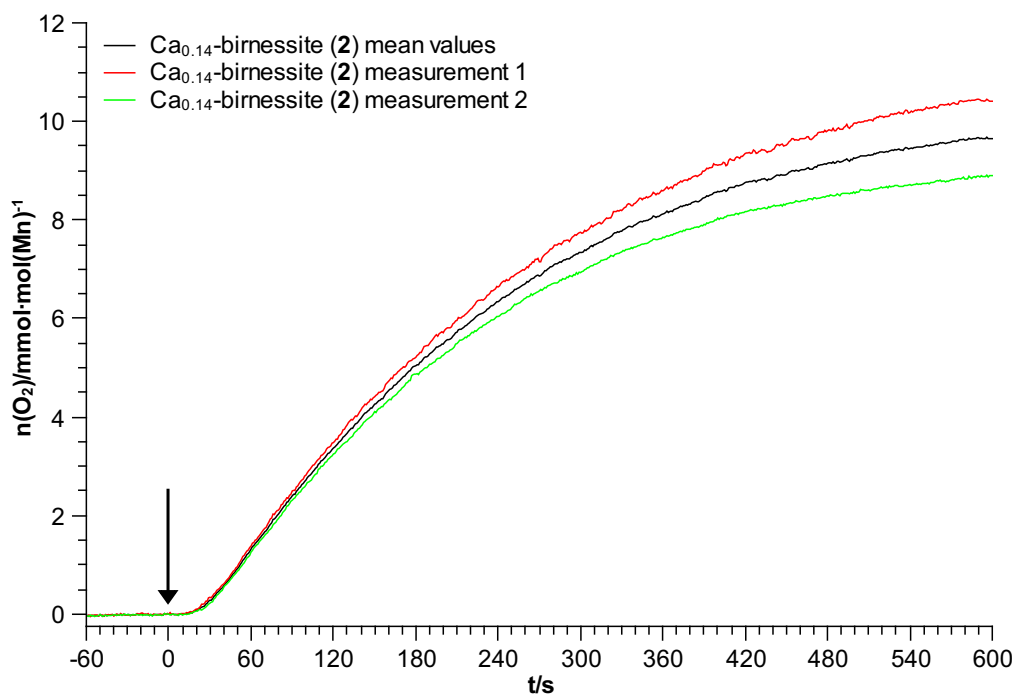


**Figure A.1.** Oxygen evolution traces recorded for **2**, using  $(Ru^{III}(acbp)_3)^{3+}$  as oxidant. Light was switched on at  $t=0$  s (indicated by the arrow).

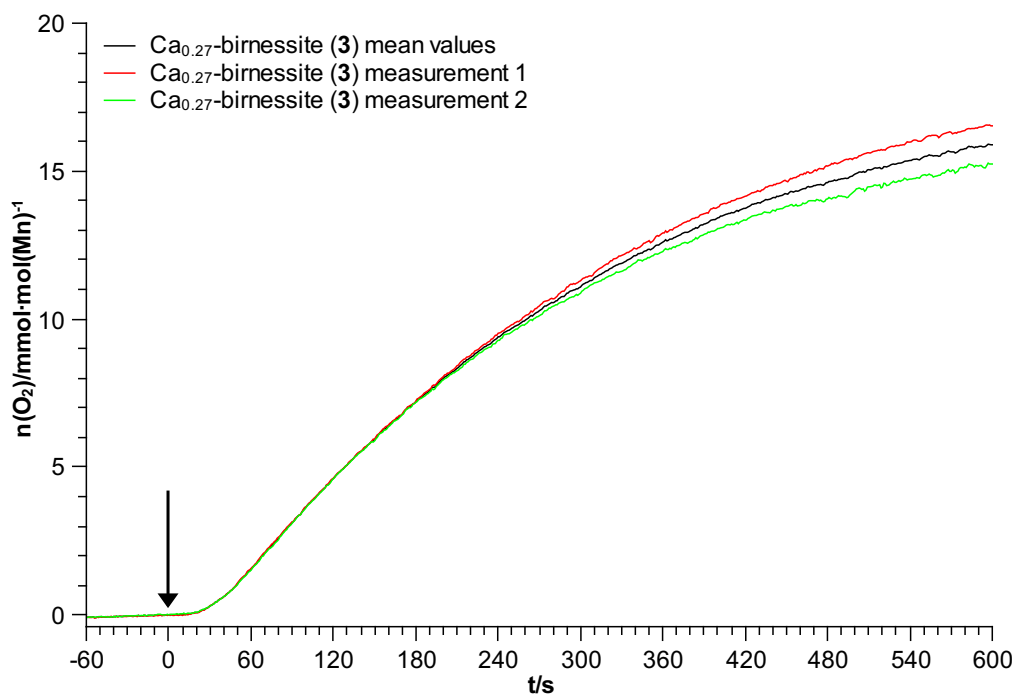


**Figure A.2.** Oxygen evolution traces recorded for **3**, using  $(Ru^{III}(acbp)_3)^{3+}$  as oxidant. Light was switched on at  $t=0$  s (indicated by the arrow).

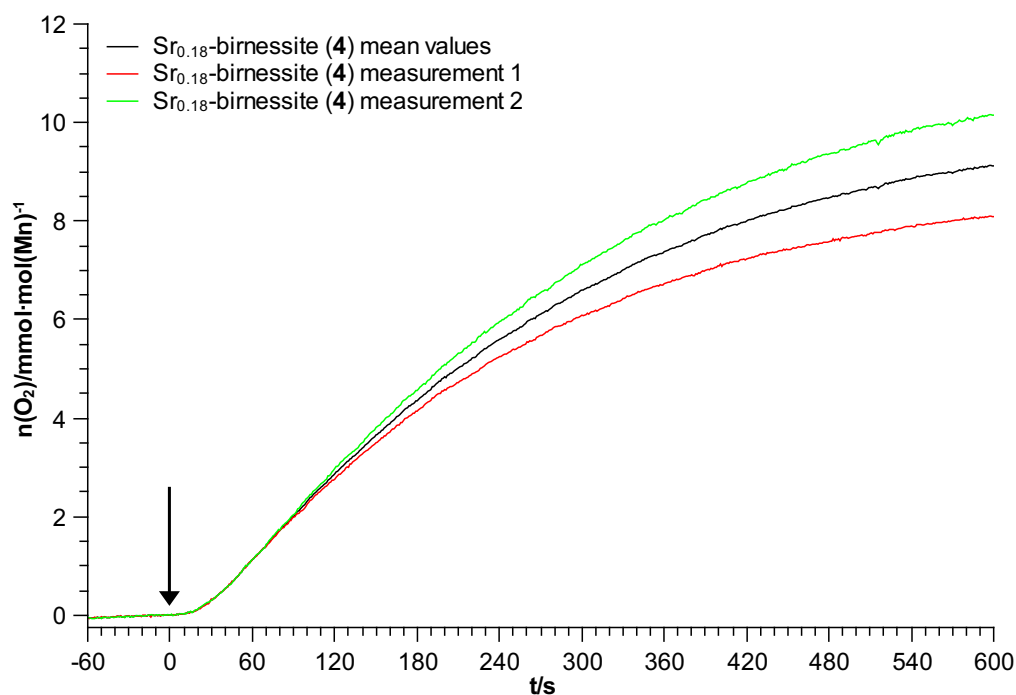


**Figure A.3.** Oxygen evolution traces recorded for **4**, using  $(\text{Ru}^{\text{III}}(\text{acbp})_3)^{3+}$  as oxidant. Light was switched on at  $t=0$  s (indicated by the arrow).

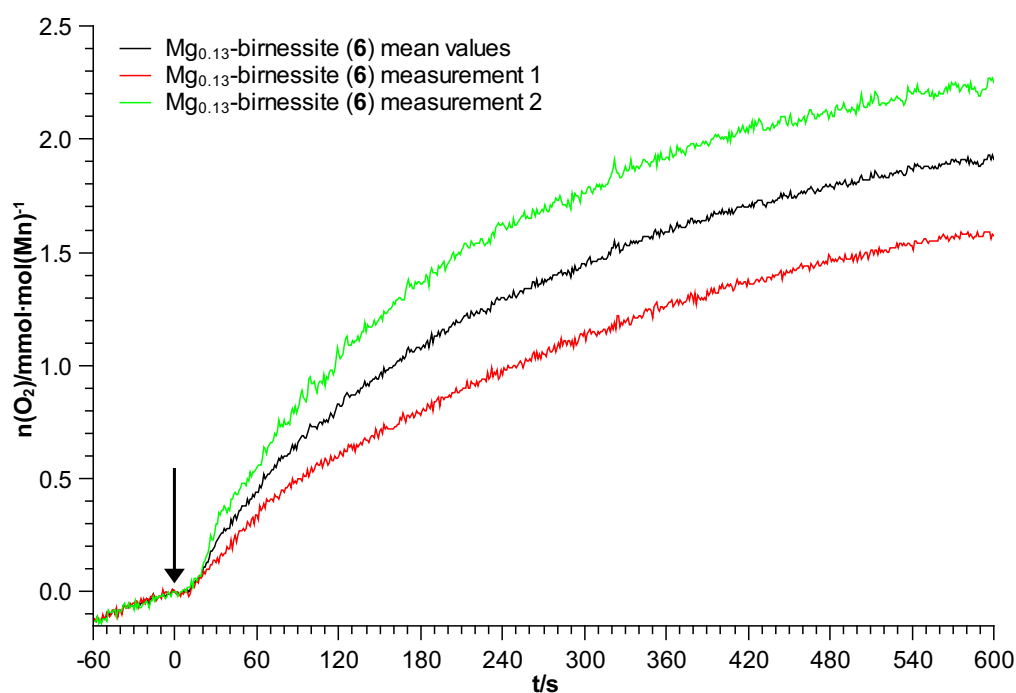


**Figure A.4.** Oxygen evolution traces recorded for **6**, using  $(\text{Ru}^{\text{III}}(\text{acbp})_3)^{3+}$  as oxidant. Light was switched on at  $t=0$  s (indicated by the arrow).

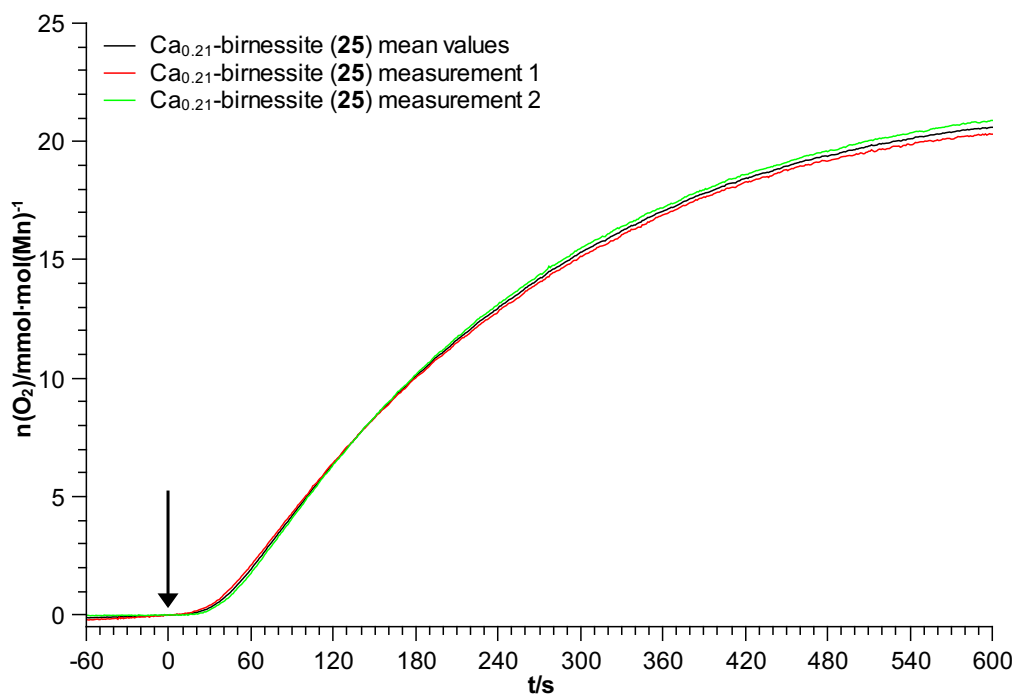


**Figure A.5.** Oxygen evolution traces recorded for **25**, using  $(Ru^{III}(acbp)_3)^{3+}$  as oxidant. Light was switched on at  $t=0$  s (indicated by the arrow).

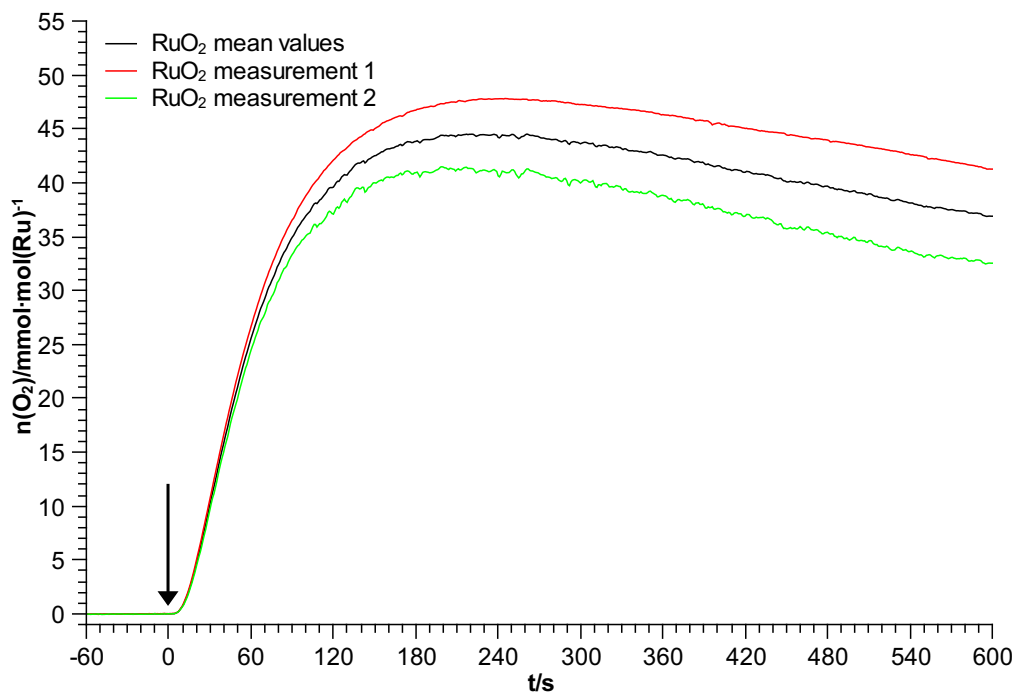


**Figure A.6.** Oxygen evolution traces recorded for  $RuO_2$ , using  $(Ru^{III}(acbp)_3)^{3+}$  as oxidant. Light was switched on at  $t=0$  s (indicated by the arrow).



# Acknowledgements

To accomplish the research project presented in this thesis wouldn't have been possible without the encouragement and support of many persons. Thus, I would like to thank the people at the Institute for Inorganic Chemistry at Christian-Albrechts-Universität Kiel. I would particularly like to thank:

- Prof. Dr. Felix Tuczek for giving me the opportunity to be a part of his team and for his general support of my research project
- Prof. Dr. Philipp Kurz for his patient mentoring, the helpful discussions, having always an open door and for encouraging me to follow own ideas during the research project carried out as a member of his group
- Prof. Dr. Holger Dau and Dr. Ivelina Zaharieva for the fruitful collaboration, kind discussions and helpful suggestions
- Prof. Dr. Wolfgang Bensch, Prof. Dr. Norbert Stock and Prof. Dr. Christian Näther for providing their equipment and Michael Hinz, Antje Modrow, Felix Niefind, Matthias Regus, Nele Reimer, Helge Reinsch and Christian Stoltenberg for support of the analysis of the prepared manganese oxides
- Hans-Martin Berends and Anne Westphal for their kind integration of me as a member of the Kurz team
- Anne-Marie Manke for much more than being a nice colleague
- Bruce Seung Young Lee for spreading his enthusiasm in the laboratory
- Stephan Bernt for all the conversations and for reviewing the manuscript of this thesis
- John Djamil for a nice conference trip and all the discussions on water-splitting and beyond
- the Tuczek team, in particular Henning Broda, Christian Gradert, Svea Hinrichsen, Sven O. Schmidt, Ludger Söncksen and Thomas Weyrich
- Monika Schneeweiß and Ursula Cornelissen for their support of AAS and IR spectroscopy
- Ralf Suren and his team and Peter Puddig for their technical support
- the students who worked together with me in our research laboratory: Igor Kunz, Benjamin Reinke, Anne Päplow, Sebastian Zimmermann, Michael Poschmann, Sebastian Mangelsen, Jan Schumacher, Stephan Segler, Joss Wiese, Thorben Reinert and Sabine Stanke
- FCI and DFG for financial support



## Curriculum vitae

Born in Steinheim (Westphalia) in 1982, Mathias Wiechen grew up in Gießen and later in Arnsberg-Neheim where he received his higher education entrance qualification in 2002 at the St.-Ursula-Gymnasium Neheim.

After his school days he started to study chemistry at the Technische Universität Dortmund in 2003, where he developed an interest in biochemistry. During his undergraduate studies, he focused on DNA chemistry as well as bioinorganic chemistry. In 2008 he completed his diploma degree with a thesis on self assembled DNA-nanostructures at solid surfaces under the mentoring of Dr. Barbara Saccà and Prof. Dr. Christof M. Niemeyer.

In 2009 he started his graduate studies on the investigation of manganese oxides for bioinspired water-oxidation catalysis at the Institute for Inorganic Chemistry at the Christian-Albrechts-Universität Kiel in the Kurz group. As a member of this group, he participated in several research conferences on water-splitting catalysis and alternative energy production as a poster presenter and also as a speaker. This research project was finished in early 2013.





# Eidesstattliche Erklärung

Hiermit erkläre ich, Mathias Wiechen, an Eides statt, dass diese Abhandlung – abgesehen von der Beratung durch meine Betreuer, Prof. Dr. Philipp Kurz und Prof. Dr. Felix Tuczek – nach Inhalt und Form meine eigene Arbeit ist.

Diese Arbeit hat weder ganz, noch zum Teil einer anderen Stelle im Rahmen eines Prüfungsverfahrens vorgelegen und ist nicht veröffentlicht worden oder zur Veröffentlichung eingereicht. Des weiteren erkläre ich, dass die Arbeit unter Einhaltung der Regeln guter wissenschaftlicher Praxis der Deutschen Forschungsgemeinschaft entstanden ist.



Mathias Wiechen